Development of laser spectroscopy for scattering media applications

Andersson, Mats

2007

Development of Laser Spectroscopy for Scattering Media Applications

Mats Andersson

Doctoral Thesis
2007

Lund University

Development of Laser Spectroscopy for Scattering Media Applications

Printed in Sweden by Media-Tryck, Lund, 2007

Division of Atomic Physics
Department of Physics
Faculty of Engineering, LTH
Lund University
P.O. Box 118
SE–221 00 Lund
Sweden

http://www.atom.fysik.lth.se

ISSN 0281-2762
Lund Reports on Atomic Physics, LRAP-383

ISBN: 978-91-628-7252-6

Better late than never

Abstract

Laser spectroscopy for both large and small spatial scales has been developed and used in various applications ranging from remote monitoring of atmospheric mercury in Spain to investigation of oxygen contents in wood, human sinuses, fruit, and pharmaceutical solids. Historically, the lidar group in Lund has performed many differential absorption lidar (DIAL) measurements with a mobile lidar system that was first described in 1987. During the years the lidar group has focused on fluorescence imaging and mercury measurements in the troposphere. Five lidar projects are described in this thesis: fluorescence imaging measurement outside Avignon, France, a unique lidar project at a mercury mine in Almadén, Spain, a SO_2 flux measurement at a paper mill in Nymölla, Sweden, and two fluorescence imaging projects related to remote monitoring of vegitation and building facades characterization.

A new method to measure wind speed remotely in combination with DIAL measurements is presented in this thesis. The wind sensor technique is called videography and is based on that images of plumes are grabbed continuously and the speed is estimated by the use of image processing.

A technique that makes it possible to measure a gas in solids and turbid media, non-intrusively, is presented in this thesis. The technique is called gas in in scattering media absorption spectroscopy (GASMAS) and has been used since 2001. The GASMAS concept means that a traditional spectroscopy instrument, based on tunable diode lasers, is used but the gas cell or optical path is replaced by a material that strongly scatters light. Mostly, wavelength modulation spectroscopy has been utilized. Four projects using the GASMAS technique to measure gases in fruit, wood, pharmaceutical solids, and human tissue are presented. Two applications have shown a great potential so far; to be able to diagnose the health of human sinuses and gas ventilation in sinuses, and to measure gas inside pharmaceutical solids. A performance analysis of the GASMAS technique is included. This thesis also presents a technique to suppress optical noise in fiber lasers and how to construct a compact tunable diode laser spectroscopy system based on plug-in boards for a standard computer.

Populärvetenskaplig sammanfattning

I Nationalencyklopedin står det att spektroskopi är en metod för att studera molekyler, atomer och atomkärnor med hjälp av dess spektra. Man använder både elektromagnetisk strålning och partikelstrålning inom spektroskopin. Spektroskopi används inom astronomi, kemi, fysik och medicin. Ordet spektroskopi kommer ifrån latinet och betyder "att titta" vilket förklaras av att historiskt sett så använde man endast synligt ljus för att studera gaser, vätskor och fast kroppar.

Alla ting absorberar och sprider elektromagnetisk strålning olika vilket förklarar varför bladet är grönt, varför himlen är blå osv. när de belyses av solljus. Solljuset innehåller som bekant alla regnbågens färger. Samma sak gäller gaser som absorberar ljus med färgfördelning som är beroende på typ av gas, tryck, temperatur osv. Man brukar säga att en gas har ett fingeravtryck vilket nyttjas inom laserbaserad spektroskopi där lasern ställs in, likt en radiosändare, på den våglängd hos gasen som man vill mäta på.

I denna avhandling används uteslutande laserbaserad spektroskopi för att studera koncentrationen av gaser i atmosfären och i fasta material som frukt, trä, växter och mänsklig vävnad. Syftet med avhandlingen är att utveckla och använda laserbaserade metoder för att mäta gaser i atmosfären och i fasta kroppar. Avhandlingen beskriver ett antal projekt där metoder används och utvecklas successivt. Det finns också beskrivet projekt som beskriver mätningar av fluorescens hos organiska växter och byggnader.

För att mäta gaser i atmosfären används en optisk radar där sändaren består av en kraftig laser som skickar ut korta ljuspulser i atmosfären. Teknikens utveckling påbörjades på 1960-talet och kallas för lidar (light detection and ranging). En liten del av ljuset reflekteras i atmosfären av små partiklar (aerosoler) och når ett teleskop där ljuset samplas in. Denna effekt kan även ses om man går ut en mörk kväll och lyser rakt upp med en ficklampa. Man kan då se ljuskäglan eftersom små partiklar i luften reflekterar

ljuset tillbaka. Genom att växelvis skicka ut ljus som absorberas och som inte absorberas av aktuell gas kan koncentrationen av gaser som t.ex. ozon, svaveldioxid och kvicksilver mätas. Det är en utrustning som, om den placeras i ett flygplan, kan användas för att mäta på ozonhålet vid Nordpolen. Exempel på projekt som beskrivs är mätningar i Spanien där koncentrationen av kvicksilver vid en kvicksilvergruva studerades och mätning av svaveldioxidutsläpp vid ett pappersbruk i Nymölla, Sverige.

I avhandlingen beskrivs även en ny metod för mätning av gaser i fasta och spridande material som växter, frukt, trä och mänsklig vävnad. Metoden kallas för GASMAS (Gas in Scattering Media Absorption Spectroscopy) och forskningen initierades 2001 på avdelning för atomfysik på Lunds Universitet. Principen bygger på att laserljus skickas in i ett fast spridande material samtidigt som laserljuset sveps över den våglängd där den aktuella gasen absorberar ljus. Förloppet kan liknas med hur en operasångare testar sin röst genom att sjunga kontinuerliga skalor. En optisk detektor samlar in ljuset efter det har "skramlat runt" i provet. När laserljusets våglängd sammanträffar med gasens fingeravtryck dämpas ljuset något mer vilket är precis vad vi mäter; desto mer gas desto mer dämpning. Observera att det rör sig om mycket små förändringar av ljusstyrkan när en absorptionstopp passeras. Vi talar om en liten förändring på en del av 100000. Alltså krävs det att utrustningen är känslig. Det som ytterst begränsar metoden är hur bra ljuset tränger in i det fasta materialet. Med hjälp av GASMAS-tekniken har vi bl.a. undersökt farmaceutiska tabletter och bihålor i kind- och pannben. GASMAS-tekniken gör det möjligt att studera gasinnehållet i fasta material utan ingrepp vilket är att föredra.

Under arbetets gång har mycket tid och kraft ägnats åt att förbättra GASMAS-metoden ur teknisk synvinkel. Då det mesta av ljuset sprids och dämpas är det endast en bråkdel som når den optiska detektorn, kanske en del på 1000. Samtidigt ska en liten absorptionssignal på en del på 100000 detekteras vilket ökar utmaningen ytterligare. Avhandlingen beskriver de tekniska metoder som har använts för att nå dessa mål.

List of Publications

This thesis is based on the following papers, which will be referred to by their roman numerals in the text.

I **Remote monitoring of vegetation by spectral measurements and multi-colour fluorescence imaging**
M. Andersson, H. Edner, P. Ragnarsson, J. Johansson, S. Svanberg, and E. Wallinder.
Proc. Physical Measurements and Signatures in Remote Sensing, 835–842, Val d'Isère, France (1994).

II **Remote fluorescence measurements of vegetation spectrally resolved and by multi-colour fluorescence imaging**
J. Johansson, M. Andersson, H. Edner, J. Mattsson, and S. Svanberg.
J. Plant Physiol. **148**, 632–637 (1996).

III **A preliminary experiment on the remote sensing of historical buildings by fluorescence Lidar**
P. Weibring, M. Andersson, G. Cecchi, H. Edner, J. Johansson, L. Pantani, V. Raimondi, B. Sundnér and S. Svanberg.
SPIE **3222**, 372–382 (1997).

IV **Atmospheric mercury concentrations and fluxes in the Almadén district (Spain)**
R. Ferrara, B.E. Maserti, M. Andersson, H. Edner, P. Ragnarson, S. Svanberg, and A. Hernandez.
Atmos. Env. **32**, 3897–3904 (1998).

V **Remote monitoring of industrial emissions by combination of lidar and plume velocity measurements**
P. Weibring, M. Andersson, H. Edner and S. Svanberg.
Appl. Phys. B **66**, 383–388 (1998).

VI **Studies of gas exchange in fruits using laser spectroscopic techniques**
L. Persson, B. Anderson, M. Andersson, M. Sjöholm, and S. Svanberg.
Proceedings of FRUITIC 05, Information and Technology for Sustainable Fruits and Vegetable Production., 543–552, Montpellier, France (September 2005).

VII **Spectroscopic studies of wood-drying processes**
M. Andersson, L. Persson, M. Sjöholm, and S. Svanberg.
Optics Express **14**, 3641–3653 (2006).

VIII **Human sinus studies using monte carlo simulations and diode laser gas absorption spectroscopy**
L. Persson, E. Kristensson, L. Simonsson, M. Andersson, K. Svanberg, and S. Svanberg.
Proceedings of the International Symposium of Biophotonics, Nanophotonics and Metamaterials, 95-98, Hangzhou, China (October 2006).

IX **Approach to optical interference fringes reduction in diode laser absorption spectroscopy**
L. Persson, F. Andersson, M. Andersson, and S. Svanberg.
Appl. Phys. B **87**, 523–530 (2007).

X **Non-invasive characterization of pharmaceutical solids by diode laser oxygen spectroscopy**
T. Svensson, L. Persson, M. Andersson, S. Andersson-Engels, S. Svanberg, J. Johansson, and S. Folestad.
Appl. Spec. **61**, 784–786 (2007).

XI **Laser spectroscopy of gas in scattering media at scales ranging from kilometers to millimeters**
M. Andersson, R. Grönlund, L. Persson, M. Sjöholm, K. Svanberg, and S. Svanberg.
Laser Physics **17**, 893-902 (2007).

XII **Gas monitoring in human sinuses using tunable diode laser spectroscopy**
L. Persson, M. Andersson, M. Cassel-Engquist, K. Svanberg, and S. Svanberg.
Accepted by J. Biomed. Optics, (2007).

XIII **Flexible lock-in detection system based on synchronized computer plug-in boards applied in sensitive gas spectroscopy**
M. Andersson, L. Persson, T. Svensson, and S. Svanberg.
Submitted, (2007).

Abbreviations

AD	Analogue to digital (converter)
APD	Avalanche photodiode
DA	Digital to Analogue (converter)
DFB	Distributed Feedback
DIAL	Differential absorption lidar
DSP	Digital signal processing
ENBW	Equivalent noise bandwidth
FPGA	Field-programmable gate array
FWHM	Full width at half maximum
FFT	Fast-Fourier transform
GASMAS	Gas in scattering media absorption spectroscopy
Laser	Light amplification by stimulated emission of radiation
LED	Light Emitting Diode
Lidar	Light detection and ranging
OPA	Optical parametric amplifier
OPO	Optical parametric oscillator
PID	Proportional-integral-derivative (controller)
PMT	Photomultiplier tube
PSD	Power spectral density
RAM	Residual amplitude modulation
RIN	Relative intensity noise
RMS	Root mean square
SFDR	Spurious-free dynamic range
SNR	Signal-to-noise-ratio
SODAR	Sound detection and ranging
TDLS	Tunable diode laser spectroscopy
VCSEL	Vertical cavity surface emitting laser

Contents

Papers

Chapter 1

Introduction

Almost every day newspapers and TV programs discuss pollution and environmental health. Today this is a common issue that affects all countries and all people. Pollution can be found in soil, air, and water. During the last two decades there has been a new focus on pollution. Following September 11, 2001, Travis et al. over three days studied what impact airplanes have on the global climate by analyzing data from 4000 weather stations [1]. During these three days, airplanes in the US were grounded after the attack on the World Trade Center in New York, USA. Travis et al. could show that the average three-day temperature changed by 1.8 °C. This increase, which is more than two standard deviations from the mean value, was unique in the data recorded over thirty years. Other research groups have noted that the global sun irradiance has decreased gradually over the years by measuring the sun light irradiance daily during the period 1956 till 1987 [2]. The reported intensity drop between 1956 and 1987 was 18 %. The effect that causes reduced radiation intensity on earth is called global dimming and is probably due to air pollution, mainly aerosols. Global dimming has a cooling effect on the temperature on earth and probably masks the true effect of global warming. Thus, the impact on earth due to human activities is no doubt serious. Combustion of fuels is one of the largest contributors to global warming and to related environmental problems such as increased ozone concentration near the ground. In May 9, 1992, the United Nations Framework Convention on Climate Change (UNFCCC or FCCC) produced a document which countries can sign, making a long-term "non-binding aim" agreement to reduce atmospheric concentrations of greenhouse gases. This was later known as the Kyoto protocol that was set up in Kyoto, in 1997.

Sources of air pollution sources are in many cases difficult to find and map. Emissions are transported by wind and mixed with other species and aerosols. New species are created by chemical

reactions making it extremely difficult to understand where and how a pollution source affects the environment. Thus there is an increasing demand for good atmospheric studies and powerful remote sensing technologies. Today this task is more important than ever and is frequently discussed by people working for the Kyoto protocol. Tools to probe the atmosphere are mainly radar, lidar, and sodar [3, 4].

At the same time, people are affected by the indoor environment that in some cases has a worse quality than the outdoor air [5]. Today, houses are made of new materials to save energy and to decrease the cost of heating. Moisture and fungi are commonly a problem connected with indoor pollution. An increase of allergy, asthma, and inflammation of the human sinuses is probably connected to "sick" houses and un-natural substances in food, packages and building materials. Gases in building materials and also human sinus health are difficult to measure since the gas cavities are embedded in solids or turbid media such as tissue. Thus, there is also a need for improved probing measurement techniques that can be used to measure indoor quality and human health.

Historically, it has not been possible or very difficult to measure the gas (water vapor, oxygen etc.) content inside a material such as pharmaceutical solids, food, wood, and organic material such as human tissue. On the other hand liquid water contents in food and wood have been studied for decades. In 2001, a new technique was presented by the Atomic Physics Division in Lund making it possible to measure gas in scattering material non-invasively. The technique is based on the fact that laser light penetrates the material and the detected light is analyzed. The core of the measurement technique is that the laser light is absorbed by the gas in the sample. So far, test samples such as foam, food products, wood, pharmaceutical solids, and human tissue have been successfully tested by the use of the GASMAS technique.

1.1 Remote sensing based on Lidar

The lidar technology has over the years proved to be one of the most efficient tools for measuring gases in the atmosphere. Lidar stands for light detection and ranging and is basically a radar system that works with light instead of micro waves. The lidar technology makes it possible to map a number of species (also aerosols) in the atmosphere by sending out light pulses at the resonance wavelength of a species.

The lidar technology has been known for 60 years. It was first used in the 1930's to examine aerosols in the stratospheric layer. However, it took another thirty years until the lidar technology took a big step forward. In the 1960's the laser was invented and it has since worked as a transmitter in lidar equipment. During

the 1960's and the 1970's researchers developed lidar techniques for many atmospheric studies, where the differential absorption lidar (DIAL) has proved to be the most efficient technique to measure concentrations of species. During the 1980's and 1990's new laser technologies appeared and more complete systems were demonstrated. Lidar systems that measure hydrocarbons have also been demonstrated [6, 7]. Meanwhile researchers found new applications. During the past twenty years, lidar development has been focused on the following applications [8, 9]:

- aerosol distribution and properties (lidar)
- polar stratospheric clouds (PSCs) (lidar)
- clouds (lidar)
- water vapor (DIAL) stratospheric ozone layer (DIAL)
- atmospheric temperature and pressure (lidar and DIAL)
- wind speeds(lidar)
- pollutant mapping in the troposphere (DIAL)
- fluorescence from plants (lidar)
- hydrospheric measurements (lidar)
- fluorescence from buildings (lidar)

The atmospheric studies are divided into local, ground-based measurements, and global lidar atmospheric studies from the air and from space. The global studies are mainly run by NASA which performs several lidar measurements from airplanes, satellites, and from ground-based systems. NASA studies are mainly of the stratosphere and the upper troposphere. Typical interests are global environmental properties like aerosol distribution, water vapor, cloud studies, and ozone layer studies. Normally, each system is specialized to perform one task. It is no exaggeration to say that NASA and ESA dominate all lidar measurements from aeroplanes and satellites. The local atmosphere studies are performed by mobile systems in trucks or by in-door systems. Several comparison campaigns between different systems have been performed. Ground-based systems have larger possibilities to perform all kinds of lidar studies. A ground-based lidar system is easier to construct, run, and maintain. Furthermore, the majority of species are found near the ground.

The general aim of lidar development is to construct better tools for mapping the environment. Even if there have been advances made in developing and applying lidar systems to atmospheric and hydrospheric studies, there is still much work to be

done before lidar technology can make a large impact on the general market. Still, most systems require highly-trained people for their operation and the price is high (about one million dollars for a mobile system).

The key to success is still to develop a laser which is capable of transmitting tunable light in the UV, in the visible region, and in the IR region. Improvement in laser stability, reliability, and cost are also important steps to be taken. There is an increasing demand for low-cost mobile lidar systems which map all pollutants of interest. Today, O_3, NO, NO_2, SO_2, Hg, and toluene are the only tropospheric species measured by an ultra-violet lidar system. The resonance wavelengths of these species are found in the ultra-violet region, except NO_2 which is measured by visible light. The future looks promising, though. The fast development of non-linear materials has pushed the OPO/OPA (Optical Parameter Oscillator/Amplifier) technology forward. With OPOs most wavelengths of interest are covered. Thus, more species will be studied.

1.2 Non-invasive gas sensing in solids based on GASMAS

A relatively new spectroscopic technique has been developed to measure gas concentrations in solids and turbid media [10]. The Gas in Scattering Media Absorption Spectroscopy (GASMAS) technique is based on tuneable diode laser spectroscopy but the gas cell is replaced by a turbid solid medium that contains gas/gases. By guiding modulated laser light into a solid material, a weak gas imprint can be detected by placing an optical detector on the opposite side of the incident light, or a short distance from the laser light entrance into the material. Thus, a measurement gives information about internal gas concentrations times an expected spreading distance. Typical applications are measurements on wood, tissue (human sinuses), fruit, food packaging, pharmaceutical solids etc. Important information can be recorded that describes the health status of human sinuses, wood drying processes, gas ventilation in different wood material, in fruits and human sinuses, and characterizes of physical and structural parameters of pharmaceutical solids. So far oxygen and water vapor gas concentrations have been measured by the use of the GASMAS technique.

1.3 The aim and outline of this thesis

The aim of this work was to push the lidar and the GASMAS technique forward via development and measurements. My task was also to find new applications and to introduce techniques used in other research areas, i.e., telecommunication and acoustics. In the

beginning of my work I focused on improvement, in collaboration with a colleague, of electronics, computer control, data acquisition, and data analysis of a current lidar system at the department. A lidar system creates a lot of data and it takes highly-trained personnel to analyze and understand the measured data. A user-friendly lidar system, based on modern software, was developed in order to improve these steps. The work with upgrading the current lidar system is briefly presented in Chap. 7 and a detailed description is found in Ref. [11]. In Papers **I** and **II** remote point and image monitoring of laser-induced fluorescence from vegetation is described. Paper **III** presents an initial remote point monitoring of laser-induced fluorescence of historical buildings. A lidar campaign in Spain that focused on mercury mapping is presented in Paper **IV**. Mercury fluxes, measured by a mobile lidar system, are presented and compared with data recorded by mercury point detectors. In Paper **V** gas flux measurements of SO_2 with a combination of differential absorption lidar (DIAL) and a new wind speed detection technique are performed. Continuous images of the plume at the smoke stack are grabbed and analyzed automatically to sense the true wind speed of the plume. This was the first time the upgraded lidar system (presented in Chap. 7) was used in a campaign.

In Paper **VI** gas exchange in fruits, using the GASMAS technique, is presented. Before a measurement, a fruit was exposed to nitrogen or oxygen. The oxygen gas content was measured while the fruit was exposed to air and the gas transport was studied dynamically. Paper **VII** continues with spectroscopic measurements on wood while drying. Two GASMAS setups were used to measure oxygen and water vapor gas content in wood. Paper **VIII** is a feasibility study that presents the potential to carry out non-intrusive, in-vivo, human sinus studies by the use of the GASMAS technique. Measurements on a tissue-like phantom were performed and the results were compared with simulated data.

In 2006 we started to work with pigtailed lasers. A pigtailed laser consists of a laser and a fiber that is closely connected to the laser by the laser manufacturer. Paper **IX** presents a technical and mathematical framework to suppress optical interference that is often introduced when fiber lasers are used. In Paper **X** the potential of using GASMAS for the determination of physical and structural parameters of pharmaceutical solids is presented. Paper **XII** is an extensive study to measure the oxygen and water vapor gas content in human sinuses. Human sinus measurements based on the GASMAS technique were performed on eleven volunteers. Paper **XIII** describes a compact digital lock-in detection system for spectroscopy measurements based on coherent sampling. The system consists of two plug-in computer boards to be run on a standard computer. The aim of this work was to develop a flexible, powerful, and compact system to be used in diode

laser spectroscopy. Paper **XI** is a review article that covers recent progress in Lidar and GASMAS research at our department.

As mentioned at the beginning of this chapter, Travis et al. presented unique data based on a three-day long measurement campaign. Sometimes the time and effort behind the publication of such a unique piece of research is forgotten. My focus has always been to try to understand the physics behind the measured data and try to obtain a model of the phenomena. To do this, recording low noise data is crucial and it takes time to develop a system that measures exactly what you think it does. A lot of time should be spent on trying to specify the required performance of the measurement system and break down the system into submodules, i.e., detector module, front-end electronics etc. before a new system is built. Thus, proper knowledge and support in software development, electronics, optics, mechanics and measurement techniques are crucial. Another important fact is that it is necessary to know how to verify the required performance of each subsystem. What use is it to specify a specific performance task if you are not able to measure it? A good example of this fact is the lack of proper relative intensity noise (RIN) values of a new laser. Often, these required performance data are not available to the customer. In this thesis a lot of effort has been spent on upgrading the current lidar system and developing a flexible lock-in detection system described in Paper **XIII**.

Chapter 2

Light Propagation in Scattering Media

Visible light is a part of the electromagnetic spectrum and wavelengths range from about 400 nm to 750 nm, which is the wavelength range that can be seen by man. Radiation with a wavelength from 750 nm to 1400 nm is called near infrared (NIR), while radiation with an even longer wavelength ranging from 1400 nm to 1 mm is called infrared (IR). If the wavelength is even longer the waves are called microwaves (1 mm to 30 cm) or radio waves (30 cm to 1000 m). Normally, microwaves and radio waves are defined by frequency instead of wavelength. If the light wavelength is shorter than 400 nm it is called ultraviolet (UV). At even shorter wavelengths we speak of X-rays or gamma-rays, as shown in Fig. 2.1. The theory behind electromagnetic waves is complex and described by Maxwell's equations and quantum mechanics. Either light is seen as a particle or it is handled as a wave. When to use the different theories depends on the application. As shown in Fig. 2.1 both the wavelength and the frequency scale are presented. The relation between frequency and wavelength is given by c= $\lambda \times f$, where c is the speed of light, λ is the wavelength of the light, and f is the frequency of the light. Normally, the frequency scale is used for longer wavelengths (radio waves and microwaves) while the wavelength scale is used for light. However, there exist several units to describe the wavelength, e.g., the inverse of the wavelength expressed in cm^{-1} and the energy of a photon expressed in eV. The cm^{-1} entity is normally used for waves in the IR, the visible, and the UV while the eV entity is used for the X-ray range, and the gamma-ray range.

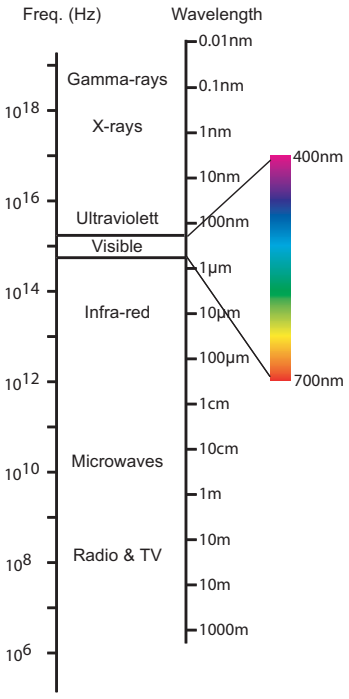

Figure 2.1. *The electromagnetic spectrum ranges from radio long-waves to gamma-rays.*

When light is treated as particles we talk about photons. A photon may be seen as an elementary particle that carries electromagnetic radiation. According to the particle theory a photon has

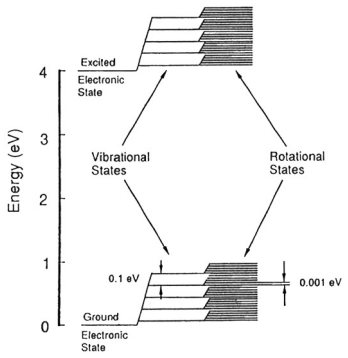

Figure 2.2. *Energy levels of a molecule; from [12].*

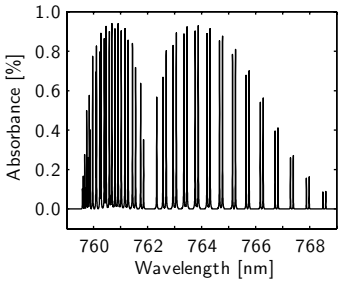

Figure 2.3. *Absorption spectrum for O_2 gas in air (33 cm path) simulated in Hitran [13].*

no mass and it travels with the speed of light and with a specific wavelength. The energy of a photon is given by

$$E = \frac{hc}{\lambda}, \tag{2.1}$$

where λ is the wavelength of a light photon, c is the speed of light, and h is Planck's constant. Light is normally treated as a wave for radio and microwaves while it is treated as both a particle and a wave for shorter wavelengths such as IR light, visible light etc.

2.1 Light absorption

When light photons propagate in gases, liquids, and solids they are absorbed and scattered at the same time. Light absorption means that a photon transfers its energy to molecules (and atoms) of the medium. This process is complex and highly dependent on the wavelength of the incident light, pressure, and temperature. Each material has unique properties regarding the wavelengths at which an energy transfer can take place and what the transition probability is for each energy transition. In atoms and molecules a number of energy states exist and photons can be absorbed only if its energy corresponds to the energy difference between two valid energy states. The slightest change of incident photon wavelength, pressure, and temperature will change the absorption properties of the scattering medium. The energy levels and transition probabilities for atoms and molecules are described by quantum mechanics.

Energy levels in atoms and molecules are basically divided into three main groups as shown in Fig. 2.2. In atoms, electronic state transitions give rise to emission in the visible or the UV range. As shown in Fig. 2.2, molecules have additional states due to vibration and rotation. When changes of states occur a forest of possible sharp transitions that correspond to photon wavelengths in the near infrared and the infrared are observed. An example of how light is absorbed at different wavelengths is shown in Fig. 2.3 corresponding to a 33 cm path through normal air and due to vibrational-rotation energy transitions in oxygen gas.

The *line strength* (line intensity)of an absorption line is determined by the transition probability of the transition in question, the population ratio between the two energy states that corresponds to the absorption line. The transition probability is determined by quantum mechanics with the so-called selection rules as its simplest manifestation. The population ratio between the states is determined by the Boltzmann distribution factor that is highly dependent on temperature. At higher temperatures the effective ground state absorption of a sample decreases since not all particles are situated in the lower state.

The light absorption in a gas is proportional to the distance the light has traveled in the sample and the partial pressure of the gas. If an electromagnetic wave with an intensity $I_0(\nu)$ and a frequency ν is transmitted through an absorbing medium the detected intensity $I(\nu)$ and the incident intensity $I_0(\nu)$ are related according to

$$I(\nu) = I_0(\nu)e^{-\sigma(\nu)NL}. \tag{2.2}$$

Eq. (2.2) is called the Beer-Lambert law. L is the length of the path (m), N is the density of the absorbing molecules (molecules/cm^3), and $\sigma(\nu)$ is the absorption cross-section for one molecule (cm^2/molecule). In some applications the factor $-\sigma(\nu)N$ is replaced by the absorption coefficient μ_a which simplifies Eq. (2.2) which becomes

$$I(\nu) = I_0(\nu)e^{-\mu_a L}. \tag{2.3}$$

The absorption coefficient is a measure of the mean distance between two absorption events.

2.2 Spectral lineshapes

According to the Heisenberg uncertainty relation the width of an absorption line is connected to the lifetime τ of the exited state. A short lifetime of an exited state results in a smeared energy level and thus a broader absorption line. As an example the lifetime of an electronic state is typically in the order of 10^{-6} s and 10^{-9} s. These values correspond to a linewidth of about 0.1 MHz and 100 MHz, respectively [14]. In theory, a measurement of the gas concentration is only valid if the area of the absorption lineshape is taken into account.

A linewidth, determined by the Heisenberg uncertainty relation, sets the lower limit of how narrow a line can be. The shape of such an absorption line is Lorentzian. Even at low pressures, the lineshape is broadened due to the Doppler effect (thermal motion of atoms and molecules). At higher pressures, atoms and molecules collide and energy is transferred between them which affects the lifetime of the exited states. Thus, the lifetime of the exited state is shortened and the lineshape is broadened. The width of an absorption line is normally expressed as the full width at half maximum (FWHM) which is also called the linewidth. At a low pressure, the line profile related to Doppler broadening is Gaussian and given by

$$\Delta\nu_D = 7.16 \times 10^{-7}\nu_0\sqrt{\frac{T}{M}}, \tag{2.4}$$

where $\Delta\nu_D$ is the linewidth, ν_0 is the laser frequency in question (Hz), T is the temperature (K), and M is the molecular mass. As

shown in *Eq.* (2.4), the linewidth is increased with increased temperature. At a high pressure, the absorption line has a Lorentzian lineshape and a linewidth $\Delta\nu_L$ according to

$$\Delta\nu_L = (\frac{T_0}{T})^n \sum_i \gamma_i p_i(T_0), \tag{2.5}$$

where T_0 is a reference temperature (K), T is the actual temperature, n is a gas- and transition-dependent parameter for which a value of 0.5 is often used. γ_i is a gas-specific, pressure broadening coefficient and $p_i(T_0)$ is the partial pressure of each gas present. For an intermediate pressure the Voigt profile is applicable. However, the equation that describes the Voigt profile is complex and a simplification of the linewidth of a Voigt lineshape function is given by

$$\Delta\nu_V = \sqrt{(\Delta\nu_D^2 + \Delta\nu_L^2)}, \tag{2.6}$$

where $\Delta\nu_D$ and $\Delta\nu_L$ are the estimated linewidths according to Eq. (2.4) and Eq. (2.5). By estimating the ratio between $\Delta\nu_D$ and $\Delta\nu_L$ it can be decided if the line shape is Gaussian, Lorentzian or has a Voigt profile. This is simply done by the use of the Hitran database [13]. In Paper **VII** both molecular oxygen gas and water vapor inside a piece of wood were measured at atmospheric pressure and room temperature. According to the Hitran database the linewidth (FWHM) for the oxygen line used, R7R7 (761.003 nm) is 3.0 GHz for a Lorentzian, 0.9 GHz for a Gaussian, and 3.2 GHz for a Voigt lineshape. The calculated ratio between the Lorentzian and the Gaussian linewidth is about three. Thus, the oxygen line R7R7 has a Voigt profile at atmospheric pressure. Corresponding estimations for the water absorption line (978.509 nm) result in that the water line has a Lorentzian profile with a linewith of 5.4 GHz.

2.3 Light emission

Energy absorbed by atoms and molecules can be re-emitted as electromagnetic waves of characteristic wavelengths. This happens for gas at low pressure. Even if the incident electromagnetic wave is beam-shaped the spontaneously emitted light is radiated in all directions from the particles. As shown in Fig. 2.4 the absorbed energy may be re-emitted at the same wavelength (resonance radiation) or at several shorter wavelengths (fluorescence). At higher pressure non-radiative de-excitation due to collisions occurs with increase of the gas temperature. In solids and liquids non-radiative transitions are dominant. The internal conversion process is also a non-radiant process. In solids and liquids the energy bands are

smeared out due to the strong interactions. This is why the fluorescence spectrum is then smeared in wavelength. Each gas, liquid, and solid has its unique fluorescence spectrum that can be used to measure specific material characteristics. This is discussed in Sect. 6.6.

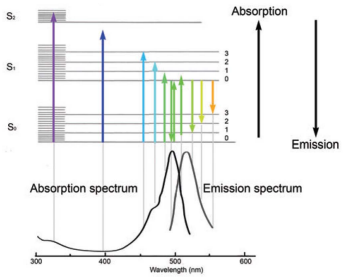

Figure 2.4. *Electromagnetic emissions via electronic and vibrational-rotational transitions; from [15].*

2.4 Light scattering

An electromagnetic wave can be scattered by a gas even if its wavelength does not match the energy-level transitions of the atom and molecules it hits. The scattering process is defined as *elastic* if the wavelength of the scattered light is equal to the wavelength of the incident light or *inelastic* if the wavelengths differ. Thus, for inelastic scattering, energy is transferred between the incident photon and the particles. Rayleigh and Mie scattering are elastic, while Raman scattering is inelastic. The scattering properties for molecular particles are characterized by the parameters $\mu_s(\mathrm{cm}^{-1})$, $\sigma_s(\mathrm{cm}^2)$, or the volume scattering coefficient β $(Wnm^{-1}sr^{-1})$. μ_s is mostly used in medical research while σ_s and β are used in lidar research.

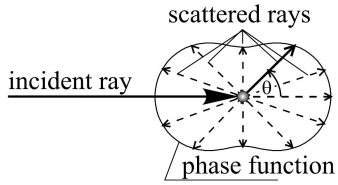

Figure 2.5. *Light distribution of Rayleigh scattered light; from [17].*

If the particles are very small compared to the wavelength (e.g. molecules) the process is called Rayleigh scattering. Rayleigh scattering is due to the electronic cloud in molecules oscillating in phase with the incident electromagnetic waves. Seen from the small molecule, the incident electromagnetic wave is spatially uniform and oscillates in time with a fixed frequency. Thus, a dipole moment is induced in the molecule with an oscillation with the same frequency as the incident electromagnetic wave. The result is that electromagnetic waves are created and transmitted with an intensity proportional to $1/\lambda^4$. A presentation of measurements to obtain true cross-sections for various gases is presented in Ref. [16]. However, if small particles ($\ll 1\mu$m) are considered instead of molecules, the intensity of light scattered by a small particle that is illuminated by an unpolarized light beam I_0, at wavelength λ, is according to Ref. [17] given by

$$I(R,\theta) = I_0(\lambda)\frac{1+\cos^2(\theta)}{2R^2}\left(\frac{2\pi}{\lambda}\right)^4\left(\frac{m^2-1}{m^2+2}\right)\left(\frac{r}{2}\right)^6. \qquad (2.7)$$

R is the distance to the particle, θ is the scattering or phase angle, m is the refractive index of the scattering particle, and r is the radius of the particle. The total cross-section for Rayleigh scattering can be obtained by integrating Eq. (2.7) over the entire solid angle [18]. As shown in Eq. (2.7), the intensity of Rayleigh scattered light is proportional to $1/\lambda^4$. The light distribution in space, due to Rayleigh scattering, is determined by the phase function $(1+\cos^2(\theta))$. A diagram of how light is scattered by molecules is shown in Fig. 2.5.

Figure 2.6. *A measurement of light scattered in a human head and sinuses by the use of a IR-LED (LED760/940-04A, Roithner Lasertechnik) and a IR-CCD camera (C5999, Hamamatsu). The light source is mounted in a similar position as explained in Paper* ***XII****.*

If the particles are much larger than the wavelength of the incident light the process is called Mie scattering. The Mie scattering process is much more complicated than the Rayleigh scattering and thus more difficult to describe. Mie scattering describes spherical particles, but in general, large particles of any shape create elastic scattering but the scattering diagram depends on particle size, the shape of the particles, and the wavelength of the incident light. Normally, in scattering diagrams light directed forward dominates in the scattering process. Mie scattering dominates the Rayleigh scattering in most applications [17]. The intensity of Mie scattered light is given by

$$I(R,\theta,r,n,\lambda) = I_0 \frac{\lambda^2(|S_1(\theta,r,n)| + |S_2(\theta,r,n)|)}{8\pi^2 R^2}, \tag{2.8}$$

where I_0 is the intensity of the incident light at wavelength λ, R is the distance to the large particle, θ is the scattering or phase angle, n is the refractive index of the particle, and r is the radius of the particle [17]. $S_1(\theta,r,n)$ and $S_2(\theta,r,n)$ are intensity functions based on Legendre polynomials, Riccati-Bessel functions, and spherical Bessel functions. Normally, the wavelength dependence of Mie scattering can be assumed to be proportional to λ^{-2}. This is one reason why the sky is blue since light of short wavelength is more scattered. However, this estimation is only approximative. A detailed description of the Mie theory is found in Refs [19–21].

To estimate light propagation in turbid and solid media such as tissue, three parameters (μ_a, μ_s, g) are often used to describe the characteristics of the medium. This is due to the fact that actual scattering media are often too complex for the use of equations such as Eq. (2.8). μ_a describes the absorption property while μ_s and g describe the scattering properties. The g constant is used in the Henyey-Greenstein phase function $p(\theta)$ and is basically the average of the cosine of the scattering angle. Thus, a g value close to one means that most light is forward-scattered. For a g value of zero, the scattering is isotropic. The Henyey-Greenstein phase function is used to characterize the angular distribution of scattered light in, for instance, tissue [22]. The phase function $p(\theta)$ is described by

$$p(\theta) = \frac{1-g^2}{2(1+g^2-2gcos(\theta))^{3/2}}. \tag{2.9}$$

To model light scattering in solids and in turbid media three different techniques can be used: radiative transport theory, diffusion models, and Monte Carlo simulations [23]. However, to obtain results for a complex model in three dimensions, Monte Carlo simulations run by standardized software are preferred. Today, ray-tracing tools such as FRED^{TM}, ASAP^{TM}, and TracePro^{TM}

all have built-in support for the Henyey-Greenstein phase function according to Refs [24–26]. In Paper **XII** the Advanced Systems Analysis Program ($ASAP^{TM}$) software was used to estimate how laser light is scattered in a human head.

Fig. 2.6 shows light from an IR-LED of about 5 mW being transmitted through the head of a human. Large intensity variations are measured due to the fact that a human skull is based on a complex structure consisting of bone, teeth, and tissue. Thus, to get a true model that reflects all the parameters of the head a more complex model can be developed. Fig. 2.7 shows that light in wood is not scattered symmetrically around the propagation axis as tissue does. The light is more scattered along the channels of the wood as shown in the figure. The shape of the intensity spot depends on the type of wood. It thus becomes obvious that to model light scattering in solids and turbid media is not simple.

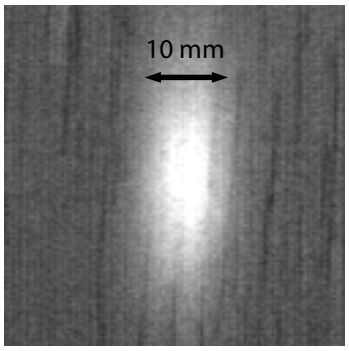

Figure 2.7. *A measurement of light scattered in a 10 mm thick balsa wood board by the use of a IR-LED (LED760/940-04A, Roithner Lasertechnik) and a IR-CCD camera (C5999, Hamamatsu). The light source is mounted behind the balsa wood board.*

Chapter 3

Gases in the Atmosphere and Solids

3.1 Properties of the atmosphere

The atmosphere contains primarily nitrogen, oxygen, and argon. Together, these species make up more than 99 % of the total content of dry air. However, the atmosphere also contains a number of gases that occur in small and variable amounts. Species like water vapor, carbon dioxide, and ozone are natural species of interest to monitor. Both natural and man-made sources of pollution exist. In Tab. 3.1 all the important gases are listed, arranged according to concentration level in a clean troposphere. Estimated pollutant levels are also shown. Furthermore, the table shows the approximate residence time in the atmosphere and in which region the resonance wavelength of each species is found. Both electronic and vibration-rotational transitions are considered.

Sulphur-containing compounds and aerosols were the first type of pollutants to disturb the environment. The combustion of coal with a high sulphur concentration resulted in the emission of sulphur dioxide (SO_2) in cities, where coal was used for heating and electric power generation. Even today, the emission of SO_2 is a big problem in eastern Europe, especially Poland and the Czech Republic. Emissions from internal combustion engines were the second type of air pollution observed. In 1945, the first urban air pollutant problem due to motor fuel was reported from Los Angeles; today air pollution from petrol and Diesel engines is a common problem in all large cities. Nitrogen compounds and hydrocarbons are also produced by engines. The chemical processes which control the balance in atmospheric are extremely complex. The atmosphere works as a reaction chamber where new species are created and others disappear through chemical reactions in differ-

Gas	Conc. clean air [ppm]	Conc. polluted air [ppm]	Residence time	Resonance wavelength region	DIAL
Nitrogen, N_2	780800	-	106 yr		
Oxygen, O_2	209460	-	10 yr	UV, NIR	X
Argon, Ar	9340	-	no cycle		
Carbon oxide, CO_2	332	350	15 yr	IR	X
Neon, Ne	18	-	no cycle		
Helium, He	5.2	-	10 yr		
Methane, CH_4	1.65	3	7 yr	IR	X
Krypton, Kr	1.1	-	no cycle		
Hydrogen, H_2	0.58	-	10 yr		
Nitrous oxide, N_2O	0.33	0.33	10 yr	IR	X
Carbon monoxide, CO	0.12	1-10	65 days	IR	X
Xenon, Xe	0.09	-	no cycle		
Ozone, O_3	0.02-0.08	0.1-0.5	?	UV, IR	X
Hydrocarbons, excl. CH_4	?	0.5-1.2	?	IR	X
Nitrogen oxides, NO_2	$(1\text{-}5)\times10^{-4}$	0.05-0.25	1 day	Visible, IR	X
Suphur dioxide, SO_2	0.001-0.01	0.02-0.1	40 days	UV, IR	X
Ammonia, NH_3	0.001	0.01-0.025	20 days	IR	X
Hydrogen sulphide, H_2S	2×10^{-4}	0.004	2 days		
HNO_3	$(0.2\text{-}3)\times10^{-4}$	0.003-0.05	1 day		
Nitrogen oxide, NO	$(1\text{-}5)\times10^{-5}$	0.05-0.75	1 day	UV, IR	X
Water vapour, H_2O	variable	-	10 days	NIR, IR	X

Table 3.1: *The most common gases in dry atmosphere at ground level. As shown in the figure all noble gases, except Helium, have no cycle. Helium is light and is diffused into space; adapted from [27, 28].*

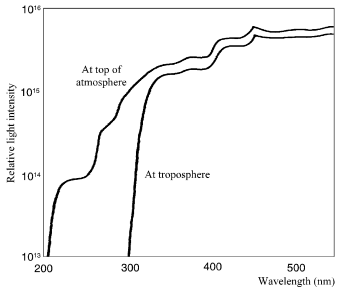

Figure 3.1. *The intensity of sun light in UV and part of the visible region measured at the top of the atmosphere and at low troposphere; from [29].*

ent layers. In order to understand how the emission of a pollutant affects the environment the whole atmosphere must be studied. A typical example is the ozone layer. Human activities disturb the ozone balance. Today, the stratospheric ozone layer at a height of 10-30 km is diminishing due to the emission of ozone-destroying gases, while the ozone concentration at ground level is too high due to the combustion of fossil fuel. Thus, different lidar measurements must be done simultaneously in order to understand the chemical processes. However, not all pollutant gases can be measured by a lidar system. This is due to facts such as a poor cross section or low concentration of the species, the resonance wavelength is difficult to produce, the absorption linewidth is too narrow, the resonance spectrum is too complex, major components of the atmosphere absorbs at the resonance wavelength, or the interest to measure the pollutant species is too low.

3.1.1 Ultraviolet and visible light absorption

For UV wavelengths, below 300 nm, the absorption of the natural species in the atmosphere has to be considered; see Fig. 3.1. O_3 and O_2 are the major absorbers. For wavelengths below 200 nm, the atmosphere totally blocks the light. The electronic absorption bands for most molecules other than O_2, O_3, SO_2, and NO_2 lie below 185 nm and cannot be measured by the lidar technique. However, in the UV region the resonance wavelength of Hg, SO_2, NO, O_3, and some aromatic hydrocarbons are found. In the visible

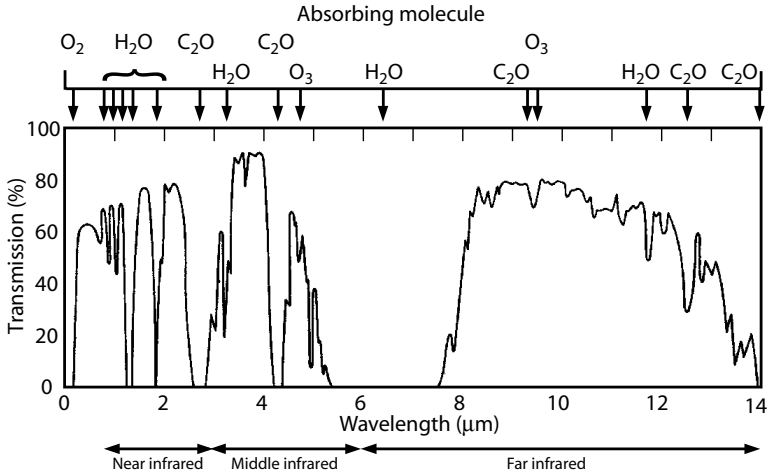

Figure 3.2. *IR transmission curve for the atmosphere; adapted from [30].*

region (400 - 700 nm), water vapor is the only absorber which can disturb a measurement. On the other hand, sunlight can be a problem since it is a strong background source. NO_2 is hard to measure in daylight, since the resonance wavelength spectrum of NO_2 is in the visible region (430 - 455 nm).

3.1.2 IR absorption

In the infrared region many atmospheric gases contribute to absorb the light, leaving only a few spectral windows that can be used for lidar measurements; see Fig. 3.2 and Tab. 3.1. CO_2 and H_2O are the major absorbers. These species have broad absorption bands in the IR region which are due to vibrational-rotation transitions. Furthermore, it is difficult to measure the concentration of molecules in the IR region by lidar since the back-scattered signal is proportional to λ^{-n}, with $1 \leq n \leq 3$ for aerosols (Mie scattering) and n=4 for molecules (Rayleigh scattering). This leads to back-scattered light from aerosols of medium density increasing the measurement range for lidar measurements on molecules in the IR region. The main back-scattering due to Rayleigh scattering depends on the dominating molecules N_2 and O_2. Molecules in the IR region can still be studied. The optical windows in the near infrared region are used for aerosol measurements. Lasers with 1 μm or 2 μm wavelengths are also used for wind lidar measurements. The Doppler shift of the back-scattered signal from aerosols is measured and thus the speed of the aerosols can be estimated. The 800 nm - 2 μm band is also used for water vapor

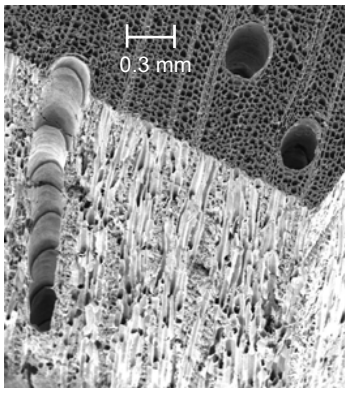

Figure 3.3. *A picture of Balsa wood taken with a sweeping electron microscope (x25 magnification). The diameter of the large channels (vessels) is about 150 - 200 μm.*

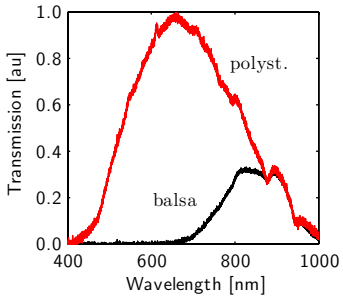

Figure 3.4. *Light transmission in dry balsa wood and polystyrene foam.*

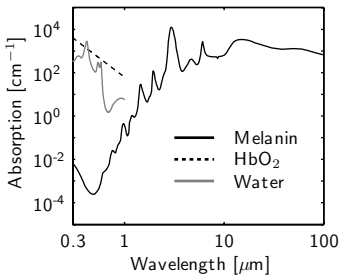

Figure 3.5. *Light absorption curves for liquid water, hemoglobin (HbO_2, and melanin [31, 32].*

measurements based on the differential absorption technique.

In the 3.1 - 3.4 μm band most hydrocarbon species have their vibrational-rotational transitions. In this band, species such as methane and propane are found. However, it is extremely difficult to measure these species since they often appear simultaneously and have overlapping absorption bands. Further up in the IR region, the resonance of O_3 and several complex species are found.

3.2 Properties of solid media

In theory, solids can contain any gas but this is normally not expected. Regardless of what is true, gas in solids is not a mature research field and more research is needed to gain knowledge of gas diffusion in solids. Normally, liquid water in solids is studied. In nature, solids are often based on a complex structure with pores making the material strong and light at the same time. A good example is wood. About 400 types of wood exist and balsa wood is the lightest type with a density of only 140 kg/m^3; see Fig. 3.3. As can seen in the figure, wood is full of small channels (cells). Normally, in a growing tree, most cells are filled with water and starch but this is not true of dried wood. Thus, wood and similar materials based on pores, are excellent materials for measurements of the internal content of, for example oxygen and water vapor by the use of the GASMAS technique. However, this is only possible if the light absorption in the scattering and absorbing material is low enough to let light penetrate the sample to reach the detector.

Fig. 3.4 shows that balsa wood absorbs visible light markedly more than polystyrene foam. A halogen lamp (LS-1, Ocean Optics) illuminates one side of a 15 mm piece of balsa wood or polystyrene foam while a spectrometer connected by a fiber (USB-4000, Ocean Optics) measures the light spectrum on the opposite side. The balsa wood absorbs visible light up to a wavelength of 650 nm. However, the polystyrene foam seems to attenuate light without a large wavelength dependance. The measured light spectrum, for the polystyrene foam is identical to the spectrum of the halogen light source. A dry piece of balsa wood contains less than 5 % of water and thus the cell walls inside the wood are almost dry. If the balsa wood is wet the light absorption is increased due to the fact that liquid water absorbs light, especially at long wavelengths, as shown in Fig. 3.5.

Fig. 3.5 shows the light absorption curves for liquid water, hemoglobin and melanin. Tissue absorbs light strongly and the influence of water, hemoglobin, and melanin is often studied in medical optics. As can be seen in Fig. 3.5, an optical window exists at around 630 - 1400 nm that makes it possible for light to penetrate into tissue. Thus, it should be possible to measure oxygen gas and water vapor in human cavities, for example, hu-

man sinuses, and lungs since the absorption lines for these gases are within that range. So far, GASMAS measurements have been carried out on human sinuses.

Chapter 4

Tunable Light Sources

Working with spectroscopy in the beginning of the 1960's must have been very exciting. In 1960 the first laser was demonstrated [33] and two years later the first diode lasers were developed at the same time by a number of research groups [34–37]. What makes a laser unique for spectroscopy is its spectral purity and its high output power in combination with the fact that certain varieties are tunable in wavelength. Today, lasers are commonly used in spectroscopy but this is not the main application. In daily life they are found in laser pointers, DVD players, optical storage devices, telecommunication systems, medical devices, bar code scanners etc. The list may be long but it is the diode laser that dominates the market, not advanced lasers for scientific use. The major applications that drive diode laser development forward are optical storage and telecommunication, as shown in Fig. 4.1. The use and the physics behind the diode laser is extensively covered in Refs [38–41] while the development of light-emitting sources are covered in Refs [41, 42].

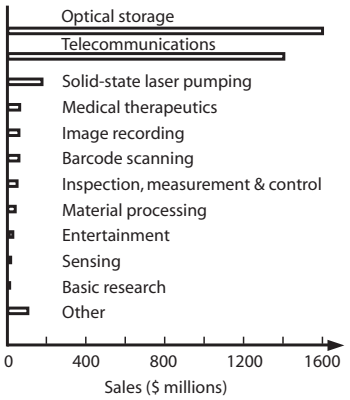

Figure 4.1. *The diode laser market in different application according to Laser Focus World 2007.*

Lidar system are normally based on high-power lasers but diode lasers may be used to pump high power lasers or act as the main transmitter in small portable systems. For ground-based and air-based DIAL measurements, tunable dye lasers, Titanium-doped sapphire, or optical parametric oscillator (OPO) lasers are usually used. In Papers **I-V** a Nd:YAG pumped dye laser has been used [43]. The Lidar system was later upgraded with an OPO laser [44]. These lasers have proved to be superior in most lidar applications. Lasers for satellite-borne lidar systems are highly specialized transmitters, which often require specific wavelengths and unusual pulse formats. They must also be highly automated and reliable to survive the environment in space. NASA develops solid state lasers to meet these needs. Typically, these lasers are specialized devices.

In gas in scattering media absorption spectroscopy (GASMAS), described in Chap. 6, tunable diode lasers are used due to their cost, size, and performance. In this application the laser is mounted closely to a scattering material which causes the laser to be exposed to backscattered light at a high level. Thus, the ultimate diode laser for GASMAS is a laser that is not affected by backscattered light. However, backscattered light does affect a diode laser and the Fabry-Pérot laser type seems to the most sensitive one. One solution is to add an optical isolator but that adds cost and complexity. Instead, it has been tested to tilt the laser to prevent backscattered light to reach the laser. Both Fabry-Pérot, distributed feedback (DFB), and vertical-cavity surface-emitting lasers (VCSELs) have been tested in GASMAS setups presented in the following papers.

4.1 Diode lasers

The first diode laser was made of pn-doped GaAs and it radiated coherently in the near infrared at 710 nm. The principle of the first diode laser is based on the fact that a p-n junction area is created when the p- and the n-doped material is mounted together. Since the laser consists of only one pn-junction it is called a homojunction diode laser. The electrons in the n-doped material recombine with holes in the p-doped material and form a junction area with a thickness of about 1-3 μm. When a forward bias current is applied the electron population in the conduction band and the hole in the valence band increases and light is emitted as electrons jump from the conduction to the valence band, as shown in Fig. 4.2. The wavelength λ of the light is determined by the band gap energy E_g of the semiconductor ($E_g = hc/\lambda$). This is the principle on which a light emitting diode (LED) functions.

In order to get a p-n junction to lase an optical feedback is required that reflects the emitted light back into the p-n junction. This action is carried out by mirrors or coated surfaces attached to the ends of the semiconductor, forming an optical resonator. In some cases cleaved facets are adequate to act as mirrors. The reflectivity of the end of a p-n junction can be about 30% due to the fact that GaAs have a very high refractive index. The forward bias current must be strong enough (above a threshold value) to achieve inverted population for the electrons in the semiconductor. When these conditions are met, the device starts to lase and its output is directly proportional to the forward bias current. The number of spontaneously emitted photons is also smaller than the stimulated photons. Until these two conditions are fulfilled, the diode laser acts as a light emitting diode only. The major drawback with the homojunction principle is that light is diffracted into and absorbed by the p- and the n-doped layer. Thus, this laser principle was used

for pulsed light only under cooled conditions. Otherwise, the laser became overheated.

In 1963, the homojunction design was followed by the double heterojunction principle by which the light was not scattered outside the junction layer [45]. The heterojunction diode laser is based on different semiconductors, with different refractive indices, being sandwiched together to form an optical wave guide along the p-n junction. This is the design that is used today and the common name of these lasers is Fabry-Pérot lasers. The forward bias current can be from a few mA to several hundreds of mA depending on the type of laser. Since the laser light is reflected inside a Fabry-Pérot resonator, several cavity modes exist along the longitudinal path. The wavelength spacing between two adjacent cavity modes is given by

$$\Delta\nu = \frac{c}{2nL}, \tag{4.1}$$

where $\Delta\nu$ is the mode separation of the laser, c is the speed of light, n is the refractive index of the p-n junction material, and L is the length of the cavity. In practice, the length of a typical Fabry-Pérot diode laser cavity is much longer than the wavelength of the light and the frequency shift between two following modes is about 150 GHz. More than one longitudinal laser mode is present when the forward bias current has reached the threshold, as seen in Fig. 4.3. This type of laser action is typical for a *multimode* laser.

If the temperature of the laser is changed, the length of the cavity is as well as the bandgap value changed. Thus, by changing the temperature of a Fabry-Pérot laser, the laser is tuned in wavelength. This technique is commonly used in diode laser absorption spectroscopy. An absorption line is scanned by changing the wavelength of the laser. The temperature of the laser may be controlled and changed using a Peltier-element to set the temperature of the laser can. The temperature can also be changed dynamically by superimposing a modulation signal to the laser current. Thus, fast wavelength scans are achieved by modulating the laser current.

If the temperature change is large, the changed length of the cavity causes the laser to jump to another laser longitudinal mode. Thus, the maximum continuous tuning range of a Fabry-Pérot laser is short, only half of the $\Delta\nu$ in Eq. (4.1) or about 75 GHz. This action of a multimode laser is called "mode jumping". Normally, the multimode laser action is less dominant if the laser current is close to maximum, as shown in Fig. 4.4. Changing the temperature of a Fabry-Pérot laser by 10°C, changes the laser wavelength by a few nm. The minimum working temperature is normally about 10°C. If lower temperatures are set, special arrangements are needed to avoid problems due to water condensation. Laser temperatures higher than 60°C decrease the lifetime

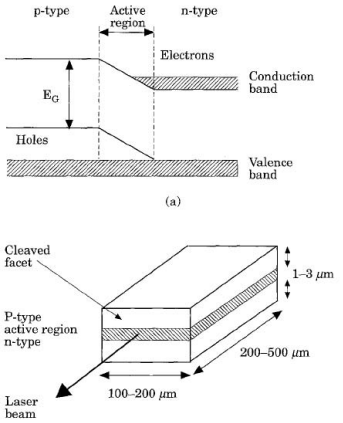

Figure 4.2. *Energy band gap diagram of a p-n doped semiconductor and the principle layout of a homojunction diode laser; from [39].*

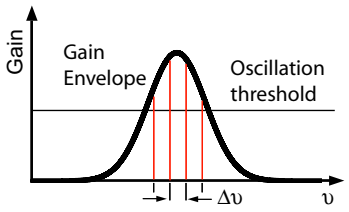

Figure 4.3. *Multimode laser principle.*

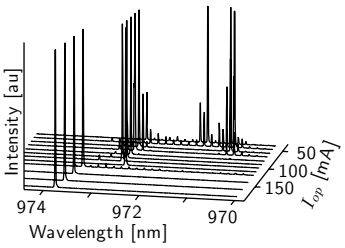

Figure 4.4. *Measured laser spectra of a 200 mW Fabry-Pérot laser for different laser currents (30-180 mA) at about 980 nm. The temperature was set to +10° C. This laser was used in Paper **VII**.*

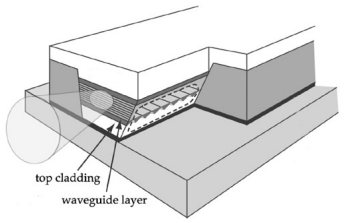

Figure 4.5. *Schematic of a DFB laser; adapted from [52].*

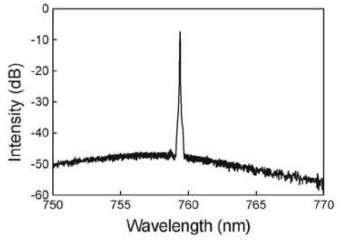

Figure 4.6. *Wavelength spectra of a DFB laser developed for diode laser spectroscopy of oxygen; from [49]. This laser type was used in Paper **VIII**.*

of the laser. In Fig. 4.4 a mode jump is shown at a laser current of 100 mA causing the laser to jump about 1.2 nm in laser wavelength. A laser is called a *single-mode* laser if the spurious laser longitudinal modes are a factor of 1000 (30 dB) lower than the main longitudinal laser mode. This is the case for the laser described in Fig. 4.4 if the laser current is stronger than 100 mA.

Over the years a number of different Fabry-Pérot lasers have been developed for the ultra violet (UV), the visible, the near infrared (NIR), and the infrared (IR) regions by the use of different semiconductor materials. Today, Fabry-Pérot laser output power ranges from a few mW to about 200 mW or more and the spectral width is in the order of 100 MHz if not special precautions are taken. Fabry-Pérot lasers were used in Paper **VI**, Paper **VII**, and Paper **VIII**.

4.1.1 Distributed feedback lasers (DFB)

In 1971 two researchers demonstrated the idea to incorporate a periodic variation (diffraction grating) inside or close to the doped semiconductor along the laser in order to obtain distributed feedback (DFB) in diode lasers [46]. This laser type is called a distributed feedback laser. It took a further four years until the first continuous wave DFB laser was functioning at room temperature [47, 48]. The principle of a DFB laser is shown in Fig. 4.5.By using diffraction gratings in a DFB laser, the temperature stability is improved and single-mode operation is easier to achieve compared to the Fabry-Pérot laser. The spurious laser modes are normally suppressed more than 35 dB, compared to the main laser mode, as shown in Fig. 4.6. This is due to the fact that the grating works as a selective mirror that reflects one wavelength only.

The major drawback of using a DFB laser is that the wavelength tuning range of the laser is decreased by a factor of five to ten compared to the Fabry-Pérot laser. Historically, DFB lasers are used in telecommunication systems due to their stable operation and high output power of about 10-30 mW. However, in recent years a number of different DFB solutions are available for tunable diode laser spectroscopy, as described in Ref. [49]. DFB lasers have become available in different packaging options with or without Peltier coolers and also in a pigtailed butterfly mount for fiber-based applications. Work to minimize the effect of backscattered light of a DFB laser is still being done [50, 51]. A DFB laser was used in Paper **VI**, Paper **VII**, and Paper **VIII**.

4.1.2 Vertical cavity lasers (VCSELs)

The design of a vertical cavity laser (VCSEL) differs from previously mentioned diode laser types since the light is emitted perpendicular to the top surface. The light beam of a VCSEL is

of circular shape unlike the asymmetric and divergent beam from edge emitters such as Fabry-Pérot and DFB lasers, as shown in Fig. 4.7. The output beam from a VCSEL is also narrow with a beam divergence of 10 to 25°. Thus, the collimator optics is simpler to design. The VCSEL is based on a number of layers that are grown on a wafer. At the top of the wafer substrate an n-doped Bragg reflector, consisting of a number of thin layers of alternating low and high refractive indices is mounted. These layers are followed by a p-doped Bragg reflector forming a short vertical cavity. Between these layers a diode junction is created forming an active medium that coherently amplifies photons if an inverted electron population is achieved. Several VCSELs can be mounted together to work in parallel or cleaved out to work as single devices. The first continuously running VCSEL at room temperature was demonstrated in 1988 [53]. The use of and the physics behind the VCSEL are extensively covered in Refs [54, 55].

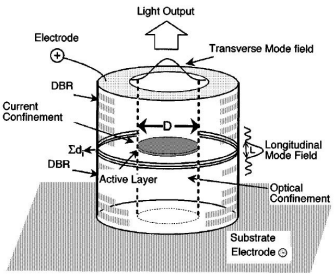

Figure 4.7. *The principle of a vertical cavity laser (VCSEL); from [55].*

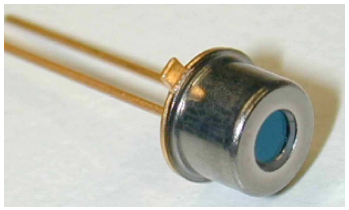

Figure 4.8. *A VCSEL laser in a standard TO 46 can without a build-in Peltier cooler; from [56].*

The performance of a VCSEL differs from ordinary diode lasers regarding the wavelength tunability and the efficiency. Only a small current is needed to get a VCSEL to lase and thus it is sensitive to current noise. The wavelength tuning by current is about a factor of ten higher compared to a DFB laser. Still, it is possible to develop a sensitive detection system for trace gas spectroscopy based on VCSELs [57]. VCSELs, though mostly used in telecommunication systems, are also used in spectroscopy. A VCSEL in a standardized package, without a Peltier cooler, is shown in Fig. 4.8.

VCSEL lasers are normally available for wavelengths from 650 nm to 1300 nm and with an output power of up to 1 mW. VCSELs, working at longer wavelengths, have been demonstrated as well by the use of materials that differ from GaAs. Currently, research is focused on the improvement of the performance of VCSELs. There is a need for higher output power, additional wavelengths, and to decrease the sensitivity to backscattered light [58–64]. It has been shown that backscattered light affects laser performance and if the backscattered light is strong, coherent collapse may occur by which the laser wavelength is changed [65]. VCSELs were used in Paper **XIII**.

4.1.3 Diode laser characteristics

As pointed out in Ref. [38], the amplitude characteristics of a diode laser are also interesting to study and not only the spectral and the spatial characteristics. In tunable diode laser spectroscopy a single-mode laser is swept over gas absorption lines that create amplitude dips in the detector signal. Thus, any noise in laser wavelength or laser amplitude (optical power variations) is picked up by the detector. Often, the data sheet of a single-mode laser presents spectral characteristics in wavelength but nothing is said

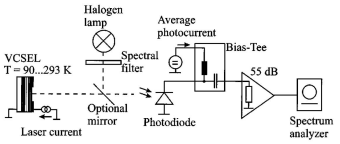

Figure 4.9. *Measurement setup for measurement of intensity noise and relative intensity noise of diode lasers; from [70]. A halogen lamp is used as an alternative light source.*

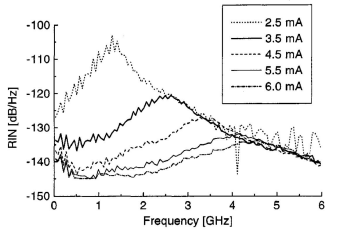

Figure 4.10. *Typical look of RIN spectra for a VCSEL. Higher drive current decrease the noise impact of the laser light and gives a lower RIN value; from [72].*

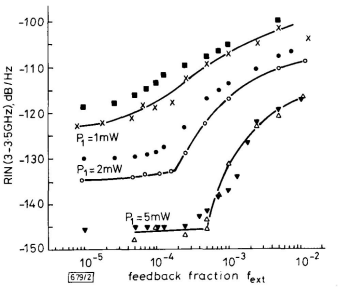

Figure 4.11. *Relative intensity noise against feedback for a distributed feedback laser (Hitachi HL1341), from [73]. The ■, the ●, and the ▼ dots correspond to calculated values while the X, the ○, and the △ dots correspond to measured values.*

about the amplitude noise spectrum. The amplitude noise of a laser is measured as the relative intensity noise (RIN). RIN is defined in a 1 Hz bandwidth as

$$RIN(f) = \frac{S_{\delta P}(f)}{P_0},$$

where P_0 is the average electrical power of the photocurrent of the detector and $S_{\delta P}$(f) the noise spectral density at a specific frequency f (power per unit bandwidth). A RIN measurement is almost the same as a power spectral density (PSD) measurement. The only difference is that the RIN values are normalized to the average power of the photocurrent of the detector. PSD describes how the power of a signal is distributed in frequency with a 1 Hz bandwidth. Often, the RIN value is expressed in decibels. If the RIN value is stated in a laser data sheet it is normally measured at 1 GHz or higher and is of little use when working with diode laser spectroscopy and wavelength modulation spectroscopy. A comprehensive overview and detailed description of how to measure laser noise is given in Ref. [66] and the theory of RIN and phase noise of lasers is found in Refs [67, 68].

The RIN value is measured by detecting unmodulated laser light with a low-noise photodiode connected to a spectrum analyzer, via a low noise amplifier. A typical example of a measurement setup to study RIN values is shown in Fig. 4.9. The RIN value indicates laser performance in the test setup and shows the maximum system performance expected for measurements with a bandwidth of 1 Hz. The measured noise is due to spontaneous emission in the laser, laser current noise, etc. The theoretical noise floor is set by shot noise at the detector. Thus, a laser with a high optical power has a potential to have a low RIN value. The impact of detector performance is checked by replacing the laser with a light-emitting diode or a halogen lamp and repeating the RIN measurement. If the light-emitting diode or halogen lamp is powered by a low-noise battery the RIN measurement is affected mainly by shot noise [69–71].

A typical example of a RIN spectrum is presented in Fig. 4.10 where the RIN spectrum is measured for a VCSEL at different drive currents. Typically, the RIN value is lower for higher laser drive currents or decreased temperature and the RIN spectrum has a noise peak at a few GHz at the relaxation frequency of the laser. A RIN value of -140 dB/Hz at 10 kHz means that the noise floor at 10 kHz, for 1 Hz, is a factor of 10^7 lower than the mean optical power. Thus, a smaller signal dip than 10^{-7}, compared to the averaged optical power, cannot be detected by a detector with 1 Hz measurement bandwidth. The RIN value indicates the highest resolution that can be expected in a trace gas absorption spectroscopy based on tunable diode lasers.

If a diode laser is mounted close to a scattering material, as in a GASMAS setup, some light is returned to the laser as feedback, inducing additional amplitude and frequency noise of the laser. As shown in Fig. 4.11, the RIN value is strongly affected by backscattered light entering the laser. The feedback fraction is the ratio between the feedback and the output optical power. The RIN value is increased by a factor of 20 dB if, for example, 1 % of the light is fed back to the laser. Please note that data presented in Fig. 4.11 are measured at above 3 GHz. If the feedback level reaches a certain level, the RIN value is increased markedly and the laser reaches the coherent collapse regime which means that the laser does not lase in single mode and may jump to another wavelength. The polarization of the laser light is also affected by feedback light, as shown in Fig. 4.12. How backscattered light affects GASMAS performance is further discussed in Chap. 8.

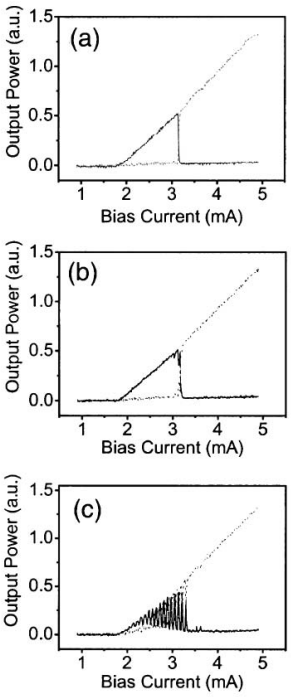

Figure 4.12. *Laser output, for different drive currents, of the VCSEL affected by polarization-preserved optical feedback. The solid and the gray dashed curve correspond to X-polarized light and Y-polarized light, respectively. The feedback fraction are (a) no feedback, (b) 3×10^{-5}, and (c) 8×10^{-3}; from [63].*

4.2 Dye lasers

The dye laser is a liquid laser based on dissolved organic dyes that are pumped by a pulsed or continuous laser working at short wavelengths [74, 75]. The dye laser was invented in 1966 by two research groups and has been used in spectroscopy since due to its tunability and wide wavelength range. An overview of dye laser development can be found in Ref. [76]. Modern dye lasers cover a broad wavelength region from 410 nm to 900 nm, as shown in Fig. 4.13. The dye laser is pumped by the 2nd or 3rd harmonic of a Nd:YAG laser or by an excimer laser. The dye laser can also be pumped by flash lamps but this results in broader bandwidth. The organic dye absorbs the pump beam and the dye molecules are excited. By radiationless transitions the molecules reach the lowest level of the excited state, and return to the ground state, emitting broad-band fluorescence light. Each dye covers about 20 to 80 nm. The dye cell is mounted in a resonator, and by a grating and mirror arrangement the wavelength is tuned. This set-up makes narrow bandwidth pulses in the order of 0.1 cm^{-1} (3 GHz) and an output energy of >10 mJ achievable. Thus, DIAL measurements on narrow absorption bands like the resonance line of mercury are possible.

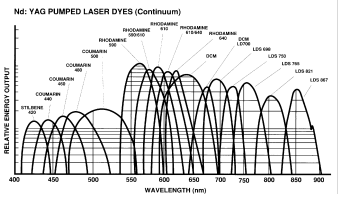

Figure 4.13. *Tuning curves for Nd:YAG pumped dye lasers. The range 400-900 nm is here covered by 17 dyes, each dye covering 20 - 80 nm.*

The DIAL technique requires two alternating wavelengths *on* and *off*; see Sect. 6.4. By allowing a rotating glass plate to alternate the laser beam inside a double resonator two alternating wavelengths are produced [77]; see Fig. 4.14. Two parallel mirrors (M_1 and M_2) in the resonator set the resonance wavelength of each laser beam. By proper synchronization, a dye laser generates alternating pulses with both *on* and *off* wavelengths, leaving the oscillator of the dye laser collinearly. Both mirrors are mounted on a turn-table shaft which is controlled by a stepper motor. The

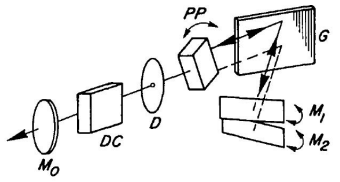

Figure 4.14. *The principal design of a dye laser to get two alternating wavelengths. The cavity consists of a dye cuvette (DC), ending mirrors (M_0,M_1, and M_2), a grating plate (G), a diaphragm (D), and a rotating parallel glass plate (PP). The rotating glass plate sets the laser beam to the two end mirrors M_1, and M_2, alternatively; from [77].*

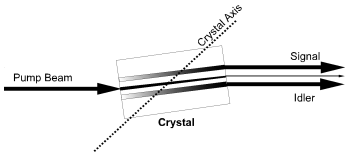

Figure 4.15. *The optical parametric process*

angle between the mirrors sets the wavelength difference between the *on* and *off* wavelengths. Even if the dye laser has been successfully used in lidar applications there are some disadvantages that should be mentioned. Each dye covers only a limited wavelength range and the lifetime of some dyes is short. Thus, a lot of different dyes must be handled and stored. Dyes have unknown properties and must be treated with care. Furthermore, the waste from dye solutions is difficult to handle and causes environmental problems. Thus, the demand for a tunable, solid state laser that replaces the dye laser is obvious and today the use of solid state lasers instead of dye lasers is common. Still, new systems are being developed, based on dye lasers, since it is a reliable design compared to a system based on an optical parametric oscillator [78, 79]. A pulsed dye laser was used in Paper **IV** and Paper **V**.

4.3 Optical parametric oscillators (OPO)

The optical parametric oscillator (OPO) is considered to be an efficient lidar source which is tunable from the UV far into the infrared wavelength region. OPOs were developed in the 1960s and were used commercially in the 1970s. However, the device almost disappeared due to limited performance. Low material damage thresholds led to crystal damage. Still, the OPO was demonstrated in a lidar system in Ref. [80]. During the 1990s non-linear materials improved and the OPO technology returned to the market.

The principle of an OPO differs from that of a conventional tuneable laser. A laser derives its gain from stimulated emission generated by a pump while the OPO, in a process similar to harmonic generation, relies on the non-linear process in a medium to convert pump photons of one wavelength to photons of longer wavelengths. In the parametric process, a non-linear material converts the high-energy photons from a pump laser into two photons of lower energy. The process can be seen as the inverse of the non-linear mixing process. Each pump photon is split into two photons with lower wavelength. The resulting beams are called signal and idler; see Fig. 4.15. However, the energy conversion requires that the energy of the pump photon equals the energy sum of the signal and idler. Since λ^{-1} is proportional to the energy of a signal, the three photons must be related as

$$\frac{1}{\lambda_{Pump}} = \frac{1}{\lambda_{Signal}} + \frac{1}{\lambda_{Idler}}, \tag{4.2}$$

where λ_{Signal} and λ_{Idler} are the wavelengths of the photons produced. The wavelengths of the signal and idler are determined by the angle between the pump wave vector and the optical axis in the non-linear crystal. The signal and idler waves grow only if all three waves travel at the same speed (phase matching). Un-

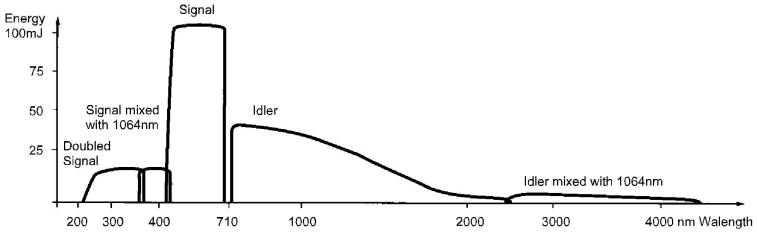

Figure 4.16. *Typical output performance from an OPO laser; from [81].*

der most circumstances, the refractive index changes with crystal angle. Thus, only a single set of wavelengths is possible for a given crystal angle and pump wavelength. If the pump wavelength is fixed and the crystal is rotated, different wavelengths are produced.

In order to increase the output energy the crystal is mounted in a resonator, where feedback causes gain in the parametric process similar to the build-up process in a laser resonator. The resonator can either be resonant at the signal (most common), idler or both wavelengths. Additional parametric stages (OPA) amplify the beam out from the OPO. A typical output performance from an OPO pumped by a Nd:YAG laser is shown in Fig. 4.16. The OPO laser pumped by a tripled Nd:YAG laser (355 nm) can be tuned from 410 nm to 700 nm (signal) and 720 nm to 2200 nm (idler).

A simple OPO has a relatively broad bandwidth ($\approx$0.2 nm) which is determined by the bandwidth acceptance of the non-linear crystal. A diffraction grating, which is mounted in the OPO resonator, provides necessary dispersion to achieve narrow bandwidth output. If an OPA is seeded by a narrow bandwidth OPO, the OPA produces higher energy pulses, thus maintaining the narrow bandwidth generated by the OPO. Output bandwidths in the order of 0.1 cm^{-1} can be achieved.

Even if OPOs show impressive output data, they are not simple to use in remote sensing. In practice, the OPO systems are extremely sensitive to temperature fluctuations and mechanical vibrations. This is due to the phase matching that takes place in-side the resonator. However, a number of OPO-based lidar systems have been successfully developed over the past ten years for measurement on ozone, sulphur dioxide, water vapor, and mercury [44, 82–84]. The techniques used to create two alternating wavelengths (a DIAL requirement) are different in these systems. Some research groups use two OPOs while others use piezoelectric transducers to control the wavelength tuning mirror,

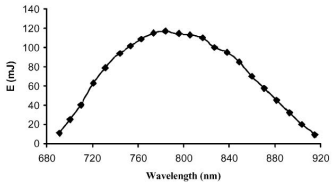

Figure 4.17. *Output performance from a Ti:Sapphire laser pumped by a Nd:YAG laser; from [87].*

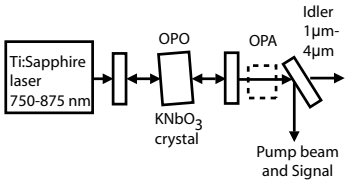

Figure 4.18. *Ti:Sapphire pumped OPO for IR lidar application [89]*

the crystal angle tuning element, and frequency-mixing and doubling stages [83]. Currently, research is going on to extend the wavelength range of OPOs beyond 2 μm, at which only a few crystals with transparency at long wavelengths exist. Crystals made of CdSe or $KTiOAsO_4$ (KTA) are used to reach the far infrared region. By placing two OPOs in series and letting the first OPO pump the second one (tandem OPO), far-infrared output is achieved [7]. The goal is to measure hydrocarbons. However, as can be seen in Fig. 4.16, the output energy is low beyond 2 μm, which limits the sensitivity of a lidar system.

4.4 Ti:Sapphire laser

The Ti:Sapphire laser is a tuneable, solid-state laser that covers the wavelength region of 680 nm to 920 nm; see Fig. 4.17. A titanium-doped sapphire crystal is used as the laser material. The output characteristics are similar to those of dye lasers. At present, Ti:Sapphire systems have the largest share of the market for tuneable, solid-state lasers and have replaced dye lasers for many applications. Both Nd:YAG lasers and flashlamps are used as pump sources. Ti:Sapphire lasers pumped by flash lamps are sometimes used in lidar systems [85, 86]. By using the fundamental, second harmonic, and the third harmonic the most important species in the UV region are measured. The double resonator technique is used in order to achieve two alternating wavelengths for DIAL measurements.

Nd:YAG-pumped, Ti:Sapphire lasers produce high-peak-power pulses. With the use of unstable resonators, the pulsed energy is suitable for driving a variety of non-linear processes [88]. By using a tuneable pump laser a wider wavelength range can be achieved. This technique is also considered for lidar systems in order to reach the 3 to 4 μm band. This band is especially interesting for hydrocarbon studies. A flashlamp-pumped, Ti:Sapphire laser is used to pump an OPO; see Fig. 4.18 [86, 89]. By tuning the pump wavelength between 750 and 875 nm the OPO covers, the whole infrared region from 1 μm to 4 μm (idler) without tracking the OPO crystal. The OPO resonates at the signal wavelength. A $KNbO_3$ crystal is used in order to extend the region beyond 3 μm. The output energy is in the order of 10 mJ. Further energy is achieved by inserting an OPA. Other OPO materials, such as $KTiOPO_4$ (KTP), KTA, and $LiNbO_3$ crystals have also been studied.

Chapter 5

Light Sensors

The performance of light sensors is an important aspect when designing an optical system for spectroscopy since it may limit system performance. Special attention should be given to the quantum efficiency of the detector, spectral cover, dynamic range, background noise, signal-to-noise-ratio (SNR), signal bandwidth, etc. When to use a particular detector is not always easy to determine. The choice depends among other things on the expected light level, the required bandwidth [90–93]. In a lidar system, the light detector should have a large bandwidth (20 MHz), an excellent SNR, and a high dynamic range since the intensity of the back-scattered laser light decreases with $1/R^2$. A photomultiplier tube has been used in Paper **IV** and Paper **V**, and the use of this detector type in a lidar system is discussed in Ref. [43].

In a GASMAS setup a sensor should have a large area (1 cm^2), a high quantum efficiency, and a large dynamic range. The large area is needed due to scattered and absorbed light by the test sample. The expected level of received light is about 1 μW, or lower, when a DFB or VCSEL laser is used as a source. Thus, received light is neither weak nor strong, which makes it difficult to decide which sensor to use. Detectors based on photodiodes, photomultiplier tubes, and avalanche photodiodes have been tested. The goal is to get near the shot-noise limit of the detected light since laser light is attenuated by about a factor of 10^2 - 10^5 in the test sample and the measurement time should be set to a minimum. The shot-noise limit defines the lowest noise level that can be recorded by a sensor. It is not possible to record a signal below this limit. The required bandwidth of the detector is of the order of 20-1000 kHz depending on the application. In this chapter, mainly sensors that were used in our GASMAS and Lidar projects are described. Expected noise performance and dynamic range at about 760 nm and 900 nm of photomultipliers, avalanche photodiodes, and photodiodes are described and discussed. The

reason that detector performance at 935 nm is not discussed is that no data at that wavelength are available for the PMT used. The wavelengths 760 nm and 935 nm are laser wavelengths used for GASMAS measurement on oxygen gas and water vapor. Expected detector performance, at a 1 Hz bandwidth is presented and the benefits of choosing a specific type of detectors for GASMAS and Lidar applications are discussed. It is assumed that the detector area is the same for the three detector types. Measured detector performance is presented in Chap. 8.

Light sensors are commonly based on the photoelectric effect. Light photons interact with a photosensitive surface of the detector and free electrons are created. An ideal detector has a quantum efficiency of 100% which means that every photon that enters the detector is transformed into a free electron. Thus, one photon entering a detector creates an electrical current of 2.61×10^{-19}A and N photons have an energy according to

$$W = \frac{Nhc}{\lambda}, \tag{5.1}$$

where λ is the wavelength of transmitted light photons, c is the speed of light, and h is the Planck constant. The theoretical radiant sensitivity S is

$$S(A/W) = \frac{\lambda q}{hc} = \frac{\lambda}{1240} \tag{5.2}$$

where λ is the wavelength, c is the speed of light, and q is the elementary charge. The radiant sensitivity number S indicates the expected detector current for a given incident light flux level. In practice the sensitivity S, in Eq. (5.2), is lower or much lower since the quantum efficiency of a detector is lower than 100%. The quantum efficiency (QE) is defined as

$$QE(\%) = \frac{1240}{\lambda} \times S_k \times 100\%, \tag{5.3}$$

where S_k is the measured sensitivity for a detector. The quantum efficiency depends on wavelength and type of detector as will be discussed later. By nature, photons are created by a random process and the intensity fluctuation of light is called photon shot noise. In an ideal detector this noise is transformed to current fluctuations (i_s) described by

$$i_s = \sqrt{2qI_{dc}B}, \tag{5.4}$$

where q is the electron charge, I_{dc} is the average current through the detector, and B is the measurement bandwidth in Hz. Shot noise has a uniform spectral power density and sets the lower limit of the theoretical maximum SNR for a detected signal. In an ideal system (no thermal or flicker noise), based on an

ideal laser, shot noise is the only limiting factor for the sensitivity. Thus, the ratio between the photocurrent on the detector and the shot noise of the current sets the SNR according to

$$SNR = \frac{I_{dc}}{\sqrt{2qI_{dc}B}}, \tag{5.5}$$

where q is the electron charge, I_{dc} is the average current through the detector, and B is the detection bandwidth in Hz. Eq. (5.5) shows that SNR increases with the amount of light and with decreasing detection bandwidth. As an example the maximal SNR for a system with a photocurrent of $10\mu A$, and a detection bandwidth of 1 Hz, is about 5.6×10^6, which corresponds to a fractional absorbance of 1.8×10^{-7}. However, few real systems show a performance close to the shot noise limit. As described in the following chapters, shot noise is normally not the only limiting factor of detector performance.

Figure 5.1. *Typical example of a head-on (co-axial) PMT 5070A, Hamamatsu*

5.1 Photomultiplier tubes (PMT)

The photomultiplier tube (PMT) existed since the beginning of the 20th century when the first secondary emission multiplier (dynode) was presented [94]. Over the years the PMT has been developed and today it is still a good choice to use for measurements of low intensity light. General information about PMT performance and properties can be found in Refs [93, 95, 96]. A PMT has several advantages since it is a standard device that can handle both weak and large signals (different gain settings needed). If required, large active areas of the sensor can be produced with a fast rise time unimpaired. Major disadvantages are a large physical dimension, that high voltage is required, that gain depends on temperature, and that the PMT is sensitive to magnetic fields and background radiation. A typical example of a head-on (co-axial) PMT is shown in Fig. 5.1. The PMT is used in both the GASMAS and the Lidar setup.

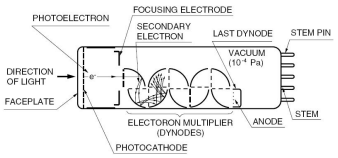

Figure 5.2. *The principle of how a head-on (co-axial) PMT works; from [95]*

Basically, PMTs consist of a photosensitive surface (photocathode), a number of focusing and multiplying electrodes (dynodes), and an anode element that collects all free electrons (photoelectrons) which originate from the photocathode but have been largely multiplied in the dynode chain. All elements are located in a vacuum tube made of glass, and a negative voltage is applied on the photocathode and dynodes as shown in Fig. 5.2. The photosensitive surface is located behind a window made of quartz glass. When incident photons enter the photocathode the energy is transferred to photoelectrons through the photoelectric effect. Since a negative voltage is applied, photoelectrons are accelerated towards the first dynode, which causes more photoelectrons to be created in an avalanche manner. These photoelectrons are then

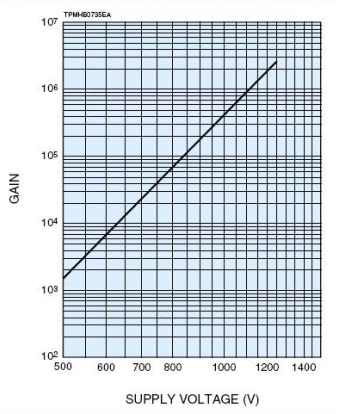

Figure 5.3. *Gain characteristics of head-on (co-axial) PMT with ten dynodes, 5070A; from [97]*

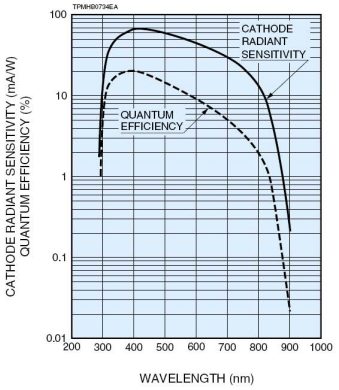

Figure 5.4. *Typical spectral response of a small PMT, from [97].*

further accelerated towards the second dynode and this process goes on until the electrons reach the anode element. Thus, when a voltage is applied on a PMT, a current flow between the anode and ground is directly proportional to the photoelectrons generated at the photocathode. The current gain G (ratio of anode current to cathode current) is proportional to the voltage applied according to

$$G = A \times V^{kn}, \tag{5.6}$$

where A is a constant, V is the voltage applied, n is the number of dynode stages, and k is a constant that is determined by the material and the structure of the dynodes. Normally the k value is set to 0.7 - 0.8. Thus, a gain voltage curve is presented as a straight line in a log-log plot and the slope is set by the kn value as shown in Fig. 5.3.

In an ideal detector one photon generates one photoelectron. This is not the case in a PMT since some photons are reflected, some photons generate heat instead of a photoelectron etc. Photocathodes are made of photoemissive material and their sensitivity to light is described as quantum efficiency (QE), as defined in Eq. (5.3) or cathode radiant sensitivity. The quantum efficiency is the percentage of photons that generate photoelectrons. The cathode radiant sensitivity is the ratio of the photocurrent produced at the cathode to the incident light power of a specific wavelength. The maximum theoretical value for QE is 100 % and the maximum cathode radiant sensitivity, at 760 nm, is 610 mA/W according to Eq. (5.3). The actual values depend on wavelength and material used in the photocathode. Curves describing the QE and cathode radiant sensitivity, for a particular cathode material, are presented in Fig. 5.4.

5.1.1 Dark current

Even if the PMT is put into complete darkness a dark current can be measured. The average value of the dark current can be subtracted from the detected signal and thus normally does not cause any problem. It is the shot noise of the dark current that might be a problem in some applications. Normally the dark current can be ignored since it is much weaker than the signal current and thus the shot noise due to dark current is also weak. However, if the applied voltage is low the dark current affects the PMT dynamic range, as will be described later. Dynamic range is the ratio of the largest signal level and the smallest signal that can be detected. If the applied voltage is close to maximum, background noise increases faster than the gain and thus decreases the dynamic range of the PMT; see Fig. 5.5. The dark current of a PMT is mainly due to:

- Leak currents
- Thermionic emission
- Field emission

The leak current is caused by non-ideal isolation materials used inside the tube and also between the connector pins of the PMT tube. A dark current in the order of 1 nA is usual since it is difficult to find isolation materials with a resistance value higher than 10^{12} Ohm. The leak current is directly proportional to the applied voltage according to Ohm's law. This means that if the applied voltage is increased the SNR is also increased since the current gain is exponentially proportional to the applied voltage as explained in Eq. (5.6). This is shown in region *a* in Fig. 5.5 where the gain slope (signal output) is much steeper than the slope of the dark current caused by the leak current.

A PMT is made of materials with a low work function (low energy needed to create photoelectrons). Thus, even at room temperature electrons are emitted and accelerated if a voltage is applied to the PMT. This process is called thermionic emission. To decrease noise due to thermionic emission cooling is applied. The noise current, due to thermionic emission is exponentially proportional to the applied voltage and the slope of the dark current is equal to the slope of the current gain (signal out), as shown in region *b* in Fig. 5.5. Thus, in this region, the highest SNR of a PMT is expected.

If an excessive voltage is applied, field emission current increases suddenly. In the presence of a strong electric field, electrons tunnel through the dynode material, towards the surface, and are emitted from the dynodes. The field emission effect adds additional current noise that is proportional to the applied voltage; see region *c* in Fig. 5.5.

Fig. 5.5 illustrates how the dark current of a PMT depends on the applied voltage. At low voltage levels the leak current dominates the noise (region *a*). At an adequate applied voltage (region *b*) thermionic noise affects the noise floor while noise due to field emission is dominant at high voltages (region *c*). In the figure, it can be seen that a constant dynamic range of the PMT is expected if the applied voltage is about 700-1400 V.

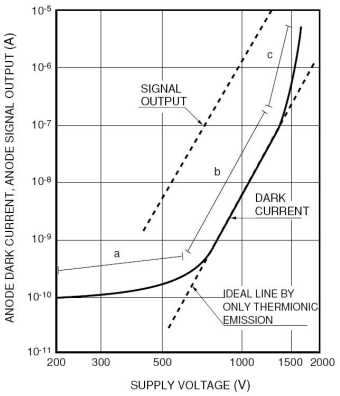

Figure 5.5. *Dark current for a PMT vs. applied voltage; from [95]*

5.1.2 PMT configuration in a Lidar setup

In a Lidar setup measurement bandwidth is important in order to temporally resolve lidar curves with a resolution of about 10 m. The signal is measured by a digitizer over a 50 Ω resistor (input impedance of the digitizer) and 50 Ω cables are used to prevent standing waves on the cable. A typical setup is shown in Fig. 5.6. The raw signal received from a lidar measurement is strongly range

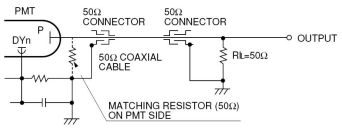

Figure 5.6. *PMT configuration in a Lidar setup. The signal is measured over a 50 Ω resistor to restore a high bandwidth. Normally, a fast digitizer (20MS or more) is used to record data; from [95].*

dependent and is thus both weak and strong. Since lidar signals, measured at a far distance are weak, short cables with double shields are preferred to suppress external noise. Regardless of how short the coax cable is between the PMT and the digitizer, Johnson noise (also called thermal noise) from the 50 Ω load resistor is added to the noise created in the PMT. Johnson noise (i_j) can be described by

$$i_j = \sqrt{\frac{4kTB}{R}} \tag{5.7}$$

where k is the Boltzmann constant, T is the absolute temperature, B is the measurement bandwidth, and R is the PMT load of 50 Ω. Since the required bandwidth is of the order of 20 MHz (PMT rise time $\sim$ 10 ns), the noise contribution from the load resistor is of the order of 80 nA or 3.9 μV. We will come back to how this affects a lidar measurement in Sect. 5.1.4.

As described in Sect. 6.3 the backscattered light intensity decays proportional to $1/R^2$. This means that the required dynamic range of a lidar detector is of the order of 10^5 or higher since signals are detected from a distance of 10 m to about 3000 m. Due to this fact a fast digitizer with 16-bit resolution is required and such a device is still difficult to find. Thus, by modulating the dynodes in the PMT the current gain may be changed dynamically to compensate for strong signals at short distances [43, 98]. A similar result is achieved by mounting a logarithmic amplifier between the PMT and the digitizer. However, the dynamic range requirements can be reduced by effective use of so called geometrical compression [99]. By using these methods a digitizer with a resolution of 8-12 bits is adequate.

5.1.3 PMT configuration in a GASMAS setup

In a GASMAS setup a standardized transimpedance amplifier (TIA) is connected to the PMT. The main task for the transimpedance amplifier is to convert a weak current signal to a voltage output; see Fig. 5.7 and Fig. 5.8. Since most of the gain takes place in the PMT, the gain and the noise requirements of a transimpedance amplifier for PMT applications, are modest. A transimpedance gain of 10^5 and a bandwidth of 20-100 kHz is enough. This means that a small input current of 10 μA results in an output level of 1 V. However, one should make sure that the internal noise in the transimpedance amplifier is lower than the expected noise of the signal from the PMT. In practice, it would be enough to connect a load resistor of 10^5 Ω to the PMT and measure the voltage drop over it to get similar results as when a transimpedance amplifier is used. However, this setup is sensitive to the impedance of the instrument used, e.g. an oscilloscope, that measures the voltage drop over the load resistor. The input

impedance of the oscilloscope should be much higher than the load resistor. Otherwise, the oscilloscope affects the measurement since the load is not well defined. Parasite capacitors will also affect the measurement bandwidth. If a 3 m coax cable is connected to a load resistor of 10^5 Ω, the cut-off frequency is only 5 kHz. Normally, a bandwidth of 20 kHz is required for a GASMAS setup. Thus, there is a need to use a transimpedance amplifier to get a well defined load resistance and bandwidth in combination with a signal output given at 50 Ω.

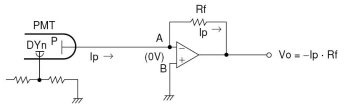

Figure 5.7. *PMT configuration in a GASMAS setup. The current signal from the PMT is transformed to a voltage output by a standardized transimpedance amplifier; from [95].*

Figure 5.8. *Typical view of a standardized transimpedance amplifier (C7319, Hamamatsu).*

5.1.4 Expected performance of a PMT

The SNR of a photomultiplier tube is defined as the ratio between the signal and the noise due to dark current, shot noise, noise in the multiplication process, thermal noise in the load resistor, etc. According to Ref. [95], the multiplication noise is caused by the cascade multiplication process and normally increases the noise level by 20-30 %. All signals are expressed in root-mean-square values. The DC level of the dark current I_{dark} is subtracted from the received signal to get a true signal that is proportional to the received light level. Normally, the dark current is low and may be ignored. In the upper end of the gain settings, often used in the Lidar setup, the dark current increases faster than the signal gain. Thus, dark current affects the signal quality recorded by a digitizer. However, in both the GASMAS and the Lidar setup, background light affects the DC level of the photocurrent and this must be subtracted from the received signal to get a true signal. The SNR of a photomultiplier tube (measured at the output of the PMT) is defined as

$$SNR_{PMT} = \frac{(I_c - I_d)G}{\sqrt{G^2 i_{sc}^2 + 2G^2 i_{sd}^2 + N_a^2 B}}, \tag{5.8}$$

where the symbols stand for:
I_c: photocurrent (A)
I_d: dark current (A)
G: PMT current gain
i_{sc}: shot noise of photocurrent (A)
i_{sd}: shot noise of cathode dark current I_d (A)
N_a: equivalent noise current ($A/\sqrt{Hz}$) of an amplifier or a resistor
B: measurement bandwidth. (Hz)

The shot noise of the photocurrent and the cathode dark current are defined as

$$i_{sc} = \sqrt{2qI_cB\frac{\delta}{\delta - 1}} \tag{5.9}$$

$$i_{sd} = \sqrt{2qI_dB\frac{\delta}{\delta - 1}}, \tag{5.10}$$

where q is the electron charge (As), B is the measurement bandwidth (Hz), and δ is the secondary emission ratio of the PMT. The ratio $\delta/(\delta\text{-}1)$ expresses the effect of multiplication noise in a PMT caused by the cascade multiplication process. A typical value of δ is 6 [95]. By combining Eqs 5.8-5.10, the signal-to-noise ratio of a PMT is defined as

$$SNR_{PMT} = \frac{I_c - I_d}{\sqrt{2.4qI_cB + 4.8qI_dB + \frac{N_a^2 B}{G^2}}}. \tag{5.11}$$

Eq. (5.11) shows that, if the gain is high, the noise of the connected resistor or amplifier has little impact on the total noise. Thus, it is important to use a high gain to perform measurements limited by being near to the shot-noise limit. Typical values in a Lidar setup, based on a PMT (9816QA, EMI) and a 50 Ω load resistor are a gain G of 10^7, a photocurrent I_c of 10 pA, a dark current I_d of 50 nA, a measurement bandwidth B of 2×10^6 Hz, and a resistor noise current of 80 nA. The expected SNR for a typical Lidar measurement (10 averages) at a great distance, presented in Paper **IV** and Paper **V**, is about one. Lidar measurements, at great distances, give noisy signals and are mainly limited by shot noise. Thus, for data signals recorded at great distances, the bandwidth is decreased in order to increase the SNR of the Lidar signal [100]. This is done by averaging data corresponding to different ranges. The drawback of limiting the bandwidth of the Lidar signal is that the range resolution is decreased. At short distances the SNR is large and there is no need to average data.

Typical values in a GASMAS setup, based on a PMT (5070A, Hamamatsu) and a transimpedance amplifier (C7319, Hamamatsu) are a gain G of 1000, a light input level to the PMT of 1 μW (760 nm wavelength), a cathode dark current I_d of 7×10^{-15} A, and an amplifier noise current of 1.5 nA (according to data sheet, 20 kHz bandwidth).

According to the data sheet of the PMT, the cathode radiant sensitivity (mA/W), at 760 nm, is 20 mA/W which means that the calculated photocurrent I_c should be 20 nA. Thus, the expected SNR for a PMT working under the conditions described above and width, a 1 Hz measurement bandwidth is

$$SNR_{PMT} = \frac{2 \times 10^{-8}}{\sqrt{7.7 \times 10^{-27} + 5.4 \times 10^{-33} + 5.6 \times 10^{-33}}}, \tag{5.12}$$

which is equal to 2.3×10^5 or 107 dB ($20\log(2.3 \times 10^5)$). This SNR is enough to resolve a weak signal dip of about 1×10^{-5}

compared to the averaged light level. The average output signal level, after the transimpedance amplifier, is about 2 V since the photocurrent I_c of 20 nA is amplified by a factor of 1000 by the PMT and by a factor of 10^5 by the transimpedance amplifier.

At 900 nm, the cathode radiant sensitivity is, according to the data sheet, only 0.2 mA/W, which means that the calculated photocurrent I_c should be only 0.2 nA. In order to get a similar DC level at the transimpedance amplifier output as for the measurement at 760 nm, the gain of the PMT is increased to 10^5. Thus, the expected SNR for a 1 Hz measurement bandwidth is

$$SNR_{PMT} = \frac{2 \times 10^{-10}}{\sqrt{7.7 \times 10^{-29} + 5.4 \times 10^{-33} + 5.6 \times 10^{-37}}}, \quad (5.13)$$

which is equal to 2.3×10^4 or 87 dB ($20 \log(2.3 \times 10^4)$).

As shown in Eq. (5.12) and Eq. (5.13), the detected signal is limited mainly by shot noise since the contributions from the dark current and the amplifier are lower than the shot noise from the photocurrent. It is also shown that a high quantum efficiency is an important aspect if low noise measurements are required. Since the SNR of a measurement limited by shot noise is proportional to $\sqrt{I_c}$, the expected SNR value is decreased by a factor of 10 if the cathode current is decreased by a factor of 100. Thus, even if a PMT manages shot-noise-limited measurements, the SNR is decreased, compared to other detector types, if the quantum efficiency is too poor.

If the incident light level is high and the PMT voltage is set to about 115 V, the noise contribution from the amplifier is equal to the photocurrent shot noise. Thus, a supply voltage of the PMT below 400 V is not recommended. If strong light levels are expected one should not use a PMT as a detector.

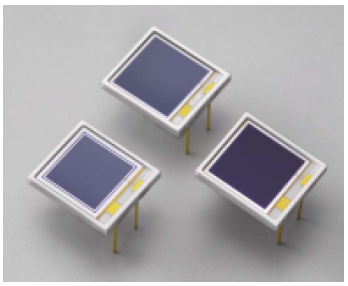

Figure 5.9. *Large area photodiodes (S3590-01, Hamamatsu Photonics).*

5.2 Photodiodes

A photodiode (PD) is a p-n doped semiconductor light sensor that creates a small current proportional to the illuminating light. A photodiode, based on silicone, is a common light sensor in strong light applications. It is a detector which is cheap and simple to produce. Since the photocurrent is weak it is common that a transimpedance amplifier, which transforms the current into a voltage, is connected close to the photodiode. A typical view of a large-area photodiode is shown in Fig. 5.9.

The p-n doped photodiode consists of a thin (about 1 μm) p-layer close to the detector surface and a thick n-layer mounted behind the p-layer, as shown in Fig. 5.10. At the border between the p- and n-layer, electrons from the n-layer enter the holes in the p-layer, thus forming a depletion layer. When a light photon, with

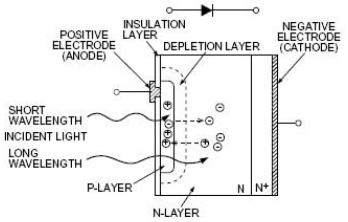

Figure 5.10. *Photodiode cross section, from [101].*

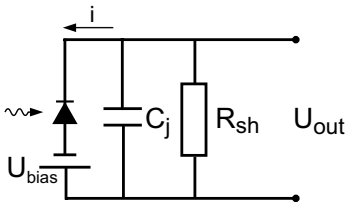

Figure 5.11. *An equivalent circuit of a silicon photodiode.*

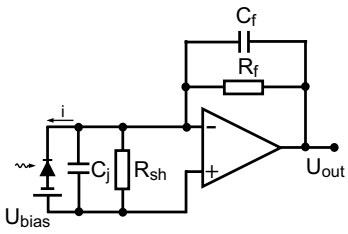

Figure 5.12. *Photodiode configuration in GASMAS setup. The current signal from the photodiode is transformed to a voltage output by an ideal transimpedance amplifier.*

an energy exceeding the band-gap of the semiconductor, enters the depletion layer, a free electron-hole pair is created and the electrons and holes are accelerated toward the n- and the p-layer. The photocurrent is proportional to the incident light intensity. To speed up a photodiode an un-doped intrinsic layer, based on a pure semiconductor, is mounted between the p- and the n-layer of a photodiode. Such a photodiode is called a *PIN* photodiode.

The photodiode may be described electronically by an equivalent electronic circuit. Since a current is produced, the equivalent circuit, for a photodiode, consists mainly of a current source combined with a junction capacitor (C_j) and a shunt resistor (R_{sh}) according to Fig. 5.11. The value of the junction capacitor is proportional to the area of the photodiode and the thickness of the depletion layer. As shown in the figure, the photodiode can be reversely biased by an external voltage source. If the photodiode is designed to be used without any bias the photodiode works in a *photovoltic* mode that has a high shunt resistance value and thus low thermal noise. On the other hand, if a photodiode is designed to work in a *photoconductive* mode the junction capacitance is decreased (due to the thicker depletion layer) and thus the bandwidth is increased. By using the photoconductive mode, the dark current is increased, which adds noise. In an ideal case, the junction capacitor should be about 100 pF and the shunt resistance should be several GΩ. However, such photodiode values are difficult to achieve, but as a rule of thumb the shunt resistance should be as high as possible while the junction capacitance should be kept as low as possible. Thus, it is a trade-off between dark current and bandwidth to use a photodiode based on photovoltic or photoconductive mode. General information about photodiodes can be found in Ref. [90].

5.2.1 Photodiode in a GASMAS setup

If the detected light level is high, it is enough to connect the photodiode directly to a resistor. By measuring the voltage drop over the resistor, information about the incident light level is gathered since the photocurrent is proportional to the incident light. The voltage drop can be measured by an oscilloscope or a voltmeter. However, high light levels are not always the case in GASMAS measurements due to the great absorption and scattering of the laser light in the material. Expected light levels at the detector range from 100 nW to 10 μW. Low or medium light applications require that a transimpedance amplifier is connected to the photodiode to transform and amplify the weak current from the photodiode into a voltage; see Fig. 5.12. The transimpedance amplifier should be connected to the photodiode with as short connections as possible. If not, the signal is drowned in the noise since parasitic capacitors pickup external noise and decrease the detection bandwidth.

Even though the principle of the transimpedance amplifier connected to a photodiode is relatively simple, careful design is needed to get a low noise level and a high bandwidth from the amplifier. Special attention should be given to the cable shields, parasitic capacitance, operational amplifier performance, and low-noise power supplies. The operational amplifier should have low input current noise, low offset voltage noise, and as high gain as possible. However, even if an ideal operational amplifier is used, the feedback resistor (R_f) and feedback capacitor (C_f) affect the detector performance. Normally, the feedback resistor (R_f) has a lower value (about 1MΩ) compared to the shunt resistance (R_{sh}). Thus, the feedback resistance (R_f) is the dominant source of noise since its thermal noise is proportional to

$$i_j = \sqrt{\frac{4kTB}{R_f}}. \tag{5.14}$$

If the feedback resistance is reduced the bandwidth goes up but the thermal noise does so as well. To minimize noise from a transimpedance amplifier, the feedback resistance should be set to a minimum value with the result that the shot noise from the photodiode is equal to, or higher, than the thermal noise from the feedback resistor according to

$$i_s = i_j \Longrightarrow I_{diode} R_f = \frac{2kT}{q}. \tag{5.15}$$

The junction and the feedback capacitors (C_j) and (C_f) also add noise but they affect mainly the bandwidth of the transimpedance amplifier. To get a high bandwidth, the capacitor value should be kept as low as possible.

As shown above, what seems simple to construct, is only so if one has experience of low-noise electronic design. How to build a high-performance light detector, based on photodiodes and transimpedance amplifiers, is explained in Refs [102–106].

5.2.2 Expected performance of a photodiode

In Sect. 5.1.4 an incident light level at 760 nm of 1μW was assumed. If the calculations according to Eq. (5.12) are instead based on the use of a large area *PIN* photodiode is used, the photocurrent is increased by a factor of 43.5 (I_{diode} = 870 nA). This is due to the fact that the quantum efficiency of the photodiode (S3584-08, Hamamatsu), at 760 nm, is about 87 % compared to 2 % for the PMT (5070A, Hamamatsu). This means, according to Eq. (5.15), that the expected feedback resistor value should be about 60 kΩ. Practically, the feedback resistor value is set to 1MΩ or 10MΩ corresponding to an amplification of 10^6 and 10^7, respectively. Thus, thermal noise from the feedback resistor does not

limit the SNR of a detector based on a photodiode and a transimpedance amplifier in this case. If a feedback resistor value of 10^7 is used, the photocurrent should be as low as 5 nA, before the thermal noise from the feedback resistor limits the SNR. The SNR for the combination described above is defined as

$$SNR_{PD} = \frac{I_{diode} - I_{dark}}{\sqrt{2qI_{diode}B + 2qI_{dark}B + N_a^2 B}} \tag{5.16}$$

where the symbols stand for:
I_{diode}: photocurrent of the photodiode (A)
I_{dark}: dark current of photodiode (A)
q: elementary charge (As)
N_a: equivalent input noise current ($A/\sqrt{Hz}$) of an amplifier
B: measurement bandwidth (Hz)

The first part in the denominator is the shot noise of the photocurrent, the second part is the shot noise of the photodiode dark current, and the last part is the noise of the transimpedance amplifier, including the thermal noise of the feedback resistor.

Let us assume that the PMT is replaced by a large-area PIN photodiode (S3204-08, Hamamatsu) in combination with a low-noise transimpedance amplifier (DLPCA-200, Femto). The incident light intensity is still the same as used in Eq. (5.12) (1μW), which causes a photocurrent of the photodiode of about 870 nA. The expected dark current of the photodiode is, according to the data sheet, 4 nA. The expected input noise of the transimpedance amplifier is 43 $fA/\sqrt{Hz}$. Thus, expected SNR for a photodiode working under the conditions described above and with a 1 Hz measurement bandwidth is

$$SNR_{PD} = \frac{8.7 \times 10^{-7}}{\sqrt{2.8 \times 10^{-25} + 1.3 \times 10^{-27} + 1.8 \times 10^{-27}}}, \tag{5.17}$$

which is equal to 1.6×10^6 or 124 dB ($20 \log(1.6 \times 10^6)$). This is a factor of about 7 better than if a PMT is used; see Sect. 5.1.4. If the calculations are carried out again for measurements at 900 nm, the expected SNR is similar compared to measurements at 760 nm. This is due to the fact that the quantum efficiency at 900 nm is still high (87 %). Thus, the expected SNR at 900 nm for a GASMAS setup based on photodiodes is a factor of about 70 better than if a PMT is used; see Sect. 5.1.4.

5.3 Avalanche photodiodes

Even if the first avalanche photodiode (APD) was reported in the 1960s, it was not possible to buy a large-area APD until the 1990s.

One reason was that it was difficult to develop detector materials that could stand a high voltage without creating a high dark current. Leakage current and detector cooling were additional issues. Today, these obstacles have been overcome and the APD is an alternative to the PMT in some low light-level applications, especially in the near infrared region (800-1050 nm). In this spectral range the APD is more sensitive than to a PMT. The quantum efficiency of an APD is of the order of 80-90 %, while a PMT could have a quantum efficiency below 1 %. The APD detector is often offered as a detector module, containing cooling electronics, the APD device, and a transimpedance amplifier to convert the amplified current to a voltage; see Fig. 5.13. Normally, an APD can handle signals from DC to 10 MHz or more. Large-area APDs are available from, among others, Hamamatsu and Advanced Photonix.

Figure 5.13. *View of a red enhanced silicon large area (ϕ=10 mm) APD module (SD394-70-72-661, Advanced Photonix).*

Basically, the APD works as a reverse biased photodiode and with a similar spectral response. The major difference between an APD and a photodiode, both made of silicon, is that for an APD an internal current gain is obtainable, mediated by a high reversed bias voltage of 1500-2000 V. The internal current gain is proportional to the applied bias voltage. The basic diagram of how an APD is constructed is shown in Fig. 5.14. For more information regarding expected performance and basic characteristics; see [107, 108].

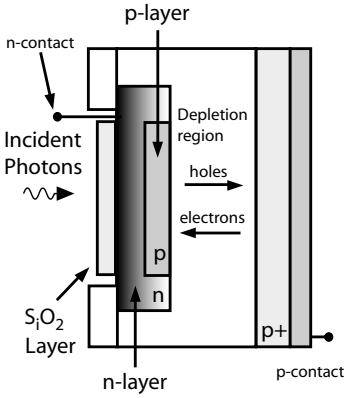

Figure 5.14. *The principle of an avalanche photodiode.*

When incident photons enter the depletion region, electron-hole pairs are created and accelerated by the high electrical field caused by the reversed bias voltage. Electrons are accelerated towards the cathode and holes are accelerated towards the anode. Since the applied voltage field is high, the electron-hole carriers collide with the crystal lattice and new carriers are created via ionization. Thus, each photoelectron starts an avalanche effect that increases the photoelectron current by a factor of 50-300. The SNR of an APD detector is given by

$$SNR_{APD} = \frac{I_{diode} - I_{dg}}{\sqrt{2q(I_{diode} + I_{dg})BF + \frac{2qI_{dark}B}{G^2} + \frac{4kTB}{R_L G^2}}}, \quad (5.18)$$

where the symbols stand for
I_{diode}: photocurrent (A)
G: current gain
F: excess noise factor
I_{dg}: dark current to be amplified (A)
I_{dark}: dark current (A)
B: measurement bandwidth (Hz)
q: elementary charge (As)
R_L: resistor load of the APD (Ω)
k: Boltzmann constant (J/K)

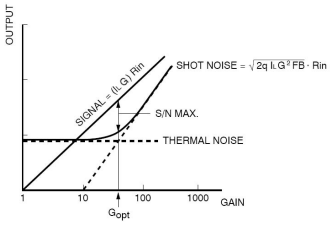

Figure 5.15. *The noise characteristics of an avalanche photodiode (APD); from [101].*

As can be seen in Eq. (5.18), the noise originates from a sum of four noise sources; from the left in Eq. (5.18), shot noise due to incident light, shot noise of amplified dark current in the APD device, non-amplified dark current, and thermal noise from the load resistor. According to Eq. (5.18) the G setting affects the suppression level of the thermal noise and noise due to dark current. However, the excess noise factor F is dependent on the gain and thus affects the expected SNR. Thus, there does exist a gain setting that results in a maximal SNR as shown in Fig. 5.15. The gain should be increased until the shot noise is equal to thermal noise level.

5.3.1 Expected performance of a large-area APD

Let us assume that the PMT is replaced by a large-area APD (SD394-70-72-661, Advanced Photonix) and measurements are carried out at 760 nm. The assumed incident light intensity is still the same as in Eq. (5.12) (1μW) which causes a photocurrent of the APD of about 870 nA. This is the same value as for the GASMAS setup based on a photodiode Eq. (5.17). The expected dark current I_{dark} of the APD is, according to the detector data sheet, 20 nA and the dark current I_{dg} to be amplified is 6 pA. The excess noise factor F is estimated to be 5 and the resistor load is set to 10^4 Ω. The internal gain G is set to 300. Thus, the expected SNR for a large-area APD working under the conditions described above and a 1 Hz measurement bandwidth is

$$SNR_{APD} = \frac{8.7 \times 10^{-7}}{\sqrt{1.4 \times 10^{-24} + 7 \times 10^{-32} + 1.8 \times 10^{-29}}}, \quad (5.19)$$

which is equal to 7.4×10^5 or 117 dB. Thus, even if the excess noise is higher for an APD compared to a PMT, the SNR at 760 nm is slightly higher for medium light levels; see Eq. (5.12). This is due to the fact that the quantum efficiency of an APD or a photodiode is about a factor of about 43 times higher than for the PMT at 760 nm. At 900 nm, the quantum efficiency of the APD, according to the data sheet, falls off to 57 %. Still, the expected SNR for an APD working at 900 nm, is much higher than the expected SNR of a PMT and is comparable to the SNR of a photodiode setup. At very low light levels the excess noise and the thermal noise affect performance. However, compared to the PMT, the APD is preferable for use in some applications such as remote sensing and medical imaging. The APD described above was used in Paper **XIII**.

5.4 Sensor characteristics

As described in Sects 5.1-5.3 the large-area photodiode is estimated to have the highest SNR (760 nm wavelength), followed by the APD detector and the PMT, when incident light intensity is of the order of 1 μW. The photodiode has even higher performance at 900 nm compared to the PMT and the APD detector types used. This is due to the fact that the quantum efficiency of the PMT used drops off at wavelengths close to 1 μm.

The reason is obvious: At high and medium light intensity, the shot noise of the photocurrent limits the SNR of a detector. Detectors with the highest quantum efficiency have the highest SNR [71, 91, 92, 109]. However, if the expected incident light intensity is low or of the order of 1 nW these statements are not always true.

The expected SNR for a PMT working under the conditions described in Eq. (5.12), except an incident light level of 1 nW at 760 nm, is equal to 7.2×10^3 or 77 dB ($20\log(7.2 \times 10^3)$). If similar estimations are done for photodiodes and APDs according to Eq. (5.17) and Eq. (5.19), the expected SNR would be 1.5×10^4 or 83 dB ($20\log(1.5 \times 10^4)$) for photodiodes and 2.3×10^4 or 87 dB ($20\log(2.3 \times 10^4)$) for APDs.

At these low light levels, the shot noise of the photocurrent still dominates the noise contribution of the PMT and the APD. However, this is not the case for the photodiode setup. At this low incident light level, noise contributions from the transimpedance amplifier and the dark current of the photodiode are higher than the shot noise of the photocurrent. Thus, if an incident light level lower than 1 nW is expected, the photodiode is maybe not a good choice of detector type, especially not if a high bandwidth is required in combination with a high sensitivity [91].

Chapter 6

Spectroscopic Techniques

The world spectrum comes from the Latin verb specere which means "to look at" which explains why historically spectroscopy covered only the visible light range. In the beginning the interaction between visible light and matter was studied, while today all kinds of radiation (electromagnetic waves and particles) can be used in spectroscopy. In absorption spectroscopy the absorption of radiation in matter is studied. Both active and passive techniques exist. In many applications, based on absorption spectroscopy, the absorption of light is weak, in particular for trace gas detection. A common requirement in such systems is to detect a fractional absorbance of 1×10^{-4} to 1×10^{-8}. In combustion applications the spectral sampling time is also critical since the measurement sample is not stable in time. Thus, fast sampling systems are preferred. In lidar systems a number of steps is taken to improve performance. High output power of the laser, large-area telescopes, filtering of background light, and signal averaging are some techniques to improve the sensitivity of the system. In diode laser spectroscopy similar steps are taken together with advanced modulation techniques, balanced detection, sample modulation techniques, etc. In all absorption measurements the Beer-Lambert law governs the attenuation of light. This chapter is an overview of different spectroscopy techniques used in tunable diode laser spectroscopy and remote sensing based on lidar techniques.

6.1 Absorption spectroscopy

In absorption spectroscopy lasers are often used as a light source due to its size, cost, narrow linewidth, and tunability in wavelength. The laser light is scanned over atomic and molecular absorption lines by superimposing a modulation current that changes the temperature of the laser and thus the wavelength of the laser

light. If the sweep rate is slow it is also possible to sweep the laser wavelength by changing the temperature of the laser can. This is often carried out by a Peltier element which is a thermoelectric device that both can heat and cool laser devices. Laser spectroscopy, based on tunable diode lasers, has been used for decades. Reviews of applications and recent developments in spectroscopy, based on diode lasers, are presented in Refs [110–114].

The sensitivity of a trace gas detection system, based on absorption spectroscopy, is normally defined as the minimum detectable concentration level of a gas expressed in ppm, ppb, or ppt depending on the species being measured. However, to be able to compare the performance of different systems, the fractional absorbance is used. The absorbance in optics based on a thin sample ($\sigma(\nu)NL \ll 1$), by the use of the Beer-Lambert law in Eq. (2.2), is defined as

$$A_\lambda = \ln \frac{I_0}{I} \approx \frac{\Delta I}{I_0} = 1 - \exp^{-\sigma(\nu)NL} \approx \sigma(\nu)NL, \tag{6.1}$$

where I_0 is the incident intensity, $\Delta I = I_0 - I$, L is the length of the path (m), N is the density of the absorbing molecules (molecules/cm^3, and $\sigma(\nu)$ is the absorption cross-section for one molecule (cm^2/molecule). Thus, the fractional absorbance $\Delta I/I_0$ is a measure of the detection limit of the system. There are two ways to improve the sensitivity; increasing the length of the measurement path is one way, while lowering the noise level is another. According to Chap. 5, the SNR of a measurement limited by shot noise is proportional to $\sqrt{\frac{I_{dc}}{B}}$. Thus, the only way to decrease the noise further, is to increase the measurement time or increase the light level. Normally, system performance is defined in 1 Hz detection bandwidth and with a SNR of one. This means that the recorded signal level equals the noise level of the system.

No spectroscopy measurement system is better than its light source. Thus, the power spectral density of the laser used should be measured before system development and calibration. This is an efficient method to identify external noise sources, measure the characteristics of the laser, and identify the frequencies at which the laser should be modulated. Fig. 6.1 shows measured spectral noise density for an unmodulated VCSEL that was used in Paper **XIII**. The measurement method is described in Refs [70, 71]. As shown in the figure the amplitude noise is higher at low frequencies. This is due to flicker noise of the laser. Often, flicker noise limits the performance of a spectroscopy system, especially if no or a low modulation frequency is used for the laser. This is due to the fact that it is not possible to suppress flicker noise by the use of signal averaging [115]. It is also shown in Fig. 6.1 that a standardized laser driver adds noise compared to the case when the

VCSEL is powered by a low noise battery. Please note the noise peak at 100 kHz and noise peaks at 100 Hz, etc. A light emitting diode (LED), operating at 760 nm, is used as a reference since it is normally less affected by flicker noise than a laser. Please note the theoretical shot noise level ($2qI_{dc}$) at 1×10^{-23} A^2/Hz. This level is never reached due to thermal noise in the transimpedance amplifier and in the large-area PIN photodiode.

Signal averaging is often used to increase the SNR in absorption spectroscopy. If the noise is random, which is the case for thermal noise and shot noise, the SNR value is proportional to $\sqrt{N}$, where N is the number of averages. This relation can also be seen in Eq. (5.5), since the SNR is proportional $1/\sqrt{B}$. The detection bandwidth is proportional to N^{-1}. However, in a true measurement, signal averaging is efficient only in a limited time frame. Further averaging does not improve the SNR and sometimes the noise level goes up again if long time averaging is used. This is due to the fact that the instrument stability limits the sensitivity of a measurement [116].

To study the stability of an instrument, data are often analyzed by the use of Allan variance [116, 117]. The Allan variance method was historically developed for measuring the stability of atomic clocks. Today Allan variance is used in many fields, including spectroscopy, to check stability of measurement systems and the characteristics of recorded data. The Allan variance is a measure of how recorded data vary in time. An infinite time series of recorded data x(t), with no dead time, is investigated by dividing the data into adjacent segments and calculating the variance of the average values $\overline{y}_k$ of the segments. This procedure is repeated until the data are divided into two intervals only, as shown in Fig. 6.2. The Allan variance $\sigma_y^2(n\tau)$ is given by

$$\sigma_y^2(N\tau) = \frac{\sum_{k=1}^{\frac{M}{N}-1}[\overline{y}_{k+1}(N\tau) - \overline{y}_k(N\tau)]^2}{2(\frac{M}{N}-1)}, \qquad (6.2)$$

where M is the number of finite measurement points with a minimum interval τ, $\overline{y}_k$ is the average value of y in the kth segment, and N is a factor controlling the size of each interval ($N \times \tau$). The Allan variance $\sigma_y^2(n\tau)$ is first calculated for N=1,2,3... and presented in an Allan plot; see Fig. 6.3. On the y-axis, Allan variance is presented while the length of the measurement segment is presented on the x-axis. By studying an Allan plot, a measurement time that results in maximum SNR can be estimated.

As shown in Fig. 6.3, the variance is decreased if the measurement time ($N \times \tau$) is increased proportionally to $\sqrt{N}$. This is a typical behavior of recorded signals that are mostly affected by uncorrelated white noise such as thermal noise. However, if the number of averages are increased further, the noise improvement fails and the slope of the curve in Fig. 6.3 becomes a horizontal

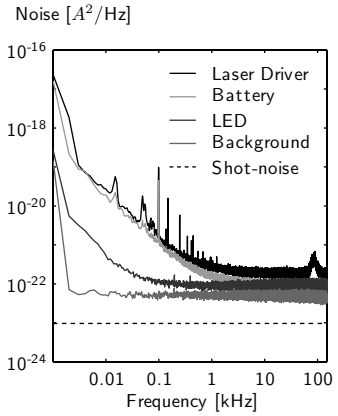

Figure 6.1. *Noise spectra of the light intensity variations for a VCSEL and a LED. The VCSEL is tested with a laser driver (LDC200, Thorlabs) or a low-noise battery as a power supply. The shot noise level of a photocurrent of 30 μA is indicated in the figure. The VCSEL was used in Paper **XIII**.*

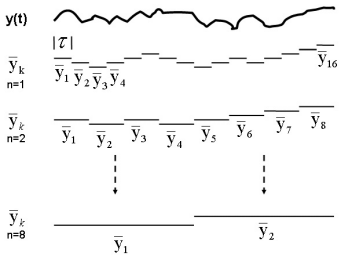

Figure 6.2. *Simulated data of 16 points that fluctuates in time, y(t). Adjacent measurement points are sequentially added together forming adjacent intervals with durations τ, 2τ, 3τ etc. See text for more details.*

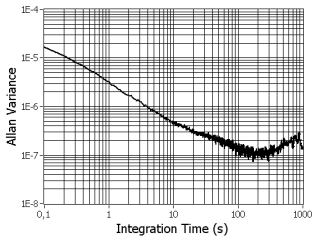

Figure 6.3. *Simulated data presented in an Allan plot. The data are affected by white noise, flicker noise and random walk noise. See text for more details.*

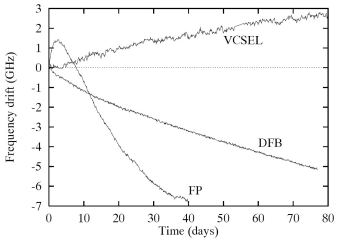

Figure 6.4. *Typical laser drift of Fabry-Perot lasers, DFB lasers, and VCSELs; from [118].*

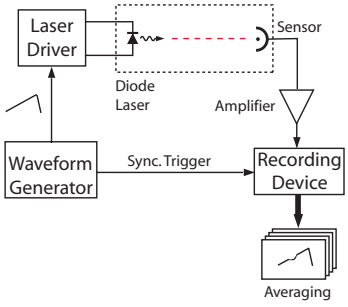

Figure 6.5. *The setup for a measurement based on the sweep integration method. The laser is modulated by a waveform generator that causes the laser to be tuned over an absorption line of interest. The recorded data are averaged by an oscilloscope or by a computer if a data acquisition board is used. The sync. trigger signal controls the start of recording a scan.*

line. This is a typical case when the system is limited by flicker noise. Longer integration time will not improve SNR. According to Ref. [115], it is not possible to improve SNR by the use of data averaging if recorded data are affected by flicker noise. Instead, one has to record data in such a way that flicker noise is avoided.

If an even longer averaging time is used, the Allan variance increases and the SNR of the instrument is decreased. This is due to the fact that random-walk noise affects the system. Typical errors that create random-walk noise are long term laser drift, laser driver instability, inadequate regulator settings of the temperature controller of the laser. According to Ref. [118], there is a large spread in frequency drift between different laser types but also between lasers of the same kind. Thus, if a high SNR is required and long measurement times are used, additional techniques are needed. This is further discussed in Chap. 8.

6.1.1 Sweep integration

The sweep integration method is a basic setup to improve the performance of a spectroscopy instrument and has been used for several decades [111]. Historically, this method is called the direct absorption method or the multi-time averaging method. The setup is fairly simple, as seen in Fig. 6.5. The diode laser is scanned across an absorption line by superimposing a current ramp continuously on the laser driver current. The laser light intensity is decreased when an absorption line is passed and the signal intensity is recorded by a sensor. At the beginning of a scan, a synchronization trigger is sent to the recording device which records signal scans continuously and averages recorded data. The recording device can be a digitizer, an oscilloscope, a data acquisition board, etc.

Fig. 6.6 shows the behavior of a sensor signal when laser light is scanned 25 GHz, over an oxygen line (P11P11) and is transmitted through 10 cm of air. The fractional absorbance equals 2.45×10^{-3}. Note the background slope that is typical when a diode laser is tuned in wavelength. The lower figure shows the absorption dip after subtraction of a fitted line. As shown in the lower part of Fig. 6.6, the noise level is about 10 % of the absorption dip. Thus, if lower fractional absorbance is to be measured, averaging of recorded data is required.

The shape of the absorption line sets the lower limit of the sampling speed of the recording device. If a FFT is performed on the lower figure in Fig. 6.6 it will be noted that the lowest cut-off frequency of the recording device should be a factor of 200 higher than the scanning frequency. Thus, if the scanning frequency is 10 Hz, the cut-off frequency should be at least 2 kHz. To be on the safe side a cut-off frequency of ten times this value is often chosen.

The sweep integration method is associated with a limiting sensitivity corresponding to a fractional absorbance of 10^{-3}-10^{-4}. This is due to the fact that, if the scanning frequency is low, flicker noise limits the performance of the sweep integration method, especially if the scanning rate is lower than 100 Hz. As shown in Fig. 6.7, the frequency response of the recording device, of one scan, equals the measurement bandwidth. However, if a number n of averages are performed the frequency response is changed into a limited number of peaks with a peak frequency corresponding to a multiple of the scanning frequency as shown in Fig. 6.7 [115]. The bandwidth is decreased proportionally to the number of averages performed. It is this bandwidth that is called the detection bandwidth and it equals the measurement bandwidth only if one scan is performed. It is the detection bandwidth value that should be used to calculate the contribution of shot noise and thermal noise to a measurement.

Fig. 6.7(c) shows the frequency response for a long single scan with a measurement time equal to the measurement presented in (b). Thus, the detection bandwidth depends on the measurement bandwidth and the measurement time according to B_{MB}/n, where B_{MB} is the measurement bandwidth and n is the number of averages. However, the frequency response for a recording device built on one long single scan is more sensitive to flicker noise since its frequency response is located at low frequencies where the flicker noise is high, as presented in Fig. 6.7(c).

However, if the scan rate is increased to 1 kHz or higher, most of the flicker noise is avoided, as shown in Fig. 6.8. To suppress flicker noise close to DC, an active background compensation is required. This can be carried out by high-pass filtering or by subtraction of the baseline. Thus, this method is stable even in harsh environmental conditions such as combustion measurements etc. An additional advantage of this method is that no calibration of the system is required since the fractional absorbance can be estimated by studying the raw data. The two biggest advantages of using the sweep integration method is the connection between the measured and simulated line profiles and that all light is active to measure the line profile [119]. In other methods, such as wavelength and frequency modulation, the light frequencies are smeared out in wavelength which decreases the intensity of the light that is used for measuring the absorption line. Thus, the theoretical SNR of the sweep integration method should be higher than the SNR of the wavelength modulation method since both methods operate at similar frequencies (about 10 to 20 kHz). Since the absorption lines are recorded directly by using this method, it is not difficult to measure complex gases with overlapping absorption lines. Today, the sweep integration method is used by some research groups, especially by those who develop flexible spectroscopy instruments [119–122].

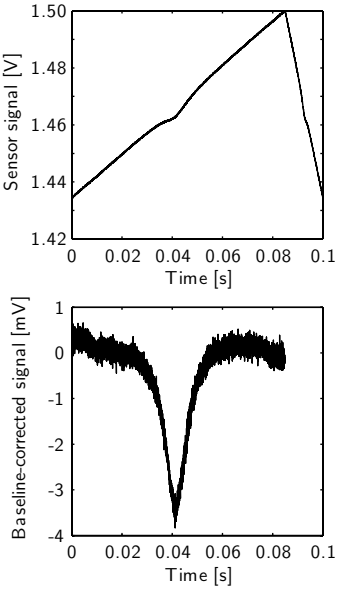

Figure 6.6. *Typical behavior of the signal from a sensor when a diode laser is scanned once over an absorption line.*

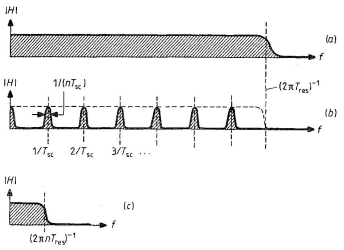

Figure 6.7. *Frequency response curves, according to the sweep integration method, for (a) a single scan where T_{res}, the resolution time, is set by the measurement bandwidth of the recording device, (b) multiple scans, and (c) a single scan of a length n times the scan in (a). T_{sc} is the scanning time; from [115].*

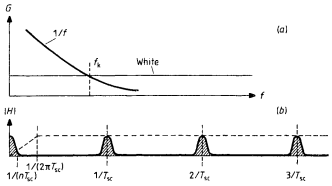

Figure 6.8. *1/f noise reduction by the use of the sweep integration method. (a) shows a typical noise spectrum of a sensor illuminated by unmodulated laser light. (b) shows the frequency response of a recording device with a scan rate in the kHz range; from [115].*

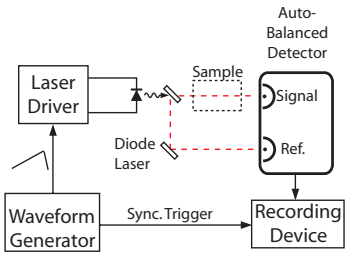

Figure 6.9. *Experimental setup for spectroscopy measurements based on the balanced detection scheme. The laser light is split into two beams; one goes through the sample (signal), the seconds acts as a reference.*

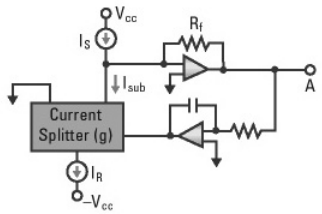

Figure 6.10. *A feedback loop in the auto-balanced detector is controlling a current splitter in a way so that no low frequency current wave enters the transimpedance amplifier; from [124].*

6.1.2 Balanced detection

The balanced detection technique is mostly a hardware-based solution to suppress low frequency noise in an optical setup. The influence of, for instance, flicker noise is reduced, up to 50 dB (a factor of about 320) or more, by subtracting the response from two identical sensors that are illuminated by one light source. The setup is similar to the sweep integration setup but the detector is replaced by an auto-balanced detector based on two matched photodiodes; see Fig. 6.9. The auto-balanced detector can be used in combination with the sweep integration method and with the wavelength modulation technique [123]. The laser beam is divided into two beams that enter the detector. One passes the sample (signal) while the second are used as a reference. Any common-mode noise in the laser beam, at low frequencies, can be reduced extensively, but the outcome depends on the level of the incident light as well as on the ratio between the intensity of the beams. However, any signal dip due to light absorption in the sample is not suppressed. The principle of the balanced detection technique is presented in Fig. 6.10. Incident light on the upper photodiode causes a current I_s that is amplified by a transimpedance amplifier. This signal controls a current splitter via a negative feedback amplifier in such a way that the current I_{sub} and I_s cancel out. The bandwidth of the feedback loop is set by the capacitor.

Fig. 6.11 shows noise levels measured for an about 25 μW signal beam with and without the auto-balanced detector function turned on. The power ratio between the reference beam and the signal beam is a factor of about nine. A spectrum analyzer was connected to the auto-balanced detector, and unmodulated laser light, from a pigtailed VCSEL laser, was split via a 10/90 splitter, and entered the signal and the reference photodiodes. As shown in Fig. 6.11, the noise spectrum of the signal is dominated by flicker noise while the auto-balanced response is clean. The noise level at 100 Hz is reduced by a factor of about 25 dB which corresponds to a current noise drop of a factor of 18. At higher frequencies, above the cut-off frequency of the feedback loop, the noise level of the auto-balanced signal increases.

The auto-balanced detector shows powerful performance only if the power ratio between the beams is fixed at a level of about two and if the incident intensity is of the order of 1 mW. The reference beam must be stronger than the signal beam, otherwise, the feedback loop does not work [125]. Thus, this solution works well in a laboratory where most parameters can be controlled.

The auto-balanced detector was developed by Hobbs and Haller [126, 127]. Today, a number of research groups use this technique successfully to reach the near shot-noise limit of received light [57, 128]. The advantage of using this method is that true absorption line data are measured and no calibration is needed since

both a balanced and a raw signal can be measured simultaneously. An extensive overview of how to develop an auto-balanced detector is found in Ref. [129].

In Paper **IX** we used an analog auto-balanced detector, built according to Ref. [130], to compare the performance of an analog and a digital approach to balanced detection. The solution presented in Ref. [130] is simpler to use compared to the design made by Hobbs, since our application required different detectors and a large distance between the reference and the signal detector.

6.1.3 Wavelength modulation

In Papers **VI** - **XIII** modulation frequencies from 10 kHz to 133 kHz were used to detect oxygen and water vapor lines with an absorption width in the GHz range. The wavelength modulation method, especially 2nd-order harmonic detection (also called 2f detection), is the most frequently used technique to improve the sensitivity of a spectroscopy instrument for trace gas detection. It was first demonstrated in the 1970's and has since then been further developed and used [111, 131, 132]. Both the wavelength modulation (WM) and the frequency modulation (FM) techniques are phase modulation techniques and basically the same method. The major differences are the modulation frequency range and the choice of detection technique to use. The wavelength modulation technique covers modulation frequencies from a few kHz to 1 MHz while the frequency modulation covers modulation frequencies from several MHz to the GHz range.

The main idea behind the use of phase modulation on lasers is that the detected signal frequency is moved to several kHz for WM and several MHz or GHz for FM. By moving the detection frequency the detected light is not greatly affected by low-frequency flicker (1/f) noise from the laser. There are additional advantages to use the wavelength modulation and second-order harmonic detection, namely, the sloping background is suppressed, the system is not sensitive to intensity fluctuations due to wavelength-independent changes, and the system can be insensitive to pressure changes in the sample if a specific modulation signal level is used. The drawback compared to the sweep integration method, is that the system has to be calibrated prior to a measurement. The information about the light intensity of the laser is lost in the 2f signal.

Fig. 6.12(a) shows the characteristics of phase modulated laser light. A small sinus signal is superimposed on the laser current to modulate it in wavelength. In addition, the laser light is amplitude-modulated as well. This effect is often called residual amplitude modulation (RAM). Normally, the laser light intensity is proportional to the laser current. Thus, no overtones of the modulation signal are created. Fig. 6.12(b) shows what happens when phase-

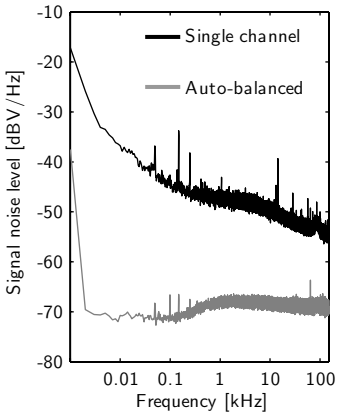

Figure 6.11. *Measured performance of a standardized auto-balanced photo receiver (2007, New Focus). See text for more details.*

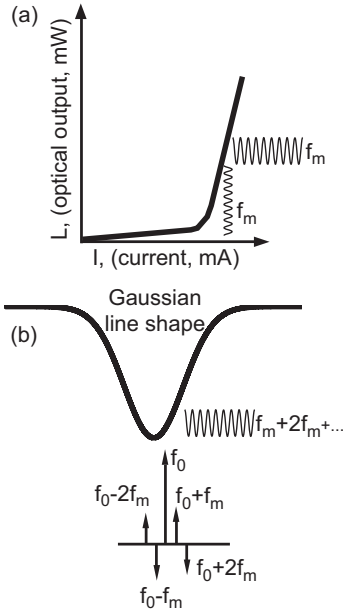

Figure 6.12. *Diagrams showing how a superimposed sinus current modulation signal affects laser light that is tuned over an absorption line. (a) shows the laser light intensity, (b) shows how the modulation harmonics are created.*

modulated laser light is scanned over an absorption line. The frequency spectrum of phase-modulated laser light consists of a carrier f_0 and a number of sidebands that are positioned at an equal frequency distance of f_m. Each pair of sidebands is symmetric for unaffected, phase-modulated light. However, when modulated laser light meets an absorption line the sidebands are attenuated differently and harmonics of the modulation frequency are created. Fig. 6.12(b) shows the behavior of FM-modulated laser light when affected by an absorption line. The principle is the same for WM laser light but this is difficult to illustrate in a figure.

The theory describing wavelength modulation spectroscopy is complex and can be found in Refs [133–136]. In this chapter, a basic description will be presented according to Refs [137–140]. These references give a more detailed description. To simplify the theory, it is assumed that the laser light intensity is linear proportional to the modulation current, the phase shift between the RAM signal and the frequency modulation signal is zero, and that the laser is slowly tuned over an absorption line compared to the frequency of the modulation signal. If a diode laser is modulated by a sinus signal, via the superposition of a current on the laser, the instantaneous laser frequency, $\nu(t)$, and laser intensity, I_0, are given by

$$\nu(t) = \overline{\nu} + acos(\omega t), \tag{6.3}$$

$$I_0(t) = \overline{I_0} + i_0 cos(\omega t + \psi), \tag{6.4}$$

where ω is the modulation frequency, ψ is the phase shift between the amplitude modulation and the frequency modulation signal. $\overline{I_0}$ and $\overline{\nu}$ are the instantaneously averaged laser intensity and frequency, respectively. a is defined as a frequency modulation amplitude and i_0 is defined as the amplitude of the RAM signal.

The intensity of light that passes an absorbing medium is given by the Beer-Lambert law which can also be expressed by the transmission coefficient $\tau[\nu(t)]$ according to

$$I_t(t) = I_0(t)e^{-\sigma(\nu(t))NL} = I_0(t)\tau[\nu(t)], \tag{6.5}$$

where L is the length of the path(m), N is the density of the absorbing molecules (molecules/cm^3), and $\sigma(\nu)$ is the absorption cross-section for one molecule (cm^2/molecule). The transmission coefficient $\tau[\nu(t)]$ is a periodic, even function in ωt, based on a Fourier cosine series, according to

$$\tau(\overline{\nu} + a\cos(\omega t)) = \Sigma_{k=0}^{\infty} H_k(\overline{\nu}, a)\cos(k\omega t), \tag{6.6}$$

where $H_k(\overline{\nu}, a)$ is given by

$$H_0(\overline{\nu}, a) = \frac{1}{2\pi}\int_{-\pi}^{\pi} \tau(\overline{\nu} + a\cos\theta)d\theta, \tag{6.7}$$

$$H_k(\overline{\nu}, a) = \frac{1}{\pi}\int_{-\pi}^{\pi} \tau(\overline{\nu} + a\cos\theta)\cos k\theta d\theta. \tag{6.8}$$

Thus, the expected intensity, oscillating at 2ω [137], should be given by

$$\begin{aligned} I_{t,2\omega} &= i_0\cos^2(\omega t)H_1(\overline{\nu}, a) + \overline{I_0}H_2(\overline{\nu}, a)\cos(2\omega t) + \\ & \quad i_0\cos(\omega t)H_3(\overline{\nu}, a)\cos(3\omega t), \end{aligned} \tag{6.9}$$

$$I_{t,2\omega} = \frac{i_0}{2}H_3(\overline{\nu}, a) + \overline{I_0}H_2(\overline{\nu}, a) + \frac{i_0}{2}H_1(\overline{\nu}, a). \tag{6.10}$$

Eq. (6.10) shows that the signal received, oscillating at 2ω is also affected by the first and the 3rd harmonic Fourier component; see Fig. 6.13. Since the first and the third harmonic Fourier components are odd periodic functions, they do not affect the second harmonic signal at the line center. Thus, it is preferred to measure the peak value of the 2f signal only [137].

For optically thin gas samples ($\sigma(\nu)NL \ll 1$), Eq. (6.8) is simplified and the second harmonic Fourier component H_2 is given by

$$H_2(\overline{\nu}, a) = -\frac{SNL}{\pi}\int_{-\pi}^{\pi} g(\overline{\nu} - \nu_0 + a\cos\theta)\cos 2\theta d\theta, \tag{6.11}$$

where S is the *line strength* of the absorption line, N is the density of the absorbing molecules (molecules/cm^3), L is the length of the path (m), and g is the function of the line shape. As shown in Eq. (6.11), H_2 is affected only by the function of the line shape $g(\nu - \nu_0)$. It turns out that the peak amplitude of H_2 (P_{max}) depends on the frequency modulation amplitude *a*. Generally, the ratio of the frequency modulation amplitude and the width of the absorption line in question is expressed in a modulation index m according to

$$m = \frac{a}{\Delta\nu}, \tag{6.12}$$

where $\Delta\nu$ is the half width at half maximum (HWHM) of the absorption line. As shown in Fig. 6.14 the amplitude of the 2f signal increases for higher modulation indices. The maximum peak value is recorded if m equals 2.2 irrespective of type of line [139]. If the modulation index exceeds a value of 2.2 the amplitude of the 2f peak the signal decreases. This is due to the fact that the width of the modulated laser light corresponds to about half of the full width of the absorption line. Any further widening of

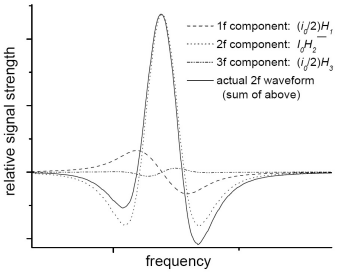

Figure 6.13. *Simulation, based on Eq. (6.10), of how Fourier harmonic components affect the shape of the 2f signal. This effect is caused by the RAM signal; from [137].*

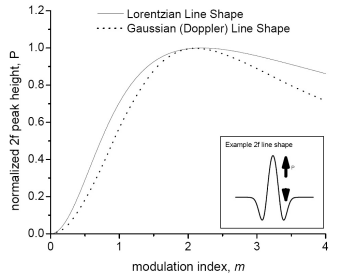

Figure 6.14. *Normalized 2f peak amplitude for different modulation indices. It is shown that the peak value is maximum for m=2.2; from [137, 139].*

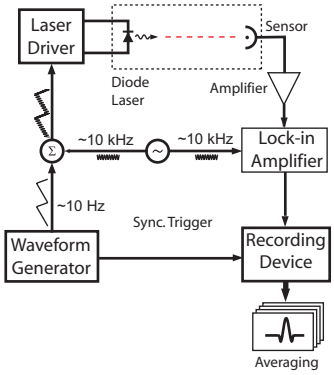

Figure 6.15. *Experimental setup for spectroscopy measurements based on wavelength modulation. The laser light is split into two beams; one goes through the sample (signal), the seconds acts as a reference.*

the frequency-modulated laser light decreases the amplitude of the recorded signal.

According to Ref. [139], the maximum 2f signal amplitude, at a modulation index of 2.2, depends on the line shape. P_{max} values, compared to a direct absorption dip, for a Lorentzian and for a Gaussian line shape are 0.343 and 0.438, respectively. P_{max} is a measure of the peak value of the 2f signal to the direct absorption signal amplitude [139]. The corresponding P_{max} value for the first harmonic is $\pm$ 0.5 [140]. Thus, the 1f signal cannot be larger than the direct absorption signal.

The measurement setup for wavelength modulation spectroscopy is presented in Fig. 6.15. Usually, two signal generators are used to modulate the laser with a slow current ramp to scan the laser over the absorption line and to modulate the laser current with a sinus modulation wave, in the kHz range. A lock-in detector is used to detect the amplitude of the 1f or the 2f signal. An oscilloscope or a data acquisition (DAQ) board is often used as an averaging and recording device. A sync trigger starts each scan recorded by the oscilloscope or the DAQ board.

Lock-in amplifiers are often used in spectroscopy to improve performance in trace gas detection. The modulation signal also acts as a phase reference and is fed to the lock-in amplifier as shown in Fig. 6.15. The lock-in amplifier is then capable of filtering out harmonic components (1f, 2f, 3f, etc.) generated when light passes an absorbing sample/gas cell. The major reason for using lock-in detection is to suppress noise by moving the detection frequency to a range that is normally less affected by noise (above 1 kHz).

The principle of a lock-in amplifier is shown in Fig. 6.16. The measured signal of a frequency f_s is mixed with a reference signal of similar frequency f_o. The phase of the reference signal is adjusted for maximal output level. After the mixer, both a low frequency signal ($f_0 - f_s$) and high-frequency signal ($f_0 + f_s$) exist. A low-pass (LP) filter (RC) filters out the low-frequency signal from the mixer; see Fig. 6.16(e). The bandwidth of the low-pass filter limits the detection bandwidth of the instrument. However, since the measured signal of an frequency f_s can have a frequency both slightly higher or lower than f_0, the input acceptance bandwidth being twice the bandwidth of the LP filter.

The noise equivalent bandwidth (ENBW) of the LP filter is, according to Ref. [104], $1/4T_c$ for a first order LP-filter (6 dB/octave) and $1/8T_c$ for a second order LP filter (12 dB/octave). T_c is the time constant of the LP filter in the lock-in amplifier. It is this filter that limits the measurement bandwidth of a spectroscopy instrument based on wavelength modulation. Analog lock-in amplifiers usually contain these two previously mentioned LP filter options. Fig. 6.16(g) shows the importance of choosing a steep LP filter in order to suppress an interfering signal close to the modulation frequency. A second order LP filter is from the point of view of sig-

nal processing rather flat. Thus, strong interfering signals located close to the modulation signal will definitely affect system performance. It is recommended to use a spectrum analyzer, before a modulation frequency is chosen, to identify strong interference signals and other external noise sources.

A question that is sometimes asked is whether wavelength modulation results in a higher performance than the sweep integration method. Assume a wavelength modulation spectroscopy instrument based on a ramp scanning frequency of 4 Hz, a wavelength modulation frequency at 10 kHz, and 100 measurement averages (25 seconds). The modulation index is set to 2.2. The time constant of the LP filter (second order) in the lock-in amplifier is set to 1 ms. Since the modulation index is set to 2.2, the estimated 2f signal has a peak value that is about 44% of the amplitude dip caused by the absorption line. Now, the measurement bandwidth is defined by the ENBW of the LP filter which in this case equals 125 Hz ($1/8T_c$). Since 100 averages are carried out the detection bandwidth of the measurement is about 1.25 Hz. If a similar system, based on the sweep integration method, is developed to measure the direct absorption signal, the scan rate is set to 10 kHz. Thus, flicker noise is equally avoided in both systems. To be able to record the absorption line without distortion, the cutoff frequency of the sensor and the recording device should be at least 1 MHz. During 25 seconds 2.5×10^5 averages are recorded by an oscilloscope, a digitizer, or a data acquisition board. The detection bandwidth of this system would be about 4 Hz, which is a factor of four more compared to the detection bandwidth estimated for the setup based on the wavelength-modulation technique. However, since the 2f signal is a factor of 2.3 times weaker than the absorption dip, the detection bandwidth of the measurement based on 2f detection should be a factor of five (2.3^2) smaller than when the sweep integration method is used. Thus, it is not obvious which technique to use since the estimated detection bandwidth and the expected signal strength are almost the same. The outcome depends on the application.

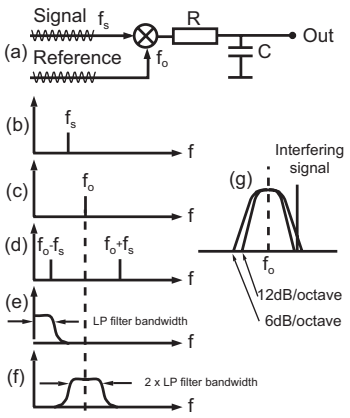

Figure 6.16. *Principal description of a lock-in amplifier and expected signal spectra. (a) shows the basic components of a lock-in amplifier, (b) and (c) spectra of signal and reference input channels, (d) signal spectrum after mixer, (e) spectral bandwidth of the low-pass filter, (f) input acceptance bandwidth, (g) filter setting to suppress a strong interference signal.*

6.1.4 Coherent sampling

In Paper **XIII** coherent sampling is introduced, which is a technique that makes it possible to combine the sweep integration and the wavelength modulation technique at the same time. By using this technique it is possible to average and store raw data from a number of channels of a spectroscopy measurement based on the wavelength-modulation technique. Lock-in detection of recorded data can be carried out before or after the data are stored. Thus, no hardware-based lock-in amplifier is needed. Only one master clock is used in coherent sampling to record data via synchronized analog to digital (AD) converters. The system architecture

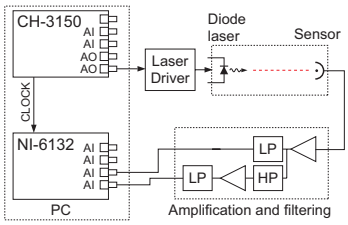

Figure 6.17. *Experimental setup for measurement on ambient air by the use of the coherent sampling technique implemented in two computer plug-in boards. The laser is modulated by an arbitrary waveform that is generated in a data acquisition board. The amplified and high-pass filtered signals from the detector are sampled coherently and synchronically by a four-channel A/D board.*

is presented in Fig. 6.17. Coherent sampling increases the spectral resolution of a Fast Fourier Transform (FFT) when the following conditions are met [141, 142];

$$\frac{f_{in}}{f_{sample}} = \frac{N_{cycles}}{N_{record}}, \tag{6.13}$$

where f_{in} is the frequency of the recorded signal, f_{sample} is the sampling frequency (the frequency or a multiple of the master clock), N_{record} is the number of data points in the sampling window corresponding to one scan, and N_{cycles} is an integer number of cycles within the sampling window.

In Paper **XIII** the ramp frequency and the modulation signal frequency are chosen such that they both meet the condition in Eq. (6.13). Further, the creation of the ramp signal and the modulation signal are carried out by an arbitrary waveform generator board that is clocked by the master clock which is also used to clock the AD board. Thus, the ramp signal and modulation signal are averaged coherently by the AD board since only one master clock is used. This system is not affected by timing jitter of the synchronization trigger that may affect the performance of a spectroscopy instrument based on the sweep-integration or the wavelength-modulation technique. In Paper **XIII** a master clock with a frequency of 2.469 MHz was used to clock a four-channel, synchronized AD converter PCI board. A ramp frequency of 130 Hz and a modulation frequency of 133.120 Hz were used. By the use of the coherent sampling technique, implemented in two plug-in boards for a standard computer, a compact and flexible spectroscopy instrument was developed.

6.2 Gas in scattering media absorption spectroscopy (GASMAS)

Tunable diode laser spectroscopy of free gas dispersed in scattering materials is a relatively new field of research which was initiated in the beginning of this century [10]. The birth of GASMAS is a result of decades of research in lidar, diode laser spectroscopy and medical laser physics at the Atomic Physics Division of Lund University, Sweden. The principle, compared to traditional diode laser spectroscopy, is at a glance small from a technological point-of-view. The GASMAS concept means that a traditional spectroscopy instrument, based on tunable diode lasers, is used but the gas cell or optical path is replaced by a material that strongly scatters light. Mostly, the 2f detection scheme has been used. However, to use a scattering material as a measurement sample introduces new challenges. In principle, any gas that can be measured by a traditional diode laser spectroscopy instrument, can also be measured by the GASMAS technique. The depth of light penetration into

a scattering material, at the selected wavelength, sets the limit of which gas can be measured by the GASMAS technique. In Papers **VI** - **XIII** different approaches (mostly 2f detection) and materials such as fruit, wood, pharmaceutical tablets, tissue etc. have been used to investigate gas content and the transport of gas, for instance, during a drying process. Oxygen gas and water vapor have been measured so far. These gases are easier to measure compared to other gases, since the absorption lines are located inside the optical window of tissue (650 nm to 1200 nm). Similar behavior is expected in wood since liquid water absorbs strongly above 1200 nm; see Fig. 3.5 in Sect. 3.2.

As shown in Fig. 6.18, the light is strongly scattered in the material. Thus, no defined path length exists and it is not possible to measure the true gas concentration by the use of the GASMAS technique only. If the gas concentration is the measurement required, additional measurements are required to estimate the actual path length of the scattered light. This can be done by the use of time-resolved measurements or by phase measurements [143–145]. Usually, the mean path length of the scattered light is a factor of ten or more than the thickness of the material. Thus, a GASMAS measurement gives information of an estimated equivalent mean path times a known gas concentration. The GASMAS system for oxygen and water vapor is, prior to a measurement, calibrated in ambient air by sequentially adding a precise, additional path length. This procedure is called the standard addition method and is commonly used in chemistry; see Paper **IX**. As shown in Fig. 6.18 two measurement geometries can be used in GASMAS; the reflection and the transmission geometry. The transmission geometry is the most straight forward method while the reflection geometry can be used in more complicated measurement setups. The reflection geometry was used in Papers **VI** and **VIII** while the transmission geometry was used in Papers **VII**, **X**, **XII**, and **XIII**.

According to *Eq.* (6.11) the recorded 2f signal is proportional to the incident light intensity times the peak amplitude of the second Fourier harmonic (H_2). Thus, to record a true estimation of the equivalent mean path length, the recorded 2f signal must be normalized to the incident light intensity; see Fig. 6.19.

In Fig. 6.19 the reflection geometry used in Paper **VI** is presented together with the typical behavior of the recorded signals. The signal defined as the GASMAS measurement signal (GMS) is the true estimation of the equivalent mean path length of a measured gas (oxygen or water vapor). However, specific caution should be taken when water vapor is measured since it varies greatly with temperature and environmental circumstances.

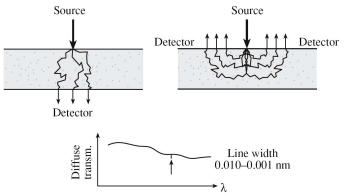

Figure 6.18. *The principles of GASMAS. The sharp absorptive features of free gas and the transmission and reflection measurement geometries are illustrated; from Paper **XI**.*

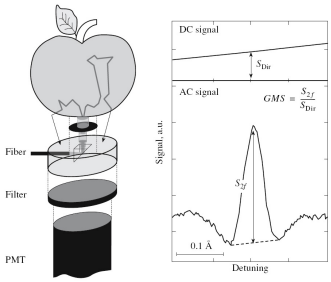

Figure 6.19. *GASMAS setup for the reflection geometry applied on oxygen measurement in apples. Please note that the separations of the components are heavily exaggerated for clarity; in practice, they are touching each other. The direct absorption signal and a 2f lock-in recording of an oxygen line are also shown; from Paper **XI**.*

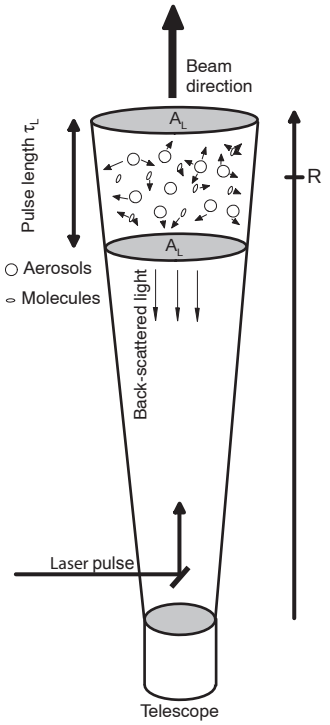

Figure 6.20. *The principle of a lidar with laser pulses entering the atmosphere.*

6.3 Light detection and ranging (Lidar)

Lidar technology has many similarities to radar. Light is used in lidar systems instead of micro waves. Radar technology was mainly developed during the Second World War, while the lidar technology development emerged during the 1960's when the laser was invented. In the lidar technique, light pulses are sent out into the atmosphere, and back-scattered light from particles and molecules is detected and analyzed in a computer; see Fig. 6.20. By measuring the time it takes for the light to go and return from a point at distance R it is possible to calculate at what distance the molecules and aerosols are located [28].

The laser transmits short light pulses which are assumed to be rectangular to have a duration of τ_L and have an output energy E_L. While it travels through the atmosphere to reach a point at distance R, the pulse is attenuated by molecules and aerosols which are located along the beam path. It follows from the Beer-Lambert law that the energy, which reaches the particles at a distance R is given by

$$E(R) = E_L \cdot e^{-\int_0^R \kappa(\lambda_L, r)dr}, \tag{6.14}$$

where $\kappa(\lambda_L, r)$ is the attenuation coefficient for the molecules and aerosols at the laser wavelength λ_L. At the point at distance R the laser beam covers an area A_L where the light interacts with the molecules and aerosols. Some laser light will be scattered, some will be absorbed by the molecules and aerosols. This process is described by the volume backscattering coefficient $\beta(\lambda_L, \lambda, R)$. To simplify the calculations, we assume that β is constant over A_L and that the scattering process is elastic (Mie or Rayleigh scattering). Thus the scattered wavelength equals the laser wavelength ($\lambda_L = \lambda$) and depends only on R. Another simplification is that only single-scattering events are considered. However, only a part of the scattered light returns to the lidar system. Most of the light is scattered out into the atmosphere. The A_0/R^2 factor represents the solid angle of the receiver telescope seen from the scattering volume. A_0 represents the area of the telescope mirror. To simplify the equations further we assume that the acceptance angle of the receiver matches the divergence of the outgoing laser beam. Since the laser pulse length is not infinitely short, the detector will receive light at time t simultaneously from a distance range of $R - \frac{c\tau_L}{2}$ to R; see Fig. 6.20. At time t/2, the center of the pulse is located at the distance R. The total scattered laser power received at time t at the detector will be

$$P(\lambda_L, t) = A_0 \int_{R-\frac{c\tau_L}{2}}^{R} \frac{E_L \cdot \beta(\lambda_L, R) \cdot e^{-2\int_0^R \kappa(\lambda_L, r)dr}}{\tau_L} \cdot \frac{dR}{R^2} \tag{6.15}$$

and, since $R \gg c\tau_L/2$, the expression is approximated to

$$P(\lambda_L, t) = A_0 \cdot E_L \cdot \beta(\lambda_L, R) \cdot e^{-2\int_0^R \kappa(\lambda_L, r)dr} \cdot \frac{c}{2R^2}. \quad (6.16)$$

However, the detector and the electronics have an effective response time τ_d which leads to the need to integrate the received signal from time t to t+τ_d. Thus, the energy strength of the received signal from the returning laser light is given by

$$P(\lambda_L, t) = A_0 \cdot \xi(\lambda_L) \cdot E_L \cdot \beta(\lambda_L, R) \cdot e^{-2\int_0^R \kappa(\lambda_L, r)dr} \cdot \frac{c\tau_d}{2R^2}, \quad (6.17)$$

where $\xi(\lambda)$ is the spectral transmission factor of the receiver. This factor includes the influence of any spectrally dependent component in the detector. Eq. (6.17) is normally called the basic scattering lidar equation. The effective range resolution for a lidar system is $c(\tau_d + \tau_L)/2$. As could be seen in the basic scattering equation, there is one equation and two unknown parameters $\beta(\lambda_L, \lambda, R)$ and $\kappa(\lambda, R)$. The volume back-scattered coefficient is given by

$$\beta(\lambda_L, \lambda, R) = \sum_i N_i(R) \left[\frac{d\sigma(\lambda_L)}{d\Omega}\right]_i^s \zeta_i(\lambda), \quad (6.18)$$

where $N_i(R)$ represents the number density of scattered species i at the distance R; $[d\sigma(\lambda_L)/d\Omega]_i^s$ represents the differential scattering cross-section of the species being irradiated with laser light at wavelength λ_L; and $\zeta_i(\lambda)\Delta\lambda$ represents the fraction of the scattered laser light that falls into the wavelength interval $(\lambda, \lambda + \Delta\lambda)$. If we are dealing with elastic scattering, the scattered light will be at the laser wavelength λ_L, leading to a simplification of the lidar equation. The atmospheric attenuation coefficient $\kappa(\lambda, r)$ describes how a laser beam is attenuated according to the Beer-Lambert law while it travels through the atmosphere. A model can be described as

$$\kappa(\lambda, r) = \sigma_{mi}(\lambda)N_{mi}(r) + \sigma_{aj}(\lambda)N_{aj}(r), \quad (6.19)$$

where $\sigma_{mi}(\lambda)$ is the absorption cross-section for the molecule, $\sigma_{aj}(\lambda)$ is the absorption cross-section for the aerosol type j; N_{mi} and N_{aj} are the number densities of molecules and aerosols located at the distance r. In practice, the information given by the back-scattered laser light is extremely difficult to analyze. Normally, the atmosphere contains a mixture of species and aerosols which complicate the evaluation of lidar data. The problem becomes even worse if the target is fluorescent. However, some applications can be found where it is possible to evaluate the back-scattered data from a single-wavelength laser. For example, in the near

infrared the aerosols are the main scatters (Mie scattering) and the molecular scattering can be neglected. To solve Eq. (6.17), both κ and β have to be considered. In most cases there is no natural relation between them, and an analytical solution requires extensive knowledge about their behavior. The Klett inversion method is valid in some cases [146, 147].

6.4 Differential Absorption Lidar (DIAL)

In order to measure molecular species in the atmosphere, the differential absorption lidar technique (DIAL) has been developed. The DIAL technique was pioneered in the 1960's but the theory was not fully understood until the early 1970's. Two alternating laser pulses of different wavelengths are used: one matching the resonance wavelength of the molecule of interest λ_{on} and one slightly off, λ_{off}. By comparing the results from the pulses received, the number of resonating molecules as a function of the distance R from the lidar system is estimated. By forming the ratio of the two basic lidar equations a simplified expression is obtained. The DIAL equation is given by

$$\frac{P(\lambda_{on},t)}{P(\lambda_{off},t)} = \frac{\xi(\lambda_{on})\cdot\beta(\lambda_{on},R)}{\xi(\lambda_{off})\cdot\beta(\lambda_{off},R)}\cdot e^{-2\int_0^R(\kappa(\lambda_{on},r)-\kappa(\lambda_{off},r))dr}, \tag{6.20}$$

where $P(\lambda_{on},t)$ represents the signal energy received from the back-scattered laser pulse that corresponds to the resonance wavelength; $P(\lambda_{off},t)$ represents the received signal which has a slightly different wavelength ($\lambda_{off}=\lambda_{on}+\delta\lambda$). The output power of the laser is assumed to be equal at both wavelengths. If $\delta\lambda$ is small, the only thing by which $P(\lambda_{on},t)$ differs from $P(\lambda_{off},t)$ is that molecules with a resonance wavelength λ_{on} have attenuated the laser beam as it travels to and returns from a a point at a distance R. Thus a total attenuation coefficient is defined as

$$\kappa(\lambda,r) = \overline{\kappa}(\lambda,r) + \sigma_m^A(\lambda)N_m(r), \tag{6.21}$$

where $\overline{\kappa}(\lambda,r)$ is the attenuation coefficient with the contribution from the measured molecule excluded; $N_m(r)$ is the number density of the molecule being measured and represents the absorption cross-section for the molecule being measured. To simplify *Eq.* (6.21) the differential absorption cross-section is introduced, which is given by

$$\sigma_{diff}^A(\lambda_{on},\lambda_{off}) = \sigma_m^A(\lambda_{on}) - \sigma_m^A(\lambda_{off}), \tag{6.22}$$

where $\sigma_m^A(\lambda_{on})$ and $\sigma_m^A(\lambda_{off})$ represent the absorption cross-sections for the *on* and *off* resonance wavelengths, respectively. This parameter can be determined by looking at the absorption

value for each wavelength in a gas cell. Since each laser has its specific line shape and line width, the same laser must be used for differential cross section determination and for DIAL measurements. If the equations (6.20)-(6.22) are combined, the expression for the number density of the measured species becomes

$$\begin{aligned} N(R) &= \frac{1}{2\sigma^A_{diff}(\lambda_{on},\lambda_{off})} \cdot \frac{d}{dR}\left\{\ln\left[\frac{P(\lambda_{off},R)}{P(\lambda_{on},R)}\right]\right\} \\ &\quad - \frac{1}{2\sigma^A_{diff}(\lambda_{on},\lambda_{off})} \cdot \frac{d}{dR}\left\{\ln\left[\frac{\beta(\lambda_{off},R)}{\beta(\lambda_{on},R)}\right]\right\} \\ &\quad + \frac{1}{2\sigma^A_{diff}(\lambda_{on},\lambda_{off})} \cdot \left[\overline{\kappa}(\lambda_{off},R) - \overline{\kappa}(\lambda_{on},R)\right], \end{aligned} \tag{6.23}$$

where it is assumed that the spectral transmission factor of the receiver is constant for small wavelength differences $\delta\lambda$. If $\delta\lambda$ is small we can also assume that β and κ behave as constants. In that case the solution is

$$N(R) = \frac{1}{2\sigma^A_{diff}(\lambda_{on},\lambda_{off})} \cdot \frac{d}{dR}\left\{\ln\left[\frac{P(\lambda_{off},R)}{P(\lambda_{on},R)}\right]\right\}, \tag{6.24}$$

which is the most common solution used in DIAL measurements. To determine the number density N(R) the derivative of the DIAL curve has to estimated.

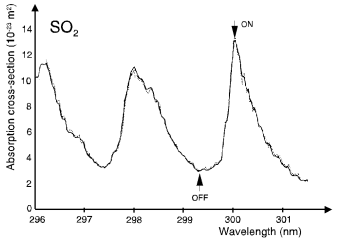

Figure 6.21. *Absorption cross section of SO_2; from [148].*

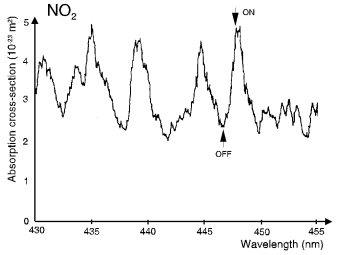

Figure 6.22. *Absorption cross section of NO_2; from [149].*

6.4.1 Measurements of SO_2 and NO_2

SO_2 and NO_2 were the first species to be measured with the DIAL technique. The first measurement was performed in the early 1970's. Normally a frequency-doubled Nd:YAG-pumped dye laser is used to reach the peaks in the absorption bands. For SO_2 one uses 300.02 nm as the *on* wavelength and 299.30 nm as the *off* wavelength; see Fig. 6.21. Since $\delta\lambda$ is less than 1 nm no β or κ correction is needed. For this *Eq.* (6.24) can be used. However, factors like interference from other molecules and the atmospheric transmission have to be considered. For NO_2 one can use 448.03 nm as the *on* wavelength and 446.60 nm as the *off* wave-length; see Fig. 6.22. Normally a Nd:YAG-pumped dye laser is used to reach the *on* and *off* wavelengths.

6.4.2 Measurements of O_3 and NO

O_3 (Ozone) measurements with the DIAL technique have turned out to be one of the most successful lidar applications [150]. Even if the first measurement was performed in 1975 the number of ozone

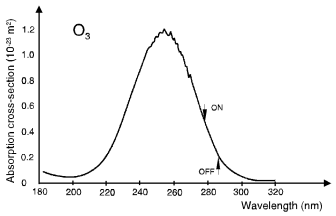

Figure 6.23. *Absorption cross section of O_3; from [151].*

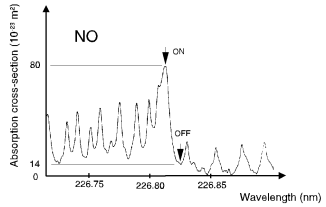

Figure 6.24. *Absorption cross section of NO; from [152].*

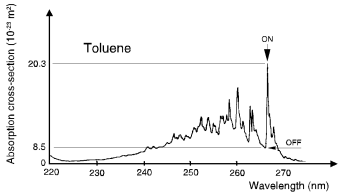

Figure 6.25. *Absorption cross section of toluene; from [155].*

measurements have increased extensively in both the troposphere and the stratosphere during the last ten years. Normally excimer lasers and/or Nd:YAG lasers, combined with Raman-shifting techniques, are used. Since the absorption bands of ozone are broad, the laser can be tuned to several wavelengths to achieve a proper absorption coefficient.

Normally, for tropospheric measurements the *on* wavelength is 270 - 280 nm while the *off* wavelength is closer to 300 nm; see Fig. 6.23. For stratospheric measurements the corresponding wavelengths are typically 308 nm and 355 nm. In this case the absorption bands are weaker but stratospheric concentrations are higher and the lidar range of a system is increased for longer wavelengths. Thus, stratospheric ozone can be measured by ground-based systems with high-power lasers and large receiving telescopes. Since $\delta\lambda$ is of the order of 10 nm or more, Eq. (6.23) should be used instead of Eq. (6.24). This depends on the volume back-scattered coefficient and the attenuation coefficient behaving differently for the *on* and *off* wavelengths, especially if the aerosol concentration is high.

Far down in the UV spectral region the NO molecule has strong absorption bands; see Fig. 6.24. Normally, frequency-doubled Nd:YAG-pumped dye lasers are used to reach the *on* wavelength of 226.81 nm and the *off* wavelength of 226.825 nm. The fundamental output of a dye laser can be used to measure NO_2 at the same time as the second harmonic investigates NO [153].

6.4.3 Measurements of mercury and toluene

Mercury is the only metal atom that is measured in the troposphere with the DIAL technique [154]. The absorption line has its peak at 253.652 nm and the *off* wavelength is chosen at 253.665 nm. The absorption line of mercury corresponds to a pure electron transition and the line is very narrow. A frequency-doubled Nd:YAG-pumped dye laser is used to reach the mercury line. However, since the absorption line is narrow, the linewidth of the laser must be of the order of 0.1 cm^{-1}. In this application it is necessary to accurately control the laser wavelength during a measurement to make sure that the laser hits the absorption line. An example of a mercury study is described in Paper II. Toluene is another species that can be found in the near UV spectral region; see Fig. 6.25. An absorption band is found in the 240 - 270 nm region. The proposed *on* and *off* wavelengths are 266.9 nm and 266.1 nm, respectively [155]. A frequency-doubled Nd:YAG or an excimer-pumped dye laser can be used as a transmitter.

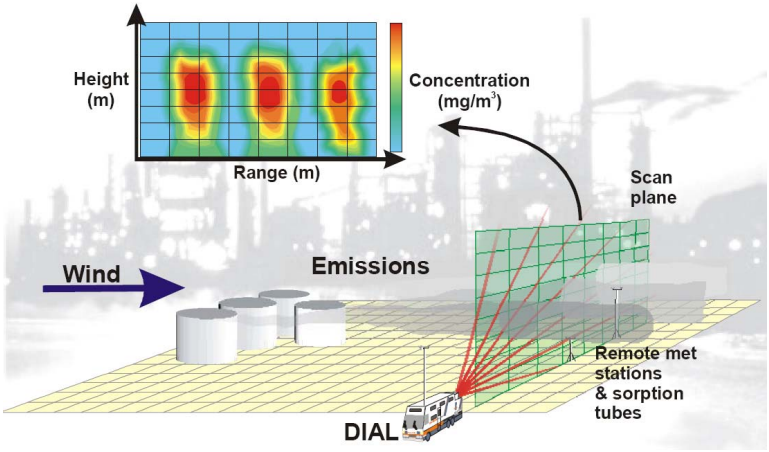

Figure 6.26. *Schematic diagram of a DIAL system measuring gas fluxes; courtesy of Spectrasyne.*

6.5 Measurements of gas fluxes

The lidar technique has proved to be a valuable tool for atmospheric studies. Over the years the technique has been developed and the measurement accuracy is today in the vicinity of 3 - 10 %. Normally lidar results are presented together with an accuracy analysis. However, this is not simple for flux measurements on smoke stack plumes done by mobile lidar systems. In this application the measurement accuracy can be limited to 20 - 25 % [6, 156]. This is due to the difficulties in estimating the wind speed around the plume. Several techniques exist. Normally, a vane anemometer close to the lidar system is used. The wind speed around the plume is estimated by correcting the measured wind speed at low height. The flux value (g/s) is estimated by multiplying the value of the integrated volume density (g/m) over the cross-section of the plume with the estimated wind speed perpendicular to the cross-section (m/s). A view of a lidar setup is shown in Fig. 6.26, and examples of successful gas flux measurement campaigns, based on lidar measurements, are presented in Paper **IV** and Refs [157–159].

6.5.1 Vane anemometers

A vane anemometer is a small device with a propeller that turns proportionally to the wind speed. For each turn the propeller generates sinus wave signals of which the frequency is proportional to the wind speed. The device also measures the wind direction. Vane anemometers are widely used at airports and at meteorological stations. This device can be used in combination with a lidar

Figure 6.27. *Scintec MFAS Acoustic Antenna without the enclosure.*

system to determine flux values. The accuracy is greater than 5 %. A vane anemometer which is mounted close to the lidar system instead of close to the plume causes large systematic errors. In order to improve the accuracy, the vane anemometer has to be mounted close to the plume. The position of the lidar system can be several hundred meters away from the smoke stack.

6.5.2 Sodar

Sodar stands for sound detection and ranging and it can be described as a radar that works with sound waves instead of micro waves. A sodar system measures wind speed profiles by transmitting sound pulses into the atmosphere and analyzing the Doppler shift of the back-scattered sound pulses. The sodar technique is based on the fact that sound waves are scattered by regions with a changing sound refraction index due to different temperature layers. Since these regions are moving with the wind, the evaluated Doppler shift gives a true value of the radial wind speed. A sodar system measures the radial wind speed in three directions in order to estimate the horizontal wind vector. An extensive overview of the sodar theory is presented in [160]. A mini sodar system consists of a phased array antenna of small electromechanical transducers; see Fig. 6.27. The electrical power of a transmitted pulse is about 50 W and the frequency is chosen between 1650 - 2750 kHz. The measurement range is in the vicinity of 30 - 1000 m [161]. The radial resolution is of the order of 10 m. A mini sodar system is not large, about 0.7 times 0.7 m.

Some lidar systems are equipped with sodar instrumentation to estimate wind speed profiles at low altitudes [162]. This technology gives more accurate values than a mechanical wind monitor but it is more complex and more expensive. The cost of a standardized mini sodar system is still high. One system costs around $50,000. However, since sodar technology has been used for over 25 years no decrease in price is expected [163, 164]. Today sodars are used at international airports in many countries and at nuclear power plants in Germany. Sodars give important information about wind profiles in case of a nuclear accident.

6.5.3 Video graphical techniques

A video graphical technique for wind speed measurement is presented in Paper **V**. The main motivation for this project was to find a cheap and accurate method to measure the speed of a plume for lidar applications. The video graphical technique is based on a frame grabber which repeatedly transfers images of a plume with a CCD camera, and by studying the plume movement the plume speed is estimated. The distance between the lidar system and the plume is another important parameter to be measured. By

pointing the laser beam of a lidar at the plume the distance to the plume is measured by observing the lidar echo. The theory behind the technique is based on the fact that each graph contains a fixed background and a plume which moves horizontally. Each column of a graph matrix is added, thus creating a vector which contains information about the contents of the graph; both background and plume information. The procedure is shown in Fig. 6.28. In order to remove the background information, from each vector an average vector which is created from a number n of previously grabbed graphs is subtracted. The remaining vector should contain information only about the plume. By looking at the cross correlation between two subsequent vectors, the plume movement from t_0 to t_0+dt is estimated.

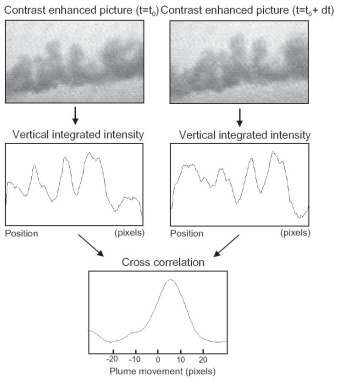

Figure 6.28. *Example of plume velocity measurement using image correlation techniques; from Paper* ***V****.*

The video graphical technique is an accurate method to estimate plume speeds. According to Paper **V** the measurement accuracy increased by a factor of 5 - 40 compared to when a vane anemometer was used. However, further research is required before this technology is fully developed. Since this application is not well tested, there are many parameters which have to be optimized. Different color filters should be tested in order to improve the contrast of the plume graph. In the case of an invisible plume, an IR camera is proposed to catch the plume movement. Moreover, this method can be even cheaper today since the quality of cheap, firewire-connected cameras are adequate for this application.

6.6 Fluorescence spectroscopy

The study of environmental stress in vegetation has become important due to changing environmental conditions. Remote sensing has been developed in order to study such stress. The possibility of using laser-induced fluorescence was described in the 1970s [165]. However, the theory is not fully understood. The technique is based on a UV laser exciting a target, and by observing the fluorescence emitted from the target. In this way specific information can be obtained. Fluorescence studies from airplanes and mobile systems have been performed. Both ground and water targets have been considered. The lidar group in Lund has focused its interest on fluorescence studies of chlorophyll in vegetation. The mobile lidar system has been used in several field tests. A campaign that took place outside Avignon in 1993 is described in Paper **I**. A remote sensing system for combined fluorescence spectral recordings and multi-color fluorescence imaging on vegetation is presented in Paper **II**. The chlorophyll in plants has broad absorption bands and specific fluorescence bands. A UV laser ($<$ 400 nm to avoid damage to the eye) is used to excite the molecules and the fluorescence spectrum is recorded by a spectrum analyzer. The fluorescence spectrum from chlorophyll has two peaks at 685 and 730 nm;

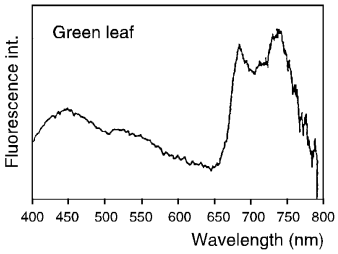

Figure 6.29. *Fluorescence spectra from a green beech leave recorded remotely, 355 nm excitation wavelength; from [166].*

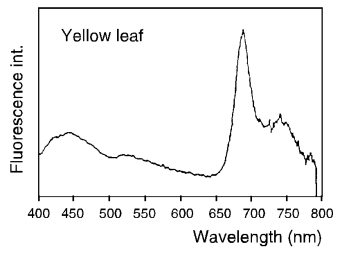

Figure 6.30. *Fluorescence spectra from a yellow beech leave recorded remotely, 355 nm excitation wavelength; from [166].*

see Fig. 6.29 and Fig. 6.30. The peak at 685 nm overlaps the absorption band of the chlorophyll and thus the relative intensity of the two peaks are affected by reabsorption. By measuring the intensity ratio, the chlorophyll concentration can be determined. Thus, low chlorophyll concentration in tree leaves and in plants, due to environmental stress, can be detected remotely. The laser-induced fluorescence technique probes the process of photosynthesis, making it possible to obtain information about early changes. There are some difficulties, however. It has turned out that the induced fluorescence spectra are different depending on the intensity of the surrounding light, at which the leaf is encountered and how much water the leaves contain. More laboratory work needs to be done before this application can be used as a general tool to map stress in the environment.

The mobile lidar system has also been used for remote surface sensing of historical buildings. Previously, fluorescence from algae growing on historical buildings, was investigated by point measurements that resulted in subsequent laboratory analysis. In Paper **III** a preliminary experiment related to remote sensing of historical buildings by fluorescence lidar is presented.

Chapter 7

Lidar System Design

The lidar group in Lund has performed many successful campaigns based on a mobile lidar system that was first described in 1987 [43]. At that time, the lidar group focused on mercury and sulphur dioxide measurements in the troposphere, and on fluorescence imaging. The original lidar system was based on a computer controlled Nd:YAG-pumped dye laser, a receiver unit consisting of a 40 cm Newtonian telescope, and a steerable mirror to control the vertical direction of the laser beam and the telescope angle. The horizontal direction was controlled by turning the telescope by the use of a stepper motor. The lidar system is a co-axial unit which means that the laser beam is transmitted via the center of the telescope by the use of a small prism. This prism is controlled via two servo motors controlled by the system computer. The software was based on Fortran and the user interface was elementary. All equipment was contained in a Volvo F610 truck with a custom-made compartment; see Fig. 7.1.

Figure 7.1. *Mobile lidar system based on a design described in [43].*

When new projects were introduced that included imaging, automation, large data handling etc., it became clear that the system needed an upgrade. Thus, the lidar system design was gone through once again and then re-designed to meet new requirements. The initial work has been presented in an internal report at the division [11]. In this chapter a brief overview of that work is described and some of the text originates from that technical report. Before the system upgrade was initiated, it was decided that the main focus of the new system was to:

- use standardized components
- keep the cost low
- make the system user-friendly
- make the design compact
- to make the module design easily accessible for future upgrades
- make large data handling possible

Our experience from the use of the old system was that the amount of data created problems. There was an increasing demand for software that takes care of all measured data and presents these data in an easily understood mode. After some initial studies we decided to design a new software, based on LabVIEW, to obtain a user-friendly lidar system. Another experience was that it is difficult to maintain home-made electronic design, especially if it is connected to software. Thus, standardized plug-in boards for computers were chosen since software drivers for external instruments and data acquisition boards are included in a software license for LabVIEW. The photograph of the new interior is presented in Fig. 7.3.

The new design is based on two computers: One is used for system control and data recording. A second computer is used for data evaluation and data presentation that can take place in real-time. A third computer, configured by the laser supplier, has to be included in the system to control the dye laser. A block diagram of the new design is presented in Fig. 7.2.

The system computer contains four standardized plug-in boards to control the system and record data; see Fig. 7.2. A GPIB plug-in board is used for instrument control of the digitizer, one digital IO board is used mainly to control two stepper motors that control the telescope, a network board is used for data transfer to the evaluation computer, and a multi-function board to record current wind speed and direction, control of servo motors etc. All cabling was connected to the control unit. From there, connections were made to a number of sensors, relays, motors, etc.

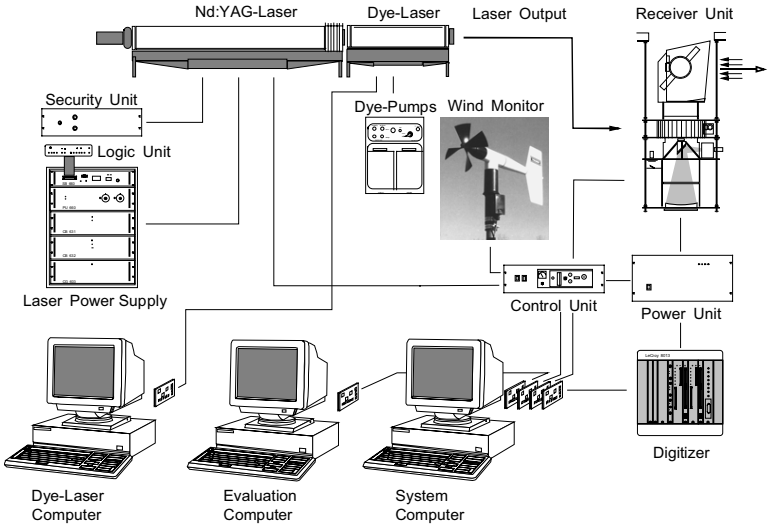

Figure 7.2. *Block diagram of the new lidar system design; from [11].*

All electronics and computers are mounted in a system cabinet (a standard 19 inch rack) as shown in Fig. 7.3 and Fig. 7.4.

In the lidar system, the system computer controls the measurement procedure and raw data storage. All data are sent to the evaluation computer via a local network for either real-time analysis or for later evaluation and presentation. It is also possible to perform an evaluation and presentation on the system computer. The lidar program consists of six menus. Each menu corresponds to a typical task that can be performed by the lidar system.

When the system is started the *Manual Control* menu is activated to control the dome direction and other basic functions such as the laser light chopper which is used to block the laser light from reaching the atmosphere. This is a basic menu that is used only at startup.

After the laser is running, the *Live Curve* menu is used to calibrate and diagnose the lidar return signal. In this menu the controls for the dome direction are used to set the correct direction of the beam and to adjust the settings of the digitizer, such as number of samples to record and offset values. In this menu it is also possible to adjust the laser beam direction compared to the optical axis of the telescope (overlap). This is done by controlling the tilt angle of the prism in the telescope by the use of two servo motors. The *Live Curve* menu is typically used at the beginnings of measurement to check the quality of the recorded data (laser beam overlap, possible measurement angles etc.).

Figure 7.3. *Interior of the mobile lidar system after upgrade.*

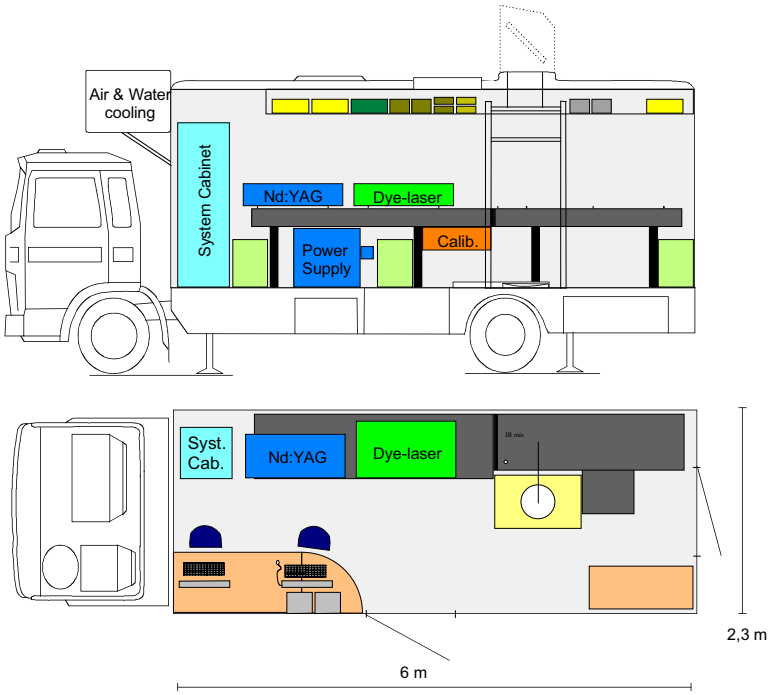

Figure 7.4. *Overview of the mobile lidar system after upgrade.*

In the *Define Measurement* menu it is possible to define a measurement sequence and, at the same time, preliminarily evaluate the raw data recorded. The defined measurement sequence can later be easily repeated from the *Run Measurement* menu. The *Run Measurement* menu executes a measurement sequence which has been defined in the *Define Measurement* menu.

The *Evaluation* menu, which is executed on the evaluation computer, evaluates raw data files and creates evaluated measurement files. Directions can be evaluated separately or all together with the same evaluation parameters. The *Presentation* menu reads evaluated data files and presents the result as concentration maps on the computer screen. The *Presentation* menu can also read evaluated temporary files from the *Run Measurement* menu in the system computer. This allows real-time display of the measurement situation. By the use of standardized software, such as LabVIEW, we managed to upgrade the lidar system in a limited time frame. Later, additional features such as a laser wavelength calibration unit, a wind video-graphical unit, and an OPO laser were added to the system. This resulted in an additional system upgrade [44, 167].

Chapter 8

GASMAS Performance Analysis

In the first GASMAS article a sensitivity corresponding to a fractional absorbance of 2.5×10^{-5} was reported for measurements on fruit, wood, and polystyrene foam. The measurement setup was based on the tunable diode laser spectroscopy (TDLS) technique using wavelength modulation at 55 kHz. A Fabry-Perót diode laser was used as a tunable light source while a large area PMT (EMI 9558 QA) was used as a detector [10]. Meanwhile, other research groups have reported a minimum fractional absorbance of 1×10^{-7}[123, 168]. In this chapter it will be discussed why the resolution in a GASMAS setup differs froms to what is reported for other TDLS instruments.

8.1 Light absorption

In an ideal spectroscopy system (no flicker noise or thermal noise) shot noise is the only limiting factor of the SNR of the system,s as described in Chap. 5. Its SNR value is given by

$$SNR = \sqrt{\frac{I_{dc}}{2qB}}, \tag{8.1}$$

where q is the electron charge (As), B is the measurement bandwidth (Hz), and I_{dc} is the current at the sensor(A). Eq. (8.1) shows the importance of getting much light to the detector and to use a detector with a high quantum efficiency since the SNR value is proportional to $\sqrt{I}_{dc}$. Thus, the maximal theoretical SNR, at a wavelength of 760 nm at a 1 Hz bandwidth, for a TDLS system based on a 1 mW laser should be about 4.3×10^7. This SNR value corresponds to a fractional absorbance of 2.3×10^{-8}. The estimation is based on the assumption that all light from the laser is received by a detector with 100 % quantum efficiency.

In a practical system the light is scattered and attenuated while it travels from the laser towards the sensor. This happens especially in a GASMAS setup, where only a fraction of the transmitted light is detected, depending on the sample and the setup geometry. This difference is one reason why the potential performance of a TDLS system for GASMAS is lower compared to traditional TDLS systems. Typical values of detected light levels are only 1 % to 0.01 % of the transmitted laser light. A light attenuation of 10^4 decreases the minimum detectable absorbance by a factor of 100 if the same detection bandwidth is used. A detailed description of how the minimum detectable absorbance of a tunable diode laser spectroscopy system is affected by the incident light level of the detector is found in Ref. [116].

8.2 Detector performance

The design of a detector for GASMAS is critical and it should have a high dynamic range since this is one factor that limits the performance of the system. It is important that the actual noise floor is low at the frequency where the 2f signal is detected. However, in practice, shot noise is not the only source of noise in a sensor. Thermal noise from resistors and flicker noise from amplifiers do affect detector performance. Thus, the performance of the PMT used, the photodiode, and the large area APD discussed in Chap. 5, was measured by the use of a low-noise spectrum analyzer and an unmodulated IR-LED (760 nm) as a light source. These measurements should show similar SNR values, as estimated in Chap. 5. However, the area of the light sensors used differs and this gives rise to an error in the result. Thus, a lower SNR value is expected for the avalanche photodiode (APD) since its area is smaller than for the photodiode and the PMT. The area of the PMT is 3.5 cm^2, the area of the photodiode is 3.2 cm^2, and the area of the APD is 0.8 cm^2. These measurements should be seen only as an example of how to estimate which detector to use in a GASMAS setup. The measurement principle is similar to the one described in Ref. [70].

In this chapter the signal-to-noise value (SNR), expressed in dB, is used. This is because it is an expression of the quality of a signal compared to surrounding noise. It is often used in spectrum analyzers and presented for a bandwidth of, for example, 1 Hz. The SNR of data presented in a spectrum analyzer is defined as

$$SNR = 10\log_{10}(\frac{V_s^2}{V_n^2})dB, \tag{8.2}$$

where V_s and V_n are the root-mean-square (rms) amplitudes of the signal and noise, respectively. In this case, the V_s value corresponds to the rms value of the constant DC level recorded by

the sensor. The V_n value is measured at different frequencies. The SNR at different frequencies is estimated by studying the result of RIN measurements of the detectors. In this case it is interesting to study in particular the SNR at 20 kHz. The principle of the RIN measurement is described in Sect. 4.1.3.

By studying the RIN value at different frequencies external noise sources can be found and system performance can be estimated. This is due to the fact that the peak of the 2f signal is similar to the amplitude of the direct absorption dip (44% of a direct absorption dip of Gaussian shape); see Sect. 6.1.3. In other words, the expected peak amplitude of the 2f signal should be a factor of 2 - 3 lower than the direct absorption dip, depending on the shape of the absorption line which corresponds to about 6 dB in a RIN diagram.

An IR light-emitting diode (LED) is used as a light source since it is normally less affected by flicker noise than a laser. The LED is powered by a low-noise battery via a metal film resistor. A neutral density filter (OD 1.0 or 3.0) is mounted in front of the sensor. The light that falls onto the sensor is of the order of 1 μW if the OD 3.0 filter is used. The sensor is connected to a low-noise data acquisition board (PCI-4472, National Instruments) and the spectrum analyzer is based on a toolkit for LabVIEW (Sound and Vibration Toolkit 4.0, National Instruments). The data acquisition board is run at maximum speed and the spectrum analysis is carried out with a 1 Hz resolution bandwidth, and a Hanning time window is used [169]. However, the Hanning time window introduces a spectral leakage that corresponds to an increase of the noise bandwidth by a factor of 1.5. Thus, the actual measured SNR is 3.5 dB ($20 \times \log 1.5$) higher than the value measured directly.

As shown in Fig. 8.1, the total gain of the cathode current of the PMT is of the order of 1.2×10^8. A gain of 1200 originates from the PMT itself while the gain of the transimpedance amplifier is 10^5. The measured SNR at 20 kHz is about 103.5 dB (100 + 3.5) which indicates that a minimum detectable absorbance of 1×10^{-5} can be detected if 2f detection is used with an detection bandwidth of 1 Hz. The estimated SNR value in Sect. 5.1.4 was 107 dB. However, these estimations are rough, and careful analysis is needed to get a detailed estimation. Please note the drop off at about 10 kHz due to a low-pass filter in the transimpedance amplifier.

Fig. 8.2 shows that the total gain of the diode current of the APD is of the order of 1.3×10^6. The SNR at 20 kHz is of the order of 113.5 dB (110 + 3.5) which indicates a minimum detectable absorbance of 4×10^{-6} can be detected if 2f detection is used with a detection bandwidth of 1 Hz. The estimated SNR value in Sect. 5.3 was 117 dB.

The most promising detector type discussed in Chap. 5 is the photodiode. The measured performance of a large area PIN photodiode is shown in Fig. 8.3. The SNR value at 20 kHz is 118.5 dB

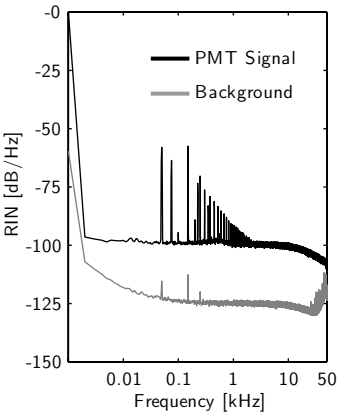

Figure 8.1. *Measured noise spectra of a PMT (5070A, Hamamatsu) in combination with a transimpedance amplifier (C7319, Hamamatsu). Incident light level of the LED is of the order of 1μW. The PMT and TIA were used in Paper **IX** and in Paper **X**.*

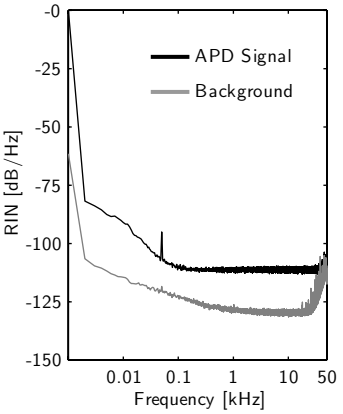

Figure 8.2. *Measured noise spectra of a large area APD(SD394-70-72-661, Advanced Photonix). Incident light level of the LED is of the order of 1μW. The large area APD was used in Paper **XIII**.*

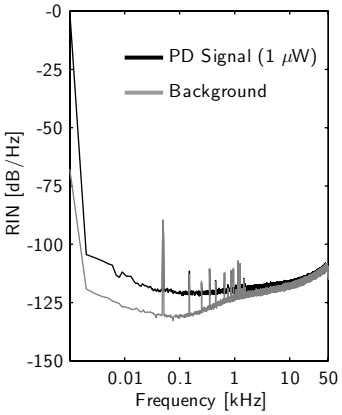

Figure 8.3. *Measured noise spectra of a large area photodiode (S3204-08, Hamamatsu). Incident light level of the LED is of the order of 1μW and the gain of the amplifier is set to 10^6.*

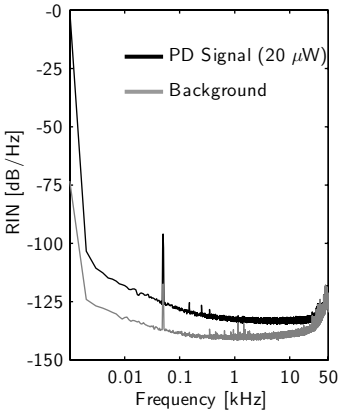

Figure 8.4. *Measured noise spectra of a large area photodiode (S3204-08, Hamamatsu). Incident light level of the LED is of the order of 20μW and the gain of the amplifier is set to 10^5.*

(115 + 3.5) which is about 6 dB lower than the estimated value (124 dB) in Sect. 5.2. However, strange noise at high frequencies is noticed but not if the incident light level is increased by a factor of 20 and the gain is dropped by a factor of ten. At low frequencies the SNR is of the order of 125 dB.

The increased noise at higher frequencies is due to the fact that the voltage noise of the input of the transimpedance amplifier feeds the junction capacitance of the photodiode [170]. This effect is normally small but not for an unbiased, large-area photodiode such as model S3204-08 from Hamamatsu. The additional noise current caused by the junction capacitance is given by

$$i_{cap} = 2\pi u_n C f, \tag{8.3}$$

where i_{cap} is a current noise at the amplifier input caused by the capacitance, u_n is the input voltage noise of the transimpedance amplifier, C is the capacitance of the junction capacitor of the photodiode, and f is the spot frequency. Since the junction capacitance is about 2 nF and the voltage noise is about $4\text{nV}/\sqrt{Hz}$, the current noise is about 1 pA at 20 kHz. If this current noise is squared and added to the denominator in Eq. (5.15) this will decrease the expected SNR at 20 kHz to 117 dB. Thus, the use of a large-area photodiode at high frequencies requires that it is biased to decrease the junction capacitance. However, if the level of the incident light is higher, this effect can be neglected; see Fig. 8.4.

8.3 Backscattered light

As discussed in Sect. 4.1.3 a laser is sensitive to backscattered light. It turns out that the laser RIN value is decreased if the level of backscattered light is high. If the level of the backscattered light becomes too high, coherence collapse occurs and the laser wavelength is changed and the device does not run as a single-mode laser. In a GASMAS setup, the level of backscattered light is always high since the laser light is directed towards a scattering solid material. However, we have noticed that the influence of backscattered light decreases if the laser or fiber is tilted towards the surface of the sample. Thus, the specular reflection of the light does not re-enter the laser cavity.

The sensitivity of backscattered light was investigated by measuring the RIN value of both a Fabry-Pérot laser, a pigtailed DFB laser, and a VCSEL by mounting small pieces of balsa, plastic, and polystyrene foam in front of the laser or the fiber. A typical recording of the RIN value is presented in Fig. 8.5. It turned out that all three laser types were sensitive for backscattered light but the Fabry-Pérot laser turned out to be the most sensitive one. All three laser types showed a decreased RIN value of about 20 - 30 dB below a frequency of 1 kHz. More investigations are needed

to investigate whether an optical isolator is required in a GASMAS setup or whether it is enough to tilt the laser.

8.4 Laser stability

If a high intensity resolution measurement is required, long time averaging is needed. To improve the minimum fractional absorbance by a factor of ten the measurement time must be increased by a factor of 100. However, this action does not always help since noise due to laser drift affects the measurement [116]. One method to improve the performance is to add a reference cell containing the gas that is measured and use that gas cell to keep track of the laser wavelength. Either this information can be used to regulate the laser current or the averaging process can shift the recorded data in wavelength to compensate for the laser drift [168, 171].

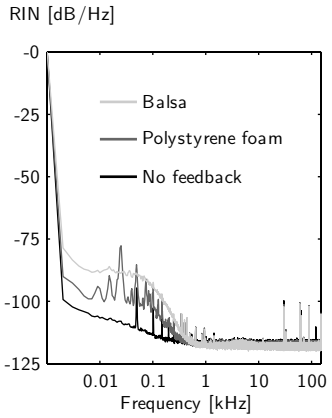

Figure 8.5. *Measured RIN value for a Fabry-Pérot laser. Small pieces of balsa and polystyrene foam were mounted in front of that laser to test the performance for different feedback conditions.*

8.5 Optical interference fringes

The worst type of noise in a tunable diode laser system is optical interference fringes. The fringes frequently affect system performance when the required minimum fractional absorbance is below 10^{-4}. In traditional instruments based on tunable diode laser spectroscopy there are methods to suppress optical interference fringes. One method is to increase the length of the path by the use of multi-pass gas cells. However, a multi-pass gas cell introduces additional fringes but these may be suppressed by frequently emptying the gas cell and measuring the background signal. The fringe contribution can be suppressed by subtracting the background signal from the actual measurement. However, this cannot be done in a GASMAS setup since it is normally not possible to empty the sample of the gas measured since the gas is embedded in the material. Thus, the only way to suppress systematic errors due to fringes, is to shake the test setup. It is important that the vibration action is arbitrary.

In Paper **IX** and Paper **XIII** pigtailed diode lasers were used. Pigtailed lasers are, in some cases, more appropriate since the laser source is not located close to the sample. However, as discussed in Ref. [123], fiber connections should be based on fusion-spliced or angle-polished FC/APC connectors to suppress etalon fringes caused by the fiber. In practice, this approach is powerful only of all fiber connectors are clean, which is not easy to maintain when the equipment is used in the field. Dirty fiber tips cause etalon fringes that degrade system performance. In Paper **IX** a method to suppress etalon fringes, caused by the fibers is presented. The main motivation of this paper was to improve the performance of a tunable diode laser spectroscopy instrument based on a pigtailed

DFB laser. In Paper **XIII** this technique was reused on a pigtailed VCSEL. The system performance was improved by more than a factor of ten.

Chapter 9

GASMAS Applications

As discussed in Paper **XI** the GASMAS technique has a potential in many different applications. So far, test samples such as foam, food products, wood, pharmaceutical solids, and human tissue have been successfully tested by the use of the GASMAS technique. The greatest benefit of using the technique is that it is non-intrusive and makes it possible to measure gas inside a solid material. However, the most successful application may not have been found yet since our main focus has been on the two most promising applications so far. One has to remember that it takes a long time to develop new research techniques and to identify the most successful use of new research, especially if resources are limited. It has taken us about one year to improve the sensitivity of a GASMAS measurement by a factor of about 20. GASMAS research was initiated in 2001.

Two applications have shown a great potential so far; to be able to diagnose the health of human sinuses and gas ventilation in sinuses as described in Paper **XII** and in Ref [172]. The second application is to measure gas inside pharmaceutical solids. By measuring gas in tablets, more knowledge is gained of how tablet manufacturing parameters are connected to the dissolution of the tablet, as discussed in Paper **X** and in [173].

To our knowledge no other method that is able to measure gas ventilation in human maxillary sinuses exists today. Other methods have been tried but only one of them is non-intrusive. However, this technique is based on using either a radioactive or stable Xe gas together with single-photon emission computerized tomography (SPECT) or repeated computerized tomography (CT) scans of the cavity filled with slightly radio-opaque Xe. In both cases the patient is exposed to high doses of ionizing radiation, and the approaches are thus not appropriate as standardized tools. Ultra-sound techniques are also used to diagnose human sinuses but the results are not clear.

The market for oxygen sensors should be relatively large since there is a number of companies that develop and sell oxygen sensor probes. Today, small oxygen sensors (7 mm times 7 mm), based on a fluorescence technique can be bought in large volumes from companies such as *Sensors for Medicine and Science Inc* and *OxySense*. The sensor is based on a small dot that fluoresces proportionally to the concentration of oxygen. The small dot can either be mounted on the probe or placed inside a sample. However, the method is intrusive since the fluorescent material must be placed inside the sample to be studied. There is no such need for an instrument based on the GASMAS technique.

The GASMAS technique can be used to measure other gases than water vapor and oxygen. In theory, any gas that has been measured by the use of a traditional TDLS system can be measured by a GASMAS setup. However, it is the penetration depth at the wavelength in question into the sample that limits the performance of the GASMAS technique. Nevertheless, GASMAS should have a potential in applications where oxygen probe sensors are used today.

In our recent research, water vapor has only been studied in two projects and thus it is difficult to predict the potential of applications based on water vapor measurements by the use of the GASMAS technique. However, water vapor is an important issue in the food industry and in the pharmaceutic industry. Thus, more research on water vapor in solids is needed before additional GASMAS applications are established.

Concerning the development of an instrument based on the GASMAS technique, much can be learned by studying portable methane detectors as described in Refs [174, 175]. Today, an advanced instrument, based on advanced optics, mechanics, electronics and software, can be developed in a limited time frame and at a reasonable cost. However, optical interference fringes will still be the sources of noise most difficult to handle, especially if the sample is based on an inorganic material.

Comments on the Papers

I **Remote monitoring of vegetation by spectral measurements and multi-colour fluorescence imaging**
This paper is a review of remote monitoring of laser-induced fluorescence from vegetation within the LASFLEUR project. A mobile lidar system was used to record fluorescence point and imaging measurements.

I participated in the planning and took part in all measurements. I also contributed to evaluation and manuscript preparation.

II **Remote fluorescence measurements of vegetation spectrally resolved and by multi-colour fluorescence imaging**
A remote sensing system for combined fluorescence spectral recordings and multi-color fluorescence imaging of vegetation is presented.

I participated in the planning and took part in all the experiments. I also contributed to evaluation and manuscript preparation.

III **A preliminary experiment on the remote sensing of historical buildings by fluorescence Lidar**
Initial fluorescence point and remote monitoring measurements on stone materials from different locations is presented. The aim was to study algae concentration on different stone samples and to compare recorded data from different instruments. A joint project of Lund University, Sweden and IROE-CNR, Italy.

I did a substantial part of the construction and took part in some initial measurements.

IV **Atmospheric mercury concentrations and fluxes in the Almadén district (Spain)**
Mercury point monitoring and flux measurements close to a mercury mine in Spain are described. The flux measurements were performed by the use of a mobile lidar system capable of measuring atomic mercury in the atmosphere.

I participated in the planning and took part in all lidar measurements. I also contributed to the evaluation and to the manuscript preparation.

V **Remote monitoring of industrial emissions by combination of lidar and plume velocity measurements**
A new method to measure wind speed remotely in combination with DIAL measurements on SO_2 emissions at a paper mill is presented. The wind sensor technique is called videography and is based on images of plumes being grabbed continuously, while the speed is estimated by the use of image processing. Simultaneous measurements of the distance and the integrated concentration of SO_2 across the plume were provided by the DIAL technique. A comparison between traditional vane anemometers and the videography method was performed.

I participated in a substantial part of the system development, integration, and experiment and made a minor contribution to the evaluation and the preparation of the manuscript.

VI **Studies of gas exchange in fruits using laser spectroscopic techniques**
The gas content in fruit is studied by the use of tunable diode laser spectroscopy. The assessment of oxygen gas in apples and oranges is demonstrated. This technique has a potential in fruit management.

I participated in some experiments and made a minor contribution to the preparation of the manuscript.

VII **Spectroscopic studies of wood-drying processes**
The use of diode laser spectroscopy at two wavelengths, water vapor and oxygen monitoring during wood drying processes, is described in this paper. The aim of this paper was to study oxygen and water vapor content in wood during the drying process. A comparison of measurement with resistive and capacitive moisture meters is performed. The true moisture content of the wood was measured by a scale.

I had the major responsibility for this project, involving a substantial part of the planning, construction, experiments, evaluation, and manuscript preparation.

VIII **Human sinus studies using monte carlo simulations and diode laser gas absorption spectroscopy**
An overview that focuses on the possibility of non-intrusive in-vivo human sinus studies by diode laser gas absorption spectroscopy. Measurements on the human frontal sinus and a tissue-like phantom are described and compared with simulated results by the use of the software ASAP. The results from the experiments and the simulations show good agreement for both the tissue-like phantom measurements and the measurements on the healthy volunteer

I introduced ASAP to the Atomic Physics Division and provided software support. I made minor contributions to the manuscript preparation.

IX **Approach to optical interference fringes reduction in diode laser absorption spectroscopy**
A method to suppress noise caused by pigtailed lasers is described in the article. The technique suppresses optical interference fringes by the use of a software-based, balanced detection of light from a pigtailed, single-mode laser.

I participated in the planning and took part in some of the experiments and developed electronics for the experiments and software for data acquisition. I contributed to the preparation of the manuscript.

X **Non-invasive characterization of pharmaceutical solids by diode laser oxygen spectroscopy**
Characterization of solid pharmaceuticals by the use of diode laser oxygen spectroscopy is described. The aim of this article was to show that information related to gas dispersed within highly scattering (turbid) materials can be measured by the use of the GASMAS technique.

I took part in some experiments and made minor contributions to the manuscript preparation.

XI **Laser spectroscopy of gas in scattering media at scales ranging from kilometers to millimeters**
This paper is an overview of measurement techniques used in our group and their connection. Thus, it does not contain any new measurement data. Obviously, I was involved in some of the measurements and the corresponding data analysis.

XII **Gas monitoring in human sinuses using tunable diode laser spectroscopy**
A demonstration of a novel non-intrusive technique based on tunable diode laser absorption spectroscopy of oxygen at 760 nm and water vapor at 935 nm to investigate the human sinuses in vivo. Molecular oxygen was detected in the maxillary sinuses on 11 volunteers.

I participated in planning, experiments, and evaluation and made minor contribution to manuscript preparation.

XIII **Flexible lock-in detection system based on synchronized computer plug-in boards applied in sensitive gas spectroscopy**
By the use of plug-in boards for standardized computers, a compact, powerful and flexible detection system for gas spectroscopy, based on coherent sampling, was developed. Coherent sampling allows raw data to be analyzed in real time or post-processed in the time- or frequency domain. The capabilities of the system are demonstrated by measurements of molecular oxygen in ambient air, as well as dispersed gas in scattering materials, such as plants and human tissue.

I introduced the technology to the Atomic Physics Division. My contribution was a major part of the planning, construction, experiments, evaluation, and manuscript preparation.

Acknowledgements

This thesis could not have been completed without generous help from several members of the Atomic Physics Division in Lund, and the encouragement from my friends and my family. I would especially like to express my thanks to Prof. Sune Svanberg, for being my supervisor and for giving me the opportunity to perform advanced research. I have never met anyone with such enthusiasm for physics in combination with endurance when it comes to working late and keeping focus on what should be delivered in the end. I also appreciate my co-supervisor Hans Edner for his pedagogical touch.

I would like thank my former colleague Petter Weibring, for having patience and trust and always being willing to share the hard work, disregarding where on earth Petter might be. Today, Petter lives in Boulder, USA. Special thanks go to Linda Persson for her capacity to run projects day and night. Without your collaboration the number of articles would have been smaller.

Special thanks go also to Tomas Svensson, Lars Rippe, and Johan Mauritsson for collaboration and fruitful discussions regarding how to perform good measurements by the use of different techniques.

I should also like to point out the valuable help by Prof. Ove Axner who has enlightened us with his experience in wavelength modulation spectroscopy.

Thanks to my room mates, co-workers, and former co-workers Rasmus Grönlund, Mikael Sjöholm, Märta Cassel-Engqvist, Ulf Gustafsson, and Jonas Sandsten for always being there for all kinds of support or telling a joke.

I am also grateful to all the people at the department who make things run smoothly in a friendly manner; Minna Ramkull, our present secretary who takes care of all practical details without hesitation and Henrik Steen who keeps track of where the money goes. I have a special dept of thanks to Bertil Hermansson, for his help with computer configuration and software support. He is always willing to do marvelous tricks with computers when they do not work. I am grateful to Åke Bergqvist and Thomas Wendel,

for their help with electronic design. They always find a way to make the electronic boards work for you.

Thank you Microsoft for the "Remote Desktop" function in Windows XP. Without this feature I do not think it is possible for a parent of small children to get a PhD degree.

I am very grateful to my parents and my parents-in-law, especially Alice Hinz, for helping me and Susan with our children, and finally, to my partner Susan Hinz for encouragement and for always being there.

References

1. D. J. Travis, A. M. Carleton and R. G. Lauritsen. *Contrails reduce daily temperature range. A brief interval when the skies were clear of jets unmasked an effect on climate.* Nature **418**, 601–602 (2002).

2. G. Stanhill and S. Moreshet. *Global radiation climate in Israel.* Clim. Change **22**, 121–138 (1992).

3. Åke Rosenqvist, A. Milne, R. Lucas, M. Imhoff and C. Dobsone. *A review of remote sensing technology in support of the Kyoto Protocol.* Env. Science Policy **6**, 441–455 (2003).

4. J. M. Wilczak, E. E. Gossard, W. D. Neff and W. L. Eberhard. *Ground-based remote sensing of the atmospheric boundary layer: 25 years of progress.* Bound.-Lay. Meteorol. **78**, 321–349 (1996).

5. J. A. Hoskins. *Health effects due to indoor air pollution.* Indoor and Built Environment **12**, 427–433 (2003).

6. H. L. Walmsley and S. J. O'Connor. *The accuracy and sensitivity of infrared differential absorption lidar measurements of hydrocarbon emissions from process units.* Pur Appl. Opt. **7**, 907–925 (1998).

7. P. Moulton, A. Dergachev, Y. Isyanova, B. Pati and G. Rines. *Recent advances in solid state lasers and nonlinear optics for remote sensing.* Proc. SPIE **4893**, 193–202 (2003).

8. C. S. B. Grimmond. *Progress in measuring and observing the urban atmosphere.* Theor. Appl. Climatol. **84**, 3–2 (2006).

9. P. H. Flamant. *Atmospheric and meteorological Lidar: From pioneers to space applications.* C. R. Phys. **6**, 864–875 (2005).

10. M. Sjöholm, G. Somesfalean, J. Alnis, S. Andersson-Engels and S. Svanberg. *Analysis of gas dispersed in scattering media.* Opt. Lett. **26**, 16–18 (2001).

11. M. Andersson and P. Weibring. A user friendly lidar system based on LabVIEW. Technical report , Lund Reports on Atomic Physics LRAP-201, Lund, Sweden (1996).

12. S. Svanberg. *Atomic and molecular spectroscopy.* Springer-Verlag, Lund (1992).

13. L. S. Rothman, A. Barbe, D. C. Benner, L.R. Brown, C. Camy-Peyret, M.R. Carleer, K. Chance, C. Clerbaux, V. Dana, V.M. Devi, A. Fayt, J.-M. Flaud, R.R. Gamache, A. Goldman, D. Jacquemart, K.W. Jucks,

W.J. Laerty, J.-Y. Mandin, S.T. Massie, V. Nemtchinov, D.A. Newnham, A. Perrin, C.P. Rinsland, J. Schroeder, K.M. Smith, M.A.H. Smith, K. Tang, R.A. Toth, J. Vander Auwera, P. Varanasi and K. Yoshino. *The HITRAN molecular spectroscopic database: Edition of 2000 including updates through 2001.* J. Quant. Spectr. Rad. Trans. **82**, 5–44 (2003).

14. C. N. Banwell and E. M. McCash. *Fundamentals of molecular spectroscopy.* McGraw-Hill Publishing Company (London, 1994).

15. J. W. Lichtman and J. A. Conchello. *Fluorescence microscopy.* Nature Methods **2**, 910–919 (2005).

16. M. Sneep and W. Ubachs. *Direct measurement of the Rayleigh scattering cross section in various gases.* J. Quant. Spec. Rad. Trans. **92**, 293–310 (2005).

17. D. Jackel and B. Walter. *Modeling and rendering of the atmosphere using Mie-scattering.* Comp. Graph. For. **16**, 201–210 (1997).

18. A. J. Cox, A. J. DeWeerd and J. Linden. *An experiment to measure Mie and Rayleigh total scattering cross sections.* Am. J. Phys. **70**, 620–625 (2002).

19. H. C. van de Hulst. *Light scattering by small particles.* Dover Publications (Dover, 1981).

20. C. F. Bohren and D. R. Huffman. *An experiment to measure Mie and Rayleigh total scattering cross sections.* John Wiley & Sons Inc. (New York, 1998).

21. M. Kelker. *Scattering of light & other electromagnetic radiation.* Academic Press (New York, 1969).

22. L. Henyey and J. Greenstein. *Scattering of light & other electromagnetic radiation.* Astrophys. Jour. **93**, 70–83 (1941).

23. C. Abrahamsson. *Time-resolved spectroscopy for pharmaceutical applications.* PhD thesis , Lund Reports on Atomic Physics LRAP-348, Lund, Sweden (2005).

24. L. Wang, S. L. Jacques and L. Zheng. *MCML Monte Carlo modeling of light transport in multi-layered tissues.* Comp. Meth. Prog. Biomed. **47**, 131–146 (1995).

25. B. Michael and T. J. Beck. *Raytracing in medical applications.* Laser + Photonik **5**, 38–41 (2005).

26. Lambda Research Corporation. Tracepro and Oslo in medical applications. Technical report , Lambda Research Corporation (2005).

27. J.H. Seinfeld. *Atmospheric chemistry and physics of air pollution.* John Wiley and Sons (New York, 1995).

28. R.M. Measures. *Laser remote sensing.* John Wiley and Sons (New York, 1984).

29. C. Bairel. *Environmental chemistry.* Freeman & Co (New York, 1995).

30. R. D. Hudson and J. W. Hudson. *The military applications of remote sensing by infrared.* In *Proc. IEEE* volume 63 pages 104–128. Wiley, New York (1975).

31. S. L. Jacques, R.D. Glickman and J.A. Schwartz. *Internal absorption coefficient and threshold for pulsed laser disruption of melanosome isolated from retinal pig-mented epithelium.* Proc. SPIE **2681**, 468–477 (1996).

32. S. A. Prahl. *A Monte Carlo model of light propagation in tissue.* (Portland, OR: Oregon Medical Laser Centre) http://omlc.ogi.edu/spectra/hemoglobin/index.html **5**, 105–111 (1999).

33. T. H. Maiman. *Stimulated optical radiation in ruby.* Nature **187**, 493–494 (1960).

34. R. N. Hall, G. E. Fenner, J. D. Kingsley, T. J. Soltys and R. O. Carlson. *Coherent light emission from GaAs junctions.* Phys. Rev. Lett. **9**, 366–368 (1962).

35. M. I. Nathan, W. P. Dumke, Jr. G. Burns, Frederick H. Dill and G. Lasher. *Stimulated emission of radiation from GaAs p-n junctions.* Appl. Phys. Lett. **1**, 62–64 (1962).

36. N. Holonyak, Jr. and S. F. Bevacqua. *Coherent (visible) light emission from* $Ga(As_{1-x}\ P_x)$ *junctions.* Appl. Phys. Lett. **1**, 82–83 (1962).

37. T. M. Quistand R. H. Rediker, R. J. Keyes, W. E. Krag, B. Lax, A. L. McWhorter and H. J. Zeigler. *Semiconductor maser of GaAs.* Appl. Phys. Lett. **1**, 91–92 (1962).

38. C. E. Wieman. *Using diode lasers for atomic physics.* Rev. Sci. Instrum. **62**, 1–20 (1991).

39. P. M. Ripley. *The physics of diode lasers.* Laser. Med. Sci. **11**, 71–78 (1996).

40. L. A. Coldren, G. A. Fish, Y. Akulova, J .S. Barton, L. Johansson and C. W. Coldren. *Tunable semiconductor lasers: a tutorial.* J. Lightwave Technol. **22**, 193–202 (2004).

41. D. K. Mynabaev and L. L. Scheiner. *Fiber-optic communications technology.* Prentice Hall (2001).

42. C. Weisbuch. *The development of concepts in light-emitting devices.* Braz. J. Phys. **26**, 21–42 (1996).

43. H. Edner, K. Fredriksson, A. Sunesson, S. Svanberg, L. Unéus and W. Wendt. *Mobile remote sensing system for atmospheric monitoring.* Appl. Optics **26**, 4330–4339 (1987).

44. P. Weibring, H. Edner and S. Svanberg. *Versatile mobile lidar system for environmental monitoring.* Appl. Optics **42**, 3583–3594 (2003).

45. H. Kroemer. *A proposed class of hetero-junction injection lasers.* In *Proc. IEEE* pages 221–222 (1963).

46. H. Kogelnik and C. V. Shank. *Stimulated emission in a periodic structure.* Appl. Phys. Lett. **18**, 152–154 (1971).

47. M. Nakamura, K. Aiki, J. Umenda and A. Yariv. *Cw operation of distributed-feedback GaAs-GaAlAs diode lasers at temperatures up to 300 K.* Appl. Phys. Lett. **27**, 402–405 (1975).

48. W. Streifer, D. R. Scifres and R. D. Burnham. *Status of distributed feedback lasers.* In *Electron Devices Meeting* pages 117–121 (1976).

49. J. Seufert, M. Fischer, M. Leggea, J. Koeth, R. Werner, M. Kamp and A. Forchel. *DFB laser diodes in the wavelength range from 760 nm to 2.5 μm.* Spectrochim. Acta A **60**, 3241–3247 (2004).

50. S. Bauer. *Nonlinear dynamics of semiconductor lasers with active optical feedback.* PhD thesis Faculty of Mathematics and Natural Sciences II Humboldt-Universität zu Berlin (2005).

51. Y. Nakano, Y. Deguchi, K. Ikeda, Y. Luo and K. Tada. *Resistance to external optical feedback in a gain-coupled semiconductor DFB laser.* In *Semiconductor Laser Conference* pages 72–73 (1990).

52. T. Aellen, S. Blaser, M. Beck, D. Hofstetter, J. Faist and E. Gini. *Continuous-wave distributed-feedback quantum-cascade lasers on a Peltier cooler.* Appl. Phys. Lett. **83**, 1929–1931 (2003).

53. F. Koyama, S. Kinoshita and K. Iga. *Room temperature CW operation of GaAs vertical cavity surface emitting laser.* IEICE Trans. **E71-E**, 1089–1090 (1988).

54. K. Iga. *Surface emitting semiconductor lasers.* J. Sel. Top. Quant. Electr. **24**, 1845–1855 (1988).

55. K. Iga. *Surface-emitting laser - Its birth and generation of new optoelectronics field.* J. Sel. Top. Quant. Electr. **6**, 1201–1215 (2000).

56. D. Wiedenmann, M. Grabherr, R. Jäger and R. King. *High volume production of single-mode VCSELs.* In *Proc. SPIE* volume 6132 (2006).

57. P. Vogel and V. Ebert. *Near shot noise detection of oxygen in the A-band with vertical-cavity surface-emitting lasers.* Appl. Phys. B **72**, 127–135 (2001).

58. C. Masoller and M. S. Torre. *Influence of optical feedback on the polarization switching of vertical-cavity surface-emitting lasers.* J. Quant. Electr. **41**, 1–6 (2005).

59. Y. Hong, P. S. Spencer and K. A. Shore. *Suppression of polarization switching in vertical-cavity surface-emitting lasers by use of optical feedback.* Opt. Lett. **29**, 2151–2153 (2004).

60. Y. Hong, R. Ju, P. S. Spencer and K. A. Shore. *Investigation of polarization bistability in vertical-cavity surface-emitting lasers subjected to optical feedback.* J. Quantum Electron **41**, 619–624 (2005).

61. J. Kaiser, C. Degen and W. Elsässer. *Polarization-switching influence on the intensity noise of vertical-cavity surface-emitting lasers.* J. Opt. Soc. Am. B **19**, 672–677 (2002).

62. J. M. Ostermann, F. Rinaldi, P. Debernardi and R. Michalzik. *VCSELs with enhanced single-mode power and stabilized polarization for oxygen sensing.* Phot. Tech. Lett. **17**, 2256–2258 (2005).

63. Y. Hong, P. S. Spencer and K. A. Shore. *Suppression of polarization switching in vertical-cavity surface-emitting lasers by use of optical feedback.* Opt. Lett. **29**, 2151–2153 (2004).

64. K. Petermann. *External optical feedback phenomena in semiconductor lasers.* J. Sel. Top. Quant. Electr. **1**, 480–489 (1995).

65. C. H. L. Quay, I. Z. Maxwell and J. A. Hudgings. *Coherence collapse and redshifting in vertical-cavity surface-emitting lasers exposed to strong optical feedback.* J. Appl. Phys. **90**, 5856–5859 (2001).

66. R. P. Scott, C. Langrock and B. H. Kolner. *High-dynamic-range laser amplitude and phase noise measurement techniques.* J. Sel. Top. Quant. Electr. **7**, 641–655 (2001).

67. R. Schimpe. *Theory of intensity noise in semiconductor laser emission.* Z. Phys. B **52**, 289–294 (1983).

68. C. H. Henry. *Phase noise in semiconductor lasers.* J. Lightwave Technol. **LT-4**, 298—311 (1986).

69. D. Wiedenmann, P. Schnitzer, C. Jung, M. Grabherr, R. Jäger, R. Michalzik and K. J. Ebeling. *Noise characteristics of 850 nm single-mode vertical cavity surface emitting lasers.* Appl. Phys. Lett. **73**, 717–719 (1998).

70. D. Wiedenmann, M. Kicherer, C. Jung, M. Grabherr, M. Miller, R. Jäger and K. J. Ebeling. *Sub-Poissonian intensity noise from vertical-cavity surface-emitting lasers.* Appl. Phys. Lett. **75**, 3075–3077 (1999).

71. S. L. Rumyantsev, M. S. Shur, Y. Bilenko, P. V. Kosterin and B.M. Salzberg. *Low frequency noise and long-term stability of noncoherent light sources.* J. Appl. Phys. **96**, 966–969 (2004).

72. L.G. Zei, S. Ebers, J. R. Kropp and K. Petermann. *Noise performance of multimode VCSELs.* J. Lightwave Technol. **19**, 884–892 (2001).

73. N. Schunk and K. Petermann. *Measured feedback-induced intensity noise for 1-3 μm DFB laser diodes.* Electr. Lett. **25**, 63–64 (1989).

74. F. P. Schäfer, W. Schmidt and J. Voltze. *Organic dye solution laser.* Appl. Phys. Lett. **9**, 306–309 (1966).

75. P. P. Sorokin and J. R. Lankard. *Stimulated emission observed from an organic dye, chloro-aluminum phthalocyanine.* IBM J. Res. Develop. **10**, 162–163 (1966).

76. F. J. Duarte. *Organic dye lasers. Brief history and recent development.* In *Optics & Photonics News* pages 20–25. Optical Society of America (2003).

77. D. H. Nguyen and P. Brechignac. *Tunable alternate double-wavelength single grating dye laser for DIAL systems.* Appl. Optics **27**, 1906–1908 (1988).

78. S. C. Choi, D. K. Ko, J. Lee, D. H. Kim and H. K. Cha. *The development of a mobile remote monitoring system by using differential absorption lidar technology.* J Korean Phys. Soc. **49**, 331–336 (2006).

79. T. Nayuki, K. Marumoto, T. Fujii, T. Fukuchi, K. Nemoto, A. Shirakawa and K. I. Ueda. *Development of a differential-absorption lidar system for measurement of atmospheric atomic mercury by use of the third harmonic of an LDS-dye laser.* Appl. Optics **43**, 6487–6491 (2004).

80. D. J. Brassington. *Differential absorption lidar measurements of atmospheric water vapor using an optical parametric oscillator source.* Appl. Optics **21**, 4411–4416 (1982).

81. *Quanta-Ray MOPO-730 Optical Oscillator, Instruction Manual.* Spectra Physics Inc. (1996).

82. G. Poberaj, A. Fix, A. Assion, M. Wirth, C. Kiemle and G. Ehret. *Airborne all-solid-state DIAL for water vapour measurements in the tropopause region: System description and assessment of accuracy.* Appl. Phys. B **75**, 165–172 (2002).

83. P. Weibring, J. N. Smith, H. Edner and S. Svanberg. *Development and testing of a frequency-agile optical parametric oscillator system for differential absorption lidar.* Rev. Sci. Instrum. **74**, 4478–4484 (2003).

84. S. W. Lee, J. McNeil, T. Zenker and T. H. Chyba. *Methane concentration measurements with a mid-infrared optical parametric oscillator-based differential absorption lidar system.* In *Proc. CLEO* pages 272–273 (1999).

85. W. Situ and R.J. De Young. *Two-wavelength Ti:sapphire laser for ozone DIAL measurements.* In *Proc. CLEO* pages 438–439 (1998).

86. H. Kneipp, J. Kolenda, P. Rairoux, B. Stein, D. Weidauer, J. P. Wolf and L. H. Woeste. *Ti:sapphire-laser-based lidar systems.* In *Proc. SPIE* pages 270–278 (1992).

87. S. W. Lee, J. McNeil, T. Zenker and T. H. Chyba. *Ti:sapphire-laser-based lidar systems.* Opt. Laser Eng. **37**, 233–244 (2002).

88. H. H. Zenzie and P. F. Moulton. *Tunable optical parametric oscillators pumped by Ti:sapphire lasers.* Opt. Lett. **19**, 963–965 (1994).

89. D. Mondelain, A. Thomasson, E. Frejafon, V. Boutou, B. Vezin and J. P. Wolf. *Frequency agile infrared lidar based on a nontracking $KNbO_3$ optical parametric oscillator.* Appl. Optics **39**, 3620–3625 (2000).

90. R. A. Yotter and D. M. Wilson. *A review of photodetectors for sensing light-emitting reporters in biological systems.* IEEE Sens. J. **3**, 288–303 (2003).

91. K. Kaufmann. Choosing your detector. Technical Report 25–27 SPIE Magazine (2005).

92. Getting the best out of photodiode detectors. Technical report Gray Cancer Institute (2005).

93. A. G. Wright. Light sensors & detection methods for TLD. Technical report Electron Tubes Limited (2005).

94. H. Bruining. *Physics and applications of secondary electron emission.* McGraw-Hill Co. Inc. (New York, 1954).

95. R. J. Allen and W. E. Evans. Photomultiplier tubes basics and applications. Technical report Hamamatsu Photonics K. K. Electron Tube Division (2006).

96. S. Flyckt and C. Marmonier. Photomultiplier tubes: Principles & applications. Technical report Photonis (2002).

97. Photomultiplier tube 5070A, data sheet. Technical report Hamamatsu Photonics (2004).

98. R. J. Allen and W. E. Evans. *Laser radar (LIDAR) for mapping aerosol structure.* Rev. Sci. Instrum. **43**, 1422–1432 (1972).

99. J. Harms, W. Lahmann and C. Weitkamp. *The art of electronics.* Appl. Optics **17**, 1131–1135 (1978).

100. T. Lindström, U. Holst, P. Weibring and H. Edner. *Analysis of lidar measurements using nonparametric kernel regression methods.* Appl. Phys. B **74**, 155–165 (2002).

101. Photodiode technical information. Technical report Hamamatsu Photonics (2005).

102. P. C.D. Hobbs. *Photodiode front ends the real story.* In *Optics & Photonics News* pages 42–45 (2001).

103. P. C. D. Hobbs. *Building electro-optical systems: Making it all work.* John Wiley & Sons, Inc (New York, 2000).

104. M. Johnson. *Photodetection and measurement: Maximizing performance in optical systems.* McGraw-Hill Professional (New York, 2003).

105. S. Bickman and D. DeMille. *Large-area, low-noise, high-speed, photodiode-based fluorescence detectors with fast overdrive recovery.* Rev. Sci. Instrum. **76**, 113101 (2005).

106. K. Hyyppa and K. Ericson. *Low-noise photodiode-amplifier circuit.* IEEE J. Solid-State Circ. **29**, 362–265 (1994).

107. Characteristics and use of SiAPD (Avalanche Photodiode). Technical report Hamamatsu Photonics (2004).

108. Avalanche photodiodes: A user's guide. Technical report PerkinElmer (2003).

109. R. H. Kingston. *Optical sources, detectors, and systems fundamentals and applications.* Academic Press Inc (San Diego, 1995).

110. G. Galbács. *A review of applications and experimental improvements related to diode laser atomic spectroscopy.* Appl. Spectrosc. Rev. **41**, 259–303 (2006).

111. K. Song and E. C. Jung. *Recent developments in modulation spectroscopy for trace gas detection using tunable diode lasers.* Appl. Spectrosc. Rev. **38**, 395–432 (2003).

112. P. Werle. *A review of recent advances in semiconductor laser based gas monitors.* Spectrochim. Acta A **54**, 197—237 (1998).

113. P. Werle, F. Slemr, K. Maurera, R. Kormann, R. Mucke and B. J. Anker. *Near- and mid-infrared laser-optical sensors for gas analysis.* Opt. Laser Eng. **37**, 101–114 (2002).

114. M.G Allen. *Diode laser absorption sensors for gas-dynamic and combustion flows.* Meas. Sci. Technol. **9**, 545–562 (1998).

115. T. M. Wilmshurst. *Signal recovery.* Taylor & Francis Group (New York, 1990).

116. P. Werle, R. Miicke and F. Slemr. *The limits of signal averaging in atmospheric trace-gas monitoring by tunable diode-laser absorption spectroscopy (TDLAS).* Appl. Phys. B **57**, 131–139 (1993).

117. T. J. Witt. *Using the Allan variance and power spectral density to characterize DC nanovoltmeters.* IEEE T. Instrum. Meas. **50**, 445–448 (2001).

118. I. Linnerud, P. Kaspersen and T. Jaeger. *Gas monitoring in the process industry using diode laser spectroscopy.* Appl. Phys. B **67**, 297–305 (1998).

119. D.D. Nelson, M.S. Zahniser, J.B. McManus, C.E.Kolb and J.L. Jimenez. *Comparison between measurements obtained with a meteorological mast and a rass sodar.* Appl. Phys. B **67**, 433–441 (1998).

120. D.D. Nelson, J.H. Shorter, J.B. Mcmanus and M.S. Zahniser. *Sub-part-per-billion detection of nitric oxide in air using a thermoelectrically cooled mid-infrared quantum cascade laser spectrometer.* Appl. Phys. B **75**, 343–350 (2002).

121. J. Röpcke, L. Mechold, M. Käning, J. Anders, F. G. Wienhold, D. Nelson and M. Zahniser. *IRMA: A tunable infrared multicomponent acquisition system for plasma diagnostics.* Rev. Sci. Instrum. **71**, 3706–3710 (2000).

122. G. Toci, P. Mazzinghi and M. Vannini. *A diode laser spectrometer for the in situ measurement polar stratospheric clouds.* Am. Meteorol. Soc. **16**, 1295–1303 (1999).

123. R. Engelbrecht. *A compact NIR fiber-optic diode laser spectrometer for CO and CO_2: analysis of observed 2f wavelength modulation spectroscopy line shapes.* Spectrochim. Acta A **60**, 3291–3298 (2004).

124. A survey of methods using balanced photodetection. Technical report New Focus (2002).

125. Nirvana auto-balanced photoreceivers. Technical report New Focus (2002).

126. P. C. D. Hobbs. *Shot noise limited optical measurements at baseband with noisy lasers.* In *Proc. SPIE* volume 1376 pages 216–221 (1990).

127. K. L. Haller and P. C. D. Hobbs. *Double beam laser absorption spectroscopy: shot noise-limited performance at baseband with a novel electronic noise canceller.* SPIE **1435**, 298–309 (1991).

128. M. G. Allen, K. L. Carleton, S. J. Davis, W. J. Kessler, C. E. Otis, D. A. Palombo and D. M. Sonnenfroh. *Ultrasensitive dual-beam absorption and gain spectroscopy: Applications for near-infrared and visible diode laser sensors.* Appl. Optics **34**, 3240–49 (1995).

129. P. C. D. Hobbs. *Ultrasensitive laser measurements without tears.* Appl. Optics **36**, 907–920 (1997).

130. C.M. Lindsay, R.M. Rade and T. Oka. *Survey of H_3^{-1} Transitions between 3000 and 4200 cm^{-1}.* Journ. Mol. Spectr. **210**, 51–59 (2001).

131. E. I. Moses and C. L. Tang. *High-sensitivity laser wavelength-modulation spectroscopy.* Opt. Lett. **1**, 115–117 (1977).

132. P. A. Martin. *Near-infrared diode laser spectroscopy in chemical process and environmental air monitoring.* Chem. Soc. Rev. **31**, 201–210 (2002).

133. P. Kluczynski and O. Axner. *Theoretical description based on Fourier analysis of wavelength-modulation spectrometry in terms of analytical and background signals.* Appl. Optics **38**, 5803–5815 (1999).

134. P. Kluczynski, Å. M. Lindberg and O. Axner. *Background signals in wavelength-modulation spectrometry with frequency-doubled diode-laser light. I. Theory.* Appl. Optics **40**, 783–793 (2001).

135. J. M. Supplee, E. A. Whittaker and W. Lenth. *Theoretical description of frequency modulation and wavelength modulation spectroscopy.* Appl. Optics **33**, 6294–6302 (1994).

136. A. N. Dharamsi, P. C. Shea and A. M. Bullock. *Reduction of effects of Fabry Pérot fringing in wavelength modulation experiments.* Appl. Phys. Lett. **72**, 3118–3120 (1998).

137. J.T.C. Liu, J.B. Jeffries and R.K. Hanson. *Wavelength modulation absorption spectroscopy with 2f detection using multiplexed diode lasers for rapid temperature measurements in gaseous flows.* Appl. Phys. B **78**, 503–511 (2004).

138. L.C. Philippe and R.K. Hanson. *Laser diode wavelength-modulation spectroscopy for simultaneous measurement of temperature, pressure, and velocity in shock-heated oxygen flows.* Appl. Optics **32**, 6090–6103 (1993).

139. J. Reid and D. Labrie. *Second-harmonic detection with tunable diode lasers - comparison of experiment and theory.* Appl. Phys. B **26**, 203–210 (1981).

140. R. Arndt. *Analytical line shapes for Lorentzian signals broadened by modulation.* J. Appl. Phys. **36**, 2522–2524 (1965).

141. Coherent sampling vs. window sampling. Technical report Maxim (2002).

142. T. Fernholz, H. Teichert and V. Ebert. *Digital, phase-sensitive detection for in situ diode-laser spectroscopy under rapidly changing transmission conditions.* Appl. Phys. B **75**, 229–236 (2002).

143. T. H. Pham, O. Coquoz, J. B. Fishkin, E. Anderson and B. J. Tromberg. *Broad bandwidth frequency domain instrument for quantitative tissue optical spectroscopy.* Rev. Sci. Instrum. **71**, 2500–2513 (2000).

144. C. Abrahamsson, T. Svensson, S. Svanberg and S. Andersson-Engels. *Time and wavelength resolved spectroscopy of turbid media using light continuum generated in a crystal fiber.* Opt. Express **17**, 4103–4102 (2004).

145. C. Abrahamsson, J. Johansson, S. Andersson-Engels, S. Svanberg and S. Folestad. *Time-resolved nir spectroscopy for quantitative analysis of intact pharmaceutical tablets.* Anal. Chem. **77**, 1055–1059 (2005).

146. J.D. Klett. *Stable analytical inversion solution for processing lidar returns.* Appl. Optics **20**, 211–220 (1981).

147. J.D. Klett. *Lidar inversion with variable backscatter/extinction ratios.* Appl. Optics **24**, 1638–1643 (1985).

148. D.J. Brassington. *Sulfur dioxide absorption cross-section measurements from 290 nm to 317 nm.* Appl. Optics **20**, 3774–3779 (1981).

149. N. Takeuchi, H. Shimizu and M. Okuda. *Detectivity estimation of the DAS lidar for NO2.* Appl. Optics **17**, 2734–2738 (1978).

150. W.B. Grant. *Lidar for atmospheric and hydrospheric studies: A survey.* Marcel Dekker Publishing Co. (New York, 1995).

151. L.T. Molina and L.J. Molina. *Absolute absorption cross section of ozone in the 185- to 350 nm range.* J. Geophys. Res. **91 D**, 14501 (1986).

152. H. Edner, A. Sunesson and S. Svanberg. *NO plume mapping by laser-radar techniques.* Opt. Lett. **13**, 704–706 (1988).

153. H. J. Kölsch, P. Rairoux, J. P. Wolf and L. Wöste. *Simultaneous NO and NO_2 DIAL measurement using BBO crystals.* Appl. Optics **28**, 2052–2056 (1989).

154. H. Edner, W. G. Faris, A. Sunesson and S. Svanberg. *Atmospheric atomic mercury monitoring using differential absorption lidar techniques.* Appl. Optics **28**, 921–930 (1989).

155. M. J. T. Milton, P. T. Woods, B. W. Jolliffe, N. R. W. Swann and T. J. McIlveen. *Measurements of toluene and other aromatic hydrocarbons by differential-absorption lidar in the near-ultraviolet.* Appl. Phys. B **55**, 41–45 (1992).

156. R. Grönlund, M. Sjöholm, P. Weibring, H. Edner and S. Svanberg. *Elemental mercury emissions from chlor-alkali plants measured by lidar techniques.* Atm. Env. **39**, 7474–7480 (2005).

157. A. Chambers and P. Eng. Well test flare plume monitoring phase II: DIAL testing in Alberta. Technical report Alberta Research Council Inc. (2003).

158. A. Chambers, P. Eng and M. Strosher. Refinery demonstration of optical technologies for measurement of fugitive emissions and for leak detection. Technical report Alberta Research Council Inc. (2006).

159. R. A. Robinson, A. S. Andrews, T. D. Gardiner, I. J. Uprichard and P. T. Woods. Differential absorption lidar measurements of voc emissions from Wytch Farm crude oil gathering station. Technical report NPL (1998).

160. I. Antoniou, H. E. Jorgensen, F. Ormel, S. Bradley, S. von Hnerbein, S. Emeis and G. Warmbier. On the theory of sodar measurement techniques. Technical report Risø National Laboratory, Roskilde, Denmark (2003).

161. Acoustic wind profilers product information. Technical report Scintec AG (2007).

162. Z. Zelinger, M. Střižík, P. Kubát, Z. Jaňour, P. Berger, A. Cerný and P. Engst. *Laser remote sensing and photoacoustic spectrometry applied in air pollution investigation.* Opt. Laser Eng. **42**, 403–412 (2004).

163. R. L. Coulter and M. A. Kallistratova. *Two decades of progress in SODAR techniques: a review of 11 ISARS proceedings.* Meteorol. Atmos. Phys. **85**, 3–19 (2004).

164. M. A. Kallistratova and R. L. Coulter. *Application of SODARs in the study and monitoring of the environment.* Meteorol. Atmos. Phys. **85**, 21–37 (2004).

165. M. L. Chappelle, F. J. Wood, Jr. J. E. McMurtrey and W. W. Newcomb. *Laser-induced fluorescence of green plants. 1: A technique for remote detection of plant stress and species differentiation.* Appl. Optics **23**, 134–138 (1984).

166. H. Edner, J. Johansson, S. Svanberg, E. Wallinder, M. Bazzani, B. Breschi, G. Cecchi, L. Pantani, B. Radicati, V. Raimondi, D. Tirelli, G. Valmori and P. Mazzinghi. *Laser-induced fluorescence monitoring of vegetation in Tuscany.* EARSeL Adv. Rem. Sens. **1**, 119–130 (1992).

167. F. Mellegård. Development and construction of an automatic calibration unit for a differential absorption lidar system. Technical report Lund Reports on Atomic Physics LRAP-264, Lund, Sweden (2001).

168. P. Weibring, D. Richter, A. Fried, J.G. Walega and C. Dyroff. *Ultra-high-precision mid-IR spectrometer II: System description and spectroscopic performance.* Appl. Phys. B **85**, 207–218 (2006).

169. The fundamentals of FFT-based signal analysis and measurement in LabVIEW and Labwindows/CVI. Technical Report 1–26 National Instruments (2006).

170. Personal communication, Femto messtechnik GmbH (2007).

171. P.W. Werle, P. Mazzinghi, F. D' Amato, M. De Rosa, K. Maurer and F. Slemr. *Signal processing and calibration procedures for in situ diode-laser absorption spectroscopy.* Spectrochim. Acta A **60**, 1685–1705 (2003).

172. L. Persson, K. Svanberg and S. Svanberg. *On the potential of human sinus cavity diagnostics using diode laser gas spectroscopy.* Appl. Phys. B **82**, 313–317 (2005).

173. T. Svensson, M. Andersson, L. Rippe, S. Svanberg, S. Andersson-Engels, J. Johansson and S. Folestad. *VCSEL-based oxygen spectroscopy for structural analysis of pharmaceutical solids.* Manuscript in preparation (2007).

174. B. van Well, S. Murray, J. Hodgkinson, R. Pride, R. Strzoda, G. Gibson and M. Padgett. *An open-path, hand-held laser system for the detection of methane gas.* J. Opt. A **7**, S420–S424 (2005).

175. T. Iseki. Laser methane a portable remote methane detector. Technical report R&D Division, Technology Development Dept., Sensing & Controls Center Tokyo Gas Co., Ltd. (2004).

Papers

Paper I

Remote monitoring of vegetation by spectral measurements and multi-colour fluorescence imaging

M. Andersson, H. Edner, P. Ragnarsson, J. Johansson, S. Svanberg, and E. Wallinder.

Proc. Physical Measurements and Signatures in Remote Sensing, 835–842, Val d'Isère, France (1994).

REMOTE MONITORING OF VEGETATION BY SPECTRAL MEASUREMENTS AND MULTI-COLOUR FLUORESCENCE IMAGING

M. Andersson, H. Edner, J. Johansson, P. Ragnarson, S. Svanberg and E. Wallinder
Department of Physics, Lund Institute of Technology
P.O. Box 118, S-221 00 Lund, Sweden

ABSTRACT:

A brief review of remote monitoring of laser-induced fluorescence from vegetation is given together with examples of results from measurements during field campaigns within the European LASFLEUR project. A mobile fluorescence lidar system was used in the Swedish activities. Measurements were performed in a spectrally resolving mode yielding a full fluorescence spectrum in one selected point, and in an imaging mode, where spatially resolved data are captured in four selected spectral bands simultaneously. As a transmitter a Nd:YAG laser system operating at 20 Hz was used, either frequency tripled with an output at 355 nm, or, preferentially, Raman shifted to obtain an output wavelength at 397 nm. A 40 cm diameter telescope was used to collect fluorescence photons, that were analysed either in an optical multichannel analyser system or in a four-colour imaging system, both equipped with intensified CCD detectors. This system has been used in field campaigns during the last few years in Italy, Germany and France, monitoring several species, such as beech, spruce and maize. Detailed studies on spruce and maize have been made to identify the optimum excitation wavelength. From the results obtained, and also taking into consideration eye-safety regulations, 397 nm was chosen as the optimum wavelength. The daily cycle of these species was studied for samples under parallel plant physiological control. Maize grown under different conditions with regard to nutrition and water supply was also investigated. Fluorescence imaging was performed with a maximum distance of 100 m. Detailed studies were made on maize plants at a distance of 40 m. Four fluorescence images were recorded at selected wavelengths, including the two chlorophyll peaks at 685 and 735 nm. The simultaneous recording of fluorescence images makes the system less vulnerable to wind movements of the vegetation. Sequential single-colour fluorescence imaging, yielding sharper images was also evaluated.

KEY WORDS: multi-colour imaging, laser-induced fluorescence, vegetation, remote sensing, spectral analysis

1. INTRODUCTION

Several areas in Europe exhibit damage to the vegetation due to environmental pollution of air, soil and water. It is of considerable interest to be able to perform early detection and mapping of the damaged vegetation. One possibility to map large areas in a short time is the use of reflectance spectroscopy performed with satellite-borne multi-spectral imagery [1]. Active remote sensing using a transmitter can provide additional information [2]. On excitation with laser light in the UV or blue region, vegetation exhibits characteristic fluorescence from chlorophyll. The chlorophyll gives rise to two red fluorescence peaks, one at 685 nm and one at 735 nm. The relative intensity of these peaks is a measure of the physiological status of the plant [3]. In addition, a broadband fluorescence in the 450-600 nm region is also obtained [4]. The molecules giving rise to this fluorescence are not yet fully identified, but several fluorophores, carotenoids [5], riboflavin [5], cinnamic acids [6], coumarine [6] and NADPH [7,8] have been suggested. Also, contributions from the surface wax layer can be seen in the blue region. The possibility to use this blue fluorescence to decide on the plant status is investigated by several groups [9]. Swedish remote fluorescence work started in 1978. Early experience is described in [10].

Three years ago the European LASFLEUR project was started. The aim of the collaborative project is to develop an airborne fluorosensor that can detect early damage on vegetation. Within the LASFLEUR project several field campaigns have been performed. The participation from the Swedish side has been in Pian di Novello (I) [11], Oberpfaffenhofen (D) [12], Karlsruhe (D) [13] and Avignon (F). Our experience from this work is presented below, with special focus on the Avignon campaign, September 1993.

2. INSTRUMENTATION

Remote fluorescence measurements using the Swedish fluorescence lidar system were performed in two different modes [14]. In the spectrally resolved mode a full fluorescence spectrum is obtained in a selected remote point, while in the imaging mode spatially resolved data can be recorded in four selected wavelength bands simultaneously. The two systems are adopted to the 40 cm diameter optical receiving telescope of our mobile lidar system, a system primarily intended for air pollution analysis [15]. Fig. 1 shows a scenario for remote fluorescence monitoring.

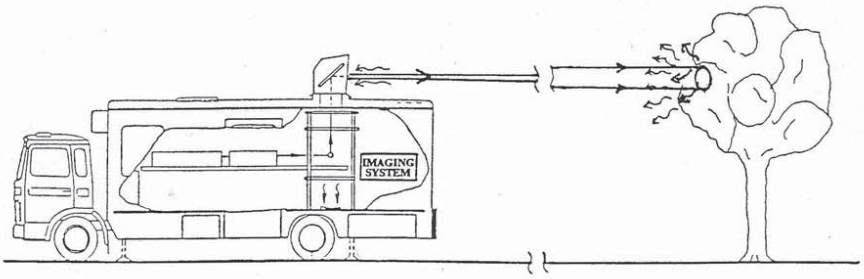

Fig. 1. *Remote fluorescence imaging of vegetation.*

The general lay-out of the fluorescence lidar system is shown in Fig. 2.

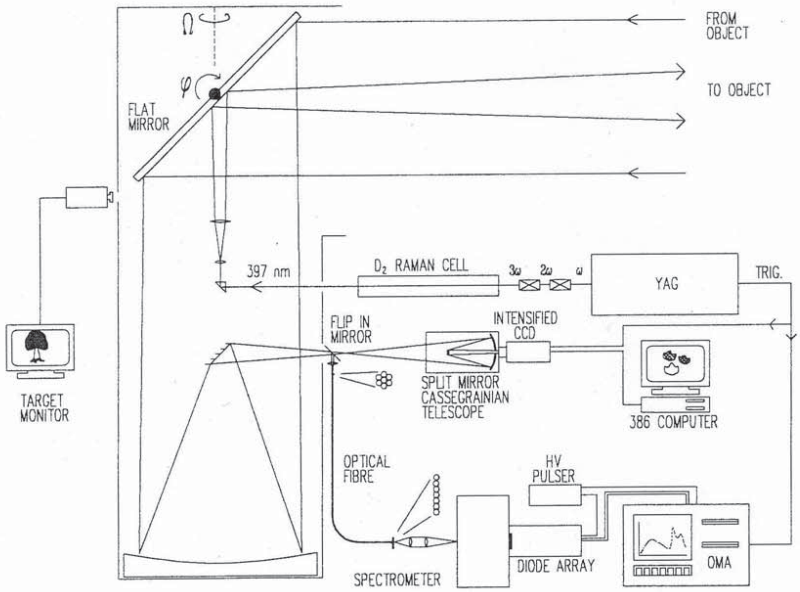

Fig. 2. *Set-up for remote recordings of fluorescence spectra and multi-colour fluorescence images of vegetation. As an excitation source a Raman cell pumped by a frequency tripled YAG laser was used. The output pulse energy was about 30 mJ. By using a flip-in mirror switching between the OMA system and the multi-colour imaging system was possible. An optical fibre bundle consisting of 7 fibres was used to couple the light into the spectrometer of the OMA system.*

The laser transmitter of the lidar system is a Nd:YAG laser with frequency doubling or tripling. In order to induce chlorophyll fluorescence while still staying eyesafe, the output from the frequency-tripled laser was Raman-shifted in a high-pressure deuterium cell to achieve 397 nm. The radiation was transmitted in a divergent beam towards the target area. The backscattered fluorescence light was collected by the lidar telescope and directed into a second Cassegrainian telescope. The image plane of the lidar telescope coincided with the object plane of the Cassegrainian telescope. In the image plane of the Cassegrainian telescope an intensified CCD camera was placed. The telescope has its first mirror cut into four segments that can be individually adjusted. By tilting the four mirror segments, each segment produces an image at the image intensifier, arranged as four quadrants of the detector. Before each mirror section an interference filter or coloured-glass filter was placed. The peak transmission of the filters were chosen as to match the interesting features of the fluorescence spectra.

When the system was used in the spectrally resolving point monitoring mode, a flip-in mirror was placed in the focal plane of the lidar telescope. The detected light was directed towards a white screen in which a hole had been pinched. The target area could be seen on the screen. An optical fibre was mounted in the centre of the hole, which transmitted light from the point that was to be analyzed. The fluorescence light was guided through the optical fibre to a small spectrometer. The detector was an image-intensified 1024 channel diode array. The signal was displayed on the screen of the OMA mainframe.

In both types of measurements the detection was gated in order to suppress ambient daylight. In order to increase the signal-to-noise ratio, averaging was used. In the measurements performed in Avignon, a new detector was employed for the spectrally resolved mode, a Spectroscopy Instruments Model ICCD-576. The sensitivity of this device was several times larger than that for the one used before. This meant that less shots were necessary to get an adequate signal-to-noise ratio.

3. RESULT AND DISCUSSION

The choice of wavelength to use for exciting vegetation fluorescence must be done with great care. Fig. 3 shows spectra taken in the lab for different excitation wavelength on the same leaf of maize.

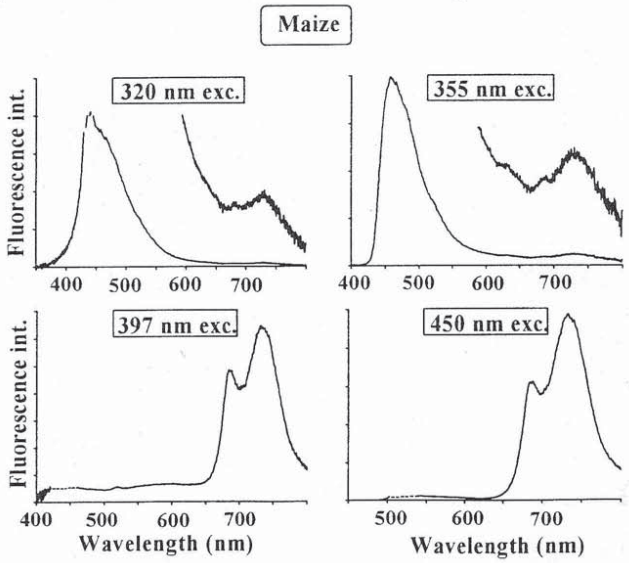

Fig. 3. *Fluorescence spectra from the upper side of a maize leaf recorded inside the van using different excitation wavelengths. Magnification of parts of the spectra are included in the figure.*

The wavelengths chosen in this example were the first Anti-Stokes component, the fundamental, and the first and second Stokes component generated from a deuterium-filled Raman cell, pumped by 355 nm radiation. The wavelengths were selected one at a time and transmitted through an optical fibre to the

sample. As can be seen in Fig. 3, the light cannot excite the chlorophyll molecules very well for the lower wavelengths. This is partly due the UV-protecting outer layer of the leaf, consisting of wax and UV-screening pigments, and partly due to the smaller absorption cross section of the chlorophyll molecules at these wavelengths. The strong blue fluorescence has its origin in the the outer layer of the leaf. When 450 nm is used, the excitation wavelength coincides with the maximum absorption peak of chlorophyll, which is the reason for the very high chlorophyll fluorescence exhibited. This wavelength is, however, a bit too long to efficiently excite the blue fluorescing compounds that might be used to decide on the plants status. Furthermore, eye safety regulations do not allow high-power optical radiation in the visible region. All this considered, our choice of exciting wavelength was 397 nm, which can provide chlorophyll fluorescence as well as blue fluorescence, while making it relatively easy to comply with eye safety regulations.

Figure 4 shows examples of characteristic fluorescence spectra for four different plants. They were recorded remotely with the spectrally resolving point monitor during the field test in Avignon. The plants are maize, cypress, sorghum and poplar.

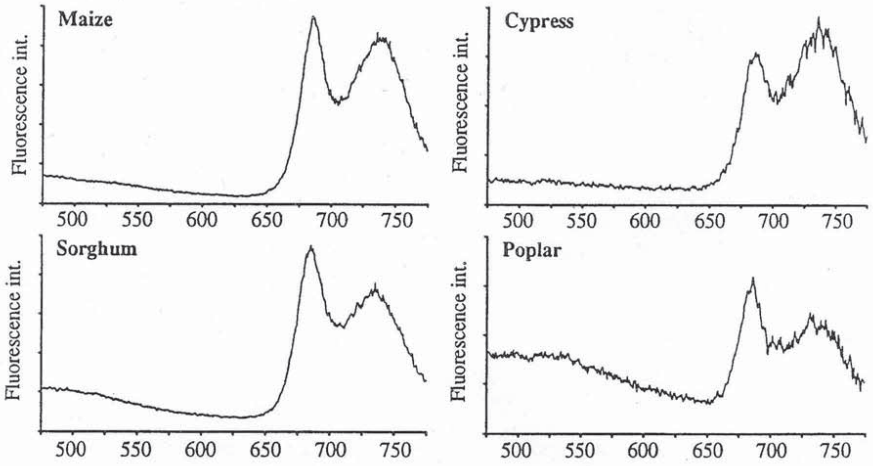

Fig. 4. Characteristic fluorescence spectra for maize, cypress, sorghum and poplar.

An example of the signal-to-noise ratio can be studied in Fig. 5. Measurements were performed with the spectrally resolved system equipped with the new sensitive detector.

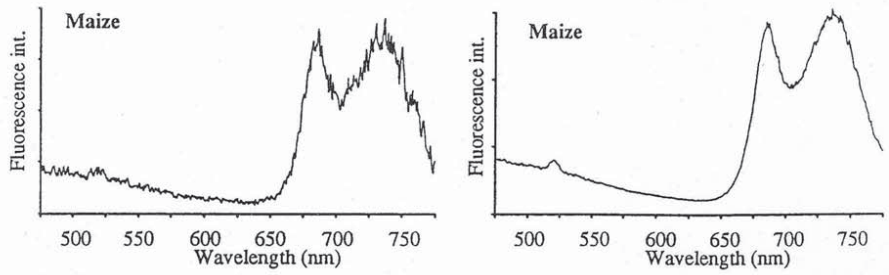

Fig. 5. Fluorescence spectra of a maize plant at a distance of 40 m. The spectrum to the right was integrated over 100 laser shots while the spectrum to the left was recorded with a single laser shot only. The laser pulse energy was about 30 mJ.

This detector does not only have a larger detection area than the previous detector, which permits a larger part of the collected light to be utilized, it can also be cooled to lower temperatures, which reduces the noise considerably. The spectrum to the right was integrated for 100 shots at a distance of 40 m. The laser pulse energy was about 30 mJ. In the spectrum to the left a single laser shot was used for the recording. It is obvious that even with single-shot detection, the signal-to-noise ratio is very good.

Some examples of remote sensing are shown in Fig. 6. Spectra for poplar, cypress and plane-tree were recorded at distances of 64 m, 125 m and 210 m, respectively. In Fig. 6a-c 100 shots are integrated. A single-shot recording for cypress is also shown in Fig. 6d.

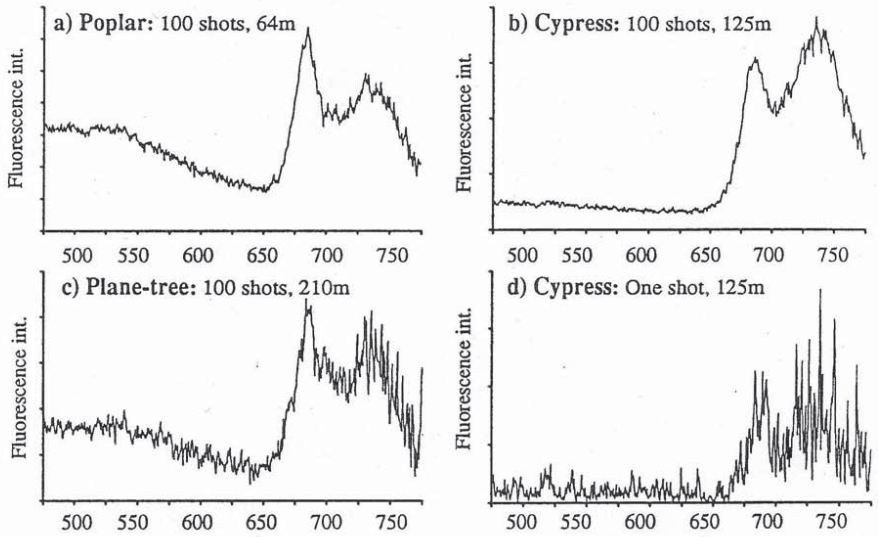

Fig. 6. *Remote fluorescence spectra for poplar, cypress and plane-tree. 100 shots are averaged in a-c, for distances 64 m, 125 m and 210 m, respectively. A single-shot recording at 125 m distance is shown in d.*

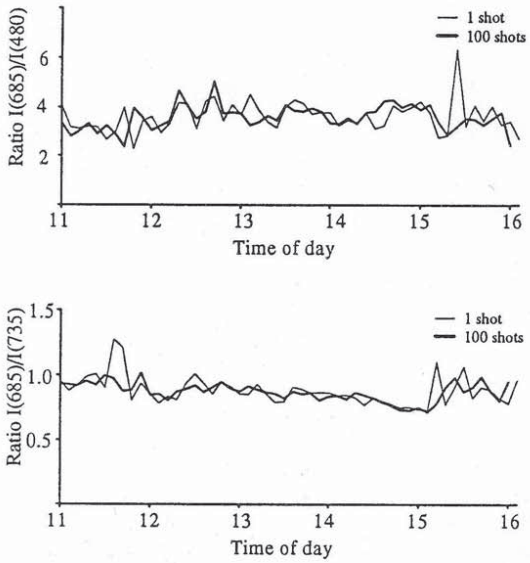

Fig. 7. A daily cycle recorded on maize. The upper diagram shows the ratio I(685)/I(480) and the lower I(685)/I(735). In each point a single-shot and an integrated measurement over 100 shots are shown.

In Fig. 7 a daily cycle recorded on maize is shown. The upper panel shows the ratio I(685)/I(/735) and the lower I(685)/I(480). It can be seen that the signal-to-noise ratio is just slightly less in the single-shot case than in the case of 100 shots integrated.

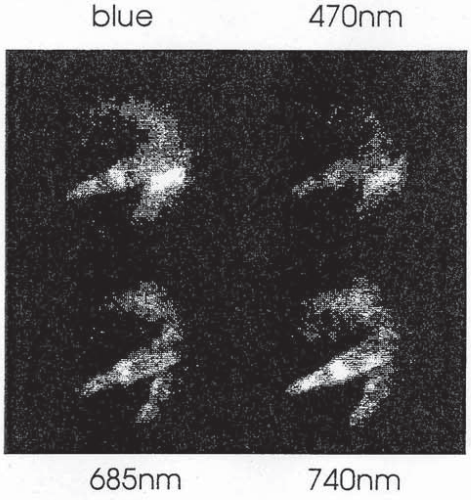

Fig. 8. Example of multi-colour fluorescence imaging for a maize plant. The optical filters used in front of each telescope segment were BG7 (blue), and interference filters centred at 470, 685 and 740 nm, respectively. Below the four sub-images, a processed image is shown, displaying the ratio of I(685nm)/I(blue). The excitation wavelength was 397 nm and the distance was about 40 m. The target diameter was about 40 cm.

Fig. 8 is an example of a measurement performed with the imaging system on a maize plant. The upper part of the picture is the raw image achieved with the system. The filters used were a blue cut-off coloured-glass filter transmitting the broadband feature of the blue fluorescence, and three interference filters with peak transmission at 470, 685 and 740 nm, transmitting a narrow blue band and the two chlorophyll peaks, respectively. In the lower part of the picture the signal from 685 nm is divided with the blue broadband fluorescence signal. In this figure the laser hot spots are lost in the division, and the true ratio is displayed. This measurement was performed just before the field was sprayed with the herbicide DCMU. DCMU binds at the Q_B-site in Photosystem II, hindering the electron transport from Photosystem II to Photosystem I. This results in a higher chlorophyll fluoroscence in the DCMU treated plants. This can be seen in Fig. 9. The upper part is exactly the same picture as the divided picture in Fig. 8, but the scale is slightly different. The lower part of Fig. 9 is the same plant after treatment with DCMU shown on the same intensity scale. It can be seen that the chlorophyll-to-blue fluorescence ratio increased, probably due to the expected increase in chlorophyll fluorescence.

4. CONCLUSIONS

Some examples of fluorescence measurements performed on different sites in Europe have been presented. The measurements performed with the new detector of the spectrally resolving system show that the

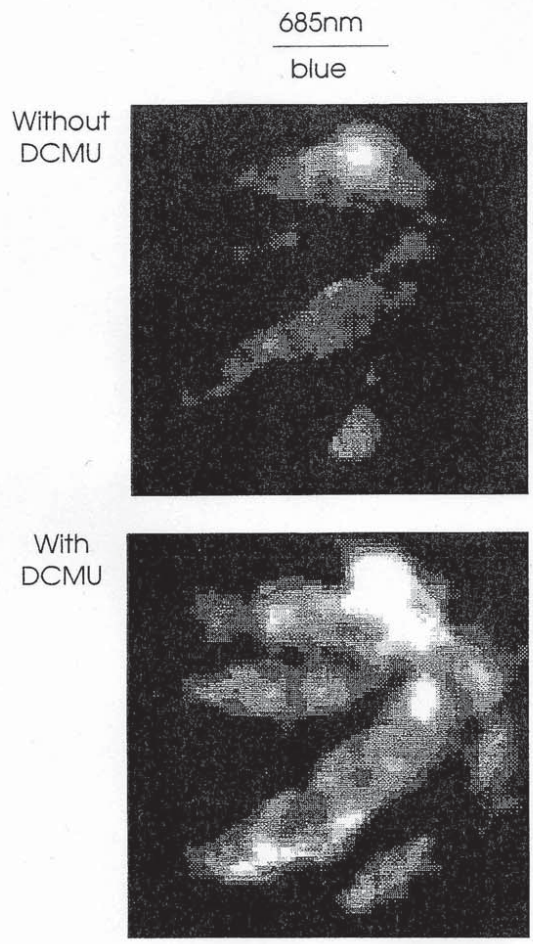

Fig. 9. *Processed multi-colour fluorescence images of a maize plant displaying the fluorescence ratio I(685nm)/I(blue). The upper image is the same as the processed image in Fig. 8 and the lower image is recorded half an hour later after application of the herbicide DCMU.*

remotely measured spectra have a very good signal-to-noise ratio even for single-shot recordings. The measurements performed with the imaging system show that particularly the divided image, where influences of distance and non-uniform laser intensity are eliminated, can be used to see differences in the vegetation which occur due to different environmental parameters.

5. ACKNOWLEDGEMENTS

This work was supported by the Swedish Natural Science Research Council and the Swedish Space Board.

6. REFERENCES

1. Rock B.N., J. E. Vogelmann, D. L. Williams, A. F. Vogelmann and T. Hoshizaki, 1986, "Remote detection of forest damage," BioScience 36, 439-445.
2. Pantani L., R. Reuter, eds., 1992, Lidar in remote sensing of land and sea, EARSeL Advances in Remote Sensing, Vol. 1.
3. Lichtenthaler H.K., U. Rinderle,1988, "The role of chlorophyll fluorescence in the detection of stress conditions in plants," CRC Critical Reviews in Analytical Chemistry 19, S29-S85.
4. Celander L., K. Fredriksson, B. Galle and S. Svanberg, 1978, "Investigation of laser-induced fluorescence with applications to remote sensing of environmental parameters," Göteborg Institue of Physics Reports, GIPR-149, Chalmers University of Technology, Göteborg .
5. Chappelle E.W., J.E. McMurtrey and M.S. Kim, 1990, "Laser induced blue fluorescence in vegetation," in Proc. Internat. Geoscience Remote Sensing Symphosium IGARSS '90 ,3, 1919-1922, University of Maryland,Washington DC
6. Lang M., H.K. Lichtenthaler, 1991, "Changes in the blue-green fluorescence-emission spectra of beech leaves during the autumnal chlorophyll breakdown, " J. Plant. Physiol. 138, 550-553.
7. Duysens L.N.M., G. Sweep, 1957,"Fluorescence spectrophotometry of pyridine nucleotide in photosynthesizing cells, " Biochim. Biophys. Acta 25, 13-16.
8. Goulas Y., I. Moya and G. Schmuck, 1990, "Time-resolved spectroscopy of the blue fluorescence of spinach leaves," Photosynth. Res. 25, 299-307.
9. Lichtenthaler H.K., F. Stober and M. Lang, 1992, "The nature of the different laser-induced fluorescence signatures of plants," EARSeL Advences in Remote Sensing 1, 20-32.
10. Svanberg S., 1989, "Laser fluorescence spectroscopy in environmental science, in Optoelectronics for Environmental Science, S. Martellucci and A.N. Chester, eds., 15-27, Plenum Press, N.Y.
11. Edner H., J. Johansson, S. Svanberg, E. Wallinder, M. Bazzani, B. Breschi, G. Cecchi, L. Pantani, B. Radicati, V. Raimondi, D. Tirelli, G. Valmori, P. Mazzinghi, 1992, " Laser-induced fluorescence monitoring of vegetation in Tuscany," EARSeL Advances in Remote Sensing 1, 119-130.
12. Edner H., J. Johansson, P. Ragnarson, S. Svanberg, E. Wallinder, 1993, "Remote monitoring of vegetation using a fluorescence lidar system in spectrally resolving and multi-spectral imaging modes," EARSeL Advances in Remote Sensing, *to appear*.
13. Edner H., J. Johansson, S. Svanberg, H.K. Lichtenthaler, F. Stober, C. Schindler and L.O. Björn, "Remote multi-colour fluorescence imaging of selected broad-leaf plants", EARSeL Advances in Remote Sensing, *to appear*.
14. Edner H., J. Johansson, S. Svanberg and E. Wallinder, 1993, "Fluorescence lidar multi-color imaging of vegetation, Appl. Opt. *in press*
15. Edner H., K. Fredriksson, A. Sunesson, S. Svanberg, L. Unéus, W. Wendt, 1987, "Mobile lidar system for environmental monitoring," Appl. Opt.26, 4330.

Paper II

Remote fluorescence measurements of vegetation spectrally resolved and by multi-colour fluorescence imaging

J. Johansson, M. Andersson, H. Edner, J. Mattsson, and S. Svanberg.
J. Plant Physiol. **148**, 632–637 (1996).

J. Plant Physiol. Vol. 148. pp. 632–637 (1996)

Remote Fluorescence Measurements of Vegetation Spectrally Resolved and by Multi-Colour Fluorescence Imaging

JONAS JOHANSSON, MATS ANDERSSON, HANS EDNER, JOHAN MATTSSON, and SUNE SVANBERG*

Department of Physics, Lund Institute of Technology, P.O. Box 118, S-221 00 Lund, Sweden
* Corresponding author

Received July 7, 1995 · Accepted October 2, 1995

Summary

A remote sensing system for combined fluorescence spectral recordings and multi-colour fluorescence imaging of vegetation will be presented. The system configuration will be explained and data from several field campaigns will be shown. The excitation light pulses for remote fluorescence detection are produced by a frequency tripled Nd:YAG laser emitting at 355 nm and shifted to 397 nm in a deuterium containing Raman cell. The receiving optics includes a Newtonian telescope and is shared by an optical fibre bundle connected to an OMA system and by a secondary Cassegrainian split-mirror telescope for fluorescence imaging at four wavelength bands simultaneously. The multi colour fluorescence images are computer processed to form images of a ratio at two wavelengths or if necessary a more complex mathematical function including the four wavelength bands is used. Examples of remote multi-colour imaging of vegetation from the past field campaigns will be given. Remote fluorescence spectra from several plant species were recorded at an excitation wavelength of 397 nm. Furthermore, the system was found capable of producing high-quality single-shot spectra at a range of 125 m. Lastly, a recently developed push-broom scanning technique for fluorescence imaging will be discussed and some preliminary data will be shown.

Key words: Laser-induced fluorescence, multi-colour fluorescence, vegetation, remote sensing, spectral analysis.

Abbreviations: LIDAR = light detection and ranging; CCD = charge coupled device; OMA = optical multi-channel analyser.

Introduction

The development of new techniques for remote monitoring of vegetation has recently become more important. The forests in Europe and elsewhere are endangered by environmental pollutants and it has become obvious that methods of early detection are needed. Satellite or air-borne multispectral imagery is useful for vegetation identification and also, to some extent, for monitoring of damage to vegetation (Rock et al., 1986). These techniques seem, however, to have limited usefulness. Laser-induced fluorescence has been shown to have a potential for remote sensing of plant health (See e.g. Svanberg, 1995). The red fluorescence from vegetation depends on both chlorophyll concentration and photosynthetic functioning and has been reported to change for plants exposed to different types of stresses such as water stress and nutrition deficiency (Chappelle et al., 1984; Krause and Weis, 1984; Lichtenthaler and Rinderle, 1988). Furthermore, laser-induced fluorescence is well suited for air-borne monitoring.

The first air-borne measurements utilising fluorescence were applied to the monitoring of marine constituents and oil spills at sea (Kim, 1973; Hoge and Swift, 1981). systems have also been tested for terrestrial monitoring of vegetation

and have shown good potential also for this application (Hoge et al., 1983; Zimmermann and Günther, 1986; Cecchi et al., 1994). With the implementation of optical multichannel analysers (OMA) into remote fluorosensor systems, full fluorescence spectra have been monitored (Rosema et al., 1988; Edner et al., 1992 a). Since fluorescence spectra from green plants are very complex and depend on multiple factors, a broad spectral coverage would be desirable to be able to detect subtle damages to vegetation. So far, most measurements have been performed in a point monitoring mode. However, full imaging would be advantageous in terms of understanding and interpreting the results and would also yield better statistics than pointwise sampling. The first results on remote fluorescence imaging on vegetation were reported in 1992 (Edner et al., 1992 a). Here a multi-colour system facilitated simultaneous imaging at four wavelengths utilising a split mirror telescope (Edner et al., 1994, Edner et al., 1995). This system is very well suited for short range imaging, while air-borne application is limited by a low sensitivity. Hence, a different technique for remote fluorescence imaging was recently implemented into the system. This is a push-broom line scanning technique with simultaneous recordings at two wavelength bands. The laser beam is shaped to a linear streak of a length of about 2 m at 50 m distance and the fluorescence is imaged through the receiving Newtonian telescope and a secondary telescope consisting of two Fresnel lenses onto an image-intensified CCD detector. An important advantage of the push-broom system is that the images are constructed from single-shot data. In this paper we report on remote fluorescence imaging of vegetation and spectral point monitoring from areas within the images. Comparisons of the two imaging systems and their respective applications will be discussed here.

Material and Methods

One spectrally resolving point monitoring OMA system and two different multi-colour imaging systems, are described here. The first imaging system provides 2D imaging of a remote target, while the other is a one-dimensional line scanning (push-broom) system. The OMA system is utilised for pointwise spectral recordings at specific features within the target area, such as single leaves. The light source of the lidar system is a Nd:YAG laser with frequency doubling/tripling. In order to induce chlorophyll fluorescence efficiently while still staying eyesafe, the output from the frequency-tripled Nd:YAG laser (355 nm, 200 mJ pulse energy) was Raman-shifted in a high-pressure deuterium cell to generate radiation at 397 nm. An output pulse energy of 30 mJ was achieved at 20 Hz. The outgoing beam is directed coaxially with a vertically mounted 0.40 m diameter telescope and is transmitted towards the target via a large flat mirror in a retractable transmitting/receiving dome on the roof. Computer controlled stepper motors are used to turn the dome and to tilt the mirror. The fluorescence light was collected by the lidar telescope and directed to a fibre coupled OMA system (Spectroscopy Instruments model ICCD-576) or to a secondary telescope. The OMA based system has been described by Edner et al. (1994). In the case of 2-D imaging, the secondary telescope was a Cassegrainian telescope with its first mirror cut into four segments which can be individually adjusted. By tilting the mirror segments, each segment produces an image at the image intensifier; in total four identical images arranged as four quadrants on an image-intensified CCD detector (Spectroscopy Instruments model ICCD-576). The gate width of the image intensifier was set at 20 ns. Furthermore, different

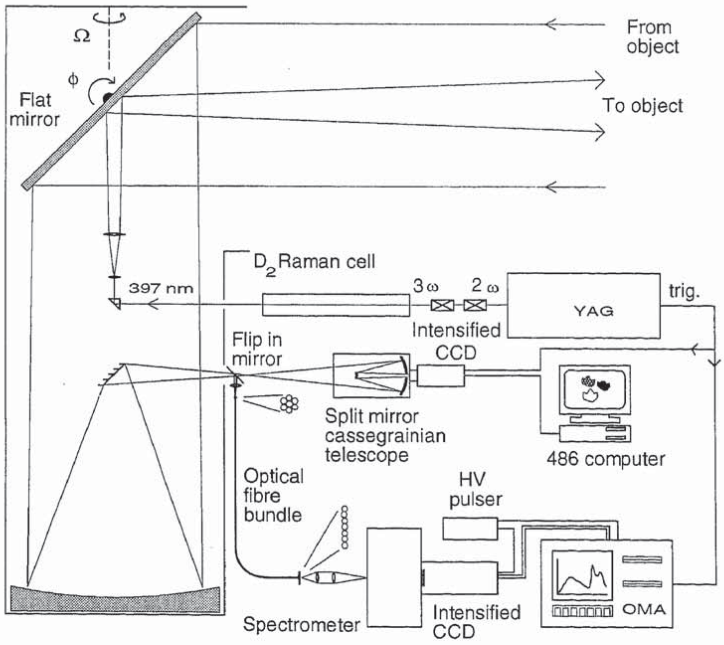

Fig. 1: Set-up of a fluorescence lidar system for point monitoring and multi-colour imaging.

interference filters or Schott coloured-glass filters were placed in front of each mirror segment matching specific features of the fluorescence spectra. Such features may include the broad-band blue-green fluorescence structures sampled e.g. at 450 nm and 520 nm and the chlorophyll fluorescence peaks at 685 nm and 740 nm. The fluorescence images are read out to a PC 486 computer. Computer processing makes it possible to generate a new image, pixel by pixel, from the four sub-images using a suitably designed spectral contrast function, which enhances features of interest. One example of such a spectral contrast function is the ratio I(685nm)/I(740nm), which yields an image that is related to the chlorophyll concentration of the target. The resulting image is shown on the screen in false colour. The system set-up is shown in Fig. 1 and was described by Edner et al. (1994).

In the case of the push-broom line scanning system, the laser beam was re-shaped to a linear streak. The length of the streak was about 2 m at 50 m distance (corresponding to 10 m at 250 m distance) and the width of the streak was about 2 cm. At the output of the Newtonian telescope, a secondary telescope was formed by two Fresnel lenses and an Al-coated plane mirror cut in two halves. Using different optical filters for each mirror segment, the image was split into two, identical images at different wavelengths. The pixels of the CCD were vertically binned into two groups forming two horizontal line scans of the fluorescence induced by the laser streak. These fluorescence intensity profiles were thus recorded simultaneously at the two selected wavelengths. Images of a size of about 2×2 m were scanned for several plant species including *Picea abies* at a distance of about 60 m. The excitation source and the receiving Newtonian telescope as well as the CCD and the electronics were the same as in Fig. 1. A close-up of the receiving optics for the push-broom system is shown in Fig. 2.

Results and Discussion

Multi-colour fluorescence images and fluorescence spectra were remotely recorded for test targets as well as for a number of different plant species. For images on a leaf level, the 2D imaging system was utilised, while the push-broom system was used for imaging on a canopy level.

A set of multi-colour fluorescence images from a maize plant at 40 m distance recorded with the 2D imaging system, is shown in Fig. 3. Fluorescence images were simultaneously recorded at four wavelength bands using a Schott BG7 (blue-green region) filter and interference filters at 470, 685 and 740 nm, respectively. The fluorescence was integrated over 100 laser shots. In the lower part of the figure, a computer processed ratio image displaying the 685 nm/"blue" ratio of the maize plant is shown. From the ratio image, a high value of the ratio is found for the smaller leaf to the right. This can also be understood by comparing the first and the third multi-colour sub-images (blue and 685 nm). In Fig. 4, remote fluorescence spectra from a part of the maize plant is shown. The first spectrum (left) is integrated over 100 laser shots, while the second (right) is a single-shot spectrum. It is interesting to note that high quality single-shot fluorescence spectra can be recorded at a distance of 40 m. Single-shot spectra at varying distance of up to 125 m were also successfully obtained. This suggests that it would be possible also to obtain remote single shot spectra from an air-borne platform,

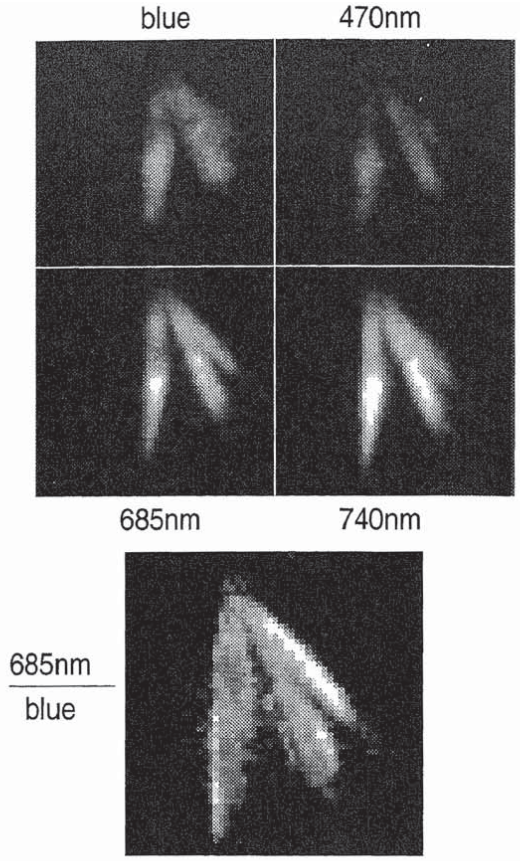

Fig. 3: Multi-colour fluorescence images (upper) and a ratio image (lower) of a maize plant. The filters used were a Schott BG7 (blue) filter and interference filters at 470, 685 and 740 nm, respectively. The ratio image was produced by division of the 685 nm and the blue image. The target distance was 40 m.

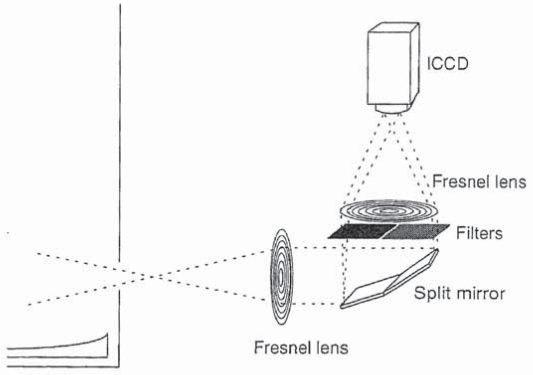

Fig. 2: Close-up of the telescope for the push-broom line scanning system for multi-colour imaging.

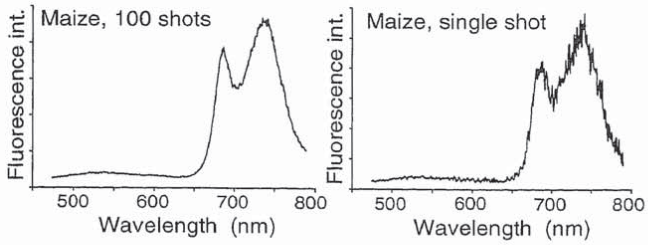

Fig. 4: Remotely recorded fluorescence spectra of a maize plant at 40 m distance. The fluorescence was integrated over 100 laser shots (left) and 1 shot (right), respectively.

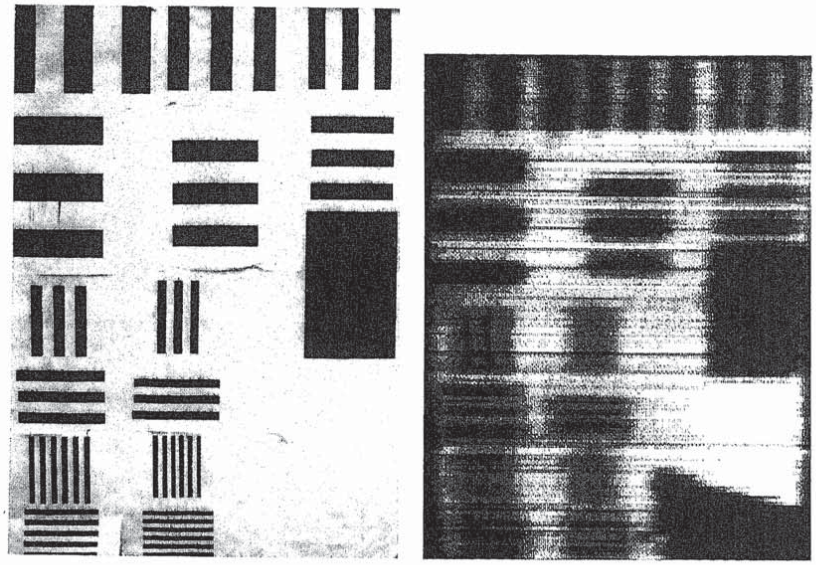

Fig. 5: (a) Photograph of a resolution test pattern made of black and white paper. (b) Scanned fluorescence image of a spatial resolution pattern. The size of the pattern was 70 × 100 cm. The target distance was 60 m.

in particular if a slight smoothing would be applied to the spectra, which was not the case here.

One limitation of the 2D imaging system is the poor signal-to-noise characteristics of single shot images (not shown here). This is partly due to a very low laser power density for larger target areas such as for whole trees. Therefore, a push-broom system utilising a line scanning technique, was developed. The first test object was a pattern of vertical and horizontal stripes on a white paper board that was utilised to determine the spatial resolution of the push-broom system. The width of the paper board was approximately 70 cm and the target distance was about 60 m. A photograph of the test pattern and the corresponding scanned fluorescence image is shown in Fig. 5. Modulation transfer functions (MTF) for the vertical and the horizontal directions were calculated and are shown in Fig. 6. As can be seen from the figure, the resolution was better for the vertical direction compared with the horizontal. An MTF value of 0.5 was reached for line pairs separated by 3 cm for the vertical direction (the scanning direction) and 5 cm for the horizontal direction. The superior vertical resolution can be explained in terms of the scanning direction. The fluorescence from the horizontal light streak is

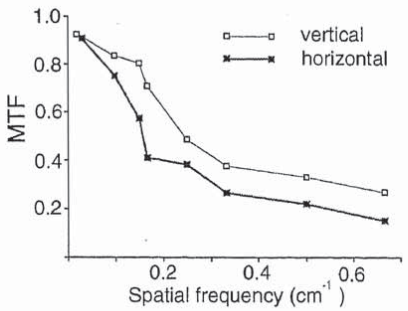

Fig. 6: Modular transfer functions (MTF) calculated from the fluorescence image in Fig. 5.

imaged on the CCD with some image aberrations. However, since the CCD is binned in the vertical direction, all available signal can be considered to originate from one and the same vertical position. In other words, we know that the fluorescence must originate from the laser illuminated streak and

the resolution will thus be determined by the 2 cm height of the laser streak. In the horizontal direction, on the other hand, no binning is performed because this is the imaged direction. Thus, in the horizontal direction the resolution will be limited by image aberrations, which are fairly large for Fresnel lenses.

Remote fluorescence images were recorded for several plant species using the push-broom system. Initially, fluorescence images were scanned at one wavelengths at a time only, without the split mirror arrangement. In these cases sequential recordings at the interesting wavelengths were performed. The ratio image was formed by calculating the ratio, line by line, through the image. Such a set of sequential images were recorded for spruce trees (*Picea abies*) using different optical filters. In Fig. 7, an example of a set of fluorescence images recorded at 480, 685 and 740 nm, are shown. The target distance was also in this case 60 m and the height of the spruce was about 2 m. To the lower right in Fig. 7, a ratio image formed by division of the 685 and 740 nm images, is shown. As can be seen, the individual branches can easily be recognised in the fluorescence images as well as in the ratio image. In the middle part of the ratio image a white vertical streak indicating a high ratio, is seen. Measurements with the OMA system (data not shown) showed that this feature originated from the stem of the tree, which was confirmed to have a high value of the 685/740-nm ratio.

In the following measurements, the split mirror arrangement was included between the Fresnel lenses and fluorescence images were scanned at two wavelengths simultaneously. The CCD read out generated two separate scans corresponding to the two binned areas on the CCD chip and the ratio image was formed in the same way as above. In Fig. 8, fluorescence images recorded with Schott colour glass filters BG7 (blue) and RG645 (red), are shown. In this case the ratio image was formed by division of the "blue" and the "red" images. As can be seen, a clear ratio image of a 2 m spruce tree can be obtained also in this double scan mode of the push-broom system. It should be pointed out here, that there were difficulties in adjusting the two detection paths to obtain a sharp focus in both of them (see «red» fluorescence image in Fig. 8). This was due to the limitations in this early version of the set-up but will be replaced by a more ridgid set-up in the future.

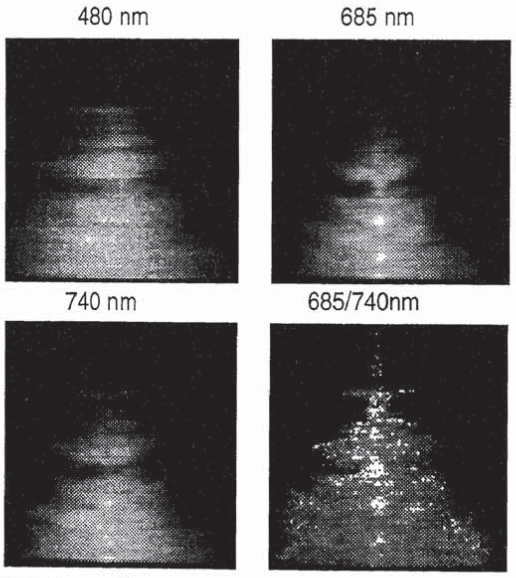

Fig. 7: Sequentially scanned fluorescence images of *Picea abies*. The selected wavelengths were 480, 685 (upper) and 740 nm (lower left). To the lower right a ratio of 685nm/740nm is shown. The spectral width of the filters were 10 nm.

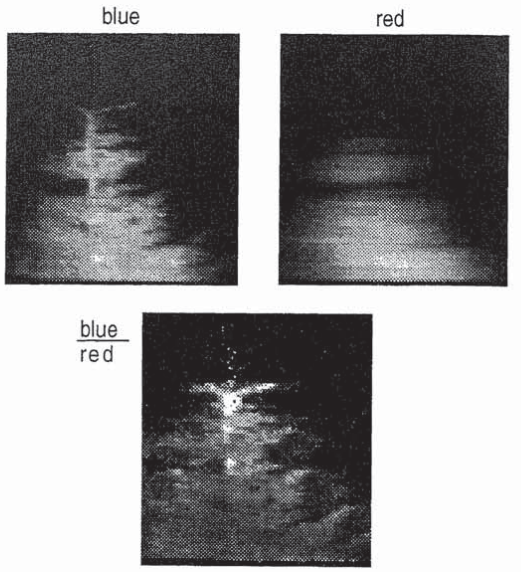

Fig. 8: Simultaneously scanned fluorescence images of *Picea abies* (upper) and a ratio image calculated by division of the «blue» by the «red» image. The optical filters were Schott BG7 (blue) and RG645 (red).

In this paper, a system for remote fluorescence recordings of vegetation, including an OMA system for spectral recordings and two different multi-colour imaging arrangements, has been presented. The OMA system is valuable for spectral recording within an image frame for a better understanding of the recorded images. The two different set-ups have their advantages and come to use in different situations. The 2-D imaging system provides a high resolution but is limited by the poor single-shot sensitivity at longer ranges and by a smaller field of view (0.5 m at 50 m distance). Thus, this system is best suited for short distance measurements where high quality images are required. The push-broom scanning system, on the other hand, provides high signal/noise characteristics at longer ranges and also a larger field of view. Therefore, the push-broom system is ideal for air-borne measurements, which are performed at long distance and where single-shot measurements are an absolute requirement due to the fast movement of an aircraft.

Acknowledgements

This work was supported by the Swedish Natural Science Research Council and by the Swedish Space Board.

References

Cecchi, G., M. Bazzani, V. Raimondi, and L. Pantani: Fluorescence lidar in vegetation remote sensing: system features and multiplatform operation. In: Proc. Internat. Geoscience Remote Sensing Symposium IGARSS '94, *1,* 637–639. California Institute of Technology, Pasadena, USA (1994).

Chappelle, E. W., F. M. Wood, and W. W. Newcomb: Laser induced fluorescence of green plants. 1: A technique for remote detection of plant stress and species differentiation. Appl. Opt. *23,* 134–138 (1984).

Edner, H., J. Johansson, S. Svanberg, E. Wallinder, M. Bazzani, B. Breschi, G. Cecchi, L. Pantani, B. Radicati, V. Raimondi, D. Tirelli, G. Valmori, and P. Mazzinghi: Laser-induced fluorescence monitoring of vegetation in Tuscany, EARSeL Advances in Remote Sensing *1,* 119–130 (1992a).

Edner, H., J. Johansson, S. Svanberg, and E. Wallinder: Remote Multi-Color Imaging of Vegetation Laser-Induced Fluorescence. Proc. CLEO'92, 432–433, Anaheim, Ca, USA (1992b).

Edner, H., J. Johansson, S. Svanberg, and E. Wallinder: Fluorescence lidar multi-color imaging of vegetation, Appl. Opt. *33,* 2471–2479 (1994).

Edner, H., J. Johansson, S. Svanberg, H. K. Lichtenthaler, F. Stober, C. Schindler, and L.-O. Björn: Remote multi-colour fluorescence imaging of selected broad-leaf plants. EARSeL Advances in Remote Sensing *3,* No. 3, 2–14 (1995).

Hoge, F. E. and R.N. Swift: Airborne simultaneous spectroscopic detection of laser-induced water Raman backscatter and fluorescence from chlorophyll *a* and other naturally occurring pigments, Appl. Opt. *20,* 3197–3205 (1981).

Hoge, F. E., R. N. Swift, and J. K. Yungel: Feasibility of airborne detection of laser-induced fluorescence emission from green terrestrial plants. Appl. Opt. *22,* 2991–3000 (1983).

Kim, H. H.: New algea mapping technique by use of an airborne laser fluoresensor. Appl. Opt. *12,* 1454–1459 (1973).

Krause, G. H. and E. Weis: Chlorophyll fluorescence as a tool in plant physiology. II. Interpretation of fluorescence signals. Photosynth. Res. *5,* 139–157 (1984).

Lichtenthaler, H. K. and U. Rinderle: The role of chlorophyll fluorescence in the detection of stress conditions in plants. CRC Critical Reviews in Analytical Chemistry *19,* S29–S85 (1988).

Rock, B. N., J. E. Vogelmann, D. L. Williams, A. F. Vogelmann, and T. Hoshizaki: Remote detection of forest damage. BioScience *36,* 439–445 (1986).

Rosema, A., G. Cecchi, L. Pantani, B. Radicati, M. Romuli, P. Mazzinghi, O. van Kooten, and C. Kliffen: Results of the ‹LIFT› project: Air pollution effects on the fluorescence of Douglas fir and poplar, In: Lichtenthaler, H. K. (ed.): Applications of Chlorophyll Fluorescence, pp. 307–317. Kluwer Academic Publishers, Dordrecht (1988).

Svanberg, S.: Fluorescence Lidar Monitoring of Vegetation Status. Physica Scr. *T58,* 79–85 (1995).

Zimmermann, R. and K. P. Günther: Laser-induced chlorophyll *a* fluorescence of terrestrial plants, In: Proc. International Geoscience and Remote Sensing Symposium IGARSS '86, 1609–1613, Zürich. ESA Publications Division, Nordwijk (1986).

Paper III

A preliminary experiment on the remote sensing of historical buildings by fluorescence Lidar

P. Weibring, M. Andersson, G. Cecchi, H. Edner, J. Johansson,
L. Pantani, V. Raimondi, B. Sundnér and S. Svanberg.

SPIE **3222**, 372–382 (1997).

A preliminary experiment on the remote sensing of historical buildings by fluorescence lidar

Petter Weibring [a], Mats Andersson [a], Giovanna Cecchi [b], Hans Edner [a], Jonas Johansson [a], Luca Pantani [b], Valentina Raimondi [b], Barbro Sundnér [c], Sune Svanberg [a]

[(a)] *Lund Institute of Technology, Atomic Physics Division*
P.O. Box 118, S-221 00 Lund, Sweden

[(b)] *National Research Council*
Istituto di Ricerca sulle Onde Elettomagnetiche "Nello Carrara"
Via Panciatichi 64, I-50127 Firenze, Italy

[(c)] *Central Board for National Antiquities*
P.O. Box 5405, S-114 84 Stockholm, Sweden

ABSTRACT

Stone surface monitoring of historical buildings is of interest in the planning of restoration work, both for assessing biodeteriogen growth and for detecting the spectroscopic features of the surface itself. Laser-Induced Fluorescence (LIF) analysis yields strong signals in the near IR region due to algal depositions, while signals through the visible region are useful for the characterisation of the stone materials. This paper reports on the first experiments carried out in the framework of a joint project of LTH and IROE-CNR aimed at the fluorescence imaging of historical buildings. We have used a fibre-optical fluorosensor for performing point measurements, and a mobile fluorescence imaging lidar system for remote measurements at a typical distance of 60 m.

Keywords: cultural heritage, conservation, biodeteriogens, fluorescence imaging, LIF analysis, fluorescence lidar

1. INTRODUCTION

Historical buildings constitute an important component of our cultural heritage: however, an extensive control of their status and their conservation can often be a very troublesome task. From this point of view the use of remote sensing techniques for the monitoring of stone surfaces is very attractive. In particular, the fluorescence lidar technique can be useful for the detection of algal depositions and fluorescent organic layers as well as for the characterisation of coating materials. All these data are helpful both for the restoration planning and for the study, from a historical point of view, of the building under investigation, for instance the identification of the site where the material was extracted.

SPIE Vol. 3222 • 0277-786X/97/$10.00

Fluorescence lidars have successfully been used for the monitoring of sea and vegetation for more than twenty years[1] and have already reached a good level of technological development which has included the implementation of high spectral resolution and fluorescence imaging lidar systems[2]. Chlorophyll fluorescence has main features in the red region and has been used for a long time as a sensitive detector of vegetal organisms in different media[3,4]. It has been demonstrated as a powerful tool for the early detection of stress in vegetation, even in remote sensing applications[5,6].

Until now, the fluorescence features of historical buildings have been mainly investigated by means of sampling operations and subsequent laboratory analysis. This procedure not only constitutes a violation of the integrity of the monument, but also rises questions about the significance of the sampling and makes an extensive monitoring almost impossible. More recently the fluorescence lidar technique was tested for the monitoring of historical buildings[7,8], showing good potential for the detection of both biodeteriogens and fluorescence features of calcareous rocks. During these experiments the LIF technique was used for the remote detection of biodeteriogen colonisations on marble substrata at a previsual stage of algal deposition and for the identification of the extraction site of the material of the monument by means of its fluorescence features. Both these experiments refer to point measurements obtained with a high spectral resolution lidar. However, fluorescence analysis of historical buildings becomes particularly attractive if it is performed with an imaging system in order to furnish a set of thematic images to the user who actually needs easy-to-read data. These images should be able to stress the fluorescence features of different kinds and the level of algal deposition, or to enhance the different fluorescence features of the investigated lithotype with respect to those of similar materials.

This paper reports on the first experiments carried out in the framework of a joint project on the fluorescence remote sensing of historical buildings. The project was undertaken by the Istituto di Ricerca sulle Onde Elettromagnetiche "Nello Carrara" of CNR (IROE) and the Lund Institute of Technology, Atomic Physics Division (LTH). It aims at the investigation of the feasibility of fluorescence lidar imaging of cultural heritage. The experiments made at the Lund Laser Centre (LLC) in January 1997, included measurements on Italian and Swedish samples, some of which affected by algal deposition. The samples were analysed either with a mobile fibre-optic fluorosensor and with a fluorescence imaging lidar. Moreover, the paper reports on a first set of measurements carried out on the external walls of the Lund Cathedral with a mobile fibre-optic fluorosensor.

2. EXPERIMENTAL

This section is divided into three parts, according to the experimental set-up used for the measurements. The first part refers to the measurement of the fluorescence signatures of lithotypes coming from different Italian and Swedish extraction areas. Some of the Swedish samples were affected by algal colonisations. The fluorescence spectra were detected with the fibre-optic fluorosensor, originally developed at LTH to detect fluorescence spectra for medical applications. In the second part of the experiment the samples were arranged into frames in order to constitute two artificial targets, the first with the Italian samples, the second with the Swedish ones. Both were scanned with the LTH imaging lidar at a distance of about 60 m. The last part of the experiment was devoted to a preliminary fluorescence analysis of the Lund Cathedral with the fibre-optic fluorosensor.

2.1 Fluorescence point measurements on the samples

Two sets of samples were analysed in the laboratory: the first set of Italian lithotypes coming from different extraction areas, the second of Swedish samples, most of which with biodeteriogen colonisations. The first included both limestones and sandstones: in particular, most of the limestones have similar petrographic features, but come from different extraction sites. Measurements on this set have been aimed at the differentiation between similar lithotypes by means of their fluorescence features. Measurements on the second set, which consists of Swedish samples, have mainly been aimed at the detection of biodeteriogens on various types of stones characteristic for historical buildings in southern Sweden.

Fluorescence point measurements were carried out in the laboratory with the fibre-optic fluorosensor. The fibre was used both for the excitation (pulsed N_2 laser, $\lambda = 337.1$ nm) and for the detection of the fluorescence light. This light, after passing through a dichroic beam splitter, is sent to the entrance slit of a monochromator coupled to a gateable, intensified CCD detector. The system is schematically shown in Fig.1, while a more detailed description of the fluorosensor can be found in Ref. 9 . The fluorescence spectra were taken by placing the tip of the fibre directly into contact with the sample surface. For each spectrum the signal is accumulated for 50 laser pulses (5 sec). In order to take into account the inhomogeneous features of the surfaces of same samples (especially those of ammonitic limestones from northern Italy) several points of the same sample were analysed.

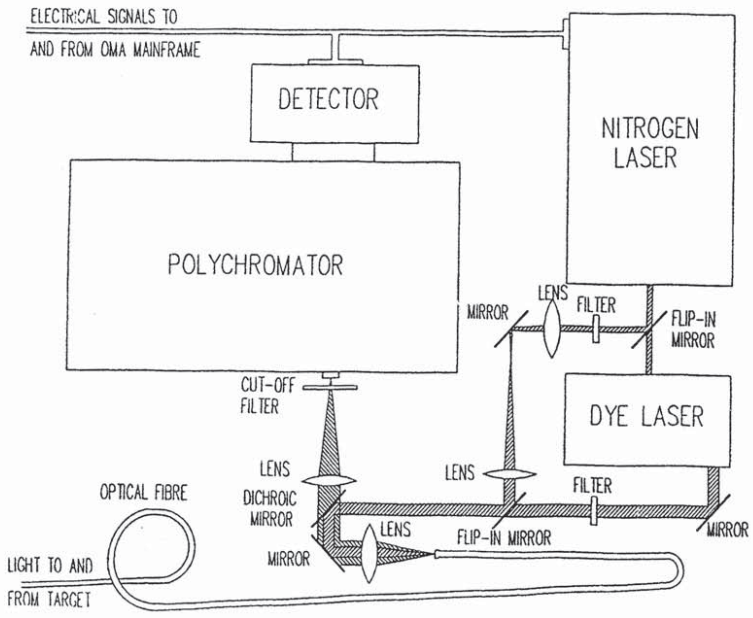

Fig. 1 - Lay-out of the fibre-optic fluorosensor (from Ref. 9).

The same rock samples, analysed in the laboratory, were used for the fluorescence imaging experiment. The samples were arranged into two frames, one containing the Italian samples and the other one made up of the Swedish samples.

The lidar system used for the measurements was designed and built at LTH for environmental monitoring[10,2]. Up to now it has been operated in three different measurement mode:

1) *point remote monitoring*, which is the 'remote' counterpart of the operation mode of the fibre-optic fluorosensor: the laser beam is directly sent onto the target and induced fluorescence light is collected by the telescope.

2) *remote multi-colour fluorescence imaging*, which enables the simultaneous detection of three or four images of the target, each at a different wavelength band, by the use of a beam expander to cover the whole target and of a split-mirror arrangement at the exit of the lidar telescope.

3) *push-broom multi-colour fluorescence imaging*, which uses an excitation beam shaped into a streak by suitable optics: the target is scanned by moving this streak over it and the fluorescence image is thus obtained streak by streak.

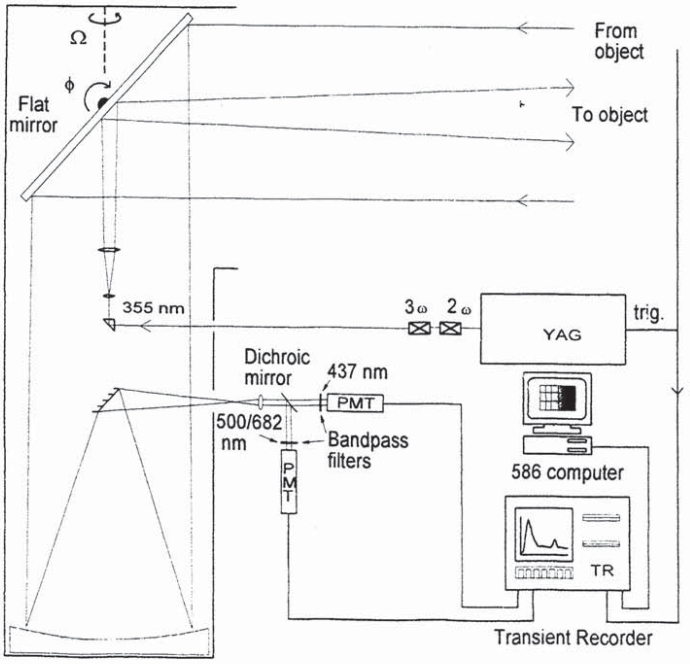

Fig. 2 - Lay-out of the LTH fluorescence imaging lidar.

375

During this experiment the target was scanned sequentially in two dimensions, using the system basically in the point remote monitoring mode, and with the detection accomplished by splitting up the fluorescence signal into two beams. Each of these was individually filtered and finally detected with a fast photomultiplier tube. In this way the final data are two fluorescence intensity matrixes which are stored with the correspondent beam-positioning (x,y) coordinates. A basic lay-out of this system arrangement is depicted in Fig. 2. The excitation consisted of a tripled Nd:YAG laser beam ($\lambda = 355$ nm, 20 Hz) expanded by a Galileian lens telescope so that the footprint at the target was had a diameter of 2 cm. The target was scanned with a computer-controlled first-surface flat mirror which collected also the fluorescence and directed it into a 40 cm diameter Newtonian telescope. Finally, the signal was sent to the detection system described above.

2.3 Fluorescence point measurements on the Lund Cathedral

The measurements on the Cathedral of Lund were carried out with the fibre-optic fluorosensor operated on the site. The Cathedral dates back to the 12th century and is one of the most remarkable examples of Romanesque style in northern Europe. Most of its parts are made of sandstone of different hardness. The external walls show evidence of biodeteriogen depositions, including different kinds of algae and lichens. Their presence and quantity, of course, depend also on the location of the surface. Further information about Swedish historical buildings and their problematics can be found in Ref. 11 .

Fluorescence spectra were detected on different areas of the walls both inside and outside the cathedral. For the measurements outside the cathedral the fluorosensor unit was still placed inside, while the optical fibre was passed through the door in order to reach the external walls. The measurements involved different areas, including some affected by biodeteriogen colonisations as well as coated with sandstone in 19th century due to restoration works. The present experiment with a point monitoring system aimed also at the identification of the optimal spectral bands to be adopted for the next experiment with the fluorescence imaging system on the Lund Cathedral, which is planned for late 1997.

3. RESULTS AND DISCUSSION

The fluorescence spectra from two different limestone samples of *Bianco Veronese* are shown in Fig. 3. The samples come from two different extraction sites: one sample (dotted line), commercially named *Corso Bianco*, was extracted in a site exploited only recently as a quarry (*Ghirardi*, Vicenza, Italy); the other one (continuous line), commercially named *Nembro*, comes from an extraction site which is also named in the historical archives. The two spectra show different shapes which should allow a discrimination between the samples. Moreover, the fluorescence intensity of the *Nembro* sample is considerably less than that of the *Corso Bianco*. This behaviour has been found in most samples coming from the old extraction area and might be due to a higher iron ions content. Iron ions are actually fluorescence quenchers in many carbonates[12] . Finally, these fluorescence spectra have features which are consistent with those found at an excitation wavelength of 308 nm (see Ref. 8).

Fig. 4 reports the spectra taken in different points on the surface of the same sample (*Corso Bianco*). The spectra were normalised to their maximum in order to enhance the variations in the spectral shape. The point referring to dark veins (dotted line) show a shape slightly different from that of the

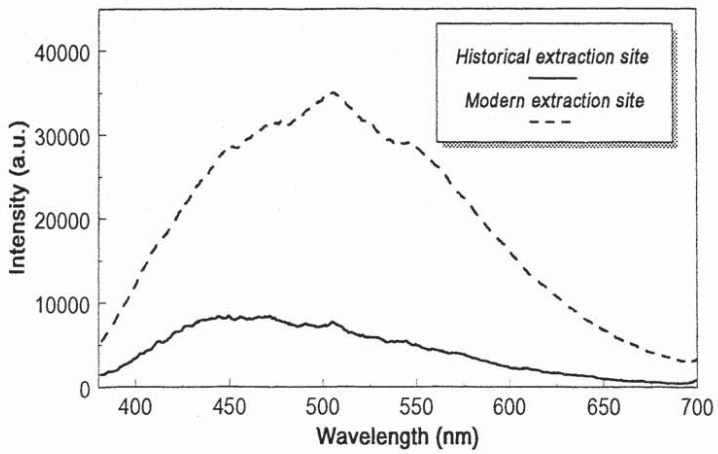

Fig. 3 - Fluorescence spectra of *Bianco Veronese* samples by using the fibre-optic fluorosensor ($\lambda_{exc.}$ = 337 nm). The samples come from two different extraction sites: 1) *Corso Bianco* from the *Ghirardi* quarry, which is an extraction site exploited only quite recently, and 2) *Nembro* from the *Bonaldi* cave, a historical extraction site known since Roman times.

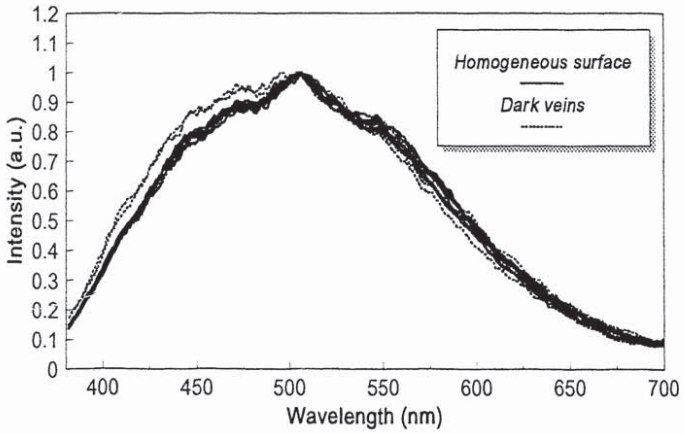

Fig. 4 - Fluorescence spectra obtained with the fibre-optic fluorosensor on the same sample (*Corso Bianco*). Each spectrum corresponds to different spots on its surface: in particular, continuous lines refer to homogeneous areas on the surface while dotted lines refer to darker veins.

homogeneous areas. The use of a fibre-optic terminated sensor allowed the discrimination between very small areas with different petrographic features.

Most of the investigated Swedish samples did not give any evidence of fluorescence due to the rock itself, probably because of the type of rock, but revealed strong signals due to algal depositions. Fig. 5 shows LIF spectra obtained on a sandstone coming from the Övedskloster Castle (Southern Sweden): the rock sample itself did not show much fluorescence as can be seen from the spectrum taken on a broken raw side of the sample (dotted line); however, the surface corresponding to a side exposed to weathering shows an intense fluorescence peak at 680 nm, clearly due to the chlorophyll contained in algal colonies.

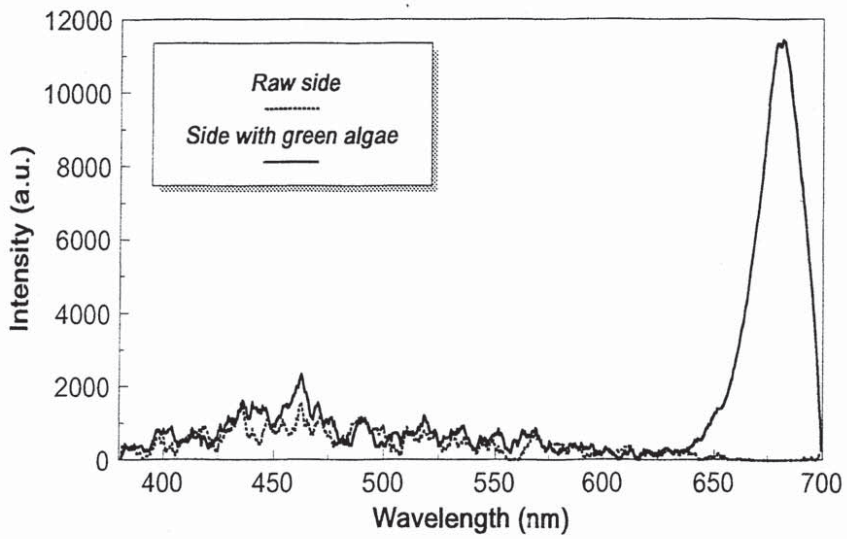

Fig. 5 - Fluorescence spectra of a Swedish sample coming from the Övedskloster Castle: the 680 nm fluorescence peak (continuous line) is due to algal deposition on the side originally exposed to the weathering.

In Fig. 6 LIF images of the Italian samples arranged into a frame are reported. The images refer to two different detection wavelengths 500 and 437 nm, top-right and bottom-right respectively. Together with the two LIF images, the target reflectance image (top-left) and the ratio between the 500 and the 437 nm images (bottom-left) are shown. The target was composed of both sandstones and limestones coming from different Italian extraction sites. The samples were disposed into the frame as follows (the commercial name of the sample is reported in italics followed by the main colour, while the extraction area is reported in brackets):

- upper row: limestone *Nembro*/pink (Bonaldi, Verona), sandstone (Siena), limestone *Corallo rosa*/pink (Bonaldi, Verona), limestone *Nembro*/white (Bonaldi, Verona), limestone *Corso Mezzo Brocato*/red (Bonaldi, Verona), limestone *Rosa*/pink (Ghirardi, Vicenza), sandstone (Firenze);

- middle row: limestone *Brocato*/rosso (Bonaldi, Verona), limestone *Corso Grosso*/red (Bonaldi, Verona), limestone *Rosso Magnaboschi*/red (Ghirardi, Vicenza), sandstone (Siena), limestone *Nembro*/yellow (Bonaldi, Verona), limestone *Corso Bianco*/white (Ghirardi, Vicenza), limestone *Scisto*/red (Val Gordana, Massa);
- lower row: marble/grey (Siena), limestone *Roan*/pink-green (Bonaldi, Verona), sandstone (Siena), limestone *Mandorlato*/green-yellow (Bonaldi, Verona), marble/red (Siena), limestone *Corso Rigato*/yellow-green (Bonaldi, Verona), marble/white (Carrara).

The target was placed at 60 m from the lidar system. The LIF images at 437 nm and at 500 nm were taken by using bandpass filters. It is to be noted that the ratio (bottom-left) is a dimensionless unit, not affected by laser intensity fluctuations, target topography, etc. and thus particularly suitable for remote sensing applications. The wavelengths of the bandpass filters were chosen by taking into account the results of the laboratory measurements, in particular the fluorescence peaks of the Italian sample spectra.

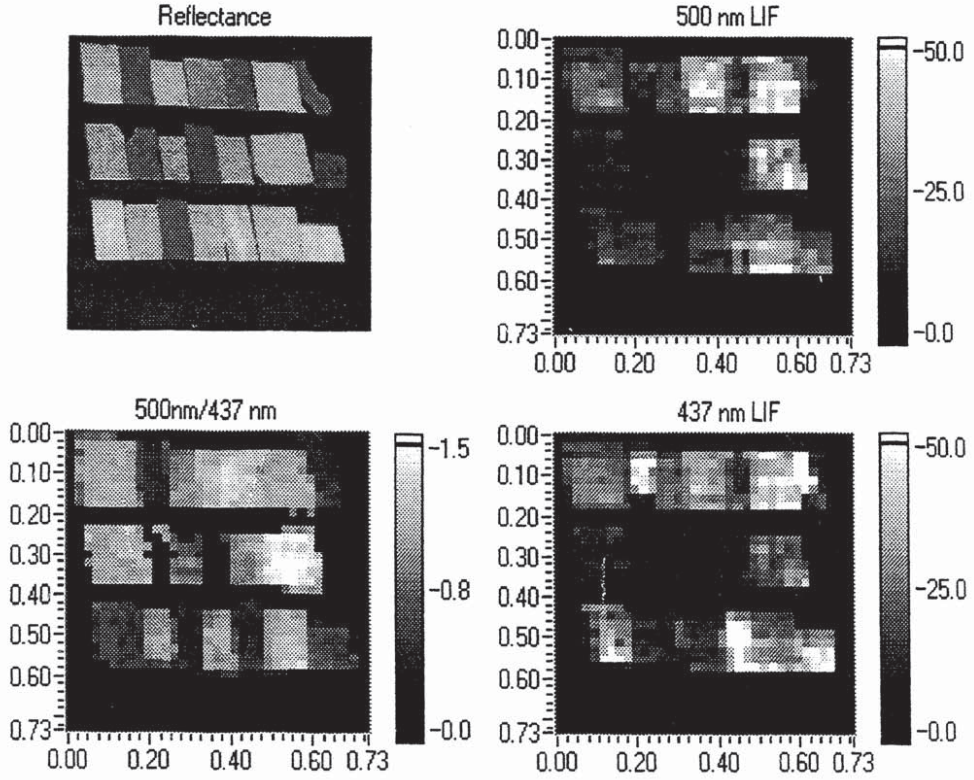

Fig. 6 - Fluorescence lidar imaging of the Italian samples: reflectance image (top-left), LIF images at 500 and 437 nm (top-right and bottom-right, respectively) and the ratio between the 500 and the 437 nm images (bottom-left). The size of the target was 0.59x0.54 m^2.

379

In Fig. 7 LIF images of the Swedish samples are shown. The experimental conditions are as described for the measurements on the frame containing the Italian samples. The samples were arranged into the frame as follows (from right to left):

- upper row: Övedskloster, Gotland sandstone (deteriorated);
- middle row: Gotland limestone, Komsta limestone;
- lower row: Gotland sandstone (new), Orsa sandstone, Höör sandstone, Bremer sandstone.

As turned out during the laboratory measurements as well, most of the Swedish samples showed little fluorescence. This is apparent from the LIF image at 437 nm where the only sample with a significant blue fluorescence intensity is the Gotland limestone (the fluorescence in the lower part is due to oil on the metal frame). The main fluorescence features of the Swedish samples are due to algal depositions, as inferable from the LIF image at 682 nm which reveals the typical peak of chlorophyll red fluorescence.

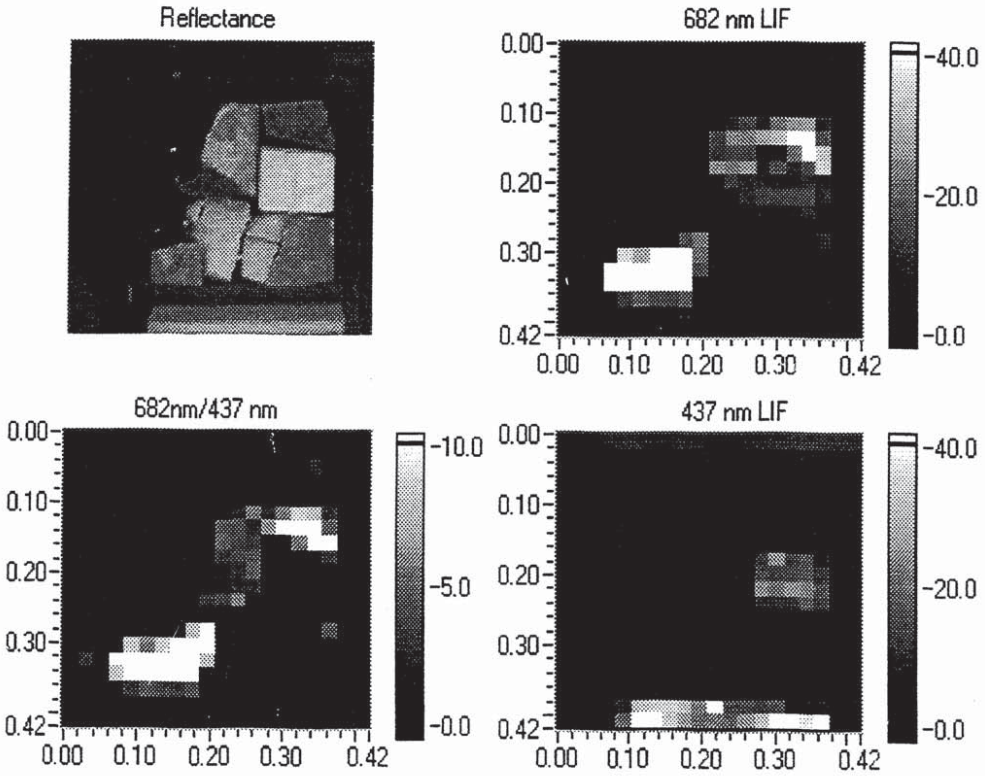

Fig. 7 - Fluorescence lidar imaging of the Swedish samples: reflectance image (top-left), LIF images at 500 and 437 nm (top-right and bottom-right, respectively) and the ratio between the 500 and the 437 nm images (bottom-left). The size of the target was about 0.2x0.2 cm^2.

Some point fluorescence spectra taken with the fibre-optic fluorosensor on the external walls of the Lund Cathedral (Sweden) are shown in Fig. 8. These measurements constitute a preliminary step and the collected data will be used to plan the second phase of our experiment which involves the detection of LIF images of the Cathedral. The fluorescence spectra refer to three different spots: a sandstone block from the 12th century, another sandstone block inserted during restoration works in the 19th century and an area with green lichens on the surface. many analysed areas of the external walls showed the fluorescence peak typical of chlorophyll (680 nm) revealing the presence of algal deposition. The wide fluorescence band which is present in both the other two spectra can be due either to the rock itself or to superficial layers: further work is needed to understand the origin of this band.

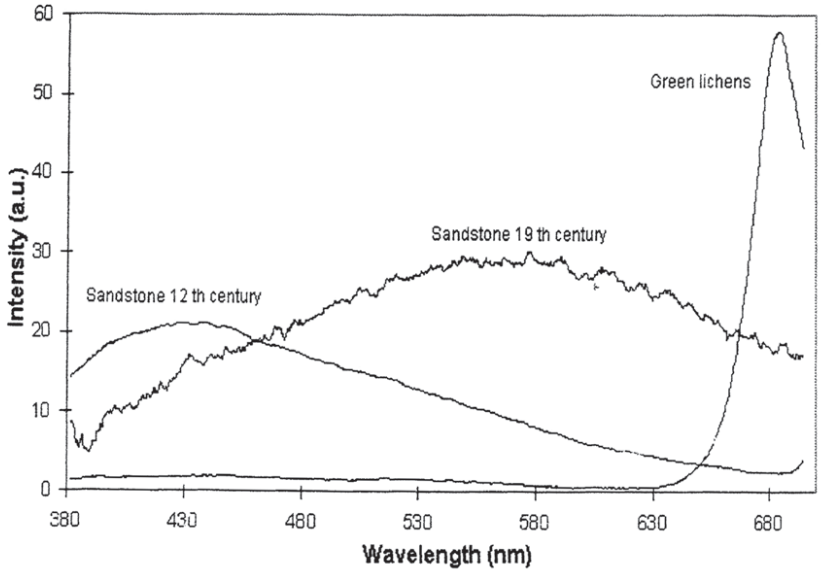

Fig. 8 - Fluorescence spectra from the external walls of the Lund cathedral obtained with the fibre-optic fluorosensor: 1) 12th century sandstone, 2) 19th century sandstone, 3) sandstone with green lichens.

4. CONCLUSIONS

The preliminary experiments have showed the feasibility of fluorescence lidar imaging on stone materials from a distance of 60 m. Fluorescence imaging data on both rock fluorescence features and photoautotrophic organisms were collected by using specially-arranged stone targets and were compared with the fluorescence point data obtained on the same Italian and Swedish samples with a portable

fluorosensor in the laboratory. The signal-to-noise ratio obtained during the fluorescence imaging measurements suggests that the detection in full sunlight should be still feasible at a distance of 100 m.

Further experiments are scheduled for late 1997 and will be mainly devoted to the fluorescence imaging of the Lund Cathedral façade with the LTH lidar, especially with regard to the monitoring of biodeteriogen colonisation.

ACKNOWLEDGEMENTS

This work was supported by the TMR Access to Large-Scale Facilities Grant ERB FMGE CT950020 (DG12) and by the Swedish Space Board.

The authors wish to thank Prof. R. Chiari (Institute of the Petrography, University of Parma) and Prof. G. Sabatini (Institute of Mineralogy, University of Siena) for having furnished the Italian samples and for information on the petrographic features.

REFERENCES

1. R. M. Measures (Ed.), *Laser remote chemical analysis*, Wiley Interscience, New York, 1988.
2. H. Edner, J. Johansson, S. Svanberg, E. Wallinder, "Fluorescence Lidar Multi-color Imaging of Vegetation", *Appl. Opt.*, **33**, pp. 2471-2479, 1994.
3. C.S. Yentsch, D.W. Menzel, "A method for the determination of phytoplankton chlorophyll and phaeophytin by fluorescence", *Deep Sea Research*, **10**, pp. 221-231 (1963).
4. D.C. Fork, P. Mohanty, "Fluorescence and other characteristics of blue-green algae (cyanobacteria), red algae and criptomonads", in *Light emission by plants and bacteria*, Govindjee, J. Amesz, D.C. Fork Eds, **16**, pp. 451-496, 1986.
5. J.F.H. Snel, O. Van Kooten, "The use of chlorophyll fluorescence and other non invasive spectroscopic techniques in plant stress physiology", *Photosynth. Res.* (*Special Issue*), **25**, pp. 146-332 (1990).
6. R. Valentini, G. Cecchi, P. Mazzinghi, G. Scarascia Mugnozza, G. Agati, M. Bazzani, P. De Angelis, F. Fusi, G. Matteucci, V. Raimondi, "Remote sensing of chlorophyll fluorescence on vegetation canopies: 2. physiological significance of fluorescence signal in response to environmental stresses", *Rem. Sens. of Environ.*, **47**, pp. 29-35, 1994.
7. G.Cecchi, L.Pantani, V. Raimondi, D. Tirelli, L. Tomaselli, G. Lamenti, M. Bosco, P. Tiano, "Fluorescence lidar technique for the monitoring of biodeteriogens on the cultural heritage", in *Remote Sensing for Geography, Geology, Land Planning and Cultural Heritage* (D. Arroyo-Bishop et al. Eds) SPIE **2960**, pp. 137-147, Bellingham, 1996.
8. G. Cecchi, L. Pantani, V. Raimondi, D. Tirelli, R. Chiari, "The fluorescence lidar technique for the remote sensing of stony materials in ancient buildings", Proc. SPIE EUROPTO Series: *Remote Sensing for Geography, Geology, Land Planning, and Cultural Heritage* (D. Arroyo-Bishop et al. Eds), SPIE **2960**, pp. 163-173, Bellingham, 1996.
9. S. Andersson-Engels, Å. Elner, J. Johansson, S.E. Karlsson, L.G. Salford, L.G. Strömblad, K. Svanberg, S. Svanberg, "Clinical Recording of Laser-Induced Fluorescence Spectra for Evaluation

of Tumor Demarcation Feasibility in Selected Clinical Specialities", Laser in Medical Science 6, pp.415-424, 1989.

10. H. Edner, K. Fredriksson, A. Sunesson, S. Svanberg, L. Uneus, W. Wendt, "Mobile Remote Sensing System for Atmospheric Monitoring", *Appl. Opt.* **26**, pp.4330-4338, 1987.

11. E. Ostlund, Ed., *Degradation of Materials and the Swedish Heritage* 1992-1995. A Report from the Air Pollution and Heritage Programme, RIK 11, Riksantikvarieambetet, Stockholm, 1994.

12. H.G. Machel, R.A. Mason, A.N. Mariano, A. Mucci, *Causes and emissions of luminescence in Calcite and Dolomite*, in Luminescence Microscopy and Spectroscopy: Qualitative and Quantitative Applications (C.E. Barker and O.C. Kopp Eds), SEPM, Tulsa, 1991.

383

Paper IV

Atmospheric mercury concentrations and fluxes in the Almadén district (Spain)

R. Ferrara, B.E. Maserti, M. Andersson, H. Edner, P. Ragnarson, S. Svanberg, and A. Hernandez.

Atmos. Env. **32**, 3897–3904 (1998).

Pergamon

Atmospheric Environment Vol. 32, No. 22, pp. 3897–3904, 1998

Printed in Great Britain

PII: S1352–2310(98)00102–2

1352–2310/98 $19.00 + 0.00

ATMOSPHERIC MERCURY CONCENTRATIONS AND FLUXES IN THE ALMADÉN DISTRICT (SPAIN)

R. FERRARA,*† B. E. MASERTI,† M. ANDERSSON,‡ H. EDNER,‡ P. RAGNARSON,‡ S. SVANBERG‡ and A. HERNANDEZ§

†CNR—Istituto di Biofisica, Via San Lorenzo 26, I-56127 Pisa, Italy; ‡Department of Physics, Lund Institute of Technology, P.O. Box 118, S-221 00 Lund, Sweden; and §Minas de Almaden y Arrayanes S.A., E-13400 Almadén, Ciudad Real, Spain

(*First received* 10 *April* 1996 *and in final form* 14 *February* 1998. *Published August* 1998)

Abstract—Atmospheric mercury levels around the world's largest mining and refining complex (Almadén, Spain) were determined during two field campaigns (September 1993 and February 1994) using both point monitors and lidar techniques. High mercury concentrations (0.1–5 $\mu g\,m^{-3}$) were measured over the village of Almadén in the prevailing wind direction. In the month of September the total mercury flux into the atmosphere was estimated to range from 600 to 1200 $g\,h^{-1}$. An attempt was made to measure the contribution from individual mercury sources. © 1998 Elsevier Science Ltd. All rights reserved

Key word index: Mercury, mine, lidar, atmosphere, fluxes.

INTRODUCTION

The area of Almadén, Spain, is an interesting challenge for researchers involved in studying the biogeochemical cycle of mercury; indeed, the Almadén district constitutes the largest and most unusual concentration of the metal in the world. It has been estimated that before mining began the area contained about 250,000 t of mercury (about a third of the earth's total known mercury resources). The natural mercury emissions from the ore deposits are increased by the presence of mining and refining operations.

The first study of mercury cycling and transport in the terrestrial and aquatic system at Almadén was conducted by ORNL (Oak Ridge National Laboratory, U.S.A.) in the years 1974–1977. The results were published as an internal report in 1980. In 1979 Lindberg *et al*. reported the results of a study on mercury uptake in plant growth on surface soils collected near the Almadén mine; the rate of volatilization of mercury from these soils was also determined in a laboratory experiment.

In addition, the distribution of mercury in vegetation at Almadén, evaluated during the ORNL field campaign, was published by Huckabee *et al*. in 1983.

In all the above-mentioned studies no data are available on mercury concentrations in the air and on atmospheric mercury fluxes from the main sources. This knowledge is particularly important because the atmospheric transport pathway, both in the gaseous and particulate forms, plays an important role in the mercury cycle in the environment (EPRI-Report TR 104214 Expert Panel, 1994). It is likely that the difficulties connected with such measurements, especially with regard to the analytical methodologies available some 20 years ago, led the authors of the preceding studies not to carry out these determinations and to concentrate their attention on the effects on organisms.

Due to this lack of information, two field campaigns, mainly devoted to the determination of atmospheric mercury levels in the Almadén district, were carried out in 1993–1994; the first results on mercury fluxes measured *in situ* from different sources in an area affected by intensive mining activity were also evaluated.

The campaigns were performed by the Institute of Biophysics (National Research Council, Italy) and the Lund Institute of Technology (University of Lund, Sweden). The Lund Institute has developed a lidar capable of obtaining three-dimensional maps of the atmospheric mercury distribution over an area of about 3 km^2. Successful applications of this laser radar technique for studying atmospheric mercury associated with industrial and mining activities and geothermal energy extraction have been reported (Ferrara *et al*., 1992a; Edner *et al*., 1992; 1993).

* Author to whom correspondence should be addressed.

SITE DESCRIPTION

The Almadén area is located in the central part of the Iberian Peninsula, 300 km south-west of Madrid. In this site the climate is semi-arid and temperate, with an average annual rainfall of 50 cm. Winds blow predominantly from the west and southwest in the shallow valley where the village of Almadén is located.

The main mine, the ore roasting ovens and the mercury distillation plant are located close to the village, the mine galleries run beneath it, and the outlets of the ventilation systems are close to the houses. The overall area of the roasted cinnabar banks surrounding the mine complex is on the order of 3×10^5 m^2. Banks are constituted of about 3,700,000 t of roasted mineral containing a mean percentage of mercury of 0.15% (0.5% in the old and 0.02% in the recently treated mineral). The anomalous area extends 20 km southeast from the village to the "El Entredicho" mine, discovered in 1984 by Hernandez. This mine is of particular interest because the cinnabar deposits are extracted from an open pit and the ore is very rich in mercury. A detailed description of the mercury deposits is reported elsewhere (Ortega and Hernandez, 1992).

Mercury grades reached 8–10 wt% historically, but more recently have been between 3 and 5 wt%. The maximum peak of production was in 1941 with 82,000 flasks of mercury ($\cong$ 2830 t). In 1990 the price collapsed and caused a crisis, with no production in 1991–1992 and very low output (20,000 flasks) in 1993–1994.

Probably the most important mercury vapor sources present in the Almadén district are:

- the 30 m tall stack of the ore roasting ovens of the complex;
- the mine's forced ventilation systems;
- the degassing from the soil and roasted cinnabar banks;
- the emissions from the mercury droplets present on the ground inside and around the complex;
- the particulate matter containing mercury, distributed to an unknown distance from the mine by wind and vehicular activity.

EXPERIMENTAL

The atmospheric mercury concentration was measured using point monitors and the lidar remote sensing technique.

Portable point monitors were made of a PVC waterproof box and contained two gold collectors through which air was sucked at a flow rate of 0.5–2 l min^{-1} controlled by a rotameter. Gaseous mercury sampled on gold collectors was electrothermally desorbed and determined by atomic absorption spectroscopy, as described elsewhere (Ferrara *et al.*, 1991).The detection limit of the instrumental device (defined as 3 $\sigma$of the background noise) is 1×10^{-5} μg of mercury.

The mobile lidar (light detection and ranging) has been described extensively by Edner *et al.* (1987,1989). Short laser pulses at 253.6 nm are transmitted into the atmosphere using a large plane mirror; backscattered radiation is collected by the same mirror and directed into a Newtonian telescope. Time-resolved detection of laser pulses enables range-resolved measurements to be made. The mirror can be rotated by computer-controlled stepping motors around both the horizontal and vertical axes, making it possible to move the measurement direction 360° horizontally and 45° vertically. The wavelength of the laser is alternately varied from the mercury absorption line to a nearby wavelength position with no absorption due to mercury. The detected changes in the backscattered light intensity are used to evaluate the mercury concentration profile along the laser beam. The detection limit is on the order of $2–3 \times 10^{-3}$ μg m^{-3}. From a vertical scan through a plume or a diffuse source it is possible to obtain the distribution of mercury in the cross section; the flux value can be estimated from the integrated value over the plume if wind direction and speed are known.

Some extensive comparisons on atmospheric mercury determinations carried out with the lidar technique and those obtained with the point monitor system have provided comparable results (Ferrara *et al.*, 1991).

Mercury emissions from the roasted cinnabar banks and soils were measured using a flux chamber similar to the one described by Xiao *et al.* (1991). Plexiglas chambers with bases having different surface areas (0.12–0.24 m^2) were used depending on the expected emission rate. The walls of the chamber have been made to penetrate for about 2 cm into the soil and externally sealed with the same soil. Ambient air was drawn into the chamber through two inlet ports: two parallel sampling trains, each consisting of two gold collectors, similar to those used in the point monitors, were connected to the two outlet ports for mercury collection. A flow rate ranging from 0.1 to 1 l min^{-1} was chosen, depending on the mercury content and temperature of the sampled soil. When measurements were conducted on highly emitting soils the smaller chamber was used with a sampling time of 5 min and a flow rate of 1 l min^{-1}; these conditions allow about a 5 time exchange of the internal air in the chamber. Due to the generally high mercury emission levels, acid washing of the chamber was necessary after each set of measurements to reduce the chamber blank ($0.5–5 \times 10^{-3}$ μg h^{-1}).

Samples of roasted cinnabar and soil were dried for 72 h at 40°C. The total mercury concentration was determined by atomic absorption spectroscopy after mineralization of 500 mg of the sample with 5 ml of a mixture of HNO_3, H_2SO_4 and HCl (5 : 3 : 2) in a pressure decomposition system at 120°C for 6 h.

The results of the analyses on the reference standard material (CRM 277) "Estuarine Sediment" issued by the Commission of the European Community (Griepink and Muntau, 1988) was $1.75 \pm 0.08\ \mu g\ g^{-1}$ compared to the certified value of $1.77 \pm 0.06\ \mu g\ g^{-1}$.

Meteorological parameters were provided by the "Minas de Almaden y Arrayanes S.A.".

RESULTS AND DISCUSSION

Atmospheric mercury concentration

Figure 1 illustrates a typical distribution of the mercury levels in the air over the Almadén village, measured about 1 m above the ground using the point monitor technique. The measurements were made between 19 September and 1 October 1993, with mostly sunny weather and a daytime temperature of around 25°C.

As was foreseeable, the highest levels ($20\ \mu g\ m^{-3}$) were measured inside the mining complex (St. 1). The values show decreasing trend towards the east, in the direction of the prevailing wind and the village centre. Particularly high values ($5\ \mu g\ m^{-3}$) were found at station 16, near one of the two ventilation systems of the underlying mine galleries and above the banks of roasted cinnabar (St. 2, 6, 7, 9, 11). Figure 2 shows the daily trend of the mercury concentration together with the trend of the ambient temperature, measured at the station no. 6. This trend, already observed in other studies (Ferrara *et al*., 1997), is mainly due to the dependence of mercury emissions on soil temperature. The determinations made at the control station "Alamillo", located about 20 km south of Almadén in a non-mineralized zone, yielded a value of $5.9 \times 10^{-3}\ \mu g\ m^{-3}$,comparable with the background levels for mineralized areas ($8–10 \times 10^{-3}\ \mu g\ m^{-3}$).

The levels of the atmospheric mercury concentrations measured over the village of Almadén on 26 September, a day after the cinnabar roasting ovens were shut down for maintenance, are particularly interesting. These values were generally about one third

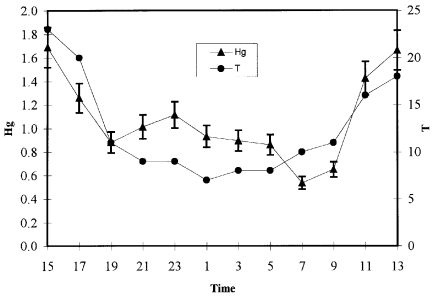

Fig. 2. Daily behavior of atmospheric mercury concentration ($\mu g\ m^{-3}$) and of air temperature (°C), measured at the sampling station no.6 (September 1993).

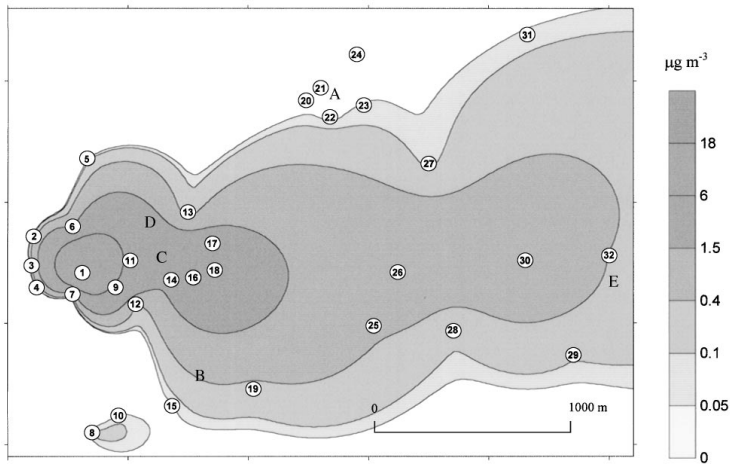

Fig. 1. Atmospheric mercury concentration ($\mu g\ m^{-3}$) over the Almadén village (area bordered with dotted lines) and over the mining complex (area bordered with continuous lines) measured by point monitors (the circles show the location of the sampling stations). A, B, C, D, E are the measurement positions of the Lidar system (September 1993).

of those observed the days the ovens were in operation. This finding indicates that the mercury emission from the stack of the ovens is particularly noticeable.

The distribution of the mercury concentration in the air was also determined using the lidar remote sensing technique on days when ovens were in operation. The main obstacle encountered during the measurements was a frequently very large atmospheric attenuation at the resonance wavelength due to high mercury concentration. This leads to poor or no signal levels from scattering at longer distances and limit the useful range from lidar system positions close to the main sources. This was especially the case for measurements made from positions C and D (Fig. 1). Figure 3 shows an example of a 360° horizontal scan from position B during low wind conditions (<2 m s^{-1}). The height of the scan was 5–20 m above ground level depending on the topography. As can be seen, the maximum concentration is more than 1.2 μg m^{-3} and was once again located above the center of the village, as was also observed in the determinations made with point monitors. The isoconcentration lines are not closed due to the limited range of the lidar system in areas where high concentrations are present.

A second short measuring campaign was carried out between 14 and 17 February 1994 in the same area using only point monitors to evaluate the influence of the variation of meteorological conditions. The air temperature during the sampling was around 8–13°C. The observed mercury concentration values (Table 1) proved to be considerably lower than those made in September 1993. These lower levels are attributable both to a decrease in the mercury emission, due to lower ambient temperatures, from the roasted cinnabar (and other similar sources), and to the fact that the roasting ovens were shut down due to overproduction of mercury with respect to the market demand. In February 1994 higher mercury concentration values were measured at the sampling stations

Table 1. Atmospheric mercury concentrations (μg m^{-3}) and standard deviation measured at some sampling stations during the two field campaigns using the point monitors technique

ST	Hg (Sep. 93)	Hg (Feb 94)
3	0.245±0.020	0.694±0.065
4	0.122±0.012	0.063±0.004
5	0.031±0.004	0.025±0.002
6	0.054±0.005	0.211±0.019
8	0.353±0.039	0.032±0.004
9	5.064±0.350	0.804±0.078
11	5.132±0.229	1.203±0.098
13	0.455±0.048	0.115±0.010
15	0.243±0.021	0.014±0.002
23	0.284±0.021	0.033±0.003
25	0.342±0.038	0.012±0.001
26	1.022±0.088	0.032±0.002
28	0.122±0.016	0.011±0.001
29	0.441±0.038	0.012±0.003

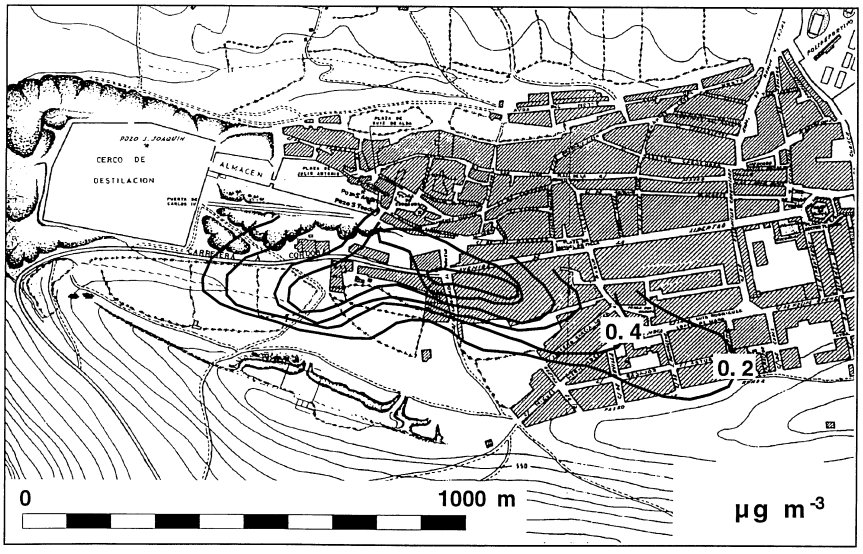

Fig. 3. Atmospheric mercury concentrations (μg m^{-3}) measured over the Almadén village, determined with the Lidar technique (September 1993).

3 and 6 which were downwind to the mercury complex while in September 1993 the same stations were upwind.

Total mercury flux

The main aim of the lidar measurements was to estimate the total flux of mercury into the atmosphere. During situations with winds stronger than 2 m s^{-1} and the plume more distributed and diluted it was possible to map the spreading plume in a vertical plane. This mapping could be combined with wind speed and direction to calculate the mercury flux. An example of such a measurement is shown in Fig. 4. This figure displays the concentration distribution in a vertical section over position E (Fig. 1) in the valley just outside and downwind from the village of Almadén. The topography under the vertical section is indicated in the figure. The lidar system was placed near the road at the lowest position in the valley and complete scans from one side over to the opposite side could be made, covering the air from a few meters above the ground and up. The main part of the plume is seen to follow the valley, with the highest concentrations in the lower parts. In Table 2 are given the hourly mean values of the deduced flux from two measurement periods at positions B and E (September 24–October 1, 1993) with all the ovens in operation. These hourly values are calculated from 3–4 individual lidar scans with a duration of 10–15 min each. The standard deviation for the individual scans was near 200 g h^{-1}, but similar mean values of the flux were obtained during the two periods, 723 and 784 g h^{-1}, respectively. The accuracy of the mean values is estimated at $\pm$ 25%, mostly due to difficulties in determining the speed and direction of the wind. There is also the possibility that a smaller part

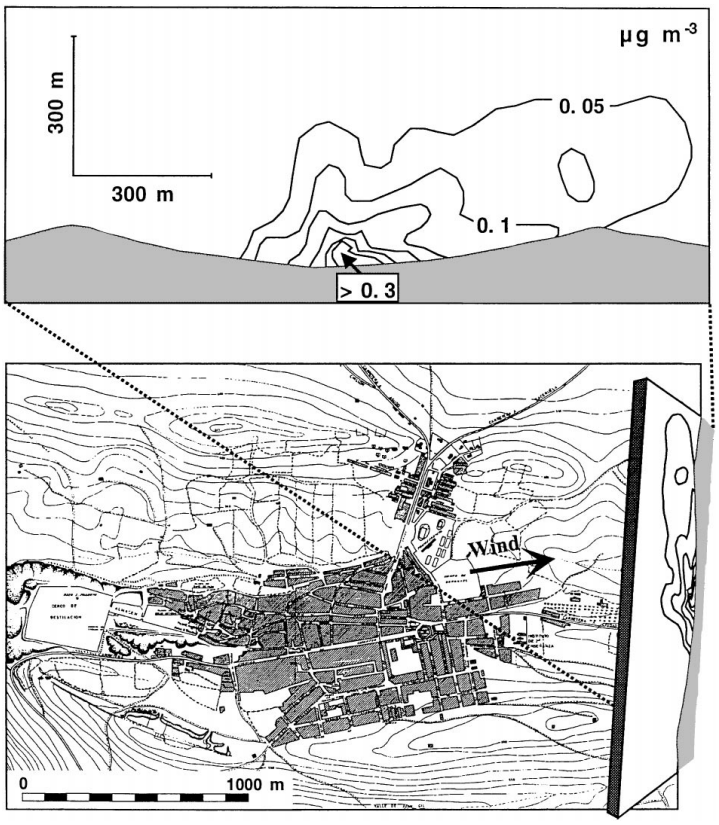

Fig. 4. Map of atmospheric mercury concentration of the spreading plume in a vertical section downwind from the Almadén village, measured with the Lidar technique (September 1993).

Table 2. Total atmospheric mercury fluxes, mean values and standard deviation determined with the Lidar technique

Sep. 24, 1993, position B		Oct. 1, 1993, position E	
Time (h)	Flux ($g\,h^{-1}$)	Time (h)	Flux ($g\,h^{-1}$)
12	787	16	688
13	625	17	737
14	757	18	896
15	735	19	879
18	709	20	718
Mean	723 ± 61	Mean	784 ± 97

of the plume might occasionally escape detection. This is due to the topography and the high concentration problem at position B and due to the distance to the main sources at position E. Thus, we estimate the total mercury flux to the atmosphere from Almadén to be in the range 600–1200 $g\,h^{-1}$ during this measurement periods. There are no local sources directly under the scanned section that could significantly influence the area-integrated concentration in the vertical section used for the flux calculations.

The values of mercury flux do not show any dependence on ambient temperature because, at the heights where the measurements were performed, the mercury levels are mainly due to the emission of the ovens stack. The mercury concentration due to the soil emission shows in fact a vertical gradient reaching background values a few meters above the ground (Ferrara *et. al*., 1992b). Several attempts were made with the lidar to differentiate the sources of the mercury flux. This proved to be difficult from the measurement positions due to the fact that all the main potentially emitting points are in close connection.

Flux from roasted cinnabar

With regard to determination of mercury emissions from the roasted cinnabar and the soil, this difficulty has been eliminated by using the chamber flux, a measuring technique that isolates a portion of the soil from the context of the other sources. Table III reports the values obtained in the stations indicated in Fig. 1 together with mercury concentrations in soils. The highest mercury flux levels were measured above the roasted cinnabar (100–400 $\mu g\,m^{-2}\,h^{-1}$), with values depending on the ambient temperature (23–38°C), and from the age of the bank. By considering the value of the surface area of the cinnabar banks, the mercury emissions is estimated to be in the range 30–120 $g\,h^{-1}$ in the meteorological conditions observed. This wide range of values can only give an indication of the magnitude of these emissions. Because of the large size of the area it would be necessary to make measurements on a great number of sampling stations.

Flux from soil

The determinations made on soils around the village of Almadén reveal rather high mercury degassing

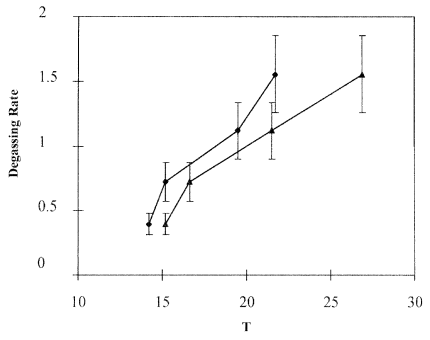

Fig. 5. Mercury degassing rate ($\mu g\,m^{-2}\,h^{-1}$) versus air (◆) and soil (▲) temperature (°C) measured in the sampling station no. 22 (September 1993).

Table 3. Mercury degassing rate (measured with the flux chamber), air temperature and mercury concentration in roasted cinnabar banks*(st. 2,11), soil close to Almaden (st. 22, 24, 28, 32), to El Entredicho open pit and to Alamillo

Station	Degassing rate ($\mu g\,m^{-2}\,h^{-1}$)	T air (°C)	Hg soil ($\mu g\,m^{-2}\,d\,w^{-1}$)
2	100	24	840*
11	150–400	23–28	710*
22	0.4–1.5	14–22	150
24	0.2–0.9	25–33	20
28	6.0	22	9
32	1.5–1.8	13–23	50
El Entredicho	1–2.5	23–28	220
Alamillo	0.1	25	0.6

rates (1.5–0.2 $\mu g\,m^{-2}\,h^{-1}$) that demonstrate how rich the surface soil is in the mineral, either naturally or by atmospheric deposition. Lindberg *et al.* (1979) using an agricultural surface soil collected in the Almadén district measured a rate of volatilization of elemental mercury of 0.3 $\mu g\,m^{-2}\,h^{-1}$ ($T = 25$°C) in a laboratory experiment. A typical trend of the flux as a function of air and soil temperature for sampling station no.22 is reported in Fig. 5. The relationship appears nearly linear because of the narrow range of temperature considered; generally the logarithmic relationship becomes evident at temperature higher than 30°C (Lindberg *et al*., 1979; Ferrara *et al*., 1997). Considering an area around the village of approximately 4 km^2, we obtain a mercury emission on the order of 0.8–6 $g\,h^{-1}$.

The degassing rate values measured near the "El Entredicho" open pit mine (1.0–2.5 $\mu g\,m^{-2}\,h^{-1}$) are particularly interesting since neither roasting and distillation plants nor roasted cinnabar are present in the area. These flux values are therefore attributable mainly to the metallic mercury contained in the rocks of this mine.

The flux value determined at the control station (Alamillo) proved to be approximately 0.1 $\mu g\,m^{-2}\,h^{-1}$ ($T = 25°C$), a value still particularly high if compared to the background values of non mineralized areas. Carpi and Lindberg (1996) found at two background field sites a mercury flux in direct sunlight of $1–2 \times 10^{-3}\ \mu g\,m^{-2}\,h^{-1}$ ($0–5 \times 10^{-3}\ \mu g\,m^{-2}\,h^{-1}$ in shaded conditions). Xiao *et al*. (1991) reported for a coniferous forest in Sweden values lower than $1 \times 10^{-3}\ \mu g\,m^{-2}\,h^{-1}$.

Flux from the ventilation systems

As described earlier, high mercury concentrations (5 $\mu g\,m^{-3}$) were observed close to the two ventilation systems of the Almadén mine. Inside the galleries of the near "Las Cuevas" mine, air mercury concentrations of around 100 $\mu g\,m^{-3}$ were determined. Assuming a similar concentration for the Almadén mines, and considering the flow rates of the ventilation systems, an estimated mercury emission of some 5–15 g h^{-1} for each system is obtained.

Flux from the refining complex

The ground around the cinnabar processing installations is highly contaminated both by visible drops of mercury and dust from the whole process. The air mercury concentration in this zone is generally over 20 $\mu g\,m^{-3}$, and the mine personnel wear special masks with active carbon filters. It was not possible to determine the mercury flux emitted from this area either with the lidar system or with flux chambers. However, it is interesting to consider that for an analogous plant on Mt. Amiata (Italy), abandoned about 15 years ago, a mercury flux of 60–100 g h^{-1} was determined in the month of July 1995 using the lidar technique (unpublished data). Considering the greater size of the Almadén plant with respect to that of Mt. Amiata, the generally higher ambient temperature and the still ongoing activity, a value of 100 g h^{-1} can be considered a lower limit for the mercury flux of the Spanish plant.

CONCLUSIONS

Despite the difficulties inherent in these kinds of determinations, we feel we have a fairly good picture of the main emission sources and their size. Using the remote sensing technique, a mean value of the total atmospheric mercury flux of approximately 750 g h^{-1} was determined above the village of Almadén (October 1). As said earlier, this value is surely lower than the real value in view of the problems created by the high mercury concentrations and the obstacles present in the study area (trees, buildings) which limit the system's range of action.

From an examination of the atmospheric mercury emission values reported in the preceding section it can be deduced that the possible mercury sources such as the roasted cinnabar banks, the soil around Almadén, the mine ventilation systems and the mine structures themselves contribute an average share on the order of 200 g h^{-1}. More than 550 g h^{-1} are therefore due to the emissions from the roasting oven stack, a value in good agreement with the value furnished by the laboratory of the Minas de Almaden y Arrayanes (1000 g h^{-1} with all the ovens in operation). This emission is therefore far greater than all the others, even though it must be kept in mind that the others are at ground level where men work and where the metal interacts with the biota. The total mercury flux from the Almadén district represents around 0.1% of the modern global anthropogenic emission rate (Hudson *et al*., 1995).

The particular orography of the site and the direction of the prevailing winds during the summer and autumn months favor the occurrence of high mercury concentrations above the village of Almadén, where values have often been found to be on the order of 1 $\mu g\,m^{-3}$. Even at a considerable distance from the main emission sources (5–10 km) in an easterly direction, high air mercury levels (0.05–0.1 $\mu g\,m^{-3}$) were observed.

The high atmospheric mercury concentrations generally observed in the Almadén district are in agreement with what was reported by Huckabee *et al*. (1983) on the mercury distribution in the vegetation of this area. These authors found that all mercury concentrations in plants during their study greatly exceeded most other values reported for other highly mineralized areas (Byrne and Kosta, 1970). We obtained similar results on the plants collected during the 1993–1994 campaign (Maserti *et al*., 1996).

Particularly interesting are the mercury degassing rate values observed at the open pit "El Entredicho", mainly due to the presence of elemental mercury in the ore. The emission values observed by us in the Alamillo control area, higher than the background values for non mineralized areas, find confirmation in the same work by Huckabee, where it is reported that also the lowest mercury concentrations in woody plants collected in a circular area within a 20 km radius from Almadén were at least ten times greater than the background levels.

Acknowledgements—The authors wish to thank Dr Angel Arredondo, director of the Minas de Almaden y Arrayanes, for logistical support and assistance during the measurement campaigns.

REFERENCES

Byrne, A. R. and Kosta, L. (1970) Studies on the distribution and uptake of mercury in the area of the mercury mine at Idrija, Slovenia (Yugoslavia). *Vesta. Slov. Kem. Drus.* **17**, 11–18.

Carpi, A. and Lindberg, S. E. (1996) Mercury emission from background and municipal sewage sludge amended soil In eds. R. Ebinghaus, G. Petersen, U. V. Tumpling, *4th International Conference on Mercury as a Global Pollutant*.

Book of Abstract, Hamburg August 4–8, 1996, pp. 460 GKSS Forschungszentrum Geesthacht-GmbH, Max Planck-Str., D-21502 Geesthacht, Germany.

Edner, H., Fredriksson, K., Sunesson, A., Svanberg, S., Uneus, L. and Wendt, W. (1987) Mobile remote sensing system for atmospheric monitoring. *Applied Optics* **26**, 4330–4338.

Edner, H., Faris, G. W., Sunesson, A. and Svanberg, S. (1989) Atmospheric atomic mercury monitoring using differential absorption lidar technics, *Applied Optics* **28**, 921–930.

Edner, H., Ragnarson, P., Svanberg, S., Wallinder, E., De Liso, A., Ferrara, R. and Maserti, B.E. (1992) Differential absorption lidar mapping of atmospheric atomic mercury in Italian geothermal fields. *Journal of Geophysical Research* **97**, 3779–3786.

Edner, H., Ragnarson, P., Svanberg, S., Wallinder, E., Ferrara, R., Maserti, B. E. and Bargagli, R. (1993) Atmospheric mercury mapping in a cinnabar mining area, Science of the Total Environment **133**, 1–15.

EPRI Expert Panel (1994) Mercury Atmospheric Processes: A Synthesis Report *Electric Power Research Institute*, Palo Alto, California, USA. Report No. TR-104214.

Ferrara, R., Maserti, B. E., Edner, H., Ragnarson, P., Svanberg, S. and Wallinder, E. (1991) Atmospheric mercury determinations by lidar and point monitors in environmental studies. In *Metal Compounds in Environment and Life*, *Vol.* 4 eds. E. Merian and W. Haerdi. Science and Technology Letters, U K.

Ferrara, R., Maserti, B. E., Edner, H., Ragnarson, P., Svanberg, S. and Wallinder, E. (1992a) Mercury emissions into the atmosphere from a chlor-alkali complex measured with the lidar technique. *Atmospheric Environment* **A26**, 1253–1258.

Ferrara, R., Maserti, B. E., De Liso, A., Edner, H., Ragnarson, P., Svanberg, S. and Wallinder, E. (1992b) Vertical profiles of atmospheric mercury concentration. *Environmental Technology* **13**, 1061–1068.

Ferrara, R., Maserti, B. E., Andersson, M., Edner, H., Ragnarson, P., Svanberg, S. (1997) Mercury degassing rate from mineralized areas in the Mediterranean basin. *Water, Air and Soil Pollution* **93**, 59–66.

Griepink, B. and Muntau, H. (1988) BCR Information-Reference Material. Commission of the European Communities Report EUR 11850 EN, 49–65.

Hildebrand, S. G., Huckabee, J. W., Sanz Diaz, F., Jansen, S. A., Solomon, J. A. and Kumar, K. D. (1980) Distribution of mercury in the environment at Almaden, Spain. *Oak Ridge*, *Tennessee*, *Oak Ridge National Laboratory*, ORNL/TM-7446.

Huckabee, J. W., Sanz Diaz, F., Jansen, S. A. and Solomon, J. (1983) Distribution of mercury in vegetation at Almaden, Spain. *Environmental Pollution* (*Series A*) **30**, 211–224.

Hudson, R. J. M., Gherini, S. A., Fitzgerald, W. F. and Porcella, D. B. (1995) Anthropogenic influences on the global mercury cycle: a model-based analysis. *Water, Air and Soil Pollution* **80**, 265–272.

Lindberg, S. E., Jackson, D. R., Huckabee, J. W., Jansen, S. A., Levin, M. J. and Lund, J. R. (1979) Atmospheric emission and plant uptake of mercury from agricultural soils near the Almaden mine. *Journal of Environmental Quality* **8**, 572–578.

Maserti, B. E., Ferrara, R., Panichi, M. A. and Storni, M. (1996). Mercury concentrations in plants and soils of the cinnabar mineralized area of Almaden (Spain). In: *4th International Conference on Mercury as a Global Pollutant*. Book of Abstract, eds. R. Ebinghaus, G. Petersen, U. V. Tumpling, Hamburg August 4–8, 1996, p. 140. (GKSS Forschungszentrum Geesthacht-GmbH, Max Planck-Str., D-21502 Geesthacht, Germany).

Ortega Girones, E. and Hernandez Sobrino, A. (1992) The mercury deposits of the Almaden syncline, Spain. *Chron. Rech. Min.* **506**, 3–24.

Xiao, Z. F., Munthe, J., Schroeder, W.H. and Lindqvist, O. (1991) Vertical fluxes of volatile mercury over forest soil and lake surfaces in Sweden. *Tellus* **43B**, 267–279.

Paper V

Remote monitoring of industrial emissions by combination of lidar and plume velocity measurements

P. Weibring, M. Andersson, H. Edner and S. Svanberg.
Appl. Phys. B **66**, 383–388 (1998).

Appl. Phys. B 66, 383–388 (1998)

Applied Physics B
Lasers
and Optics

Remote monitoring of industrial emissions by combination of lidar and plume velocity measurements

P. Weibring, M. Andersson, H. Edner, S. Svanberg

Department of Physics, Lund Institute of Technology, P.O. Box 118, S-221 00 Lund, Sweden
(Fax +46-46/2224250, E-mail: Petter@fysik.lth.se)

Received: 21 April 1997/Revised version: 28 July 1997

Abstract. We describe a new method for gas flux measurements that is a combination of differential absorption lidar (DIAL) and wind videography. The wind speed was measured by an imaging method that calculates the horizontal displacement of the plume with cross-correlation techniques. High spatial and temporal resolution is achieved with histogram equalization and window-filtering techniques. Simultaneous measurements of the distance, the direction of the plume and the integrated concentration were provided through the lidar measurements. Alternative methods of measuring the wind speed at different heights have been used to validate the precision and accuracy of the new method for different geometrical configurations. An example of remote SO_2 flux measurements from a pulp and paper mill is presented, which shows a very good correlation with in situ measurements taken at the source.

PACS: 86.70 L

Today, most industrial plants are obligated to measure their own emissions. Accurate measurements of the concentration and the flux of different gases are important, not only from an environmental point of view, but also for economical reasons, since a part of taxation may be dependent on the emission values. Different types of in situ instruments are frequently used to monitor the main emission sources, but external optical methods are becoming increasingly important. The advantages with optical methods are online evaluation of the measurement, no contamination of samples and the possibility of measuring large areas [1]. The remote sensing capability is also very useful in measurement of the total fluxes including diffuse emissions. These techniques might be successfully employed in unannounced inspections by controlling agencies.

In the differential absorption lidar (DIAL) technique, a narrowband laser is alternately tuned on and off an absorption line of the species of interest. With time-resolved detection techniques and beam steering control, a concentration cross section of an industrial plume can be generated. A concentration accuracy of $\leq 10\%$ can be achieved, by repeatedly scanning the plume cross section, calculating the area-integrated total concentration and by taking the total variance into account. The total flux is calculated by multiplying the current wind speed at the measurement point and the total concentration [2, 3]. The flux accuracy is often limited to 10–40%, because of the lack of accurate wind data at the correct height close to the measured cross section and the lack of matching time-resolution in the wind measurement.

The wind field can be measured by using wind anemometers mounted on a tall mast. However, since the main industrial emission often comes from an approximately 100-m-tall smokestack, it is difficult to reach high enough. The mast often has to be placed in a different location from where the concentration is measured. This can cause large uncertainties in the deduced wind speed and, consequently, large errors in the estimated flux. Mathematical wind profile models can sometimes be used to estimate the wind speed at other heights, differing from that where the wind anemometer is positioned. The drawbacks of these models are that they require ideal conditions, otherwise their predictions are more uncertain. In an industrial area there are usually a lot of buildings, which causes large inhomogenities in the wind profile, and thus the profiles are difficult to model. Another way of measuring the wind profile is to use a secondary laser system for measuring the aerosol pattern movement or the Doppler shift [4, 5]. These methods give accurate results, but normally require a second expensive and complex piece of laser equipment. In principle, it should be possible to use the same laser setup for both DIAL and wind measurement, but since the best geometry and directions are different, this is difficult in practice. The measurements also have to be time-shared between the two modes, and simultaneous monitoring of the concentration distribution and wind field is not possible. A third way is to use sodar that uses sound waves and the Doppler principle to measure the wind profile. The sodar technique also often requires bulky extra equipment.

We propose a new, simple and inexpensive wind speed measurement method, based on an ordinary video or CCD camera, which could be easily incorporated into an existing lidar system. The camera is pointed at the most visible part of

the plume, taking snapshots of the irregular structure, while the laser is repeatedly scanning the plume cross section, at an optimal position along the plume, for concentration measurements. The wind speed is estimated by measuring the displacement of the plume structure between two snapshots [6]. This technique, combined with wind direction and concentration measurements by the laser, gives the total flux. The variances of the area-integrated concentration and the wind speed are both taken into account to calculate the accuracy in the flux measurement. A mobile lidar system was upgraded with the equipment described above, and the technique was tested at a pulp mill, where alternative methods of measuring the wind speed at different heights were used to validate the precision and accuracy of the new method.

1 Measurement methodology

To estimate the flux in an industrial plume, the concentration, the wind speed, and the wind direction must be measured in an accurate way. Here we propose an integrated method to determine all parameters required to calculate the total flux and the variance. The technique combines wind speed measurement by using a CCD camera, and concentration and wind direction estimation by DIAL techniques. The camera is pointed at the most visible part of the plume, while the laser is repeatedly scanning the plume cross section at another position nearby, further downwind. The wind speed is estimated by taking the horizontal cross-correlation between two sequential images, given their time separation and the distance to the plume. The wind direction is calculated by measuring the distance to the source and the plume centre at the lidar scanning position and the angle between these directions.

We introduce a polar coordinate system with origin at the position of the measurement system; see Fig. 1. The compensation angles ϕ, θ, and the distance r_3 are determined by measuring the distance r_1 to the smokestack, the distance r_2 to the plume centre, and the angles α, β. If the concentration cross section is not measured perpendicularly to the wind direction, the measured total area-integrated concentration C_m has to be compensated with a factor $\sin\phi$ to evaluate the true concentration value C_c. Here we assume that the divergence of the plume is uniform and small, compared to the distance between the measurement system and the plume.

The wind speed component measured by the CCD camera is perpendicular to the direction of the camera. Thus, only when $\theta = 90°$, is the wind speed component in the wind direction correctly measured. The wind speed estimation is also dependent on the distance r_3, because of scaling effects. Therefore, we compensate the pixel movement, V_pix in the images with both an angle and a distance factor, $r_3/\sin\theta$, to get the true wind speed V_c. Combining the above expressions for wind speed and concentration gives the estimated total flux $\hat{F}_\mathrm{C}$ for a single sweep:

$$\hat{F}_\mathrm{C} = \frac{K\hat{C}_\mathrm{m}\sin\phi\hat{V}_\mathrm{pix}r_3}{\sin\theta} = \hat{C}_\mathrm{c}\hat{V}_\mathrm{c}, \tag{1}$$

where K is a calibration factor, depending on the camera focal length and the pixel size, $\hat{V}_\mathrm{pix}$ is the estimated mean pixel movement during the sweep time and $\hat{C}_\mathrm{c}$ and $\hat{V}_\mathrm{c}$ estimates of the true concentration and mean wind speed. If we assume independent estimates of the concentration and the mean wind speed, the estimated standard deviation of the total flux in a single sweep is given by

$$\sigma_{\hat{F}_\mathrm{c}} = \sqrt{(\sigma_\mathrm{V}^2\hat{C}_\mathrm{c}^2 + \sigma_\mathrm{C}^2\hat{V}_\mathrm{c}^2 + \sigma_\mathrm{V}^2\sigma_\mathrm{C}^2)} \tag{2}$$

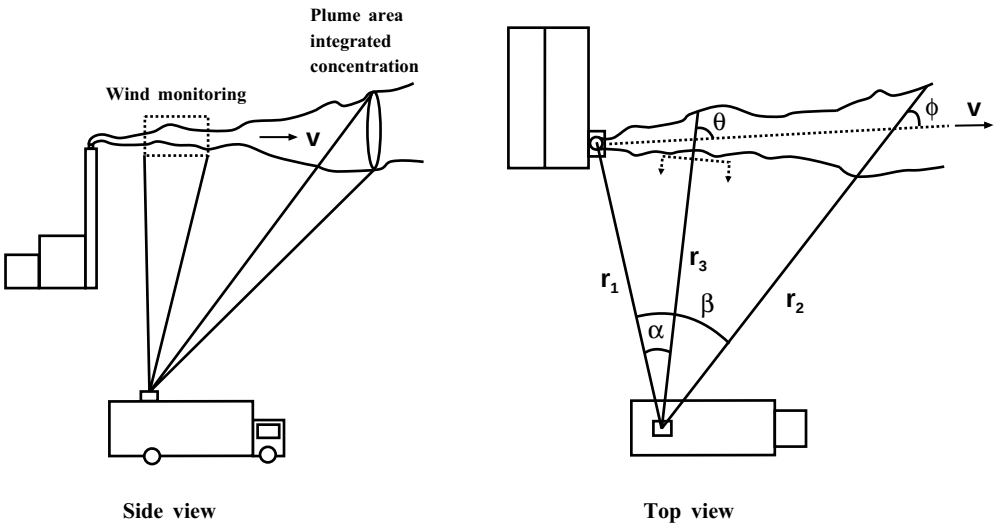

Fig. 1. Schematic of measurement arrangement

where σ_V^2 is the estimated total variance in the wind speed during the sweep time and σ_C^2 is the estimated variance in the area-integrated concentration of a sweep [7]. Note that σ_V^2 might be underestimated because we have assumed the wind observations to be independent observations.

The CCD camera is connected to a frame grabber, which takes snapshots of the plume at certain time intervals. In Fig. 2, two sequential snapshots are shown. The contrast in the images is enhanced by using histogram equalisation techniques. This technique makes a histogram of the different contrast levels in the image and then uses a transformation function, equal to the cumulative grey-level distribution, producing a new image with a uniform density. Thus the contrast is raised. The intensity distribution in the columns is then summed, building an array representing the cumulative image intensity as a function of the horizontal position. Two sequential intensity arrays are cross-correlated generating the cross-correlation array. Finding the highest cross-correlation value gives the displacement of the horizontal intensity distribution between the images. It is necessary to subtract the background, because of an intensity offset that contributes to the major intensity distribution and reduces the sensitivity of the cross-correlation. The background is calculated as the dc component of the intensity distribution in the image.

Between two sequential snapshots, a new part of the plume has entered the camera view, and another part has left. This border effect is effectively eliminated by using window techniques, with more weight on the central part of the images. Several types of windows have been tested and the smooth variants (Hanning) proved to have the best shape, removing most of the artefacts.

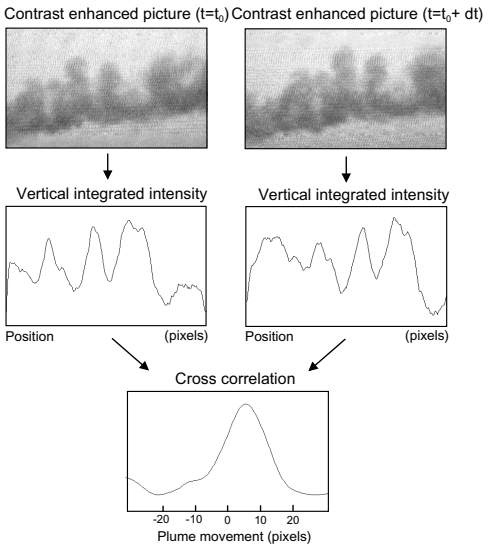

Fig. 2. Example of plume velocity measurement using image correlation techniques

This measurement scheme works well if there is a uniform intensity distribution in the background, which is usually the case for plumes with the sky as background. When there is a high contrast in the background, for example due to stationary buildings or smokestacks, the cross-correlation can be affected. It is then necessary to subtract not only the dc component of the background in every image, but also the intensity distributions from stationary objects to eliminate the artefacts. Instead of cross-correlating the intensity distribution from images taken at time t and $t - \mathrm{d}t$, we subtract the intensity distribution from the image taken at time t from that for the image taken at time $t - \mathrm{d}t$. The difference in the intensity distribution is then cross-correlated with the intensity distribution difference from images at $t + \mathrm{d}t$ and t, giving the correct cross-correlation value.

In some cases with unfavourable light conditions, for example, highly illuminated moving clouds in the background, a major contribution to the intensity distribution will still occur, causing large artefacts. To eliminate even more of the occasional background artefacts, a large number of displacements are calculated during one minute. The displacement values are median-filtered, thus removing occasional differing values, and then averaged, giving a mean value and the variance of the displacement during the last minute. Since the time interval between the snapshots and the distance to the plume are known, the displacement can be converted to the actual wind speed. The time intervals are chosen to minimise the relative variance. If the time interval is too long, the shape of the plume has changed too much, causing an incorrect cross-correlation value. If the time interval is too short, the displacement is only a few pixels on the CCD, which is not enough for good accuracy.

2 Experimental setup

The field experiment was carried out during late November 1996 at a pulp and paper mill in the south of Sweden. The weather was unsettled with occasional snowfalls and the temperature was around 0 °C; the wind changed in both direction and speed. The SO_2 emission from the pulp mill comes mainly from spent liquor, and combustion of oil and tree bark, and it is emitted from two 90-m-high smokestacks. The plume has a high content of water vapour, which makes it clearly visible.

The lidar system was positioned at two different locations in the outer part of the pulp mill industrial area in order to study the effects of different camera angles in relation to the plume direction; see Fig. 3, positions A and B. The distances to the main smokestacks were 900 m and 1000 m, respectively. Three wind speed anemometers were used to validate the camera method. The anemometers were situated at three different locations; on the lidar system at a height of 5 m, on a mast, position C, at a height of 15 m, and on a horizontal beam, extending 3 m sidewise from the top of one of the main smokestacks, position D, at a height of 90 m.

The mobile lidar system is installed in a rebuilt Volvo F610 truck, containing all the necessary equipment and powered by a trailer-mounted motor generator [2, 3]. The laser transmitter is a frequency-doubled Nd:YAG-pumped dye laser, which is equipped with a dual-wavelength unit, enabling the laser to be tuned alternately at two different

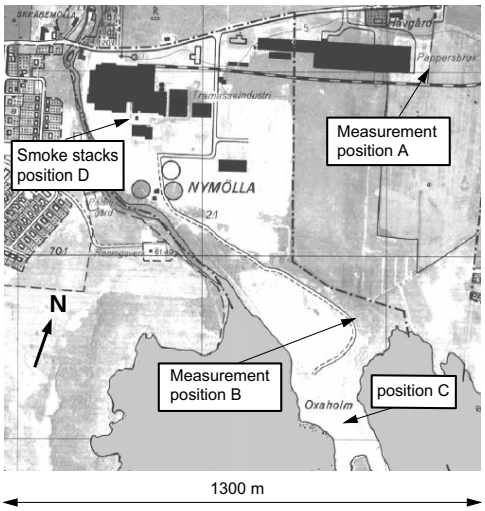

Fig. 3. Map of monitoring positions at the pulp and paper mill

wavelengths. The on and off wavelengths in DIAL measurements of SO_2 are 300.02 nm and 299.30 nm, respectively. The outgoing laser beam is directed coaxially with a vertically mounted telescope and transmitted into the atmosphere via a steerable flat mirror. The system has been recently upgraded with new software based on the LabVIEW platform which allows online control and evaluation of the measurement [8].

The camera wind speed measurement system consists of an ordinary black and white CCD camera, a frame grabber, and a computer controlled by the LabVIEW software. The system makes a plume velocity measurement approximately every other second, depending on the displacement of the plume structure. Averages of the wind speed over a period of 1 min are calculated and saved on a local hard disk together with its variances for later analysis. Data are also sent through the local network to the control computer for storage together with the concentration measurements. The wind speed measurement validation equipment consists of a LabVIEW-controlled computer with a plug-in board and propeller anemometer, specially positioned at the lidar system (positions A, B) and at the top of the smokestack (position D), with an accuracy of $\leq 3\%$. Approximately 30 wind speed measurements were made each minute. The minute average of the wind speed was calculated and saved on a local hard disk together with its variance. Because of the inaccessibility of the latter system, it was equipped with an auto start-up feature and file recovery functions in case of power failure. At position C, the wind speed equipment was controlled by the plant and it also produced minute averages of the wind speed.

The camera system was calibrated by imaging an object of known size, and by counting the number of corresponding pixels seen by the camera at different distances and zoom settings. The accuracy of the method was validated in the laboratory during measurements on moving objects with known speeds, and was found to be within 3%. The direction for lidar measurement of the SO_2 concentration in the plume was chosen so that the aerosol load in the plume was low enough to allow the laser beam to penetrate through the complete plume. The CCD camera was directed at a high-contrast region of the plume with a heavier aerosol load. This was located near the smokestack outlet, but not so close that the measurement could have been affected by the vertical component of the velocity of the emerging plume. For every lidar sweep cross section of the plume, which took a few minutes, a new wind direction was calculated. During the sweep time the mean wind speed and the variance of the wind speed were calculated and combined with the area-integrated concentration, to give the mean value and variance of the total flux.

3 Results

In order to validate the videography method for wind measurements, the results were compared with data from the different anemometers during longer runs. A comparison of the results during one night (lidar position A) is shown in Fig. 4. During the measurement period, a very good agreement between the camera measurements and the wind anemometer measurements at the top of the smokestack was usually achieved. At certain times some deviations can be seen. These are caused mainly by visibility problems arising from the occasional release of smoke or steam from the nearer factory buildings, or temporary intense snowfall. The effect of these moving objects hides the real plume or temporarily interferes with the displacement measurements. As long as these effects are on a short-time basis (less than a minute at a time) they can be corrected for as deviations from the minute trend. Long-time deviations cannot be corrected for, but can be excluded as artefacts by checking the variance. At local times 0400, 0500 and 0700, the variance was 10–30 times larger than at other times. In Fig. 5, a cross-correlation between the camera and the smokestack measurement is shown for this and additional periods during two days (lidar position A and B). The slope is 1.04 and the intersection with the camera axis is displaced by -0.3 m/s from the origin and the mean-square error is 0.83. Some data have been excluded because of an unfavorable position of the anemometer on the leeward side of the smokestack for certain wind directions.

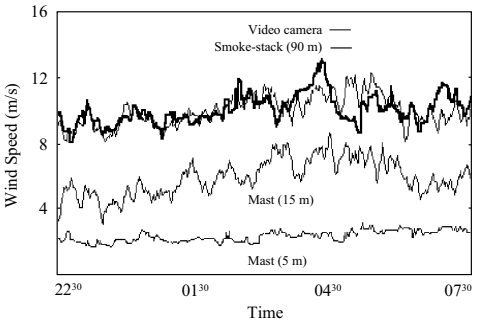

Fig. 4. Comparison between the camera method and wind anemometers at different heights during one night

The influence of the angular difference between the camera line of sight and the plume direction was examined in the range 0–90°. The standard deviation was low (≤ 10%) for angles between 30° and 90°, but for angles under 30° it increased rapidly to more than a few hundred percent. At small angles, it is difficult to identify and extract a moving structure and, where it is possible, the horizontal displacement of the plume is only a few pixels. The pixel movement/displacement is divided by $\sin\theta$, which decreases rapidly for small angles. These factors cause large errors in the determination of the wind speed. The erratic values are, however, easily identified because of their large variance. The problem with small angles causes even larger errors in the concentration and wind direction determination with the laser, and, therefore, the problem described above is not considered to be any limitation in the measurement arrangement.

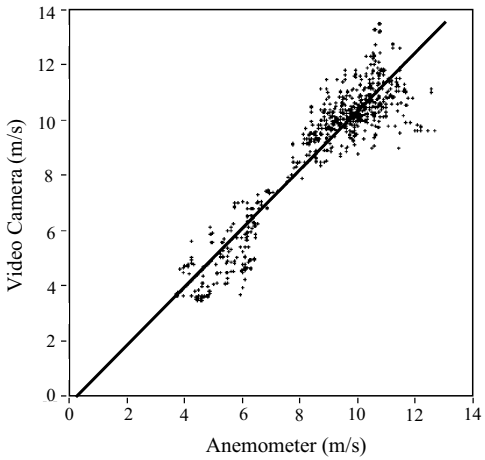

Fig. 5. Correlation between data from the camera method and the wind anemometer at the smokestack

By using wind anemometer data at the heights of 5 m and 15 m, an estimation of the wind speed at a height of 90 m can be made with a power-law-dependence calculation, with the formula $v_1/v_2 = (h_1/h_2)^{\alpha}$. This calculation gives large wind-speed errors ranging from 30% to 500%, depending on both the location of the lidar system site and the wind direction. Comparisons between different locations of the wind anemometer placed at the lidar system showed that the main cause for errors was not the distance between the wind anemometers at points A and C, or B and C, but the interactions between the wind field at low altitude and the surroundings of the lidar wind anemometer. Thus the surrounding buildings and near forest, at position A, in combination with a northerly wind, gave the largest deviations (∼ 500%). The power-law model overestimated the calculated wind speed

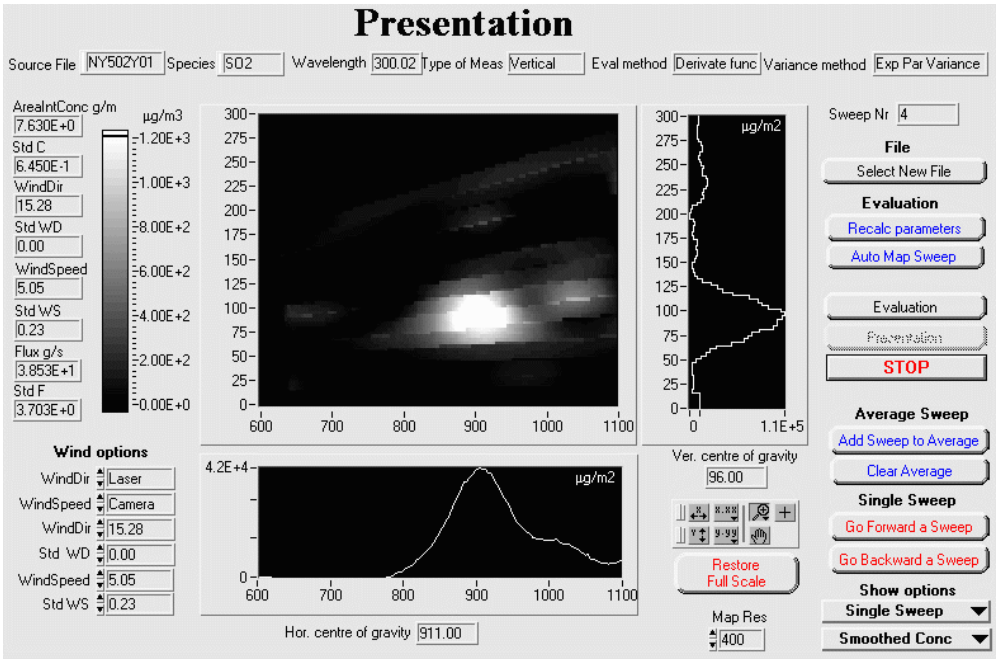

Fig. 6. Presentation of a SO_2 flux measurement

because of too-low, erratic wind speed measurements at the lowest wind anemometer. The most accurate results were achieved at both measurement points A and B, when the wind came from the sea in the south, unaffected by the surroundings influencing the wind anemometers. The mean deviation under these conditions was in the range of 30–40%. A comparison between the camera wind speed and the power-law-estimated wind speed showed that the camera method increases the accuracy of the wind speed measurement for our setup by 4–50 times, depending on the wind direction.

An example of a SO_2 flux measurement and the online evaluation menu is shown in Fig. 6. The plume scan time is around 4 min and consists of 10 measurement directions, which are individually evaluated with locally weighted least-squares kernel regression [7]. The concentrations in the different directions are then Rieman-summed in a polar coordinate system to give the area-integrated concentration. The variance of the area-integrated concentration is calculated in a similar way, by assuming independent estimates of the concentrations in the different directions. The concentration profiles in the different directions are interpolated with a bilinear method and converted to an $x - y$ coordinate system and the results are presented as a concentration map in the main diagram. Below and beside the map, two graphs displaying the vertically and horizontally integrated concentrations are shown. The input source for the wind speed can be selected from the camera, the external wind anemometer, or the keyboard. Similarly, the wind direction can be based on laser distance measurements, external wind direction meter, or a keyboard input. The mean wind speed, measured with the camera, during a single scan is multiplied by the area-integrated concentration giving the total flux in g/s. The flux is then compensated for the laser-measured wind direction. This particular measurement gave a SO_2 flux of 139 kg/h with a standard deviation of 13 kg/h, which was in good agreement with the in-stack monitoring result of 143 kg/h, made by the industry. The in situ concentration measurements were performed with a UV instrument, with an accuracy of $\leq 3\%$, and the total flux was estimated by multiplying the concentration by a calculated gas flow.

4 Conclusion

We have described a new method for wind speed measurement that can be used preferably in combination with lidar when measuring fluxes of industrial emissions. Comparison with in situ wind anemometers shows that the lidar/camera method gives a high accuracy in determining the wind field near the concentration measurement position. A more accurate estimation of the flux value is achieved with estimates of the variances, for both the area-integrated concentration and the wind field. In the measurements presented here, we have used a rather simple correlation technique for the wind velocity determinations. With more advanced image-processing techniques, it should be possible to improve the method further and overcome some limitations.

The advantages of the lidar/camera method compared with other wind speed methods are the remote measurement of the plume speed at the correct height and location, and the volume integration, which eliminates the influence of fast, local variations in the wind field. The time resolution can be matched to the time resolution of the concentration measurement. It is a simple, inexpensive method, which can easily be integrated in an existing lidar system and, where this is done, existing surveillance cameras can be used. The system start-up time is decreased because there is less work in mounting anemometers and erecting masts. All measurements can be made at long distances, which means that the lidar system can be located outside an industrial area for surveillance measurements. Simultaneous measurements of plume velocities at different heights can be accomplished by dividing the camera picture into different sections and performing a separate calculation of the plume displacement in every section.

A possible drawback is that the plume must be visible. However, it should be possible to enhance the structure for weak plumes, even if they are merely visible to the eye. This could be done if the difference in intensity is resolved by the camera. Possibly, an IR camera can further enhance the measurement capability. If the plume is extended in height, with no structures present, and the wind field is inhomogeneous, there will be the same difficulties as occur with wind anemometers in modeling the wind speed between the upper and lower parts of the plume. Diffuse emissions are not always correlated with visible plume structures, which makes the camera method difficult. They are also close to the ground and therefore a wind anemometer at the lidar system is most suitable.

The camera method can also be used in combination with passive concentrations methods, for instance the Fourier transform method [5]. A drawback is that distance and wind direction cannot be easily attained.

Acknowledgements. This work was supported by the Swedish Space Board. We want to thank Stora Nymölla AB, especially Anders Wetterling and Hans Lindström, for assistance in the field validation at the Nymölla pulp and paper mill. We also want to thank Ulla Holst at the Department of Mathematical Statistics and Gunnar Sparr at the Department of Mathematics, Lund University.

References

1. M.W. Sigrist: In *Air Monitoring by Spectroscopic Techniques*, Chemical Analysis Volume 127 (Wiley, New York 1994)
2. H. Edner, K. Fredriksson, A. Sunesson, S. Svanberg, L. Unéus, W. Wendt: Appl. Opt. **26**, 4330 (1987)
3. H. Edner, P. Ragnarsson, E. Wallinder: Environ. Sci. Tech. **29**, 330 (1994)
4. I. Matsui, N. Sugimoto, Y. Sasano, H. Shimizu: Jpn. J. Appl. Phys. **29**, 441 (1990)
5. Ch. Werner, R. Haus, F. Köpp, K. Schäfer: App. Phys. B **61**, 249 (1995)
6. K. Amnehagen, G. Sandberg: Lund Reports on Atomic Physics LRAP-173 (Lund Institute of Technology, Lund 1994)
7. U. Holst, O. Hössjer, C. Björklund, P. Ragnarsson, H. Edner: Environmetrics **7**, 401 (1996)
8. M. Andersson, P. Weibring: Lund Reports on Atomic Physics LRAP-201 (Lund Institute of Technology, Lund 1996)

Paper VI

Studies of gas exchange in fruits using laser spectroscopic techniques

L. Persson, B. Anderson, M. Andersson, M. Sjöholm, and S. Svanberg.

Proceedings of FRUITIC 05, Information and Technology for Sustainable Fruits and Vegetable Production., 543–552, Montpellier, France (September 2005).

Information and Technology for Sustainable Fruit and Vegetable Production
FRUTIC 05, 12 – 16 September 2005, Montpellier France

Studies of Gas Exchange in Fruits Using Laser Spectroscopic Techniques

Linda Persson, Benjamin Anderson[1], Mats Andersson,
Mikael Sjöholm, and Sune Svanberg

Atomic Physics Division, Lund Institute of Technology, P.O. Box 118,
SE-221 00 Lund, Sweden

[1]Permanent address: LAFOC, University of Cape Coast, Ghana

Keywords: Diode laser spectroscopy, GASMAS, food packaging, gas exchange, oxygen, apple, avocado, orange

Abstract

Non-intrusive, *in-vivo*, real-time measurements of oxygen contents and oxygen diffusion in fruits using a laser spectroscopic technique are presented, where the narrow absorption features due to the free gas in pores in the fruits are observed. The technique is referred to as gas in scattering media absorption spectroscopy (GASMAS), and is performed using tunable diode lasers. In particular, assessment of oxygen transport in apples and oranges is demonstrated. To illustrate the possibility to use the technique for studies of modified atmosphere packaging processes, measurements on sealed horticultural produces were performed. Furthermore, preliminary studies of avocados concerning the possibility to non-intrusively determine the maturity of fruits are presented. This technique has substantial potential for the development of compact devices providing new types of information in postharvest fruit management.

INTRODUCTION

Assessment of free gas in porous materials is of considerable interest in several environmental, biological and medical processes. In the present paper a novel application of a laser spectroscopic technique to the study of gas exchange in porous agricultural products, in particular fruits, is discussed. Although any gas with absorption lines in reach of tunable diode laser sources can be probed by the technique, we here focus on biologically active molecular oxygen, whose concentration is of crucial importance for the ripening process and the quality of fruits. An overview of the influence of oxygen and carbon dioxide partial pressures on selected phenomena affecting fruit and vegetable quality has been given by, e.g., Beaudry (1999).

A common way to analyse gases *in situ* is to use absorption spectroscopy that employs a sufficiently narrow-band light source in combination with the Beer-Lambertian law. However, in porous materials the radiation is heavily scattered, which results in an enhanced average absorption path length compared to the geometrical dimensions of the sample. One approach to measure non-gaseous constituents in scattering media is to use time-resolved spectroscopy employing laser-produced white light; for a recent report, see Abrahamsson et al. (2005). This type of setup was recently used for studies on apples

(Cauchard et al., 2005). The spectral resolution needed in such systems is relatively low since solid materials and liquids have broad absorption features with linewidths normally not sharper than 10 nm, while free gases typically have a linewidth 10000 times sharper (Sigrist, 1994). Thus, the small and narrow absorption imprint in the emerging, multiply scattered diffuse light due to the gas can not be detected with such systems. However, by using single-mode continuous-wave lasers combined with modulation techniques the gas can be detected sensitively, without disturbance from the broader absorption features of the bulk material. In particular, diode lasers are highly suitable for sensitive absorption spectroscopy with high spectral resolution due to their availability in different wavelength ranges, uncomplicated wavelength tunability, and their relatively low cost compared to other laser sources. This methodology to study free gas embedded in scattering materials has been denoted GASMAS (gas in scattering media absorption spectroscopy) (Sjöholm et al., 2001; Somesfalean et al., 2002).

Measurements of molecular oxygen in wood have been performed in order to illustrate the influence of the density and anisotropy of the sample on the GASMAS signal (Alnis et al., 2003). Recently, studies of gas exchange in fruits, in particular apples, have been reported (Persson et al., 2005). The gas contents in the scattering medium gives rise to a signal of a certain strength, which is determined by the gas concentration as well as the average path length travelled by the light in the scattering medium. The latter quantity can be determined by time-resolved measurements allowing the true concentration to be determined (Somesfalean et al., 2002). In particular, transport of gas through the porous medium can be studied. Here, the sample is first exposed to a gas environmental anomaly; it may be placed for a few hours in a sealed plastic bag first flushed with pure nitrogen gas. Then, the sample is placed in the GASMAS setup and the time evolution of the atmospheric oxygen re-invasion is measured spectroscopically. Such gas transport in apples was first studied by Persson et al. (2005) in transillumination geometry, and is further investigated in the present paper in a more practical backscattering geometry. The technique presented may have powerful applications in the study of fruit physiology, controlled atmosphere (CA) storage and modified atmosphere packaging (MAP) performance.

EXPERIMENTAL PROCEDURE

Experimental arrangements for GASMAS measurements are shown in Figs 1 and 2a. The optics and electronics used are similar in the two arrangements and have been described more in detail by Persson et al. (2005). Two measurement geometries have been used; transillumination (Fig. 1) and backscattering (Fig. 2a). The spectroscopic light source used was a diode laser, Sharp LT031MDO, with a nominal output power of 7 mW. The wavelength of the diode laser was scanned by ramping the driving current at a repetition rate of 4 Hz across the R7R7 molecular oxygen line, which is situated at 761.003 nm (vacuum wavelength). Additionally, sinusoidal modulation of about 9 kHz was superimposed on the diode laser injection current to achieve a wavelength modulation of the light allowing sensitive wavelength modulation spectroscopy (WMS) using a lock-in amplifier. The laser radiation was guided to the sample by a 600 µm core diameter optical fibre.

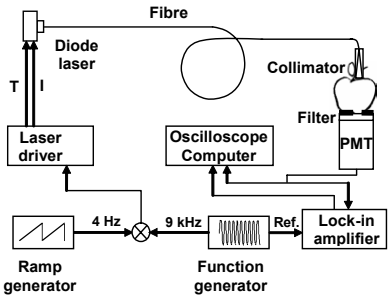

Fig. 1. Schematic layout of the GASMAS setup used for molecular oxygen detection in scattering porous materials such as fruits.

After light transport through the sample, a photomultiplier tube, Hamamatsu 5070A, detected the light. The ambient light was suppressed by a RG715 coloured glass filter used in combination with the sensitivity fall-off towards longer wavelengths for the photomultiplier tube. In the transmission geometry (Fig. 1) a circular aperture with a diameter of 6 mm was used to limit the detection area. The arrangement used in the backscattering geometry was slightly more complicated as can be seen in Fig. 2a. To launch the laser light into the scattering medium, a small right-angle prism providing total internal reflection was positioned in front of the fibre centrally located over the detector. The backscattered light that had travelled through the medium was collected in an annular aperture with an inner and an outer aperture diameter of 10 and 21 mm, respectively.

The DC and AC signals from the photomultiplier tube were detected separately. The DC signal, referred to as the direct signal, was sent to a digital oscilloscope, Tektronix TDS 520B. A high pass filter isolated the AC part and phase sensitive detection was performed with a lock-in amplifier. The component of the signal oscillating at the modulation frequency is similar to the first derivative of the direct signal, and, correspondingly, the component oscillating at twice the modulation frequency is similar to the 2nd derivative, etc. Since the direct signal is sloping, due to the simultaneous change in both wavelength and intensity as a function of injection current, the 1f signal is subject to a disadvantageous offset. This gives an advantage in using higher order components. However, the amplitude normally decreases by increasing the harmonic order. Thus, the component of the signal oscillating at twice the modulation frequency, i.e. 18 kHz, was selected as the output from the lock-in amplifier. This lock-in signal, referred to as the 2f signal, was sent to a second channel of the oscilloscope, which was computer controlled through GPIB communication by a LabVIEW program. An example of an oxygen signal recorded in backscattering geometry for the case of a 67-mm Granny Smith apple is shown in Fig. 2b.

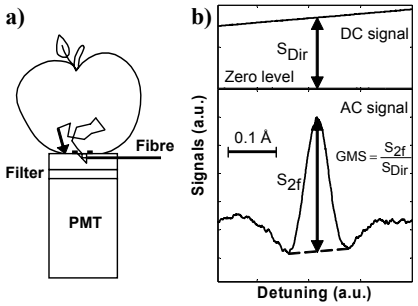

Fig. 2 (a). Modification of the GASMAS setup for backscattering (single-sided) measurements. (b). Direct absorption and second-harmonic component of the absorption for the R7R7 line in the oxygen A-band recorded from an Granny Smith apple in backscattering geometry.

As indicated in the figure the oxygen gas content can be evaluated from the peak-to-peak value of the absorption signature in the 2f signal. Clearly, the amplitude of the 2f signal is determined by the absolute size of the narrow gas absorption feature, i.e., to the fractional absorption due to the gas, and the amount of light reaching the detector. We are interested in the normalised GASMAS measurement signal, GMS, which is proportional to the fractional absorption. Thus, the AC signal (related to the oxygen content and the amount of light detected) was divided by the DC signal (related to the amount of light detected) as indicated in Fig. 2b. For small absorptions the GMS is proportional to the absorbance and thus to the product of the gas concentration and the path length travelled by the light. The standard addition method, just adding a path length of ambient air to be traversed by the laser light in addition to the scattering object under study, was adopted to calibrate a measured GMS and transform it into a more meaningful quantity. The acquired GMS values were plotted as a function of the added distance of air as discussed, e.g. by Persson et al (2005). The data points are expected to fall on a straight line, the zero intercept of which yields the equivalent distance, L_{eq}, in ambient air giving rise to a signal with the same magnitude as signal from the sample.

RESULTS AND DISCUSSION

Before presenting our new data, recorded mostly using backscattering geometry, we would like, in Fig. 3, to review some pertinent data obtained in our recent study (Persson et al., 2005). The recordings were performed in transillumination on Granny Smith apples using a setup of the type shown in Fig. 1. The gas content inside an intact fruit and the exchange of the gas was followed in real-time.

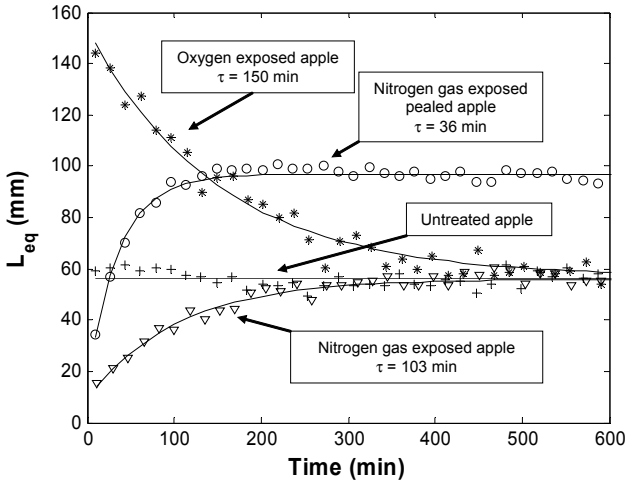

Fig. 3. Measurements of the gas exchange through differently treated Granny Smith apples in ambient air; untreated intact apple (+), intact apple pre-treated by immersion in nitrogen gas for 24 hours (□), pealed apple immersed in nitrogen gas for 12 hours (O) and another apple pre-exposed to an atmosphere with higher concentration of oxygen than in ambient air for 12 hours (). Exponential functions fitted to the data together with the estimated time constants are also included (Persson et al., 2005).

The equivalent mean path length, L_{eq}, was measured as a function of time for differently treated apples. A "flat" recording for an untreated apple, with a thickness of 70 mm, can be seen in the figure. The apple was then immersed in nitrogen gas for about 24 hours, by placing it in a plastic bag flushed with nitrogen gas before being sealed, as discussed above. Then it was brought out into ambient air and the re-invasion of oxygen containing ambient air was measured. The same apple was then pealed, immersed in nitrogen gas for 12 hours before the measurement procedure was repeated. Finally, a new apple, with a thickness of 74 mm, was exposed to an atmosphere with a higher concentration of oxygen than in ambient air for about 12 hours, before it was brought out into ambient air and the measurement procedure was again repeated. The time evolution of the oxygen equivalent mean path length was found to approximately follow a simple exponential curve, which also could be expected with the experimental procedures utilised (Sjöholm et al., 2005). The time constant for the re-invasion of oxygen into the nitrogen-exposed apple with skin was found to be around 100 min. It takes approximately 5 hours for the apple to reach the same steady-state oxygen concentration as before the treatment. It can also be seen that in the pealed apple, the concentration equilibrium of oxygen becomes twice as high as before the apple was pealed, and that the gas exchange is three times faster than in an intact apple.

Similar recordings obtained with our new more practical backscattering detection geometry (Fig. 2a) are shown for a 67-mm thick Granny Smith apple in Fig. 4. The same apple was also measured in transmission geometry, rendering a slightly slower change in the gas signal with time, which might be explained by the fact that the probed depth of the fruit is different in the two geometries (Sjöholm et al., 2005).

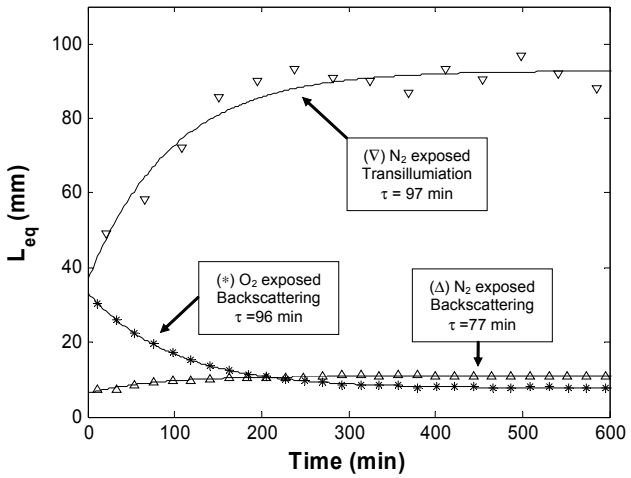

Fig. 4. Measurements of the gas exchange in transillumination and backscattering geometries in ambient air on a Granny Smith apple after different treatments; pre-treated by immersion in nitrogen gas for 24 hours in transillumination (□), pre-treated by immersion in nitrogen gas for 24 hours in backscattering geometry (□), and pre-exposed to an atmosphere with higher concentration of oxygen than in ambient air for 12 hours (). Exponential functions fitted to the data together with the estimated time constants are also included.

The same apple was also studied in backscattering geometry after oxygen exposure. As can be seen in the figure, the gas content equilibrium of oxygen becomes slightly lower, which might be due to the extreme levels of oxygen the apple has been exposed to, which might have harmed the apple. However, the reason can also be due to slightly different probed volumes of the apple.

To illustrate the possibility to use the GASMAS technique for modified atmosphere packaging issues, two different horticultural produces, apple and mushroom, with different expected respiration rates, were sealed in plastic bags and the consumption of oxygen was measured inside the produces in backscattering geometry. The results given in Fig. 5 show, as expected, that the change in the oxygen signal is faster for the mushroom than for the apple, which is a result of the faster respiration rate of the former compared to the latter (Gross et al., 2004).

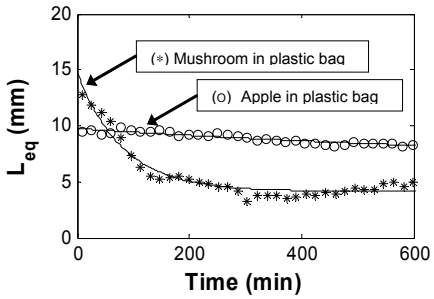

Fig. 5. The time evolution of the oxygen signal for two different horticultural produces with different respiration rates, apple (O) and mushroom (), while sealed in plastic bags, measured in backscattering geometry.

Finally, we illustrate some preliminary measurements in backscattering geometry on other types of horticultural produces such as avocado and orange. The GMS values from three avocados with different maturity are shown in Fig. 6. The hardness of the avocados was measured with a Stevens LFRA Texture Analyzer equipped with a circular probe with a diameter of 25 mm. Each avocado was compressed about 2 mm with a probe speed of 0.2 mm/s while the maximum force was measured. With increasing maturity it is noticed that the GMS values are reduced, probably related to both lower gas contents and less scattering. These aspects could be elucidated in time-resolved measurements (Somesfalean et al., 2002).

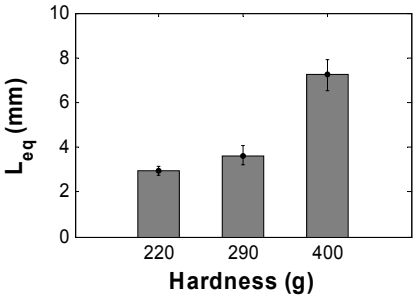

Fig. 6. The equivalent mean path length, Leq, measured for three avocados with different maturity, in backscattering geometry. Four measurements were performed on each avocado and the averages together with error bars corresponding to one standard deviation are shown.

Gas exchange into an orange, with and without peal, was measured after nitrogen exposure. In Fig. 7 the diffusion curve for the intact orange is shown, where the time constant was estimated to approximately 2.5 hours. No change in the GMS values with time could be observed for the equally treated pealed orange, which could be due to the low signal obtained compared to the background noise. However, the results indicate the possibility to study oxygen dynamics in the peal of an orange.

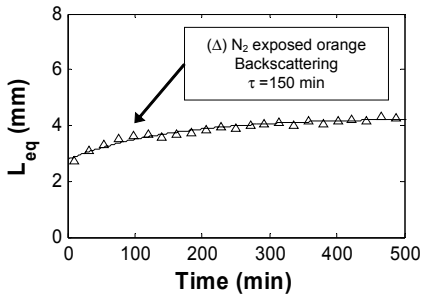

Fig. 7. Measurements of the gas exchange in backscattering geometry on an orange; intact orange pre-treated by immersion in nitrogen gas for 24 hours. Exponential function fitted to the data together with the estimated time constant is also included.

CONCLUSION

As illustrated by the preliminary work reported in the present paper and by Persson et al. (2005) the GASMAS technique has potential to non-intrusively and in real-time provide information on the conditions of horticultural produces. In contrast to other techniques, the gas is measured non-intrusively inside the tissue rather than as gas extracted from the fruits. Applications regarding basic plant physiology as well as in controlled atmosphere fruit storage and in modified atmosphere packaging processes can be foreseen. Also different stages of processing, including fermentation, could be studied. We presently aim at developing compact and realistic equipment for GASMAS studies also in the field.

ACKNOWLEDGEMENT

This work was supported by the Swedish Research Council, the Asian-Swedish partnership program of the Swedish International Development Cooperation Agency (SIDA), the International Science Programme (ISP), Uppsala, and the Knut and Alice Wallenberg Foundation. The authors gratefully acknowledge Professor Petr Dejmek at the Department of Food Engineering, Lund University Sweden, for the assistance in the measurements of fruit hardness.

References

Abrahamsson, Ch., Svensson, T., Svanberg, S., Andersson-Engels, S., Johansson, J. and Folestad., 2004 Time and wavelength resolved spectroscopy of turbid media using light continuum generated in a crystal fibre. Optics Express 12:4103-4112

Alnis, J., Anderson, Sjöholm, M., Somesfalean, G. and Svanberg, S. 2003. Laser spectroscopy of free molecular oxygen dispersed in wood material. Applied Physics B 77:691

Beaudry, R.M., 1999. Effect of O_2 and CO_2 partial pressure on selected phenomena affecting fruit and vegetable quality. Postharvest Biology and Technology 15:293-303.

Chauchard, F. et al (2005)

Gross, K.C., Wang, C.Y. Saltveit, M. 2004 Agriculture Handbook Number 66: The Commercial Storage of Fruits, Vegetables, and Florist and Nursery Stocks,

Persson, L., Gao, H., Sjöholm, M. and Svanberg, S. 2005. Diode laser absorption spectroscopy for studies of gas exchange in fruits. Lasers and Optics in Engineering, in press.

Sigrist, M.W., Ed. 1994. Air Monitoring by Spectroscopic Techniques. John Wiley and Sons, New York.

Sjöholm, M., Somesfalean, G., Alnis, J., Andersson-Engels, S. and Svanberg, S. 2001. Analysis of gas dispersed in scattering media. Optics Letters 26:16-18.

Sjöholm, M. *et al*. 2005. Determination of gas diffusion coefficients using the GASMAS technique. To appear.

Somesfalean, G., Sjöholm, M., Alnis, J., af Klinteberg, C., Andersson-Engels, S. and Svanberg, S. 2002. Concentration measurement of gas embedded in scattering media by employing absorption and time-resolved laser spectroscopy. Applied Optics 41:3538-3544.

Paper VII

Spectroscopic studies of wood-drying processes

M. Andersson, L. Persson, M. Sjöholm, and S. Svanberg.

Optics Express **14**, 3641–3653 (2006).

Spectroscopic studies of wood-drying processes

Mats Andersson, Linda Persson, Mikael Sjöholm, and Sune Svanberg

Atomic Physics Division, Lund Institute of Technology,
P.O. Box 118, S-221 00 Lund, Sweden
sune.svanberg@fysik.lth.se

Abstract: By the use of wavelength-modulation diode laser spectroscopy, water vapor and oxygen are detected in scattering media nonintrusively, at 980 nm and 760 nm, respectively. The technique demonstrated is based on the fact that free gases have extremely sharp absorption structures in comparison with the broad features of bulk material. Water vapor and oxygen measurements have been performed during the drying process of wood. The results suggest that the demonstrated technique can give information about the drying process of wood to complement that of commercially available moisture meters. In particular, the time when all the free water has evaporated from the wood can be readily identified by a strong falloff in the water vapor signal accompanied by the reaching of a high-level plateau in the molecular oxygen signal. Furthermore, the same point is identified in the differential optical absorption signal for liquid water, with a sharp increase by an order of magnitude in the ratio of the signal intensities at 980 nm and 760 nm.

OCIS codes: (000.2190) Experimental physics; (300.6260) Diode laser spectroscopy; (290.7050) Turbid media

References and links

1. J. M. Dinwoodie, "*Timber: Its nature and behaviour*," (E & FN, 2000).
2. B. Berglund, B. Brunekreef, H. Knöppel, T. Lindvall, M. Maroni, L. Mølhave, and P. Skov, "Effects of indoor air pollution on human health," Indoor Air **2**, 2–25 (1992).
3. S. Joseph Cohen and T C.S Yang, "Progress in food dehydration," Trends in Food Science & Technology **6**, (1995).
4. D. A. Skoog and M.D. West, "*Fundamentals of Analytical Chemistry*," 7th edition, (Saunders, 1995).
5. G.Müller, B. Chance, R. Alfano, S. Arridge, J. Beuthan, E. Gratton, M. Kaschke, B. Masters, S. Svanberg, and P. van der Zee, eds., "Medical optical tomography, functional imaging and monitoring," in *SPIE Institute Series*, Vol. **11**, (SPIE, 1993).
6. C. Abrahamsson, J. Johansson, S. Andersson-Engels, S. Svanberg, and S. Folestad, "Time-resolved NIR spectroscopy for quantitative analysis of intact pharmaceutical tablets," Anal. Chem. **77**, 1055–1059 (2005).
7. T. J. Farrell, M. S. Pattersson, and B. Wilson, "A diffusion theory model of spatially resolved, steady-state diffuse reflectance for noninvasive determination of tissue optical properties in vivo," Med. Phys. **19**, 879–888 (1992).
8. M. S. Pattersson, B. Chance, and B. C. Wilson, "Time-resolved reflectance and transmittance for the noninvasive measurement of tissue optical properties," Appl. Opt. **28**, 2331–2336 (1989).
9. C. af Klinteberg, A. Pifferi, S. Andersson-Engels, R. Cubeddu, and S. Svanberg, "In vivo absorption spectroscopy of tumor sensitizers using femtosecond white light," Appl. Opt. **44**, 2213–2220 (2005).
10. M. Sjöholm, G. Somesfalean, J. Alnis, S. Andersson-Engels, and S. Svanberg, "Analysis of gas dispersed in scattering media," Opt. Lett. **26,** 16–18 (2001).
11. J. Alnis, B. Anderson, M. Sjöholm, G. Somesfalean, and S. Svanberg, "Laser spectroscopy on free molecular oxygen dispersed in wood materials," Appl. Phys. B **77**, 691–695 (2003).

12. L. Persson, H. Gao, M. Sjöholm, and S. Svanberg, "Diode laser absorption spectroscopy for studies of gas exchange in fruits," Opt. Lasers Eng. **44**, 687–698 (2006).
13. L. Persson, B. Anderson, M. Andersson, M. Sjöholm, and S. Svanberg, "Studies of gas exchange in fruits using laser spectroscopic techniques," in Proceedings of Fruitic05 Symposium (Montpellier, France, September 12-16, 2005).
14. G. Somesfalean, M. Sjöholm, J. Alnis, C. af Klinteberg, S. Andersson-Engels, and S. Svanberg, "Concentration measurement of gas imbedded in scattering media employing time and spatially resolved techniques," Appl. Opt. **41**, 3538–3544 (2002).
15. L. Persson, K. Svanberg, and S. Svanberg, "On the potential of human sinus cavity diagnostics using diode laser gas spectroscopy," Appl. Phys. B **82,** 313–317 (2006).
16. L. Sandra, B. Roderick, and M. L. Roderick, "Plant-water relations and the fibre saturation point," New Phytol. **168**, 25–37 (2005).
17. P. Perré, "The role of wood anatomy in the drying of wood: Great Oaks from little acorns grow," 8th Int. IUFRO Wood Drying Conference (Brasov, Rumania, August 24–29, 2003).
18. M. Goyeneche, D. Lasseux, and D. Bruneau, "A film-flow model to describe free water transport during drying of a hydroscopic capillary porous medium," Transp. Porous Media **48**, 125-158 (2002).
19. L. James, "Electric moisture meters for wood," Gen. Tech. Rep. FPL-GTR-6. Madison, WI: U.S. Department of Agriculture, Forest Service, Forest Products Laboratory, 1988.
20. H. Forsén and V. Tarvainen, "Accuracy and functionality of hand held wood moisture content meters," VTT Publications 420 (2000).
21. P. J. Wilson, "Accuracy of a capacitance-type and three resistance-type pin meters for measuring wood moisture content," Forest Products Journal, **49**, 29–32 (1999).
22. C. Nordling and J. Österman, "*Physics Handbook*," 4th ed. (Studentlitteratur, 1987).
23. S. Matcher, M Cope, and D. Delpy, "Use of the water absorption spectrum to quantify tissue chromophore concentration changes in near infrared spectroscopy," Phys. Med. Biol. **39,** 177–196 (1994).
24. T. Svensson, J. Swartling, P. Taroni, A. Torricelli, P. Lindblom, C. Ingvar, and S. Andersson-Engels, "Characterization of normal breast tissue heterogeneity using time-resolved near-infrared spectroscopy," Phys. Med. Biol. **50,** 2559–2571 (2005).

1. Introduction

Drying processes, i.e., the removal of moisture from materials, are of utmost importance in many industrial contexts and everyday experiences. For instance, wood needs to be dried from its natural moisture before its use as a fuel or as a construction material [1]. An important issue is that moisture in building materials induces mold, especially if the ventilation is insufficient, which is of major concern in the building sector [2]. Grain and cereals need drying for storage and for further processing in the food industry [3]. Paper processing includes important drying steps as is the case also in many further industrial processes.

Many natural materials are porous and hydrophilic. The pores can be filled with air or other gases, but may also be partially or fully filled with water; a frequently undesired situation. Capillary action is an important passive process when porous materials take up water. Materials frequently swell (increase in volume) when wet. In nonporous media the process of osmosis is in action. If the material has some rigid scaffolding structure, such as wood and other building materials, the swelling is minor. Then the pores originally filled with air instead become water filled. By increasing the vapor pressure of water by heating in combination with securing an environment with reduced relative humidity, forced drying can be achieved.

The status of drying materials is often studied by handheld moisture meters that measure the water content by an indirect method relying on the fact that the electrical properties of the material is dependent on the water content. However, these instruments are not able to monitor the whole drying process and are in some cases intrusive. Recent developments in diode-laser-based spectroscopy pose an interesting alternative approach, which would be to monitor the water vapor as well as the liquid water by a more direct, noninstrusive spectroscopic approach.

The present paper deals with the study of drying of wood using high-resolution near-IR laser absorption spectroscopy. A tunable diode laser operating close to 980 nm is used to monitor gaseous water. Liquid water also exhibits a broad absorption peak in the same wavelength

region. For reference, atmospheric oxygen gas in the pores is also monitored in its A band close to 760 nm. This wavelength also provides a convenient off-resonance wavelength in the liquid-water spectrum for assessment of liquid-water contents.

Absorption spectroscopy is a very common method for measuring concentrations of substances utilizing the Beer–Lambert law and a suitable calibration procedure (See, e.g., [4]). However, the application of this method is not straightforward for natural materials such as wood, since the fact that they are inhomogeneous and porous also means that they are highly scattering, making the optical pathlength through the sample undefined. This situation is common in medical optics, where scattering and absorption are intertwined [5], as is also the case in analytical spectroscopy of pharmaceutical preparations [6]. Different techniques for handling multiple scattering of light have been developed for assessing the concentration of liquid and solid absorbing constituents. Spatially separated measurements [7] and time-resolved techniques [8] constitute two main approaches for enabling concentration determinations. A recent example on the determination of tumor sensitizer concentration in vivo is given in Ref. [9].

Such techniques have been extended to free gases present in porous media through the introduction of the Gas in Scattering Media Absorption Spectroscopy (GASMAS) technique [10]. Normally a modest resolution is used in solid-state spectroscopy because of the broad absorbing structures. However, if single-mode diode laser spectroscopy using sensitive modulation techniques is employed, then structures appear that are typically 10,000 times narrower due to free gas. So far, the GASMAS technique was applied to the monitoring of free molecular oxygen in materials as diverse as wood, polystyrene foam, and fruits [10-13]. In particular, gas transport through the media could be studied by first subjecting the material to a pure nitrogen atmosphere and then observing the time constant for the reinvasion of normal ambient (oxygen-containing) air. Concentrations could be determined by combining GASMAS measurements with time-resolved measurement, revealing the time history of the photons inside the sample [14]. The GASMAS technique was also very recently applied to the monitoring of human sinus cavities [15].

The present paper focuses on spectroscopic monitoring of the drying of wood, and the GASMAS technique has in this context been extended to water-vapor monitoring. The structure of wood and the basics of wood-drying processes are presented in the next section. Conventional methods for measuring moisture in wood are discussed in Section 3. The experimental arrangements used in the present work are then presented in Section 4. Measurements and results are described in Section 5. A discussion of the results and conclusions from the study are presented in the final section.

2. Wood structure and its drying process

2.1. Wood structure

Wood has a complicated architecture, described in detailed, e.g., in Ref. [1]. In a tree the wood structure supports the treetop, stores nutritious substances, and transfers minerals and water, which have been absorbed by the root system. Thus, it needs to be strong, hydrophilic, and flexible since a tree grows and lives in a changing environment. Even though there exist hundreds of different types of wood material, they can be divided into two groups, hardwood (deciduous) and softwood (coniferous); see Fig. 1. Hardwood is the most complicated of the two and comprise wood such as balsa, white oak, ash, mahogany, etc. The density of hardwood may vary from about 0.1 to 1.2 g/cm^3, depending on type of wood. Hardwood is characterized by a combination of complicated cell types orientated both vertically, tangentially, and radially. Softwood, on the other hand, is distinguished by a much simpler combination of cells that runs mostly vertically in a tree. Typical examples of wood that belong to the softwood group are spruce, pine, and larch. The weight of softwood may vary from 0.3 to 0.7 g/cm^3.

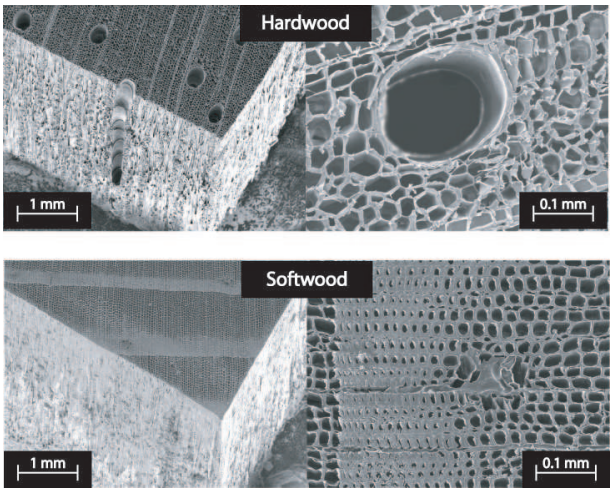

Fig. 1. Microscopic pictures of hardwood (balsa) and softwood (pine).

From a microscopic point of view wood consists of cellular structures that handle tasks carried out in a tree. Water and minerals are stored and transported vertically via cells, forming vessels, and horizontally via cell structures called rays. In total, wood cells can be classified into four different types; parenchyma (storage of nutritients), tracheids (support and conduction), fibers (support), and vessel cells (conduction).

In hardwood all four cell types are present, but tracheids are uncommon. Instead fibers and vessels are responsible for support and conduction of water and minerals. Fibers are usually 1-2 mm long and 10-20 μm wide, and their only function is support. However, vessel cells are about the same length as the fibers but up to 0.5 mm wide. Since the ends of the vessels are situated on top of each other they can make up a long tube. Thus, vessels act as an efficient water tube since the ends of the vessels are more or less dissolved.

In softwood only two cell types are present, namely parenchyma and tracheids. Tracheids are the most common cell type (about 90% of the softwood), and its main function is support and conduction of minerals and water. The size of the cell is about 2–4 mm long and about 30–50 μm wide. It is situated vertically in the tree and conducts water and minerals via small pits located on the cell surface. Parenchyma cells are small, 200 x 30 μm^2 in size, taking care of the storage of nutritients.

2.2. Wood drying processes

All types of wood consist of cellulose, hemicellulose, lignin, and extractives. The density of wood elements is about 1.5 g/cm^3, but since wood is based on a cell structure, with size that differs per type of wood, the density of wood may vary from 0.1 to 1.2 g/cm^3 if the content of water is kept low. However, since the wood cell structure is hydrophilic and full of air, wood is heavily affected by water and moisture.

The moisture content in wood is defined as the ratio between the weight of water in a piece of wood and the weight of the wood when no water is present. This means that the moisture content is higher than 100% in a living tree. During this state water is stored in cells and vessels (free water) but also in cell walls (bound water) that have expanded due to absorbed water.

If a tree is cut into pieces, the moisture content starts to decrease immediately; see Fig. 2.

At first free water is moved to the wood surface by capillary forces where it is evaporated into the atmosphere. Due to the evaporation process the surface temperature is decreased, and heat must be transferred from the environment in order to maintain the drying of the wood.

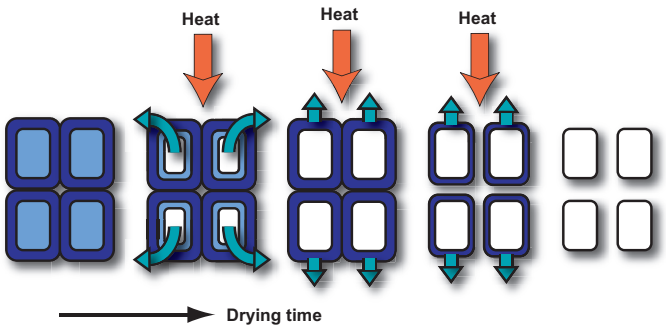

Fig. 2. Wood-drying process. At first the cells are filled with water, but in the end no free water exists, and the absorbed water in cell walls is dried out until an equilibrium state with the surrounding environment is reached.

When all free water has been evaporated the bound water starts to evaporate as well. This state of the wood is known as the fiber saturation point (FSP) and it corresponds to a moisture content of about 25–30%, depending of type of wood. Since bound water is situated inside the cell walls, more energy is needed to evaporate it. Thus, the drying rate decreases and the wood shrinks. In the end of the drying process, the wood reaches an equilibrium state with its environment. The moisture content inside wood depends on temperature and humidity level of the environment. A typical value of the moisture content for dried wood is 12–15% [16-18].

3. Commercially available moisture meters

Handheld electric moisture meters are commonly used to measure the moisture content in wood. The measurement technique was developed in the late 1930's, and today there exists a number of manufacturers that develop and sell handheld moisture meters for measuring, e.g., moisture in wood and concrete. Mainly, two different measurement principles exist: resistance and dielectric type moisture meters [19-21].

The resistance type of moisture meter measures the electric resistance in wood between two pins that are connected at the wood surface or inserted into the wood, with typical distances of centimeters between the pins. If the wood is dry it acts as an isolator, and the resistance is in the order of 10^5 MΩ. However, since water in wood contains ions, the resistance in wood decreases down to about 0.5 MΩ when the moisture content is close to the saturation point.

In order to measure the moisture content using the resistance principal, one has to know the type of wood and from what region it comes. It turns out that all species of wood have different resistance curves even for one type of wood that has grown at two different locations. Today, resistance curves for many species of wood are stored in the device and controlled by a microprocessor.

Although the resistance type of moisture meter is easy to produce and operate, precautions should be considered. At first this measurement method is intrusive. Secondly, the resistance curve for wood is affected by temperature. Thus, a temperature sensor is included in some of the meters. Other disadvantages are the limited measurement range and that the result depends on whether the pins are inserted in parallel or perpendicular to the wood fibers. The upper

limit is set by the fact that above the fiber saturation point (about 25–30% moisture content), the resistance measurement data are not reliable. The lower limit (about 7% moisture content) depends on the difficulties to measure resistance in the order of 10^5 MΩ and above.

The dielectric type of moisture meter uses a nonintrusive measurement technique that measures the dielectric constant of the combined wood and water material. Since the dielectric constant for water is much higher than that of wood (by a factor of 25), the moisture content may be estimated. Anyway, each type of wood has its specific dielectric constant. Specific wood calibration data are stored in the device and controlled by a microprocessor. The dielectric moisture meter is known to have poor performance compared to the resistance type. However, it is commonly used for relative measurements. The surface electrodes are sensitive to other materials close to the surface and density fluctuations of the wood. The measurement range varies from 5% to about 25% moisture content.

4. Setup for diode laser spectroscopy on wood

We will now describe our spectroscopic setup for moisture studies. While measurements using a light transmission or backscattered geometry can be made with the GASMAS method, the former one was chosen because of its simplicity in terms of the optical arrangement and also regarding the signal interpretation. However, a backscattering geometry is attractive in terms of optical access and is also the only possible one for thick samples. Our setup is based on two almost identical arrangements that are run simultaneously. One setup is used for oxygen measurement while the second is used to measure water vapor (moisture) contents in the same piece of wood. A schematic drawing is shown in Fig. 3. The oxygen measurement setup is explained in more detail in Refs. [12]. However, in the present setup the photo multiplier tube (PMT) sensor is replaced by a silicon detector (Photovoltaic PIN-10DP from UDT) with an active surface of 100 mm^2.

The major difference between the oxygen and the water-vapor setup is the wavelength of the diode lasers used. For the oxygen detection a diode laser (Sharp LT031MDO) with a maximum output power of 7 mW, operating at 2 mW at the sample, is used to scan across the R7R7 oxygen line at 761.003 nm (vacuum wavelength). The scan range was typically 20 GHz (0.04 nm). A near-IR Fabry–Pérot diode laser (Specdilas F760) with a maximum output of 200 mW at 980 nm, and efficiently operating at 40 mW at the sample, is used as a spectroscopic light source to detect the water-vapor line (vibration; (000)→ (121), rotation; J"=5→ J'=4, K_a"=0→ K_a'=0, K_c"=5→ K_c'=4) at 978.509 nm (vacuum wavelength). The scan range was typically 35 GHz (0.11 nm).

The basis for the measurement is that the wavelength of the laser light is scanned across the absorption lines by sweeping the operating current of the lasers by the use of a 4 Hz saw tooth ramp. To achieve wavelength modulation spectroscopy (WMS) with lock-in detection, the operating current is also modulated by a sinusoidal wave at 9 kHz with a modulation index of about 1 in both cases. The laser light is focused into a fiber that guides the light to the sample. The water vapor setup uses the same type of silicon detector as the one used for oxygen. The output from each detector is split into two signal branches. One, directly connected to an oscilloscope, is referred to as the direct signal, while the second part goes via the lock-in amplifier before being connected to another channel of the oscilloscope, and is referred to as the WMS signal. The data are stored and analyzed using a computer. Typical readings for oxygen and water vapor are shown in the lower part of Fig. 3. The peak-to-peak value of the WMS signal is measured and normalized by dividing with the direct signal value at the corresponding wavelength in order to determine the fractional absorption during the drying process.

As discussed for instance in [10], a method called standard addition, well known in analytical chemistry, is used in order to calibrate a measured normalized WMS signal and transfer it to a

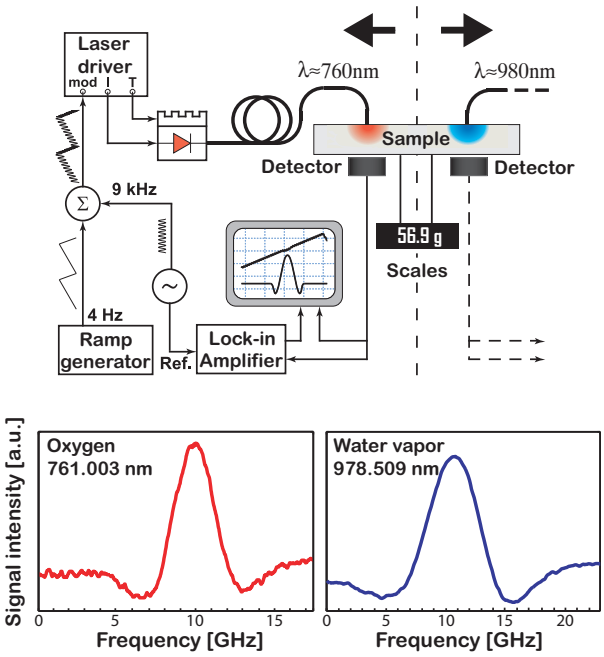

Fig. 3. Schematic drawing of the spectroscopic setup of similar diode laser spectrometers for oxygen (left) and water vapor (right). Typical readings of the WMS signals for oxygen and water vapor in wood are shown in the lower part. The half widths of the signals are of the order of a few GHz in both cases. The half widths at half maximum (HWHM) of the absorption lines are, according to HITRAN, 1.61 GHz for oxygen and 2.72 GHz for water vapor at standard conditions.

more meaningful quantity—a so-called equivalent mean path, L_{eq}. It is determined by adding free air path lengths in the collimated laser beam before it enters the test sample. The equivalent mean path length corresponds to the distance that the light has to travel in ambient air in order to obtain the same signal as in the sample $L_{eq} \cdot c_{air} = \langle L_{sample} \rangle \cdot c_{sample}$, where c_{air} corresponds to the gas concentration in air, $\langle L_{sample} \rangle$ to the mean path length in the sample, and c_{sample} to the gas concentration in the sample. The calibration procedure is carried out by removing the wood sample and placing an optical attenuation filter on top of the detector. A collimator lens was placed at the end of the fiber. The normalized WMS signal was measured for different added air distances between the collimator lens and the filter. A linear function between the normalized WMS signal and added air distance is obtained. This function can then be used to estimate the L_{eq}. The calibrations are done once for each laser, and these calibration curves are used for all experiments. Precautions were taken when the water-vapor WMS signal was calibrated. The room temperature and relative humidity were measured by a hygrometer (Testo 608-H1) sensor and the partial pressure of the water vapor was estimated.

An analog lab scale (Libror EB-280, Shimadzu) is used to measure the weight of the wood in order to calculate the average moisture content during the drying process. At the end of the drying process a commercial convection oven was used to dry the wood at 110^{o}C in order to determine the truly dry weight.

5. Measurements and results

Uniform balsa wood pieces of 10 cm width, 30 cm length, and 0.8 cm thickness derived from the same batch were used in the measurements. The figures of balsa wood shown in Fig. 1 are from the wood samples studied. The wood was kept under water for typically three days and was studied directly after being exposed to the ambient laboratory air. The drying could be followed by reading off the analog scales, onto which the piece of wood was attached.

The results of conventional measurements of the moisture contents during the drying process are shown in Fig. 4, with the instrument applied in a straightforward manner. The weight reading from the scale, expressed as moisture content, is plotted together with data from the resistance and the dielectric moisture meters. It can clearly be seen that the results from the meters poorly describe the real drying process monitored by the scale for moisture content above the FSP. Obviously there is a need for improved measurement techniques for moisture.

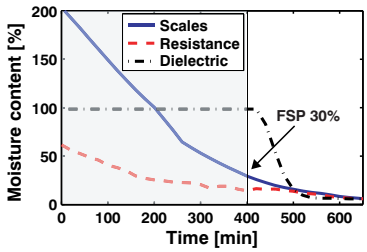

Fig. 4. Measured moisture contents during the drying process of the sample. Curves indicate moisture content (blue curve) when measured by logging the weight of the sample, (red dashed curve) when measured by using a resistance moisture meter (Protimeter Timbermaster), and (black dash-dotted curve) when measured with a dielelectric moisture meter (MC-300W, Exotek). The fiber saturation point (FSP) is indicated in the figure (moisture content=30%).

The temperature of the wood surface was also monitored with thermocouples. The measurements were performed on a different sample. In this case the sample had been soaked in water for a longer time than the case when recording the data in Fig. 4. Typical results are shown in Fig. 5(a), where the blue curve shows a weight loss to a stable value of about 33% of the original wet weight, the dry material plateau being reached after about 1200 min. The drying process is, as expected, accompanied by a lowering of the temperature. During the first 600 min the temperature was stable at 9^{o}C below the ambient value (25^{o}C), which was gradually reached after 1200 min. Local possible heating, due to laser beams, was found to be very small. This results in a marginal increase of water vapor pressure.

Since gaseous water (water vapor) is measured in our study it is interesting to consider the vapor pressure of water as a function of the temperature. The corresponding curve is given in Fig. 5(b). It shows the partial pressure of the vapor in a closed volume containing liquid water at the given temperature. We note that the vapor pressure is increasing by a factor 1.8 when the temperature rises from 16^{o}C to 25^{o}C. We also note that water vapor at ambient temperature only accounts for a small percentage of the mass in normal air. Frequently ambient air does not feature the full water vapor pressure corresponding to the ambient temperature. If there is no air movement and large amounts of distributed liquid water the relative humidity would be 100%, like in a sealed-off volume. Due to the exchange of dryer air, the effective humidity becomes less. Readings of 20–40% relative humidity (percentage of the fully saturated value at the given temperature) are common in indoor environments at wintertime in Sweden.

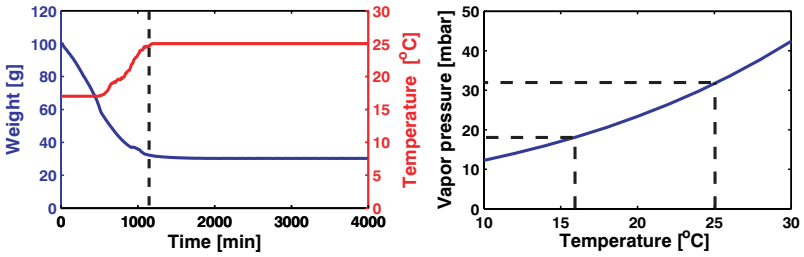

Fig. 5. (a) Measured temperature at the surface of the sample and measured weight during the drying process. (b) Vapor pressure as a function of the temperature [22].

We will now present data from our near-IR laser spectroscopic measurements. We performed simultaneous (molecular) water vapor and molecular oxygen measurements at points separated by about 10 cm on the piece of wood, assuming the material to be laterally uniform. These data were recorded simultaneously as the temperature and weight data in Fig. 5(a). A small air space was left between the sample and the detectors to allow water to homogeneously diffuse out of the sample. The setup is shown in Fig. 3. Oxygen does not have a liquid phase in the temperature range studied (it liquifies at 90K). In contrast, water has a liquid phase as well as a gaseous phase, and the vapor pressure is, as just discussed, temperature dependent.

In understanding the dynamics of wood drying it is useful to first consider the behavior of the molecular oxygen L_{eq} during the drying, which as mentioned before is proportional to the normalized WMS signal. In Fig. 6(a) the fractional oxygen absorption is plotted in red. The signal is proportional to the oxygen concentration times the effective distance travelled through the gas-filled pores, the latter factor being strongly sensitive to the degree of light scattering in the material. The signal is plotted as an equivalent path length in normal air containing 21% oxygen, as previously discussed. It should be noted that the effective path length through the material, useful in a standard Beer–Lambert law view, can be expected to change during the drying process. One aspect is that while liquid water is an index-matching fluid reducing the scattering when the pores are water filled, the scattering should increase when the air-filled inhomogeneities develop during the drying process. We notice that the oxygen signal increases from a non-zero value (there are air-filled pores even in the very wet wood) by a factor of about 8 to then stay constant at the high value, reached at about 1300 min when all the liquid water is driven out and all the pores are instead gas filled.

The simultaneously measured gaseous water signal is included in blue in Fig. 6(a). Again, the curve starts at a non-zero level (corresponding to the presence of gas-filled pores with saturated water vapor also in the very wet wood). The signal increases to a maximum at about 1200 min, reached slightly before the oxygen signal maximum. At the same time as the oxygen signal stays constant the water vapor signal gradually falls off to a steady value of about 25% of the maximum value. This could be interpreted in the following way: Around 1200 min the pores are almost void of water, as indicated by the dashed line in Fig. 5(a), but there is still a sufficient amount of water to sustain the full saturated water vapor partial pressure. Shortly thereafter, this is no longer the case, and the pores with constant volumes and situated in a material with constant scattering properties gradually lose the saturated vapor pressure and gradually attain the relative humidity value of the laboratory, which for the measurement case with an ambient temperature of 25^{o}C was separately measured to 24% with a hygrometer. This is in good agreement with the measured signal falloff to about 25% of the value with

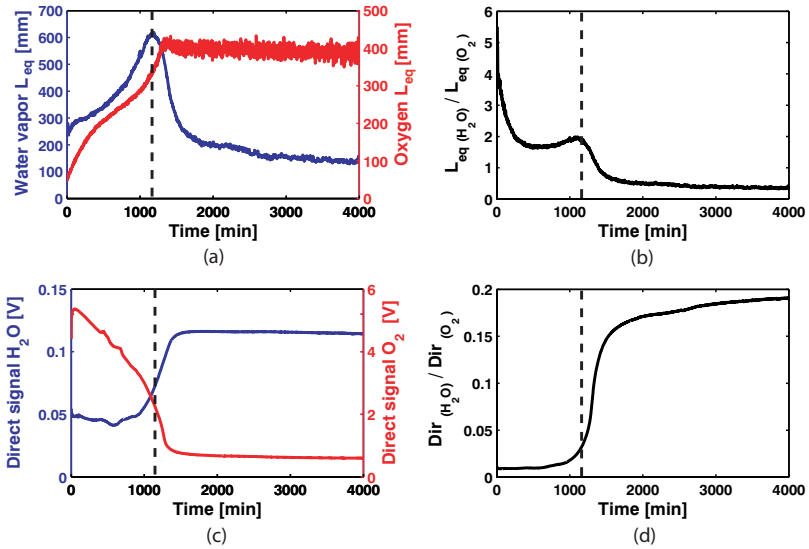

Fig. 6. (a) Equivalent mean path length for water vapor and oxygen during the drying process of balsa. (b) Ratio between detected equivalent mean path length for water vapor and oxygen. (c) Direct signals for water vapor and oxygen during the drying process of balsa. (d) Ratio between detected direct signal for water vapor and oxygen.

full saturation. The displacement of about 100 min between the reaching of the maximum for oxygen and water vapor is compatible with the typical times for air diffusion in balsa wood measured separately [11].

While the above observations are readily interpreted, the detailed behavior of the water vapor signal during the drying is due to many different influences. Let us first state that if two permanent gases such as nitrogen and oxygen had been studied, the same type of behavior (apart from small effects of different diffusivity), i.e., a constant ratio between the signals during the drying phase, would have been expected. This statement has as a prerequisite that the two gases absorb at close-lying wavelengths so that the scattering properties are similar. In contrast to this, the ratio between the water vapor signal and the oxygen signal is strongly varying during the drying process, as can be seen in Fig. 6(b). The temperature increase in the time span 400–1200 min (see Fig. 5, red curve) leads to an acceleration in the water-vapor signal level beyond that for oxygen, for which the concentration is marginally reduced (a few percent) by the temperature increase. This may explain the tendency of increase of the ratio curve toward the end of the drying period. The high initial value in the ratio curve may be related to the time constant for oxygen diffusion through the material also discussed with regard to the different times for the two gases to reach the maximum WMS signal. It should be noted that in the drying up of a pore, the walls of the cavity will be uniformly covered by liquid water due to the surface tension. This may impair the transport of oxygen through the film while the water vapor can freely build up in the central microbubble of the pore, see Fig. 2. Effects of this kind may also influence the balance between the two gases in the cavities during the drying process. As noted, when everything is dry, conditions are static with regard to scattering and the behavior of both curves is clearly understood as discussed above.

So far we have been discussing the fractional absorptive imprint of the gas (intensity on

the absorption line compared to the intensity off the line), which is decisive for concentration measurements based on the Beer–Lambert law. However, it is also interesting to study the dynamics of the total light (off the narrow absorptive features) at the two wavelengths used (980 nm and 760 nm, respectively). Such measurements were performed and the results are shown in Figs. 6(c)–(d) and in Fig. 7. The curves in Fig. 6(c) show a very different behavior with the water signal increasing in the final phase of drying from an almost constant initial level to a final value about 2.5 times higher. On the contrary, the 760 nm signal starts at a high level and, with acceleration, reaches a steady value about 5 times lower when the wood is dry. The ratio of detected direct signal for water and oxygen is shown in Fig. 6(d). In explaining these phenomena it is important to note that liquid water has quite a strong broadband absorption around 980 nm, as detailed in Fig. 7(a) and already noted in the Introduction. We note that this absorption influences the on- and off-resonance frequencies for the narrowband water-vapor signals alike, and does not influence the fractional absorption determining the water-vapor concentration. However, the laser beam is clearly attenuated by the water contents. The initial flat response of the 980 nm curve for the drying wood can be interpreted to mean that the reduction of water during the initial drying is compensated by the increased light path length due to the developing gas-filled pores. Finally, the absorbing liquid water disappears and the detected light settles on a level determined by the attenuation of the light-scattering dry wood.

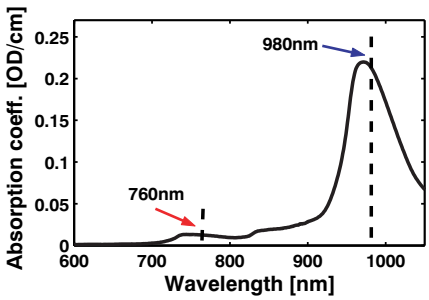

(a)

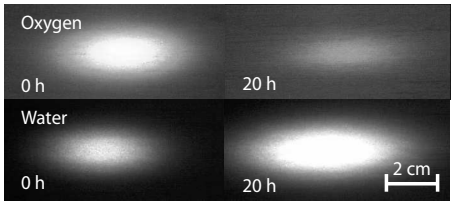

(b)

Fig. 7. (a) Absorption spectrum of 1 cm pure water reproduced from the measurements by Matcher *et al.* [23]. (b) Images of the sample on the detection side for oxygen (760 nm) and water vapor (980 nm) during its drying process.

The 760 nm light is off-resonance from the broad liquid water absorption as shown in Fig. 7(a), and bulk absorption due to the water is small, in strong contrast to the case for 980 nm. The high initial light level can be seen owing to the index-matching effect of the water in the pores, which reduces the lateral scattering and allows more light to reach the detector. As the wood dries the scattering increases and less and less light reaches the detector. Steady-state

conditions then prevail in the dry wood. The significant change in the light levels, as well as the normalized WMS signals for both wavelengths when the wood is nearly dry can be interpreted as the final dry-up of the finest compartments long after the tube structure that contained most of the water has dried up. The scattering increases a lot due to the appearance of small pores of size comparable with the wavelength. This reduces the detected 760 nm light level. Also the 980 nm light level changes due to the continued loss of bulk water absorption.

The dynamics of the transmitted light levels at the two wavelengths could also be studied using near-IR imaging of the transmitted light using standard Web cameras (Q-Tec 100). The transmitted light blobs at 980 nm and 760 nm are shown in Fig. 7(b) for fully wet and fully dry (waiting 20 h = 1200 min) conditions. The intensity in the center of the blobs (where the detector is situated) is related to the intensities given in Fig. 6(c); the 760 nm signal is greatly reduced and the 980 nm is increased. The final levels (20 h) correspond to an attenuation by the sample of the incident light of about 80% for the 980 nm signal and 99.95% for the 760 nm signal. These attenuations suggest that the wood sample thicknesses accessible in transmission measurements cannot be considerably larger than 1 cm for most wood types. For thicker samples the backscattering geometry is still applicable. From recordings, such as the ones shown in Fig. 7(b), information of the spatial distribution can also be extracted and compared with theory [7]. However, a detailed analysis of the spatial distribution is outside the scope of the present paper.

6. Conclusions and discussion

Removing moisture from materials is of major importance in fields as diverse as industrial processing, handling of construction materials, and preparation of agricultural products. The origin of excess water is frequently connected to material porosity. Optical measurement techniques are attractive since they are nonintrusive and frequently deliver data in real time. However, quantitative absorption spectroscopy is hampered by the strong scattering in inhomogeneous materials, making the Beer–Lambert law not directly applicable. In the present paper we have demonstrated the application of the GASMAS technique applied in transmission for the monitoring of water vapor in wood, using corresponding molecular oxygen measurements as a reference. The wavelengths used for the free gas monitoring, 980 nm and 760 nm, are also on- and off-resonant for a broad liquid water absorption feature, and thus information of the bulk water is also obtained. The signal intensities observed can mostly be interpreted as the result of the interplay between specific absorption and scattering, both changing during the drying process. In particular, the time when all the free water has evaporated from the wood can be readily identified by a steep falloff in the water vapor signal accompanied by the reaching of a high-level plateau in the molecular oxygen signal. The ratio between these signals, being dimensionless and largely independent of scattering, shows in particular the arrival at a fully dry sample. This situation is also identified in the differential optical absorption signal for liquid water, with a sharp increase of an order of a magnitude in the ratio of the (broadband) signal intensities at 980 nm and 760 nm.

It is thus clear that optical spectroscopy can be a valuable tool for the practical monitoring of drying processes while also yielding additional information on specifics of drying. For the practical application of the method, measurements in back-scattering geometry (as already applied in our sinusitis monitoring [15]) is of great interest. In order to further elucidate the interplay between scattering and absorption, time-resolved measurements of the photon history in the wood for the two wavelengths would provide independent information on the scattering of the material and the liquid water contents. Such measurements can be performed using white light [6,9], capturing the full spectrum, or employing a number of pulsed diode lasers selected at appropriate wavelengths [24].

Acknowledgement

The authors thank Rita Wallén from the Department of Cell and Organism Biology of Lund University for her help with the microscope pictures. We also acknowledge useful discussions with Lars-Olof Nilsson from the Division of Building Materials of the Lund Institute of Technology.

This work was supported by the Swedish Research Council and the Knut and Alice Wallenberg Foundation.

Paper VIII

Human sinus studies using monte carlo simulations and diode laser gas absorption spectroscopy

L. Persson, E. Kristensson, L. Simonsson, M. Andersson, K. Svanberg, and S. Svanberg.

Proceedings of the International Symposium of Biophotonics, Nanophotonics and Metamaterials, 95-98, Hangzhou, China (October 2006).

Human Sinus Studies using Monte Carlo Simulations and Diode Laser Gas Absorption Spectroscopy

Linda Persson*, Elias Kristensson*, Lisa Simonsson*, Mats Andersson*, Katarina Svanberg† and Sune Svanberg*
*Division of Atomic Physics
Lund University, P.O. Box 118, SE-221 00 Lund, Sweden
Email: linda.persson@fysik.lth.se
†Department of Oncology
Lund University Hospital, SE-221 85 Lund, Sweden

***Abstract*— We demonstrate the possibility of non-intrusive in-vivo human sinus studies by diode laser gas absorption spectroscopy. Molecular oxygen in tissue-like phantoms were investigated in a practical backscattering detection geometry for frontal sinus studies both experimentally and numerically using the Monte Carlo concept, implemented in the Advanced Systems Analysis Program (ASAP^{TM}) software. Light was launched into and detected from the forehead on a health volunteer. A model representing the frontal sinus measurements was implemented in ASAP^{TM} and studied. The results from the experiments and the simulations show a good agreement for both the tissue-like phantom measurements and the measurements of the healthy volunteer. Preliminary data from human maxillary sinus measurements are also shown. The results are promising and suggest further development of this technique for sinuses studies.**

I. Introduction

Within the bones of the human skull and face some air-filled cavities called the paranasal sinuses are located. The paranasal sinuses are connected to the nasal cavity through small orifices called ostia, which allow drainage and exchange of air, liquid and mucus. So far no one has convincingly been able to demonstrate any important physiologic function of the human sinuses. Different hypotheses on the possible functions have been proposed such as reduction of the skull weight, heat insulations, and increasing resonance of the voice. It seems like the only important aspect of the sinuses that everyone can agree upon is to make sure that they are kept free from diseases such as infections [1].

Sinusitis is an inflammation of the paranasal sinus mucosa, which is treated with antibiotics and often followed by one week of sick-leave. Every year, more than 37 million people in the US are diagnosed with sinusitis. Today, the diagnosis of sinusitis is mostly based on the anamnestic history of the patient, and in some cases on paraclinical investigations such as X-ray, ultrasound, and low-dose computerized tomography. Unfortunately, unnecessary antibiotic treatment is very common due to the difficult diagnosis. Therefore, there is a great need for simple, non-intrusive alternatives or complementary methods to detect sinusitis [2], [3].

In the present study we investigate the feasibility of using diode laser gas absorption spectroscopy for sinusitis diagnostics on the frontal sinuses, located within the frontal bone. The experimental method presented is based on the sharp spectroscopic absorptive imprint of molecular oxygen in the air filled cavities. A backscattering detection geometry is used where narrow-band diode laser radiation is launched through the facial skeleton to transverse the frontal sinus cavities in the forehead. The light is then diffusely scattered in the deeper lying tissues with part of the light again traversing the cavities, and again scattered in the facial tissue to reach an external detector [4]. The light propagation of the experiment is also simulated [5] by using the Monte Carlo concept, implemented in the Advanced Systems Analysis Program (ASAP^{TM}) software. Simulations and experimental data have been compared for a model based on two scattering bodies representing human tissue, with an air gap in between representing the sinus cavity. Finally, we have explored the possibility of performing imaging measurements of the frontal sinuses. The results of the simulations have been compared with results from measurements on the frontal sinuses of a healthy volunteer. Preliminary data have also been recorded on the maxillary sinuses, located within the cheekbone, of a healthy volunteer.

In the next section we describe the tools used in the study, which include the experimental setup, the computer simulations and the sinus models investigated in the latter. Experimentally obtained data are then compared with simulations. Finally, conclusions are drawn.

II. Tools used

A. Experimental setup

The gas detection setup used in this study performs absorptive laser spectroscopy of diffusely scattered light. A schematic diagram of the setup is shown in Fig. 1. A diode laser, operating around 760 nm with an output of about 7 mW, is tuned across the R7R7 absorption line of molecular oxygen by supplying a saw-tooth ramp at 4 Hz to the laser driver current. A sinus-wave at 9 kHz is superimposed to the ramp in a wavelength modulation scheme to allow sensitive lock-in detection. The light is focused into a fibre guiding the light to

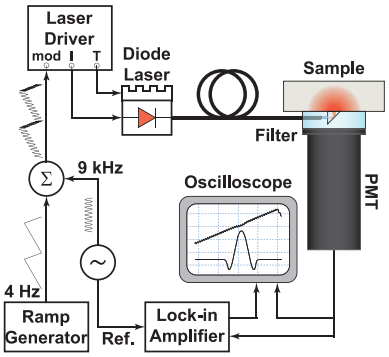

Fig. 1. Schematic drawing of the experimental arrangement for diode laser gas absorption spectroscopy in a backscattering detection geometry [4].

the sample. A small right-angle prism is positioned in front of the fibre centrally located to the detector and allowing the launching of the photons into the sample. An annular aperture, with an inner diameter of 10 mm and outer diameter of 21 mm is used to select backscattered photons. A blocking colored glass filter is placed above the detector protecting the detector from visible stray-light diluting the signal with noise. A photomultiplier is used as a detector providing efficient photon collection. The experimental setup is described in more details in Ref. [4].

The signal from the detector is divided into two parts. One part is directly sent to a computer controlled digital oscilloscope, referred to as the direct signal. The other part is sent to the oscilloscope via a lock-in amplifier where phase-sensitive detection at twice the modulation frequency is performed. This signal is referred to as the 2f signal.

The gas content in the sample is estimated using the Beer-Lambertian law, stating that for small absorptions the fractional absorption is proportional to the gas concentration. Hence, the 2f signal is normalized to the amount of light reaching the detector (the direct signal). To estimate the gas content in the sample, the peak-to-peak value of the normalized 2f signal is then estimated.

A method called standard addition was used to calibrate the obtained normalized peak-to-peak value and to transform it to a more meaningful quantity, a so-called equivalent mean path length L_{eq}, described in Ref. [4]. The method is based on adding known path lengths of air to the scattering sample and measuring the normalized peak-to-peak values. The values are then plotted as a function of added air and are expected to fall on a straight line. The zero crossing yields the $\langle L_{eq}\rangle_{exp}$. In other words, L_{eq} corresponds to how far the light has to travel in ambient air to obtain the same normalized peak-to-peak value. This is described in (1), where c_{air} corresponds to the gas concentration in ambient air, $\langle L_{sample}\rangle$ to the mean path length in the sample, and c_{sample} to the gas concentration in the sample.

$$\langle L_{eq}\rangle_{exp} \cdot c_{air} = \langle L_{sample}\rangle \cdot c_{sample} \tag{1}$$

It should be noted that the obtained L_{eq} value is dependent of both the gas concentration and the scattering properties of the medium.

B. Simulations

The simulation performed in this study is based on the Monte Carlo concept, implemented by the ASAP™ software [7]. Monte Carlo is a statistical method and the basic idea is to launch a large number of photons into the sample where each photon experiences an individual random walk through the sample based on its optical properties [8].

By studying the rays reaching the detector in the simulations, the equivalent mean path length, $\langle L_{eq}\rangle_{sim}$, could be calculated for all models used in the study. For every ray ASAP™ computes information such as the flux at every surface it enters or gets reflected off, as well as the distance it has traveled in all media. We then calculate $\langle L_{eq}\rangle_{sim}$ by adding up, for all rays, the product of the distance, L, each individual ray has traveled in the air space and its corresponding flux, ϕ, when reaching the detector, and dividing it by the total flux reaching the detector. This is described in (2) where n is the total numbers of rays reaching the detector.

$$\langle L_{eq}\rangle_{sim} = \frac{\sum_{i=1}^{n} L_i \cdot \phi_i}{\sum_{i=1}^{n} \phi_i} \tag{2}$$

C. Frontal sinus models

The tissue-like phantom model used in the simulations and the experiments is shown in Fig. 2, symbolizing measurements on the frontal sinuses. Two white Delrin-type plastic blocks were used, denoted primary scatterer S_1 and secondary scatterer S_2, respectively, with thickness l_1 and l_2, respectively, with optical properties similar to human tissue. A variable air gap was placed in between the blocks to represent measurements of the human frontal sinuses. In the simulations the optical properties of the scattering material were set to g=0.87, μ_s=14 mm^{-1}, and μ_a=0.0005 mm^{-1}, which were measured for one of the Delrin plate using the integrating-sphere technique [9].

To investigate the feasibility of imaging of the frontal sinuses, a new model was created and implemented in ASAP™. The sinuses in the model were represented by two ellipsoids (25 mm high, 20 mm wide, 10 mm deep) embedded at a depth of 10 mm in a scattering medium, with optical properties set to g=0.87, μ_s=16 mm^{-1}, and μ_a=0.0005 mm^{-1} [6]. The dimensions of the ellipsoids as well as the location and optical properties of the scattering medium are chosen to mirror reality.

The backscattering detection geometry used in the experiments was also included in the two models studied. In Fig. 2 the different parts of the detection can be seen. Like in the

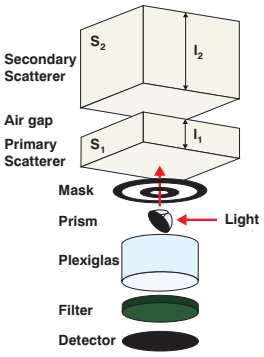

Fig. 2. Phantom models used in experiments and simulations representing measurements on the human frontal sinuses with a backscattering detection geometry [4], [5].

experiments, the photons were selected in the simulations by an annular aperture, with an inner diameter of 10 mm and outer diameter of 21 mm.

III. Results

Data obtained from experimental measurements and simulations from the tissue-like phantom are shown in Fig. 3. The influence of the air gap distance between the scatterers as well as the thicknesses of the scatterers has been investigated. In Fig. 3a l_1 has been kept constant to 3 mm and in Fig. 3b l_2 has been kept constant to 30 mm. As can be seen in the figures the agreement between the experiments and the simulations is very satisfying. In both simulation and experiment we observed an increase in the signal for an increase thickness of S_2. Intuitively thus can be understood since S_2 allows more signal photons that have traveled over the air gap to be scattered back to the detector. An increase of the signal can also be seen for a deceasing thickness of S_1. This behavior can be explained by the so-called "short-cut" photons, which are those photons that have never traveled over the air gap but only been scattered in S_1 before reaching the detector. These photons only contribute to the L_{eq} by a diluting factor. That the signal starts by increasing as the air gap increases and then falls off after a certain air gap value can be understood from the finite size of the detector. The signal behavior is explained in more detail in Refs [4] and [5], where the influence of the annular aperture of the detection geometry and the scattering properties of the two scatterers has also been investigated.

The frontal imaging simulations and the experimental results from measurements on the frontal sinuses of a healthy volunteer are shown in Fig. 4. The model used for frontal imaging simulations is shown in Fig. 4a, and in Fig. 4b the simulated L_{eq} for the model is presented. It can clearly be seen that the technique presented has the potential to spatially resolve the cavities. Fig. 4c shows measurements performed on the volunteer. About 10 measurements on and off right and left frontal sinus, respectively, were performed and an average

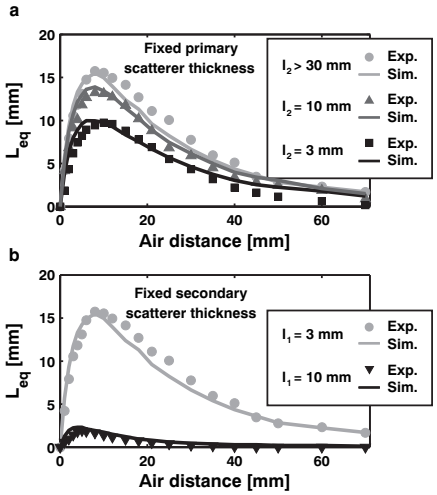

Fig. 3. The equivalent mean path length, L_{eq}, as a function of air gap distance in phantom experiments and simulations for the backscattering detection model shown in Fig. 2a, representing measurements on the human frontal sinuses. (a) Fixed primary scatterer thickness l_1=3 mm. (b) Fixed secondary scatterer thickness l_2=30 mm [4], [5].

of these measurements is presented. The measured L_{eq} values are in the same range as the simulated L_{eq} values.

Preliminary studies of the maxillary sinuses, in a transmission detection geometry, were also performed. The fibre was placed inside the mouth on the palate while the detector was positioned on the cheekbone. A larger L_{eq} is expected in this detection geometry since it avoids the problem of "short-cut" photons. Almost all photons detected must have traveled over the air-filled cavity and thus contain information about the gas of interest. An experimental curve recorded on a human maxillary sinus is shown in Fig. 5. It was recorded under very non-optimal conditions with a laser power of only 0.2 mW, and with extremely little light passing to the detector. The signal shown in the figure corresponds to an air path of about 25 mm, which is in agreement with expected size of the human maxillary sinus.

IV. Conclusion and Discussion

The presented study clearly shows the possibility of using the introduced diode laser absorption spectroscopy based technique for sinus studies. To investigate the clinical usefulness of the approach, measurements have to be performed on patients affected by inflammation and on healthy volunteers. The phantom studies have resulted in a better understanding of the possible signal behavior, which can be very valuable when performing further measurements on patients.

The experimentally obtained data and the simulated data for frontal sinus studies show a good agreement for both the tissue-like phantom measurements and the volunteer for

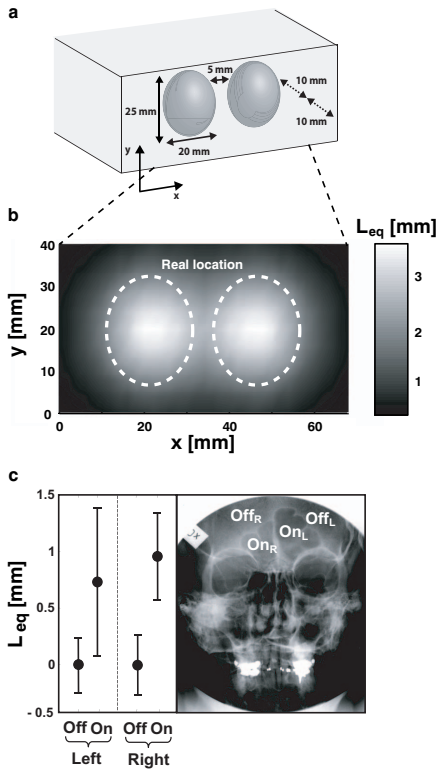

Fig. 4. (a) Model used in ASAP™ to simulate imaging of the frontal sinuses. (b) Simulated equivalent mean path length, L_{eq}, obtained when scanning over the model using backscattering detection geometry [5]. c) To the left: The average L_{eq} from measurements on and off the frontal sinus on a healthy volunteer (as shown to the right) together with error bars corresponding to one standard deviation. To the right: X-ray image on the volunteer, showing the extent of the frontal sinuses [4].

the limited setup conditions studied so far. This has given us confidence in using simulation to further guide and optimize the technique presented. Our very preliminary data on human maxillary sinuses indicate that diagnostics in such locations should also be quite feasible.

As briefly mentioned in the introduction, sinusitis normally occurs via blockage of the small tubes connecting the sinuses to the nasal cavity. It might be possible to detect sinusitis at an early state by studying the gas transport between the nasal cavity and the sinuses. By inhaling another gas such as helium, the time-constant of the gas flow into the sinuses can be measured. If the channels are totally blocked, no change in the signal should be measured [4].

In the study presented, molecular oxygen has been studied. We recently showed a possibility of detecting two gases simultaneously, molecular oxygen at 760 nm and water vapor

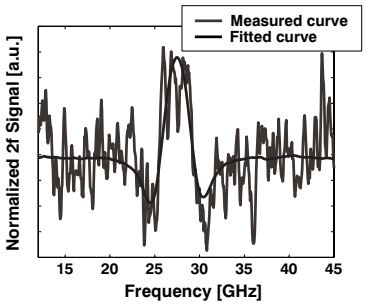

Fig. 5. Recorded normalized 2f signal, obtained due to molecular oxygen absorption, from measurements on a human maxillary sinus in a transmission detection geometry. The signal recorded corresponds to a L_{eq} value of about 25 mm.

at 980 nm, during the drying process of wood. By detecting two gases at the same time and creating the ratio of the two obtained L_{eq} values for the gases, the influence of the scattering properties of the sample could be neglected. This assumes that the scattering properties are about the same for the two wavelengths. This would then provide more reliable information on the actual gas concentration within the sinuses.

ACKNOWLEDGMENT

The authors are grateful to Stefan Andersson-Engels and Kjell Jonsson for valuable discussions. The authors would also like to thank Breault Research Inc. for providing the ASAP™ software. This research was supported by the Swedish Research Council and the Knut and Alice Wallenberg Foundation.

REFERENCES

[1] B. Drettner, *In: The nose: Upper airway physiology and the atmospheric environment*, Eds: Proctor DF, Andersson I. Elsevier Biomedical Press, Amsterdam, Holland, pp. 145 – 162, 1982.
[2] Health Matters, Sinusitis, Nat. Inst. of Allergy and Infectious Diseases, US Dept. of Health and Human Services, Bethesda, 2005.
[3] P. Stierna, G. Karlsson, I. Melén, and M. Jannert, "Aspect on sinusitis - Diagnosis and threatment in adults," Proceedings from Meeting of the Swedish Association of Otorhinolaryngol, HNS, Stockholm, 1995.
[4] L. Persson, K. Svanberg, and S. Svanberg, "On the potential of human sinus cavity diagnostics using diode laser gas spectroscopy," *Appl. Phys. B*, vol. 82, pp. 313–317, 2006.
[5] L. Persson, E. Kristensson, L. Simonsson, and S. Svanberg, "Monte Carlo simulations of optical human sinusitis diagnostics," unpublished, 2006.
[6] T. Vo-Dinh, "Biomedical Photonics Handbook," CRC Press LLC, New York, 2003.
[7] B. Michel and T. Beck, "Raytracing in medical applications," *Lasers & Photonics*, vol. 5, pp. 38–41, 2005.
[8] L. Wang, S. L. Jacques, and L. Zheng, "MCML - Monte Carlo modeling of light transport in multi-layered tissues," *Computer Methods and Programs in Medicine*, vol. 47, pp. 131–146, 1995.
[9] J. A. Jacquez and H. F. Kuppenheim, "Theory of the integrating sphere," *J. Opt. Soc. Am*, vol. 45, pp. 460–470, 1955.
[10] M. Andersson, L. Persson, M. Sjöholm, and S. Svanberg, "Spectroscopic studies of wood-drying processes," *Optics Express*, vol. 14, pp. 3641–3653, 2006.

Paper IX

Approach to optical interference fringes reduction in diode laser absorption spectroscopy

L. Persson, F. Andersson, M. Andersson, and S. Svanberg.
Appl. Phys. B **87**, 523–530 (2007).

Appl. Phys. B (2007)
DOI: 10.1007/s00340-007-2593-y

Applied Physics B
Lasers and Optics

L. PERSSON[1,✉]
F. ANDERSSON[2]
M. ANDERSSON[1]
S. SVANBERG[1]

Approach to optical interference fringes reduction in diode laser absorption spectroscopy

[1] Division of Atomic Physics, Lund University, P.O. Box 118, 22100 Lund, Sweden
[2] Centre for Mathematical Sciences, Lund University, P.O. Box 118, 22100 Lund, Sweden

Received: 6 October 2006 / Revised version: 18 January 2007

ABSTRACT The advantage of a new scheme for balanced detection has been investigated to reduce the influence of optical interference fringes when performing diode laser gas absorption spectroscopy employing lock-in amplifiers and pigtailed lasers. The influence of the fringes has been reduced by comparing the lock-in 2 f signal due to the gas sample with that of a reference beam. The frequency regions outside the absorption feature have been used to obtain information on the interference fringe impact on the signal of interest. We have demonstrated an efficient way to reduce the influence of such fringes by employing this technique combined with non-linear signal processing methods. The different steps of the algorithm are presented. In the experimental arrangement presented, a reduction of the optical interference fringes by about 10 times is achieved, as demonstrated in measurements on molecular oxygen around 761 nm. The new technique is compared with an analog technique for balanced detection and certain advantages of the computer algorithm are pointed out. In particular, the emerging field of gas spectroscopy in scattering solid media strongly benefits from the technique presented.

PACS 42.55.Px; 39.30.+w; 42.25.Hz

1 Introduction

Diode laser absorption spectroscopy is increasingly used for monitoring gases in environmental, biological, and medical contexts [1, 2]. In many applications the gas concentration is in the sub-ppm (part-per-million) range, i.e. when dealing with trace-gas detection. As a result, measurements are heavily influenced by noise, interfering signals, and drifts. Different modulation techniques have been introduced to reduce the detrimental effects of noise. These techniques are based on imposing a high-frequency modulation signal to the injection current of the light source. The signal is then detected using phase-sensitive techniques at some harmonic of the modulation frequency [2, 3]. Even though such techniques may cancel out the effect of excess laser noise and reduce background fluctuations, they do not compensate for optical interference fringes. Seldom discussed in the literature, interference fringes constitute in practice the real limitation in low-level gas analysis. Interference fringes appear in light being partially reflected at optical surfaces. A light beam vertically impinging from air onto a common optical material of refraction index n undergoes a fractional reflection of $R = ((n-1)/(n+1))^2 \approx 4\%$. The reflected light from different surfaces can interfere causing a complex pattern intensity Fabry–Pérot fringes. Even if surfaces are anti-reflection coated or tilted, residual intensity variations easily occur on the per mille intensity scale. Clearly, this is of no concern for substantial absorption signals, but can become critical in the case of very weak absorptions, for which the sensitive modulation techniques have been developed.

Interference fringes can originate from various parts of the optical path between the laser and the detector. The fringes may obscure weak absorption signals if the free spectral range of the optical fringes is in the same order as the line width of the absorption signal, the half width of the fringes being also in this range due to the low finesse ($I_{\max}/I_{\min} = ((1+R)/(1-R))^2 \approx 1.2$ for $R = 4\%$) [4]. Several techniques have been introduced over the years to reduce the influence of optical interference fringes. Specific examples include signal averaging, mechanical vibration, and balanced detection [5–8]. Mechanical vibrations, however, are not applicable when using a fixed-optical-surface pigtailed laser, which is attractive for different reasons to be further discussed.

Balanced detection is commonly used to cancel out laser intensity fluctuations such as optical interference fringes. The general idea is to split the initial laser beam into two, where one beam, called the sample beam, passes through the sample, and the other beam, called the reference beam, goes directly to a detector. The analog balanced detection techniques can be divided into two groups. The first is based on subtraction of small currents (μA range) from photodiodes [9, 10], while the second is based on subtraction of voltage signals created by two identical transimpedance amplifiers [11–14]. Both techniques commonly use a feedback loop in order to minimize the difference between the detector signals. Subtraction of current signals should give better performance but requires careful design and closely mounted matched detectors. In practice this may be hard to implement and therefore solutions based on subtraction of signals from transimpedance amplifiers have been introduced. While these methods clearly improve the signal recovery they have certain drawbacks. The two detectors should be placed close to each other, in order to minimize additional noise and to optimize performance. The analog balanced detection method also frequently assumes

✉ Fax: +46-46-222-4250, E-mail: linda.persson@fysik.lth.se

that the reference beam power is larger than the sample beam power, as well as that matched detectors and matched transimpedance amplifiers are used. In many applications these conditions are not feasible, as discussed below.

Historically, diode laser spectroscopy has been performed on well-defined atmospheric beam paths, frequently in absorption cells, where the conditions with regard to the geometry and transmission are very stable (see [14] for an extensive review of molecular oxygen diode laser spectroscopy performed under such conditions). Then the cell can be evacuated allowing a subtraction of persistent fringes. In contrast, in applications recently developed in our group [15–19], the gas cell is replaced by a test sample that attenuates and scatters light differently during the measurements or on a day to day basis, which puts new demands on the detection- and signal-processing systems. In [17], wood-drying processes were studied by spectroscopic measurement of oxygen and water vapor. It turned out that the sample beam intensity varied by a factor of 10–100 depending on the water content. Spectroscopic measurements on pharmaceutical tablets put similar demands due to the differences of thickness and density of the tablets [18]. Further applications resulting in similar demands are measurements for medical diagnostics. In [19], spectroscopic measurements on human maxillary sinuses were described. It turned out that the intensity of the sample beam varied by a factor of 20 depending on the person that was studied even if the measurement procedure was the same. Thus, it is not enough to calibrate the system for a limited intensity range or use commonly known techniques to suppress non-linear disturbances, fringes, etc. The situations with sample beam intensity varying by several orders of magnitude depending on the state of the test sample is vastly different from the conventional trace-gas measurements in an absorption cell.

We largely use pigtailed lasers since it is not practical to measure on solid test samples with ordinary lasers. Backscattered light from the sample that enters the laser, fringes due to fibre coupling based on lenses, and handling laser heads close to a test sample at measurement all can be problematic. The present paper focuses on applications based on pigtailed lasers which are easy to implement in portable measurement systems for a variety of spectroscopic studies.

In the present paper, we describe a specific way of using software-based balanced detection to remove optical interference fringes in strongly varying measurement situations as described above. Our approach is based on using parts of the recorded signals falling in the frequency range outside the absorption region in order to estimate imperfections of the measurement system. In the reference beam, unaffected by gas absorption, fringe structures are also recorded in the frequency region of the gas absorption. The regions outside the absorption can be used to estimate the fringe contribution to the gas signal. In addition, the algorithm presented compensates for possible non-linear effects in the response of the two different detection arms as well as different offsets. This method can be applied to any system and be combined with other customary techniques such as mechanical vibrations to further reduce fringes not related to the common light path.

In Sect. 2 the experimental arrangements for this study are described. The different artifacts that occur in typical diode laser absorption spectroscopy experiments are then discussed together with an explanation of the presented software-based method and a previously discussed analog method for achieving balanced detection. The procedure to evaluate the gas content from the balanced-detection signals is then discussed. Results from both the software-based balanced detection and the balanced detection achieved by the electronic circuit are then shown and discussed. Finally, conclusions are drawn.

2 Experimental arrangements

Schematic drawings of the experimental arrangements used in the software-based and the analog balanced detection approaches are shown in Fig. 1. Common for both cases (Fig. 1a), a single-mode fibre-pigtailed thermoelectrically cooled DFB laser diode (Nanoplus, Germany) was used as a light source. The laser delivered about 4 mW at around 760 nm, where the molecular oxygen A-band is located. The wavelength of the light was tuned across the R11Q12 absorption line by supplying a 4 Hz saw-tooth ramp to the laser driver current. A 10 kHz sine wave was also superimposed on the laser driver current in a wavelength-modulation scheme to achieve sensitive detection.

The light was split 90%/10% with a single-mode fibre-coupled beam splitter (Laser2000, Sweden) with an insertion loss of about 5%. The fibre carrying about 10% of the light was directly guided to a silicon detector (UDT 10DP/SB) via an attenuation filter ($\times 10$). Thus, about 0.035 mW light enters the detector, which was connected to a transimpedance amplifier. The other fibre carrying about 90% of the output from the laser was connected to a collimating lens package (Thorlabs CFC-5-760). The light then travels over a certain air distance, or an absorbing and scattering medium, before being detected with a second identical silicon detector or a photomultiplier tube (PMT), which is connected to an identical transimpedance amplifier as the one used for the reference detector. An attenuation filter was mounted in between the fibre and the detector for the case of a non-scattering sample. The collimating package was mounted on a z-translator providing variable air distances. For the amplification, Hamamatsu C7319 units were available and used.

2.1 *Setup for software-based balanced detection*

In the left-hand part of Fig. 1b the arrangement to perform software-based balanced detection is shown. The reference signal was sent to an oscilloscope via a lock-in amplifier (EG&G Princeton Applied Research 5209), where the 2 f signal was recorded. This signal will be referred to as the reference signal. The signal from the sample detector was split into two parts; one part directly was connected to the oscilloscope (referred to as the direct signal) while the second part was sent via a second lock-in amplifier (EG&G Princeton Applied Research 5209) before being connected to the oscilloscope where the 2 f signal was recorded. This signal will be referred to as the sample signal.

2.2 *Setup for analog balanced detection*

In order to test the performance of an auto balanced detection approach, based on differential transimpedance am-

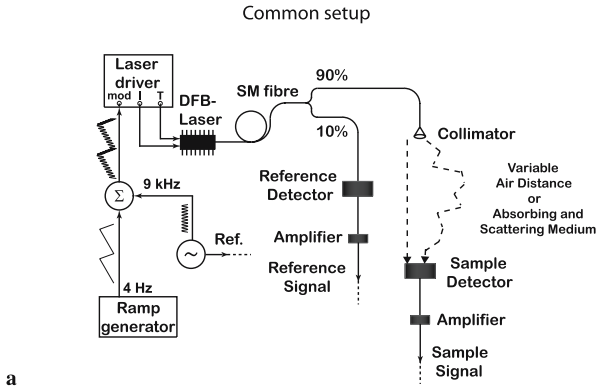

a

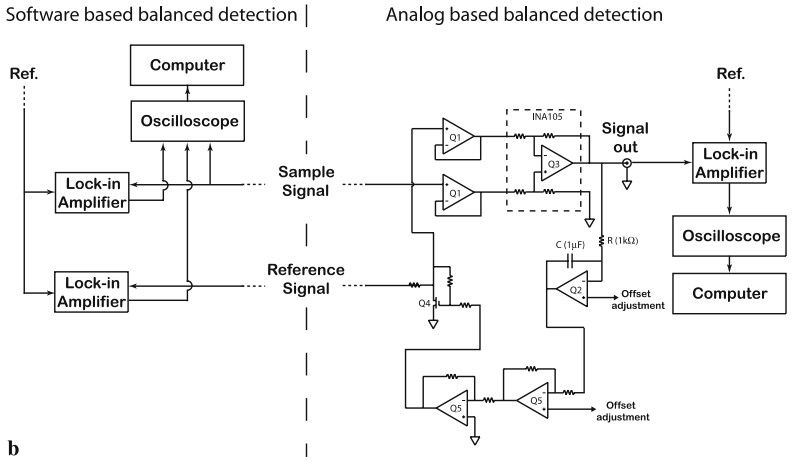

b

FIGURE 1 (**a**) Schematic drawing of experimental arrangement for diode laser gas absorption spectroscopy providing balanced detection. (**b**) In the *left-hand part* the arrangement for software-based balanced detection is shown and in the *right-hand part* the arrangement for analog balanced detection is shown [11]. The following components were used in the device: Q1 and Q5 – OP470 low-noise op-amp, Q2 – LF356 low-noise op-amp, Q3 – INA105 unity-gain differential amplifier, and Q4 – 2N5457 MOSFET

plification, we implemented an electronic cancellation device, according to [11], shown to the right in Fig. 1b. The sample signal is buffered by Q1 and fed into a unity-gain differential amplifier (INA105). The reference signal was connected to the unity-gain differential amplifier via a field-effect transistor (Q4). A feedback loop consisting of Q2 and Q5 controls the input level of Q4 (attenuation factor), trying to minimize the output of the differential amplifier. Thus, the output of the differential amplifier is proportional to $U_{\text{sample}} - U_{\text{reference}}$. The time constant of the feedback loop ($t = 0.001$ s) is set by the 1 kΩ resistor and the 1 μF capacitor mounted closely to Q2. The output of the noise cancellation circuit was led into a lock-in amplifier of the same type as used in the software-based balanced detection scheme, and the 2 f signal was recorded on an oscilloscope.

3 Data analysis

In order to achieve optimal signal retrieval for weak gas absorption signals we need to handle (a) interference fringes, (b) laser intensity noise, (c) non-linear detector response, and (d) different zero detector offsets.

Fringes mimicking real signals are most critical. They can be eliminated by studying spectral regions outside the expected absorption imprint. This could in principle be done in an exact way from the reference signal if the detection channels (detectors, amplifiers, and lock-ins) were identical, linear, and with a correct zero level. Since this might not be the case – Fig. 2 – the differential behavior between the two signals is described by a set of parameters corresponding to linear and non-linear phenomena, as discussed below.

3.1 *Software-based method for non-linear artifact suppression*

As mentioned above, two outputs from two detectors are measured; one detecting the light which has traveled over the gaseous sample to be analyzed and one measuring the reference light level. We will here denote the sample signal $p_{\text{samp}}(\nu)$ and the reference signal $p_{\text{ref}}(\nu)$. Ideally, $p_{\text{samp}}(\nu)$ and $p_{\text{ref}}(\nu)$ should be identical for ν-values outside the region of oxygen absorption. Hence, by considering the difference between the two signals we can determine the amount of oxygen in the measurement sample, since only effects of oxygen absorption should remain. The difference between the sample

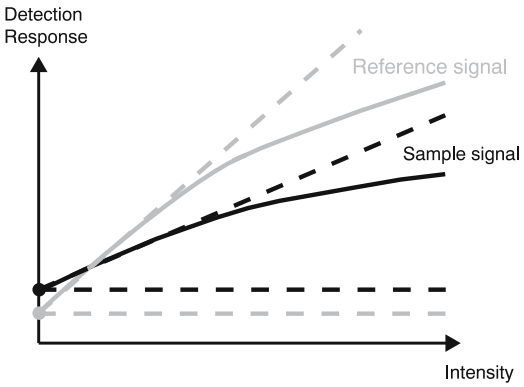

FIGURE 2 Schematic drawing of imperfections in detection arm response (heavily exaggerated)

signal and the reference signal will thus give us the balanced-detection signal, which we will denote $p_{\mathrm{bds}}(\nu)$. However, there are several practical measurement effects that need to be suppressed before constructing the balanced-detection signal.

Let $w(\nu)$ be a window function that vanishes in the neighborhood of the oxygen absorption region, and goes smoothly to 1 outside the region. We assume that data are sampled at points $\nu = \{\nu_j\}$, and introduce column vectors $\mathsf{p}_{\mathrm{samp}}$, $\mathsf{p}_{\mathrm{ref}}$, and $\mathsf{p}_{\mathrm{bds}}$, containing samplings of p_{samp}, p_{ref}, and p_{bds} at $\{\nu_j\}$, respectively. Furthermore, let W be a diagonal matrix with the values of $w(\nu_j)$ as entries. In the case of no difference in offset or in amplification, one would expect that

$$p_{\mathrm{samp}}(\nu)w(\nu) \approx p_{\mathrm{ref}}(\nu)w(\nu)\,. \tag{1}$$

However, due to imperfections of the measurement system, effects from various components bring degradation of the processing. This can be accounted for by considering non-linear effects and different background offsets in the two detectors and the downstream processing. We account for the effects by estimating their impact outside the oxygen absorption region. We expect deviations from (1) due to the effects mentioned above. Hence, we assume that

$$\begin{aligned} p_{\mathrm{samp}}(\nu)w(\nu) \approx \Big((l_0 + l_1\{\nu-\nu_0\})\,p_{\mathrm{ref}}(\nu) \\ + k_0 + k_1\{\nu-\nu_0\} + k_2\left\{(\nu-\nu_0)^2\right\}\Big)w(\nu)\,. \end{aligned} \tag{2}$$

The constants introduced have the following interpretation:

- l_0: Amplification compensation
- l_1: Non-linear response compensation
- k_0: Background offset compensation
- k_1: Intensity-dependent laser stray-light compensation
- k_2: Residual non-linear intensity compensation

all of which are due to the differential behaviors of the two individual detectors and imperfections in the subsequent signal handling.

We can thus estimate the parameters

$$\boldsymbol{h} = \left(l_0\, l_1\, k_0\, k_1\, k_2\right)^{\mathrm{T}}$$

by minimizing the residual of the matrix equation ($\mathsf{1}$ is the column vector containing 1 as elements)

$$\begin{aligned} \boldsymbol{W}\boldsymbol{p}_{\mathrm{samp}} &\approx \boldsymbol{W}\Big(\boldsymbol{p}_{\mathrm{ref}}\{\nu-\nu_0\} \circ \boldsymbol{p}_{\mathrm{ref}}\mathsf{1}\{\nu_j-\nu_0\}\left\{(\nu_j-\nu_0)^2\right\}\Big)\boldsymbol{h} \\ &= \boldsymbol{W}\,\boldsymbol{A}\,\boldsymbol{h}\,, \end{aligned} \tag{3}$$

where ν_0 is the center frequency and where $\circ$ denotes the Hadamard product [20]. Note that (3) is largely overdetermined.

We solve (3) in a (weighted) least-squares sense by forming and solving the normal equations:

$$\mathsf{h} = (\mathsf{A}^{\mathrm{T}}\boldsymbol{W}\mathsf{A})^{-1}\,\mathsf{A}^{\mathrm{T}}\,\boldsymbol{W}\,\mathsf{p}_{\mathrm{samp}}\,.$$

With these $\boldsymbol{h}$-parameters at hand, we define the balanced-detection signal as

$$\begin{aligned} \mathsf{p}_{\mathrm{bds}} = \mathsf{p}_{\mathrm{samp}} - \big((l_0 + l_1\{\nu-\nu_0\})\mathsf{p}_{\mathrm{ref}} \\ + k_0 + k_1\{\nu-\nu_0\} + k_2\{(\nu-\nu_0)^2\}\big)\,. \end{aligned} \tag{4}$$

3.2 *Standard analog artifact suppression*

The analog balanced detection device, based on [11], is in principle a PI controller (integrator with a proportional gain) that adjusts the attenuation of the signal from the reference detector by changing the dynamic resistance of a field-effect transistor (FET). The aim is to minimize the output level of the device and thus suppress low-frequency noise caused by the laser, detector, and fringes. The time constant of the feedback loop is set by two components (C and R in Fig. 1b to the right) and is on the order of 1 ms. Thus, the feedback loop is not affected by the 2 f signal at 20 kHz that is transferred more or less without any distortion. An additional advantage is that the need for lock-in amplifiers with high dynamic range has decreased due to lower signal amplitudes in the low-frequency range.

3.3 *Gas content evaluation*

The gas concentration is evaluated using the Beer–Lambert law stating that

$$I(\lambda) = I_0(\lambda)\mathrm{e}^{-\sigma(\lambda)cL}\,,$$

where $I_0(\lambda)$ is the initial intensity and $I(\lambda)$ is the intensity of the light that has traveled a distance L over a sample with the gas concentration c and the absorption cross section $\sigma(\lambda)$ [4]. Beer–Lambert's law also states that for low absorptions the fractional absorption is proportional to the concentration and the optical path length. Therefore, the balanced-detection signal must be normalized to the amount of light reaching the detector (direct signal). The amplitude of the balanced-detection signal is proportional to the gas content in the sample and is therefore the parameter of central interest in the gas analysis.

When starting a measurement, an ideal experimental absorption profile, $p_{\mathrm{i}}(\nu)$, is first measured where the noise is much smaller than the detected oxygen signal. This signal is obtained by measuring over an air distance of several meters. Once a clean balanced-detection signal is obtained, we can

match it against our computed $p_{\mathrm{bds}}(\nu)$. In the matching process, we compensate for drifts in the frequency scale. Thus, we match the balanced-detection signal against the ideal function with regard to both location and amplitude. This is done by mimicking an autocorrelation function; we convolve $p_{\mathrm{bds}}(\nu)$ with $p_{\mathrm{i}}(\nu)$ and detect the resulting peak position, denoted ν_s. Once the peak position is known, we repeat a similar approach as for the construction of the balanced-detection signal with the algorithm; we form

$$(1-\boldsymbol{W})\,p_{\mathrm{i}} = (1-\boldsymbol{W})\left(p_{\mathrm{bds}}1\right)m = \boldsymbol{W}\,\boldsymbol{B}\,m\,, \tag{5}$$

and solve it for parameters m by forming and processing the corresponding normal equations. The global intensity parameter is then estimated (peak-to-peak value of the fit), which corresponds to the gas content after calibration.

4 Results and discussion

Several measurements were performed with different added air distances to investigate the performance of the implemented software-based balanced detection method. To investigate the influence of the different components in $\boldsymbol{h}$, (3) was solved with different $\boldsymbol{h}$-parameter combinations. Figure 3a shows signals obtained during measurements with an air distance of about 10 mm. This corresponds to an oxygen fractional absorption of 2.5×10^{-4} on the R11Q12 line at 760.445 nm (vacuum wavelength). Two identical photodiodes were used to detect the sample signal and the reference signal. In the left-hand part of Fig. 3a, the unprocessed sample signals together with the fitted reference signals are shown. The balanced-detection signals obtained according to (4) are shown in the right-hand part of the figure together with the fitted ideal experimental absorption profile. As can be seen in the figure, all components of $\boldsymbol{h}$ are needed to obtain a satisfactory balanced-detected signal. However, the influence of l_1 is very small, i.e. the non-linear amplification response compensation is not of great influence when using two identical detectors in our experimental setup.

The same procedure was carried out after changing the sample detector to a PMT. The reference signal was still recorded by a photodiode. The influence of the different $\boldsymbol{h}$-parameter combinations is shown in Fig. 3b. In this figure it can be observed that l_1 is of greater influence when employing detectors of different types to record the sample signal and the reference signal than when two identical detectors are used.

The observations in Fig. 3 and our general experience can be summarized in the following points:

- In the case with identical detectors it is sufficient to parameterize with fewer variables, while in the case of different types of detectors all parameters discussed are significant.
- In applications where the light intensity varies widely (large dynamic range) residual differences between similar detectors are more important and again call for more detailed parametrization. Thus, we retain all parameters for general purposes.

To compare the presented software-based method with the analog method [11], measurements with both approaches were performed with an air distance of about 6 mm (fractional

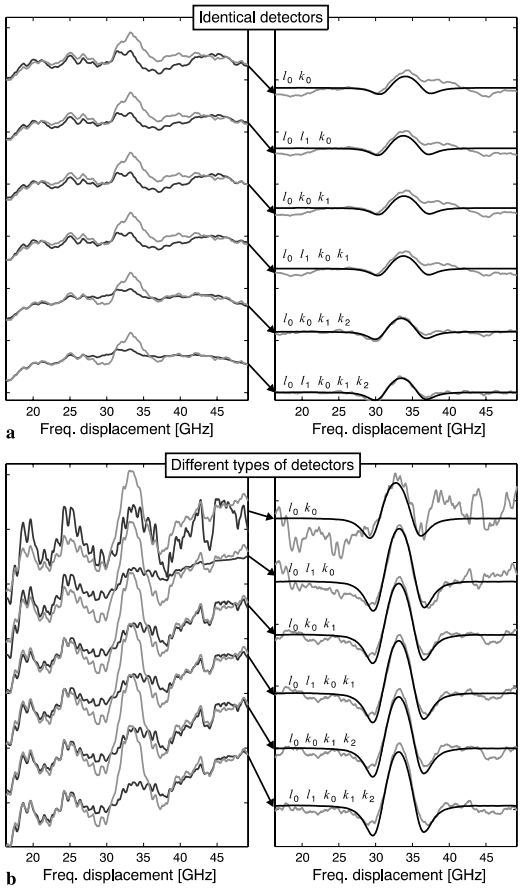

FIGURE 3 Typical curves obtained during software-based balanced detection with 10 mm of air distance. *To the left*: the *gray curves* show $\boldsymbol{p}_{\mathrm{samp}}$ and the *black curves* the fitted $\boldsymbol{p}_{\mathrm{ref}}$. *To the right*: the *gray curves* show the corresponding $\boldsymbol{p}_{\mathrm{bds}}$ and the *black curves* the fitted $\boldsymbol{p}_{\mathrm{i}}$. The influences of the different $\boldsymbol{h}$-parameter combinations are presented. (**a**) Two identical detectors have been used to detect the sample beam and the reference beam. (**b**) Two different types of detectors have been used to detect the sample signal and the reference signal

absorption of 1.5×10^{-4}). An attenuation filter was placed in front of the sample detector to provide a reference beam power 100 times the sample beam power ($P_{\mathrm{ref}}/P_{\mathrm{samp}}\approx100$). This was done to optimize the performance of the analog device. In Fig. 4a obtained balanced-detection signals from both methods are shown when using two identical detectors. The measured unprocessed sample signal is also included. It can be seen that when performing analog balanced detection a large offset remains. Attempts were made to compensate for this by adjusting the offset in the device, but no difference could be seen. An 'ideal' experimental absorption profile was fitted to the software-based balanced-detection signal. The global intensity parameter, i.e. the peak-to-peak value of the fitted ideal experimental absorption profile, was estimated to be 0.44 scale units. This corresponds to an air distance of

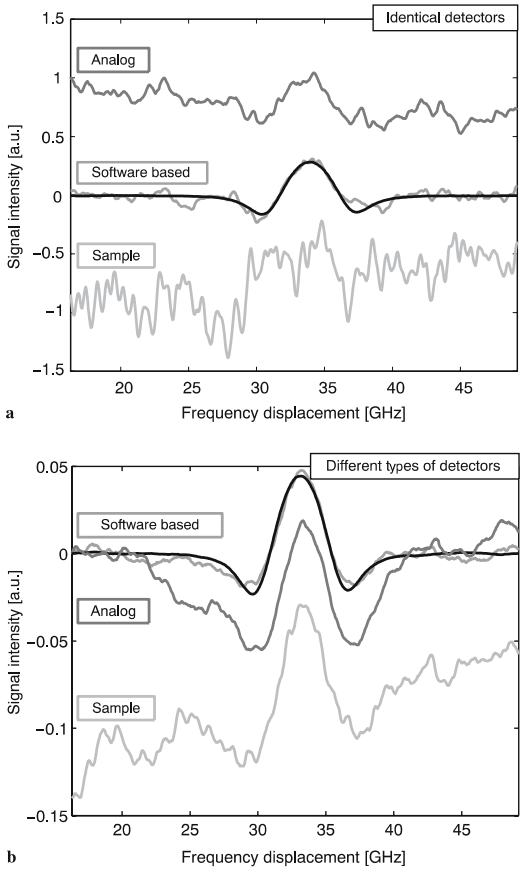

FIGURE 4 Achieved balanced-detection signals by using the software-based algorithm, $\boldsymbol{p}_{\mathrm{bds}}$, and the analog device. The unprocessed sample signal measured, $\boldsymbol{p}_{\mathrm{samp}}$, is also shown. No collimator package was used on the sample beam. (**a**) About 6 mm of added air distance. Two identical detectors were used to detect the sample signal and the reference signal ($P_{\mathrm{ref}}/P_{\mathrm{samp}} \approx 100$). (**b**) About 10 mm of added air distance. Two different types of detectors were used to detect the sample signal and the reference signal ($P_{\mathrm{ref}}/P_{\mathrm{samp}} \approx 4$). The curve with *darkest tone* is an 'ideal' experimental curve, $\boldsymbol{p}_{\mathrm{i}}$, fitted to the data

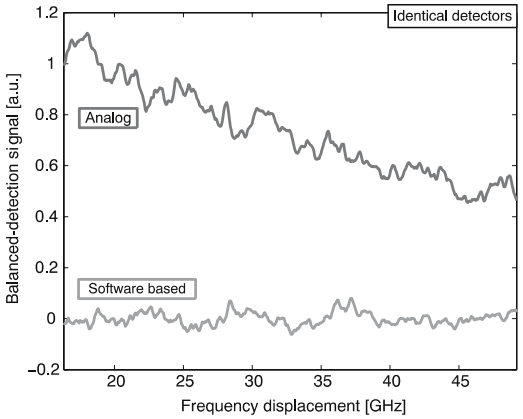

FIGURE 5 Achieved balanced-detection signals with no added air distance by using the software-based method, $\boldsymbol{p}_{\mathrm{bds}}$, and the analog device. Two identical detectors were used to detect the sample signal and the reference signal. No collimator package was used on the sample beam

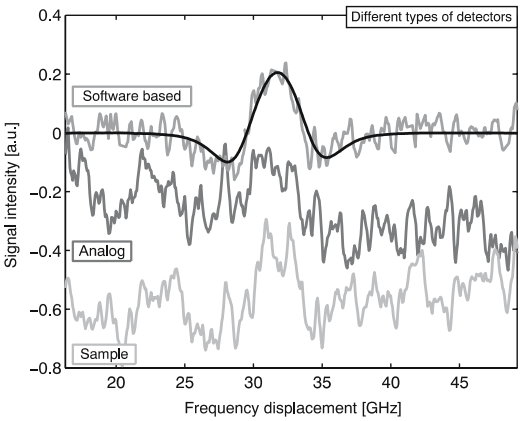

FIGURE 6 Achieved balanced-detection signals by using the software-based method, $\boldsymbol{p}_{\mathrm{bds}}$, and the analog device measured through the maxillary sinus on a human volunteer. The unprocessed sample signal measured, $\boldsymbol{p}_{\mathrm{samp}}$, is also shown. The curve with *darkest tone* is an 'ideal' experimental curve, $\boldsymbol{p}_{\mathrm{i}}$, fitted to the data

6.3 mm (calibration information is provided in Fig. 7 in the appendix).

Figure 4b shows signals obtained for a 10-mm air distance when using detectors of different types. The reference signal power was now only a factor of four larger than the sample signal power ($P_{\mathrm{ref}}/P_{\mathrm{samp}} \approx 4$). It can be seen that both methods are able to retrieve the oxygen signal; however, the software-based method is more successful. The peak-to-peak value of the fitted ideal experimental absorption profile was estimated to be 0.07 local scale units. This corresponds to an air distance of 10 mm. In Fig. 4a and b, an optical interference fringe reduction of about 10 times by the use of the algorithm approach can be seen compared to the sample signal. In the case of the analog method a baseline correction is needed, which would require a software approach. Then the full computational technique put forward in the present paper rather would come to mind.

To study the noise level remaining after performing balanced detection, and thereby the limitations of the experimental arrangement together with the algorithm, measurements were done with no air distance between the light source and the sample detector. Ideally, this should result in a zero signal, since the sample signal should not contain any oxygen imprint. Figure 5 shows the balanced-detection signals obtained with the software-based and the analog methods when using two identical detectors. In this figure it is again obvious that the analog noise reduction device does not fully compensate for offset differences between the sample signal and the reference signal. A noise level of about 0.15 scale units remains after the data are processed by the algorithm.

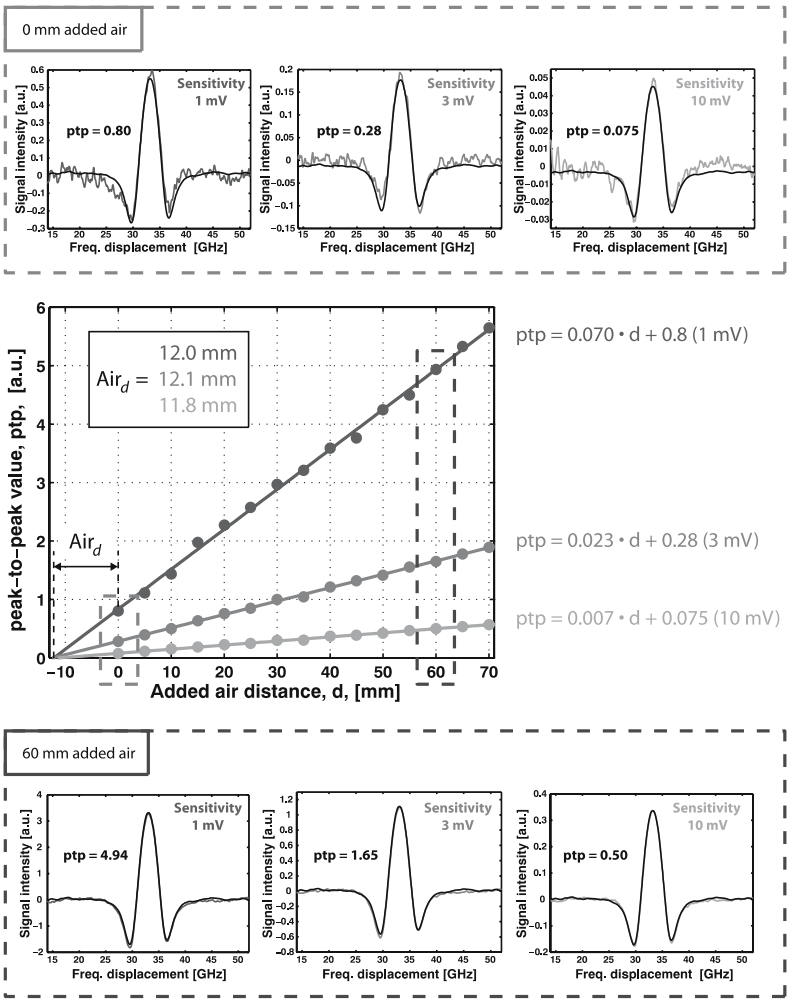

FIGURE 7 Results from measurements according to the standard addition method. Six obtained balanced-detection signals, p_{bds}, from 0 mm to 60 mm of added air distance measurements and the three different sensitivities used of the lock-in amplifier are included together with their estimated peak-to-peak values. The equations of the linear relationship between the peak-to-peak values and the added air distances for the three sensitivities are presented. The estimated unknown air distance, Air$_d$, of the collimator package was estimated to about 12 mm for all sensitivities

This corresponds to a signal of about 2 mm of air distance (a fractional absorption of 5×10^{-5}), which is a measure of the resolution of our experimental setup together with the algorithm.

As a final and most critical example we present data from a case where the sample is strongly scattering and attenuating. Here there is an unknown intensity relationship between the sample and the reference signals. Measurements on an air-filled human maxillary sinus cavity, located within the cranial skeleton below the orbital floor [19], are shown in Fig. 6. The fibre end is then placed inside the mouth on the palate and the multiply scattered light is detected externally on the cheek-bone by a handheld probe containing the PMT. The achieved balanced-detection signal in the software-based approach corresponds to an air distance of about 10 mm. In the figure it can clearly be seen that a larger 'noise floor' of the balanced-detection signal remains in the analog approach compared to the software-based method even though correction of the baseline would be performed.

The calibration of the system is discussed in detail in the appendix.

5 Conclusion

In theory, intensity perturbations from laser and fibres, before the fibre coupler, should be canceled out by the analog noise cancellation device used in the study for comparison. However, due to detector channels' imperfections with regard to non-linearities and offsets, electronic cancellation of noise, based on the design described in Fig. 1b, is, in practice, imperfect. Figure 4 shows that the performance of the analog device was a factor of about two worse than achieved in the software-based approach as evaluated by comparing the remaining 'noise floor' in the absence of an absorption signal.

The new approach is, in contrast to the analog technique, forgiving in terms of signal levels, gain settings, and offsets, since the technique adjusts for all these factors. In particular, it was demonstrated (Fig. 3b) that quite different detectors can be used and still a very satisfactory balanced detection can be achieved. However, we note that two lock-in amplifiers were employed in the software-based method in contrast to only one in the analog approach. Since intensity drifts due to optical interference fringes can be expected to occur on a slow time scale, the use of one lock-in amplifier sequentially for recording the sample and the reference signals should be feasible. Then, signal averaging individually for the two signals could be performed as customarily done in, for example, differential absorption lidar (DIAL) [21].

Clearly, the techniques presented here only compensate for 'upstream' fringes generated in and close to the laser source, while differential fringe effects in the two detector paths remain untreated. This is also the case for the analog approach.

However, major sources of such differential fringe generation (e.g. absorption cells) are not present in most of our applications. Rather, we deal with cases of free-air propagation (long-path-absorption remote sensing) or gas pores or cavities embedded in scattering media [15–19].

Our experience shows that substantial and very valuable improved signals are observed in practical measurements. As already mentioned, the technique described is particularly useful when pigtailed lasers are employed and customary fringe elimination by shaking is not possible. Possible fringes between the two detectors can still be eliminated, for example by mechanical vibration.

ACKNOWLEDGEMENTS This research was supported by the Swedish Research Council, the Swedish Foundation for Strategic Research, and the Knut and Alice Wallenberg Foundation.

Appendix

Calibration measurements

The standard addition method (see e.g. [4]) was used in order to further investigate the algorithm presented, and to calibrate our measured signals and thereby be able to estimate the air distance from a recorded peak-to-peak value. The method is based on adding known path lengths of air and measuring the peak-to-peak value for each distance. The measured values are then plotted as a function of added air. These values should be linear with regard to the added air distance, since the absorption is so low that the fractional absorption is proportional to the concentration and the distance the light has traveled. A collimator package, described in Sect. 2, was placed on the fibre end of the sample part. Due to the design of the package, an unknown air distance was added between the fibre tip and the sample detector. The collimator package was moved away from the light source, in 5-mm steps, and the peak-to-peak values of the obtained processed signals were estimated for the different air distances. Three different sensitivities (1 mV, 3 mV, and 10 mV) of the lock-in amplifier were used at each added air distance. In Fig. 7 the results can be seen. In the figure, six obtained balanced-detection signals, from 0 mm to 60 mm of added air distances, are also shown together with their estimated peak-to-peak values. As can be seen, the values follow the expected linear relationship with regard to the added air distance. The slope of the curves was estimated and can then be used as a calibration factor (included in the figure). The relationship between the different sensitivities can also be seen. The peak-to-peak values from a fixed air distance for different sensitivities of the lock-in amplifier should scale with the sensitivity of the unit. Our estimated slopes of the curves agree with this to a high precision. The unknown air distance, Air_d, in the collimator package could be estimated to be about 12 mm. Measurements from all sensitivities gave approximately the same value (also included in the figure).

REFERENCES

1 M.W. Sigrist (ed.), *Air Monitoring by Spectroscopic Techniques* (Wiley, New York, 1994)
2 P. Werle, Spectrochim. Acta A **54**, 197 (1998)
3 E.I. Moses, C.L. Tang, Opt. Lett. **1**, 115 (1977)
4 S. Svanberg, *Atomic and Molecular Spectroscopy*, 4th edn. (Springer, Berlin, 2004)
5 P. Werle, R. Mücke, F. Slemr, Appl. Phys. B **57**, 131 (1993)
6 D.R. Hjelme, S. Neegård, E. Vartdal, Opt. Lett. **20**, 1731 (1995)
7 V. Liger, Spectrochim. Acta A **55**, 2021 (1999)
8 S. Wu, T. Kimishimai, Y. Yoshi, H. Kuze, N. Takeuch, Opt. Rev. **9**, 189 (2002)
9 P. Hobbs, Appl. Opt. **36**, 903 (1997)
10 V. Liger, A. Zybin, Y. Kuritsyn, K. Niemax, Spectrochim. Acta B **52**, 1125 (1997)
11 C. Lindsay, R. Rade, T. Oka, J. Mol. Spectrosc. **210**, 51 (2001)
12 X. Zhu, D.T. Cassidy, Appl. Opt. **34**, 8303 (1995)
13 R. Engelbrecht, Spectrochim. Acta A **60**, 3291 (2004)
14 P. Vogel, V. Ebert, Appl. Phys. B **72**, 127 (2001)
15 M. Sjöholm, G. Somesfalean, J. Alnis, S. Andersson-Engels, S. Svanberg, Opt. Lett. **26**, 16 (2001)
16 L. Persson, K. Svanberg, S. Svanberg, Appl. Phys. B **82**, 313 (2006)
17 M. Andersson, L. Persson, M. Sjöholm, S. Svanberg, Opt. Express **14**, 3641 (2006)
18 T. Svensson, L. Persson, M. Andersson, S. Andersson-Engels, S. Svanberg, J. Johansson, S. Folestad, Non-invasive characterization of pharmaceutical solids using diode laser oxygen spectroscopy, manuscript in preparation (2007)
19 L. Persson, M. Andersson, T. Svensson, K. Svanberg, S. Svanberg, Non-intrusive optical study of gas and its exchange in human maxillary sinuses, manuscript in preparation (2007)
20 R.A. Horn, C.R. Johnsson, *Topics in Matrix Analysis* (Cambridge University Press, New York, 1994)
21 S. Svanberg, Differential absorption lidar (DIAL), in *Air Monitoring by Spectroscopic Techniques*, ed. by M.W. Sigrist (Wiley, New York, 1994), Chap. 3

Paper X

Non-invasive characterization of pharmaceutical solids by diode laser oxygen spectroscopy

T. Svensson, L. Persson, M. Andersson, S. Andersson-Engels, S. Svanberg, J. Johansson, and S. Folestad.

Appl. Spec. **61**, 784–786 (2007).

Noninvasive Characterization of Pharmaceutical Solids by Diode Laser Oxygen Spectroscopy

TOMAS SVENSSON,* LINDA PERSSON, MATS ANDERSSON, SUNE SVANBERG, STEFAN ANDERSSON-ENGELS, JONAS JOHANSSON, and STAFFAN FOLESTAD

Department of Physics, Lund University, Sweden (T.S., L.P., M.A., S.S., S.A.-E.); and Astra Zeneca R&D, Mölndal, Sweden

Index Headings: **Oxygen spectroscopy; Light scattering; Porosity.**

INTRODUCTION

Characterization of solid pharmaceuticals, ranging from monitoring of solid-state reactions to understanding tablet dissolution, is of great interest for pharmaceutical science.[1] The quality of the finished product highly depends on knowledge about the pharmaceutical materials used and the different unit operations involved in manufacturing of pharmaceuticals. Thus, availability of appropriate and reliable tools for measurements of physical and chemical properties of drug materials *in situ* during chemical and physical processing is a key for optimized processing. In early stages of pharmaceutical development a whole range of techniques for characterization of the solid state is available, addressing, for example, particle size and shape, density, porosity, calorimetry, thermo-mechanical properties, specific area, and crystallinity.[2] However, most of these techniques are slow and not well suited for fast laboratory-based or process applications. Process analytical technology (PAT) is a term describing a holistic approach to pharmaceutical manufacturing based on in-depth understanding through advanced process sensors and modeling tools.[3] In order to succeed with this, new tools are needed, e.g., with capability to directly measure physico-chemical attributes *in situ* of the mechanical process. In this context, tools based on spectroscopic techniques offer obvious advantages owing to their speed, compactness, versatility, and ability to perform noninvasive analysis.

By employing the spectroscopic technique referred to as gas in scattering media absorption spectroscopy (GASMAS), it is possible to extract information related to gas dispersed within highly scattering (turbid) materials.[4] In our case, the key is contrast between the sharp (GHz) absorption features of molecular oxygen located around 760 nm and the broad absorption features related to tablet bulk material. The technique is based on high-resolution diode laser absorption spectroscopy, and its main principle is illustrated in Fig. 1. Light is injected into a highly scattering sample, often utilizing optical fibers. The actual path length distribution of transmitted photons will depend on the scattering properties of the sample. Due to significant multiple scattering, the average photon path length greatly exceeds sample dimensions. For example, the average path length of photons that have traveled through a pharmaceutical tablet typically exceeds 10 cm.[5] During passages through air-filled pores, photons in resonance with an absorption line in the A-band of molecular oxygen can be absorbed. Oxygen absorption can be distinguished from bulk absorption due to the extremely narrow absorption features (GHz) exhibited by free gases. To resolve such narrow features, high-resolution spectroscopy must be employed. The resulting absorption signal depends on both the oxygen content and the scattering properties (photons path lengths) of the sample. Indirectly, it is thus related to mechanical properties such as porosity and particle size.

The GASMAS technique has previously been used to study the gas content in, for example, polystyrene foam, wheat flour, granulated salt, wood materials, fruit, and human sinuses.[4,6–9] Gas exchange dynamics has been studied by placing samples of wood and fruit in nitrogen atmospheres and monitoring the re-invasion of oxygen.[7,8]

In this paper we show the potential of using GASMAS for determination of physical and structural parameters of pharmaceutical solids. We present results from a study of pharmaceutical tablets made from two different sieve fractions (particle size distributions) and with different compression forces. In addition, the prospects of a broader use of this technique for pharmaceutical analysis are discussed.

EXPERIMENTAL

Instrumentation. A simplified schematic of the setup is given in Fig. 2. The instrumentation and corresponding data evaluation has been described in detail elsewhere.[10] Briefly, a temperature stabilized distributed feed-back (DFB) diode laser (NanoPlus, Germany) is repetitively wavelength tuned over one of the narrow absorption lines in the oxygen A-band (R11Q12, 760.445 nm vacuum wavelength). The DFB diode laser is pigtailed using a single-mode (SM) optical fiber, yielding an output of about 4 mW. Sensitivity was vastly increased by employing wavelength modulation spectroscopy (WMS), in this case implemented by imposing an $f = 9$ kHz harmonic modulation on the laser diode injection current. A 90/10% fiber splitter (Laser2000, Sweden) is used create a double-beam arrangement (reference and sample arm), allowing balanced detection. This maneuver is important in order to minimize the influence of optical interference fringes. The lower intensity optical fiber is immediately directed to a silicon photodiode (PIN-10DP/SB, UDT Sensors), producing a reference signal. The other fiber guides light to our sample (e.g., tablet).

Samples were placed in contact with a long-pass filter (Schott RG715), which in turn was placed directly on top of a photomultiplier tube (PMT, 5070A, Hamamatsu) detecting diffuse transmittance. The long-pass filter in combination with

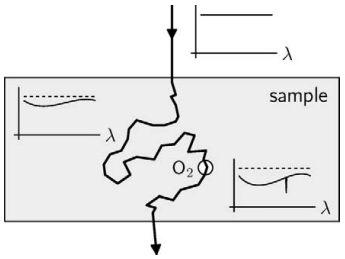

FIG. 1. The principle of GASMAS. The key is the contrast between the sharp absorption features of free gases (e.g., oxygen) and the broad absorption features related to bulk material. This is illustrated by the change in absorption spectra along a particular photon path. The gas absorption is typically much weaker than bulk absorption and is thus exaggerated in the graph.

using direct detector signals. Software-based balanced detection is employed to remove contributions originating from optical interference fringes. In addition, vibrators positioned close to the sample were used to further suppress such effects.

Data Evaluation. Acquired 2*f* signals are evaluated using curve fitting of an experimental long-path recording of the oxygen absorption feature. This recording was performed using the same setup as for tablet measurements. The oxygen imprint is measured in terms of mm of equivalent path length through air, L_{eq}. That is, if $L_{eq} = 10$ mm, the oxygen absorption exhibited by the turbid sample equals that of a 10 mm path length through ambient air. The absolute relation between the 2*f* signal and the equivalent path length is established experimentally by means of a standard addition calibration. In this particular case, the standard addition involves adding known path lengths of air to the sample arm. A detailed description of these procedures is found in a previous publication.[10]

Pharmaceutical Samples. Measurements were performed on 22 model tablets with microcrystalline cellulose as the main constituent, manufactured using a wet granulation process.[11] The influence of particle size distribution was studied by sieving the granulate, producing two different batches consisting of 11 tablets each (particle sizes: <150 μm and >400 μm). The tablets were compressed manually into various thicknesses (3–4 mm). The tablets were round, without score or engravings, and had a 10 mm diameter.

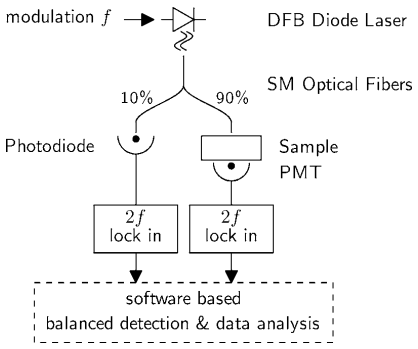

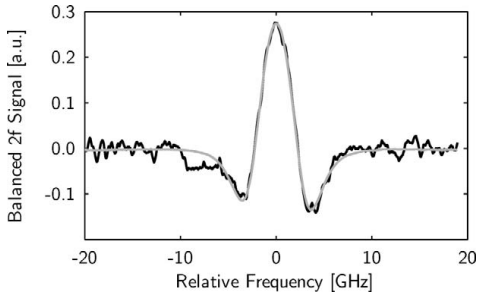

FIG. 3. Data obtained for a 3.38 mm thick tablet from PS > 400 μm. The 2*f* signal after balanced detection (black) is shown together with a fitted oxygen absorption signature (grey). The signal corresponds to an L_{eq} of 17.4 mm. The optical frequency is given relative to the oxygen absorption line (760.445 nm). The corresponding wavelength range is 760.41–760.48 nm, where the lower wavelength is to the right.

RESULTS

Examined tablets exhibited oxygen absorption corresponding to 5–50 mm propagation through ambient air. A typical example of the acquired 2*f* absorption signature is given in Fig. 3. To illustrate that obtained signals are related to oxygen absorption, additional nitrogen atmosphere experiments was performed. Tablets were then stored for several hours in plastic bags filled with nitrogen. When inserting them into the setup (while still in their plastic bags), obtained signals exhibited nothing but the ordinary 3 mm L_{eq} noise floor. When the plastic bags was opened and ventilated, the expected signal quickly appeared. This oxygen re-invasion could, however, not be temporally resolved.

The overall influence of tablet compression and particle size is shown in Fig. 4. Here, each tablet was measured four times consecutively, and the average derived L_{eq} is presented. The acquisition time was 25 s in each of the four measurements, and the standard deviation in these sets of four repetitions was on average 0.8 mm (<150 μm) and 1.0 mm (>400 μm). However, these measures of uncertainty do not include

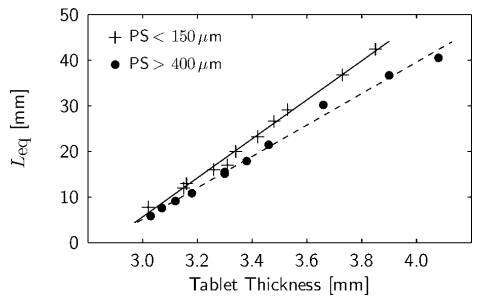

systematic errors due to optical interference fringes that remain after balanced detection. The systematic errors due to such fringes can be estimated by looking at the amplitude of interference noise in spectral regions free from oxygen absorption (consider, for example, the 10–20 GHz range in Fig. 3). Furthermore, this noise was found to be stable between the four consecutive measurements. In the current configuration, optical noise remaining after balanced detection limits the accuracy to about 3 mm L_{eq}. This corresponds to an optical absorption fraction of 7.5×10^{-5}.

In the range of examined tablet thicknesses, there is a highly linear relation between tablet thickness and equivalent path length. It is also clear that in case of comparable thickness, tablets manufactured from the smaller granule particles (<150 μm) exhibited the largest oxygen absorption.

DISCUSSION

Our results clearly show that it is possible to detect oxygen dispersed within pharmaceutical tablets. Hence, a new tool is available for characterization of pharmaceutical solids. Using the GASMAS technique, parameters such as porosity and particle size may be determined in raw materials as well as finished tablets. This may in turn lead to a better optimization of pharmaceutical manufacturing processes. Required instrumentation involves standard components and is simple and fairly compact. Further development is expected to improve data quality.

The porosity of pharmaceutical tablets is normally estimated by employing mercury intrusion porosimetry.[12] This method has several limitations: it is a destructive technique, it includes hazardous handling of mercury, and it is not suitable for fast laboratory-based or on-line analysis. Furthermore, mercury porosimetry is only sensitive to open pores, while the presented technique is sensitive to all pores containing oxygen. It would thus be of interest to compare results from this technique with results from mercury porosimetry. Moreover, this will also provide opportunities for accessing functional properties such as tablet hardness. Preliminary data on such parameters has been shown before.[13,14]

In addition to the results reported here, we propose monitoring of gas diffusion dynamics. It would be attractive to study oxygen reinvasion in samples that have been placed in, for example, a pure nitrogen environment or a vacuum chamber. Such dynamic experiments have been successfully demonstrated in, for example, wood and fruit materials.[7,9] In addition, we propose GASMAS measurements on tablets in blister packages, allowing study of gas exchange through blister materials.

Although the oxygen absorption signal clearly correlates to relevant physical parameters, a detailed understanding of the interaction of near-infrared light with the turbid sample requires further studies. The signal is influenced by both oxygen concentration and photon path length, both being unknown quantities and adding to the total response. It would thus be of great interest to separate these effects in future research. Such a separation is possible by combining GASMAS with time- or frequency-domain photon migration techniques.[6] These techniques are frequently used in biomedical optics, but have also been applied to pharmaceutical solids.[5,15] More such work is forthcoming.

1. D. E. Bugay, Adv. Drug Delivery Rev. **48,** 43 (2001).
2. D. C. Lee and M. Webb, Eds., *Pharmaceutical Analysis* (Blackwell Publishing, Oxford, 2003), 1st ed.
3. J. Workman, M. Koch, and D. J. Veltcamp, Anal. Chem. **75,** 2859 (2003).
4. M. Sjöholm, G. Somesfalean, J. Alnis, S. Andersson-Engels, and S. Svanberg, Opt. Lett. **26,** 16 (2001).
5. J. Johansson, S. Folestad, M. Josefson, A. Sparén, C. Abrahamsson, S. Andersson-Engels, and S. Svanberg, Appl. Spectrosc. **56,** 725 (2002).
6. G. Somesfalean, M. Sjöholm, J. Alnis, C. af Klinteberg, S. Andersson-Engels, and S. Svanberg, Appl. Opt. **41,** 3538 (2002).
7. J. Alnis, B. Anderson, M. Sjöholm, G. Somesfalean, and S. Svanberg, Appl. Phys. B **77,** 691 (2003).
8. L. Persson, K. Svanberg, and S. Svanberg, Appl. Phys. B **82,** 313 (2006).
9. L. Persson, H. Gao, M. Sjöholm, and S. Svanberg, Opt. Laser. Eng. **44,** 687 (2006).
10. L. Persson, F. Andersson, M. Andersson, and S. Svanberg S, Appl. Phys. B DOI:10.1007/s00340-007-2593-y (2007).
11. A. Sparén, M. Malm, M. Josefson, S. Folestad, and J. Johansson, Appl. Spectrosc. **56,** 586 (2002).
12. J. M. Haynes and P. Rossi-Dori, Eds., *Principles and Applications of Pore Structural Characterization* (Arrowsmith, Bristol, 1985).
13. T. Svensson, J. Johansson, S. Andersson-Engels, S. Svanberg, and S. Folestad, "Non-invasive determination of porosity in solids by diode laser oxygen spectroscopy: application to pharmaceutical tablets", Poster \#562 at FACSS 2004 (Portland, OR, Oct 3–7, 2004).
14. J. Johansson, S. Folestad, S. Svanberg, M. Sjöholm, G. Somesfalean, C. Abrahamsson, and S. Andersson-Engels, "Method for analysing a pharmaceutical sample", international patent PCT no. WO 03/078983 (2003).
15. Z. G. Sun, S. Torrance, F. K. McNeil-Watson, and E. M. Sevick-Muraca, Anal. Chem. **75,** 1720 (2003).

Paper XI

Laser spectroscopy of gas in scattering media at scales ranging from kilometers to millimeters

M. Andersson, R. Grönlund, L. Persson, M. Sjöholm, K. Svanberg, and S. Svanberg.

Laser Physics **17**, 893-902 (2007).

ISSN 1054-660X, Laser Physics, 2007, Vol. 17, No. 7, pp. 893–902.

QUANTUM OPTICS, LASER PHYSICS, AND SPECTROSCOPY

Laser Spectroscopy of Gas in Scattering Media at Scales Ranging from Kilometers to Millimeters

M. Andersson[a], R. Grönlund[a], L. Persson[a], M. Sjöholm[a], K. Svanberg[b], and S. Svanberg[a, *]

[a] *Division of Atomic Physics, Lund University, P.O. Box 118, SE-221 00 Lund, Sweden*

[b] *Oncology Department, Lund University Hospital, SE-221 85 Lund, Sweden*

*e-mail: sune.svanberg@fysik.lth.se

Received January 10, 2007

Abstract—Free gases are characterized by their narrow line width, and they can conveniently be studied by laser spectroscopy. The present paper discusses the monitoring of such ambient pressure gases, which are dispersed in scattering media such as aerosol-laden atmospheres, solids, or liquids. Atmospheric work basically constitutes the well-known field of differential absorption lidar (DIAL), while the study of free gas in solids and liquids was initiated more recently under the name of GASMAS (GAs in Scattering Media Absorption Spectroscopy). We discuss the connections between the two techniques, which are extensively used in our laboratory. Thus, we span the field from trace-gas mapping of gases in the lower atmosphere to gas studies in construction materials, food products, and the human body. We show that the basic ideas are very similar, while the spatial and temporal scales vary greatly.

PACS numbers: 87.64.Je, 89.60.-k, 87.80.-y, 34.50.-s, 81.05.Rm

DOI: 10.1134/S1054660X07070018

1. INTRODUCTION

Media with strong optical scattering are extremely common in the real world, and are often encountered in everyday life. Examples of scattering media are clouds, fog, ice, snow, foams, food products, wood, and human tissue. Two major aspects pertain when light is propagating in such media. First, the light path traveled by the light becomes undefined with a distribution of path lengths, which results in the absence of a well-defined Beer–Lambertian law, directly applicable for determining the concentration of an absorbing species in the scattering material. Secondly, imaging through scattering media becomes blurred. Many techniques have been developed to alleviate the detrimental effects of scattering as discussed, e.g., in [1–3].

The influence of scattered light in imaging can be removed, e.g., by gated viewing and coherent gating, where the unique feature of the shortest traveling time, and the preserved coherence, respectively, for nonscattered light is taken advantage of [4, 5]. The problem of concentration evaluation can be addressed by using time-resolved measurements, where a histogram of the path lengths of individual photons is recorded, allowing a modified Beer–Lambertian law to be established [6]. In this way, it becomes possible to determine the concentration of molecular species, e.g., in tissue related to sensitizer concentration evaluation in photodynamic therapy [7], for breast tissue characterization in optical mammography [8], or for the concentration evaluation of active components in pharmaceutical tablets [9, 10].

These types of measurements were extended to the study of free gas in scattering media using a technique which was named GASMAS (GAs in Scattering Media Absorption Spectroscopy) [11]. The technique, although operating on samples on millimeter to centimeter scales, has a clear resemblance to laser radar (lidar, or light detection and ranging) measurements in the atmosphere, where the scales are up to several kilometers [12–14]. Single-scattering events strongly dominate in clear air, allowing a straight-forward evaluation of gas concentrations to be performed using the so-called differential absorption lidar (DIAL) technique [15, 16], which, for air pollution studies, was pioneered by Walther and collaborators [17] and Grant and collaborators [18]. However, in the presence of fog or clouds, multiple scattering frequently occurs, especially when operating at short wavelengths. The field of multiple-scattering lidar is extensive and has been covered in a series of international conferences (see, e.g., [19]). The situation in multiple-scattering lidar is very similar to GASMAS measurements, except that the spatial scale is different. In our group, DIAL as well as GASMAS studies are being pursued, and, in the present paper, we show their close connection. Laser spectroscopy applied to environmental and medical research has much in common [20], which is also illuminated, as is the power of multidisciplinary multispectral imaging [21].

The present paper is organized in the following way. Experimental arrangements for lidar and GASMAS measurements are presented in the next section. Then, some results from different types of experiments are presented. Finally, in a concluding section, the techniques are discussed and new fields of investigation are proposed.

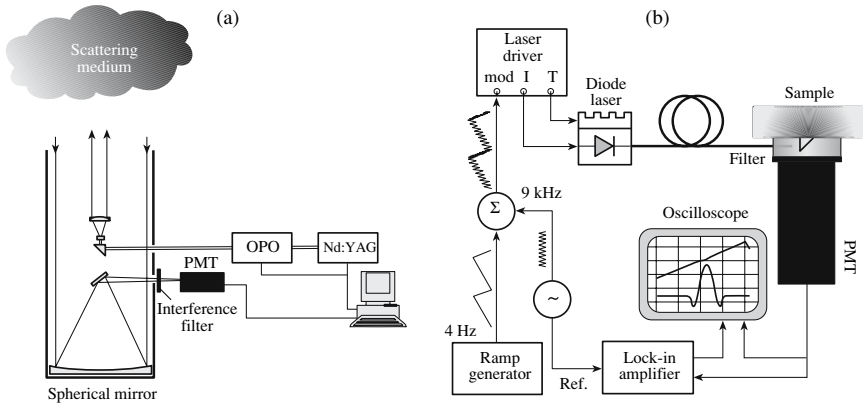

Fig. 1. (a) Schematic arrangement for lidar monitoring of atmospheric gases (left) and (b) the schematic arrangement for measurements of gases in solid or liquid scattering media (right) (from [3]).

2. EXPERIMENTAL ARRANGEMENTS

2.1. Lidar

A schematic diagram of the Lund lidar system used for range-resolved trace-gas element DIAL mapping in the atmosphere is shown in Fig. 1a. Short pulses from a tunable high-power laser are transmitted into the atmosphere, and the laser is switched between two different wavelengths—one on an absorption peak and one slightly off. The laser radiation is scattered by particles and molecules in the atmosphere and backscattered light is collected with a 40-cm-diameter Newtonian telescope and directed to a detector. The telescope has a very small viewing angle (about 1 mrad) defined by an aperture stop in the focal plane. The viewing angle matches the divergence of the laser beam, which is transmitted through a beam expander, and is mounted on the same optical axis as the receiving telescope. With this "tunnel-vision" arrangement, the probability of multiply scattered photons is strongly reduced—to the extent it is possible to be neglected in the absence of fog or clouds. The detected laser-radar signals will, for a uniform atmosphere, show a typical $1/r^2$ dependence, reflecting the diminishing solid angle of the receiving telescope presented to the scatterers along the propagating beam. This is true for the off-resonance wavelength, whereas the on-resonance signal will be additionally attenuated by absorption related to the gas of interest. Division of the on-resonance by the off-resonance curve will also eliminate the influence of nonuniform scattering particle distributions, and the slope of the ratio curve indicates the gas concentration.

The Lund lidar system [22] is housed in the cargo compartment of a Volvo truck and can easily be transported to measurement sites. The system is fully self-contained with an autonomous source of electricity. A 20 Hz Nd:YAG-pumped optical parametric oscillator (OPO) system (Spectra Physics MOPO-730), modified to make fast wavelength switching possible is used as the lidar transmitter. The OPO can be widely tuned, and, in combination with nonlinear frequency conversion techniques, the spectral range 220 nm to 3.4 μm can be covered. The vertically looking arrangement in Fig. 1a is normally complemented by a rooftop dome with a computer-controllable folding mirror to direct the radiation in any direction desired. Collected backscattered light is passed through a narrow-band interference filter, which transmits only the elastically scattered radiation onto a photomultiplier tube (PMT), while suppressing most of the ambient light.

Ultraviolet laser radiation is preferably used, since these wavelengths are essentially eye safe (below 400 nm) and a sufficiently strong backscattering is attained, which is not necessarily true in the infrared region, which otherwise is also eye safe beyond 1.4 μm.

Our group has performed measurements on several pollutants, including sulphur dioxide (SO_2), nitrogen dioxide (NO_2), nitric oxide (NO), and mercury (Hg), the last of which was recently studied in a major interdisciplinary project concerning chlor-alkali factories [23]. During these measurements, the absorption peak for Hg at 253.65 nm was used, where 5 mJ laser pulses with 4–5-ns length could be produced. The laser wavelength is switched on a shot-to-shot basis, such that there is not time for the atmosphere to change appreciably between the on- and off-resonance measurements.

2.2. GASMAS

A schematic setup for GASMAS is shown in Fig. 1b. It is employed to measure molecular gases inside scattering media by using tunable diode laser absorption spectroscopy. The laser is scanned across an absorption line of the gas to be studied by repetitively

modifying the laser driver current by supplying a sawtooth ramp. Our work has been focused on molecular oxygen [11, 24–26], which has its conveniently located A-band around 760 nm. Furthermore, water vapor around 980 nm [27] has been studied for moisture assessment. In principle, any gas with absorption lines situated at a wavelength available with a suitable laser can be investigated, provided that the bulk material is sufficiently transparent. Thus, there is a practical limitation to the optical region below 1400 nm for samples containing large concentrations of liquid water (biological tissue, fruits, foods, etc.), and from 600–1400 nm for human tissue due to the additional absorption of hemoglobin at lower wavelength.

In order to achieve sensitive detection, lock-in detection techniques are used. The laser driver current is, then, modulated by a 10-kHz sine wave. The light is fiber optically guided to the sample, which, for oxygen monitoring, has the additional advantage of suppressing a strong background signal from ambient air. In the arrangement shown in Fig. 1b, a right-angle prism is positioned in front of the fiber, centrally located over a large area photomultiplier tube (PMT) detector. The backscattered light from the sample is collected through an annular aperture, which has the function of suppressing the strong light backscattered close to the injection point of the sample, allowing deeper levels of the sample to be probed. A high-pass filter with a cut-off wavelength at 715 nm is mounted on the detector in order to reduce the influence of background light. The sharp sensitivity cut off of the PMT towards the IR region provides the matching low-pass filter function. The signal from the detector is split into two parts. One part is directly connected to a digital oscilloscope, while the other part is fed to a lock-in amplifier, where the amplitude at twice the modulation frequency is phase sensitively detected and fed to a second channel of the oscilloscope. The lock-in signal normalized to the amount of light reaching the detector is used as a measure of the gas content. The standard-addition method, where known pathlengths of ambient air are added into the laser beam, is used to calibrate the system. By doing so, a so-called equivalent mean pathlength, L_{eq}, can be estimated for the sample, corresponding to the distance light has to travel in ambient air to obtain the same signal as in the sample, where multiple scattering produces a distribution of pathlengths. We note that L_{eq} depends on both the sample scattering properties and the concentration of the distributed gas.

2.3. Comparison

By comparing Figs. 1a and 1b, we notice the close resemblance between the lidar and GASMAS techniques, which typically operate at kilometer and millimeter ranges, respectively. In the second case, strong multiple scattering can cause the effective pathlengths to be centimeters up to meters in rare cases. Thus, while a lidar system operates at photon travel times on the order of microseconds, the latter system is characterized by pico- and nanosecond time scales. Both systems can, in principle, be operated in pulsed mode yielding time resolution, or in a continuous-wave (CW) mode. The former system is normally a pulsed one, while the latter is frequently a continuous one. In continuous operation, the overwhelming signal at short range must be suppressed by a ring-shaped aperture arrangement suppressing the on-axis signal. Pulsed operation in short-range applications (high temporal resolution) is not compatible with a high spectral resolution, due to Fourier broadening. However, the phase-shift method, where a CW laser is amplitude modulated, may be compatible with spectral as well as spatial resolution in a certain parameter range.

The CW detection scheme can also be seen as a long-path absorption arrangement where the range resolution is lost. Two scenarios are depicted in Figs. 2a and 2b. An arrangement for long-path absorption measurements of air pollutants is shown in Fig. 2a, where a retroreflecting mirror, placed at a distance far away is used to effectively throw the light back to the receiver. In Fig. 2b, a magnetic resonance image (MRI) indicating the frontal human sinus cavities is shown together with a light path for probing the gas content in the sinuses. This can be considered as equivalent to a long-path absorption measurement. Here, the very nonoptimal laser transmitting optics is the frontal bone, the retroreflector is the diffusely scattering underlying tissue (i.e., the brain), and the receiving optics, again, correspond to the inefficient "frontal-bone" telescope followed by the large-area detector. Still, it is possible to measure the pathlength traveled through air in the sinuses. As compared to the atmospheric monitoring case, a huge amount of light is wasted in the sinus case due to diffuse scattering.

3. MEASUREMENT EXAMPLES

Many different aspects of applied molecular spectroscopy are pursued in our research group. Different techniques are used; however, they are frequently closely related, as pointed out in this paper. Atmospheric long-path absorption measurements can be performed using single-mode diode lasers. Frequently, cheap and easily accessible diode lasers do not necessarily emit light at wavelengths corresponding to the strongest gas absorption lines, but rather, at weak overtone or combination spectral bands. To compensate for this, sensitive frequency-modulation techniques can be used, bringing down the sensitivity to the shot-noise limit. As an example, we performed road traffic measurements of nitrogen dioxide concentrations with a cheap laser emitting around 635 nm, rather than employing the commonly used blue spectral region [28]. The two-tone frequency modulation technique, which combines a large frequency modulation, matching the pressure-broadened lines, with convenient elec-

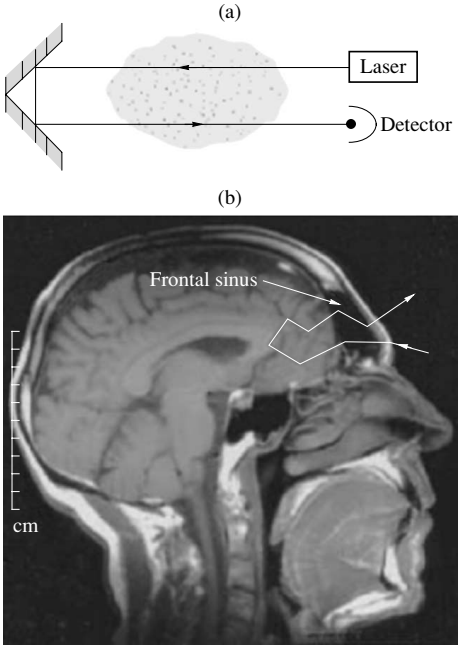

Fig. 2. The upper part (a) shows a schematic setup for a long-path absorption measurement employing a retroreflector. The lower part (b) shows an MRI image of the senior author indicating the location of the frontal sinuses. A light path illustrating the GASMAS technique measurement is also included (from [3]).

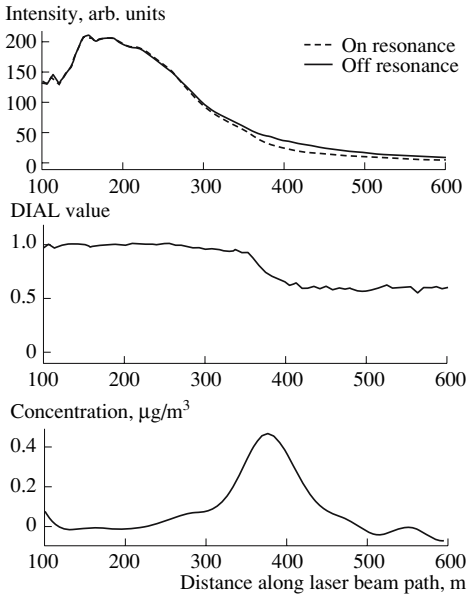

Fig. 3. Results from an atomic Hg lidar measurement: the top part shows the raw data for on- and off-resonance wavelengths, the middle part is the ratio between the two curves, and the bottom part is the evaluated range-resolved concentration (from [3]).

tronic detection around 10 MHz, was employed. A well-known problem with diode lasers is their tendency to mode hop if not accurately controlled. We have developed a new temporal correlation technique, where an uncontrolled multimode laser can be employed for gas concentration measurements. Observed intensity spikes related to modes hitting absorption lines of the atmospheric gas are correlated to the spikes observed from a laboratory cell containing the same gas [29].

As an example of a typical DIAL measurement, the signals received from a DIAL measurement on atmospheric mercury are shown in Fig. 3. The lidar beam was directed downwind from a chlor-alkali plant intersecting the atomic mercury plume. The upper part shows the on- and off-resonance lidar signals as a function of the range. We note that the signals are equal at short distances, indicating that no pollutant has been encountered. The curves run apart at about the 300-m range, indicating that the on-resonance light has been attenuated. The absolute intensity of the recorded signals depends on many different factors, including nonuniform distributions of scattering particles as discussed above, and range-modulated amplification of the detector. However, these factors are cancelled when forming the ratio between the on- and off-resonance signals, as can be seen in the middle part of Fig. 3. From the slope of the ratio curve, the range-resolved concentration shown in the bottom part of the figure can be calculated. Data from any measurement direction obtained in a fan-like scan through the plume can be merged into a cross-section image, such as the one shown in Fig. 4. Here, vertically and horizontally integrated values are also shown. By multiplying the area-integrated value by wind speed perpendicular to the cross section, the total flux of mercury from the plant can be evaluated. This was done in an extensive project at different European plants [23].

As a further DIAL example, we show data from ship-borne vertically sounding measurements of sulphur dioxide at the Italian volcano Mt. Etna in Fig. 5. Examples of on- and off-resonance lidar recordings around 300 nm are shown, and, also, the extension of the SO_2 plume from the volcano, recorded in a traverse under the plume. Passive measurements of the integrated SO_2 absorption using the blue-sky radiation as the light source were also performed. Due to the extended light source, passive measurement can be influenced by multiple scattering. Actually, the passive measurements were compared with nonaffected lidar

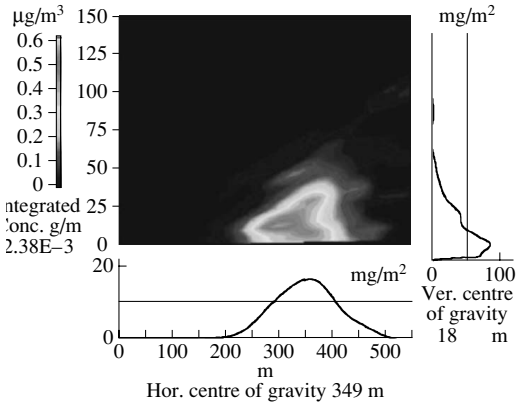

Fig. 4. Cross section of atomic mercury concentration through the emission plume from a chlor-alkali plant. Vertically and horizontally integrated values are also shown. By multiplying the total integrated value with the wind velocity perpendicular to the cross section, the total flux from the plant can be evaluated. Typical values for the case shown are around 70 g/h (from [23]).

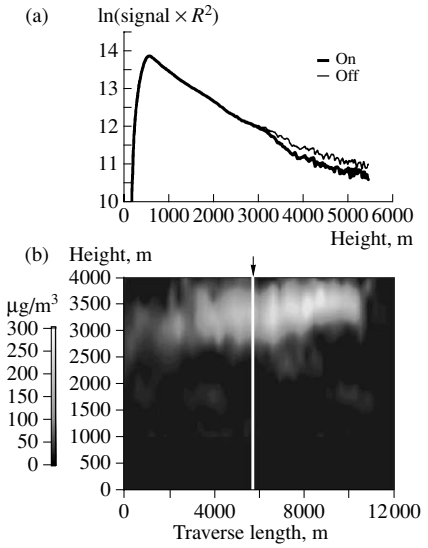

Fig. 5. Data from vertical lidar sounding of the sulphur dioxide flux from Mt. Etna, Italy. Examples of on- and off-resonance lidar curves are shown, illustrating the onset of SO_2 absorption at a height of about 3 km. The evaluated data from a ship-borne full scan under the volcanic plume are also shown (from [22, 30]).

data, and the scattering situation was also theoretically modeled [30].

The examples given constitute "conventional" single-scattering lidar cases. The data analysis is based on the time of the arrival of a photon, which is interpreted as a distance—that is, to and from its only scattering event. However, measurements through fog or clouds would be affected by multiple scattering. Multiple scattering lidar measurements—which, in fact, could be considered as large-scale GASMAS experiments—could be performed by spatially resolved measurements. In such a case, the lidar transmitter and receiver optical axes would not be aligned, but translated with respect to each other. Alternatively, the central part of the detector could be blocked with an annular aperture being left open as discussed above. In such a measurement arrangement, only the multiply scattered photons could be detected. If a DIAL measurement would be made on oxygen, the concentration is known and, thus, the optical pathlength could be calculated. Of particular interest would be to perform such measurements both at an A-band transition at about 760 nm, as mostly discussed in this paper, and at a transition around 254 nm, as encountered in [31]. Due to the strong wavelength dependence of both the dominant Mie scattering and the Rayleigh scattering, quite different behavior can be expected and the influence of multiple scattering could be further elucidated.

We will now discuss short-range lidar measurements of free gas, i.e., GASMAS experiments. The general principle is shown in Fig. 6, where transillumination and backscattering geometries are shown. Furthermore, the very narrow gas signal on a spectrally broad background absorption is highlighted. As a first example, a recording of molecular oxygen inside an apple is shown in Fig. 7 [25]. Here, an arrangement of the kind shown in Fig. 1b was used. The directly recorded backscattered light is shown, and the scanned absorption line around 760 nm is too weak to show up. However, the corresponding 2f-lock-in signal (resembling the second derivative of the true absorption line shape) is clearly seen.

Gas transport can be studied by first immersing the sample, in this case an apple, in an atmosphere of pure nitrogen (e.g., in a sealed-off plastic bag). The reinvasion of normal air (with oxygen) can then be studied as shown in Fig. 8 [25]. We note that the invasion is faster when the apple is pealed, and that the final concentration value, then, becomes almost double, illustrating the active functioning of the skin. Theoretical considerations regarding the GASMAS-based measurement of gas diffusion are given in [32].

Wood is a complex material with cellulose cells, which are partially water-filled and partially air-filled, depending of the state of drying (Fig. 9, upper part). We have studied wood-drying processes by measurements of gaseous water molecules and oxygen. In addition, liquid water, characterized by much broader absorption bands, was studied. Soaking wet balsa wood, placed on scales during the entire drying process, was used and GASMAS signals were recorded in transmission for

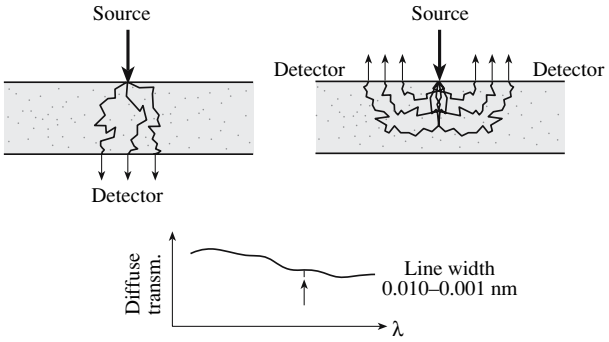

Fig. 6. The principles of GASMAS. The sharp absorptive features of free gas and the transmission and reflection measurement geometries are illustrated.

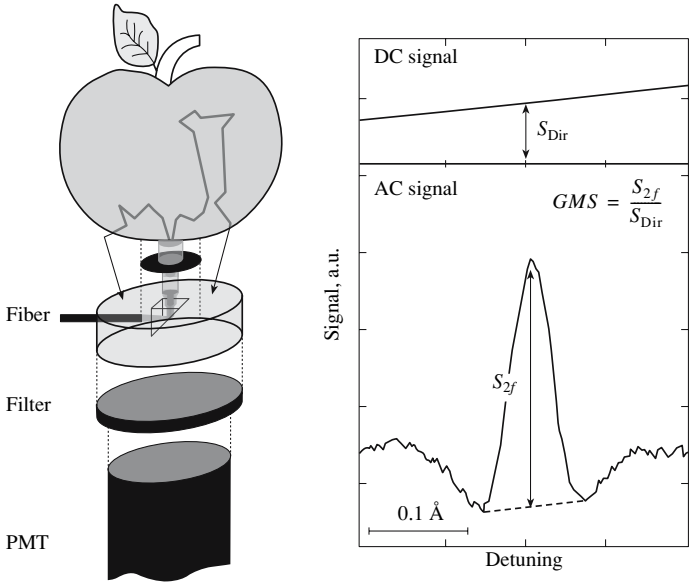

Fig. 7. GASMAS measurement of oxygen in an apple using backscattering geometry. Please note that the separations of the components are heavily exaggerated for clarity; in practice, they are touching each other. Direct transmission and 2f lock-in recordings of an oxygen line are also shown (from [25]).

both gases. The results are shown in the middle part of Fig. 9 [27]. The oxygen signal is seen to increase up to a maximum value reached when the wood is completely dry. The gaseous water signal is also increasing, because of the larger pore volumes where saturated water vapor builds up. However, when no more liquid water is available (the wood is dry), the saturation value cannot be maintained and the humidity gradually reaches that of the surrounding air. The ratio between the water and oxygen molecule signals is partly compensated for by the scattering effects and provides a useful drying diagnostic.

The lower part of the figure shows the total intensity curves for 980 and 760 nm, placed on- and off-resonance, respectively, of a broad liquid water peak. The

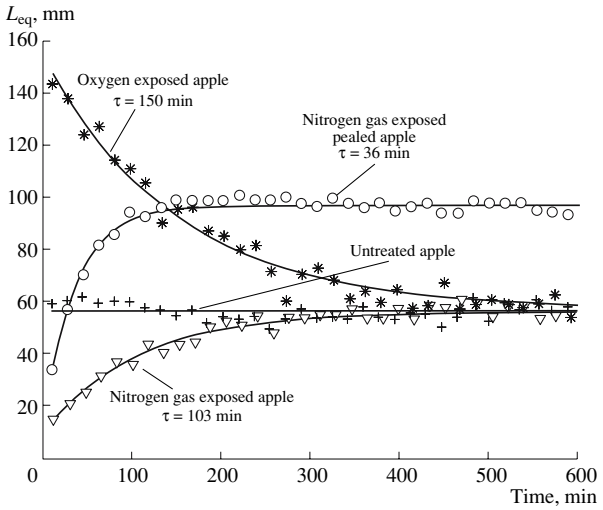

Fig. 8. Gas diffusion temporal curves are shown for apples previously exposed to pure nitrogen or oxygen (from [25]).

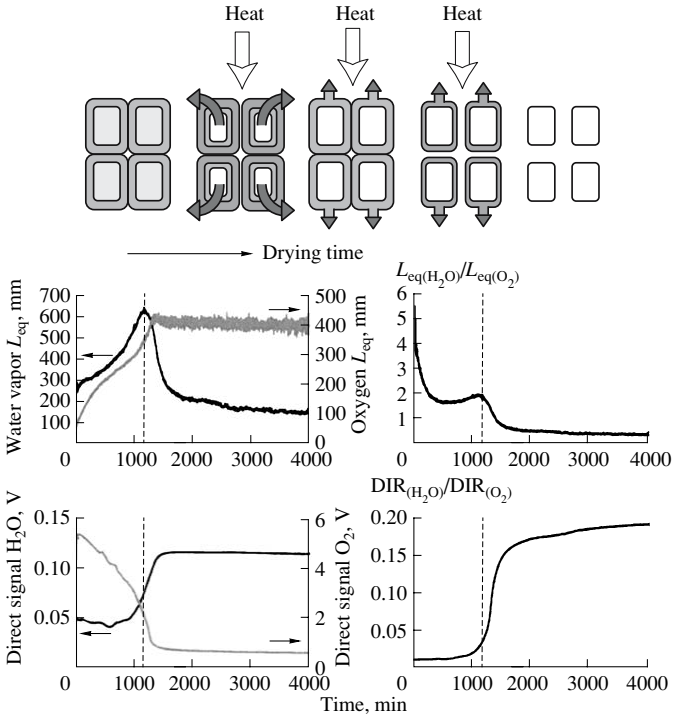

Fig. 9. Spectroscopic study of the drying of wood. Top: Schematic diagram of wood cells with different amounts of liquid water during the drying process. Middle: Recording of water vapor and oxygen GASMAS curves during drying and ratio curve (right). Bottom: Recording of total light transmission at 980 and 760 nm, corresponding to liquid water absorption and a reference wavelength, respectively. The ratio curve is also displayed (right) (from [27]).

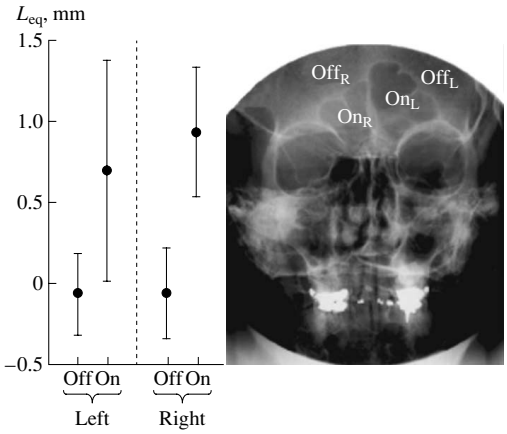

Fig. 10. Recording of molecular oxygen from the frontal sinuses of a healthy volunteer. The positions of the measurement points are indicated in the X-ray image (from [33]).

ratio curve is the differential absorption curve with partial compensation for scattering.

We will finish this section by showing how oxygen in the sinus cavities, as shown in Fig. 2b, can be detected. Here, the gas is not distributed in pores like it is in, e.g., wood, but rather a localized cavity, surrounded by strongly scattering tissue, is probed. A setup of the kind shown in Fig. 1b was used. Figure 10 shows an X-ray radiogram of the senior author with the frontal sinuses clearly visible. Recordings show the presence of oxygen in both cavities and a zero signal outside the sinus areas [33]. The case can be seen as a short-range lidar experiment, where, however, time resolution was not utilized. Instead, it was ensured that the signal was sampled from sufficient depth by blocking the close-range signal with the annular aperture.

Below the floor of the orbital cavity, the maxillary sinuses are located. They can be studied in backscattering, but also in transillumination, because of their locations. Thus, diode laser radiation can be launched through the mouth into the chin from a fiber held against the mucosa. Now, the PMT detector is placed on the outside against the cheek bone. Very distinct signals can be observed on a healthy volunteer as shown in Fig. 11 [34]. A stable amplitude is observed in repeated measurements. However, when the ipsilateral nostril is briefly flushed with nitrogen gas, a fast reduction of the signal is observed, showing that the sinus is connected to the nasal cavity by an open venting channel. When the nitrogen is taken away after 20 s, the sinus again "charges up" with oxygen. Clearly, an interesting new type of ear-nose-throat (ENT) diagnostic tool is in sight.

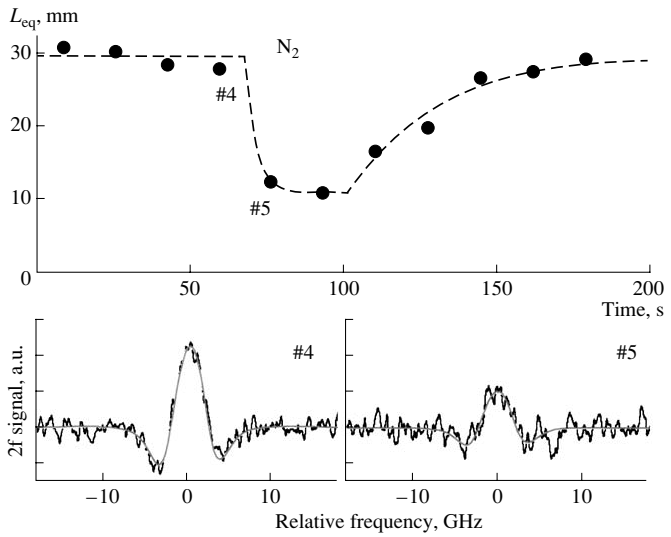

Fig. 11. Oxygen signal from the maxillary sinus of a healthy volunteer recorded in transmission. The laser light was launched fiber optically from the mouth, while the PMT detector was placed against the cheek bone. The signal change following a 20-s flushing of the nasal cavity with nitrogen is shown together with signal recordings (from [34]).

4. DISCUSSION AND OUTLOOK

Several examples showing the close connection between the lidar and GASMAS techniques were given. Multiple scattering differential absorption lidar (DIAL) measurements, i.e., large-scale GASMAS measurements, are of interest for many applications. For example, they could closely relate to studies of the Earth's radiation budget. As solar radiation passes through a cloud, it is multiply scattered. This leads to a larger gas absorptive imprint than otherwise expected. If a lidar beam is directed into a mass of distant snow or ice, the internally scattered radiation will emerge diffusely and can be picked up at a distant point, where the receiving telescope can be directed in a large-scale variety of the geometry shown in the right hand-side of Fig. 6. In particular, an annular detection geometry, such as that in the frontal sinus example, could be adopted. Gas composition in aged polar ice might be studied noninvasively. Furthermore, and more concretely, avalanche victims might be located from a helicopter-borne or stationary remote-sensing GASMAS system, detecting with high contrast exhaled carbon dioxide distributed in the strongly scattering snow.

Returning to small-scale GASMAS applications, the field of food packaging and food inspection appears interesting, in particular, since much of the considerations in this field regard the assurance that oxygen is kept away from foodstuffs. Modified atmosphere packaging is widespread. Gas penetration through plastic enclosures could readily be studied. Likewise, gas penetration through surface coatings, such as paints and veneers, could be studied for the characterization of products.

In the medical field, non-ENT applications might include nonintrusive monitoring of lung function in premature and neonatal infants. Pharmaceutical applications of GASMAS have already been demonstrated [35].

It could be noted that, by monitoring the ratio between the GASMAS signals for two gases, the influence of scattering may be eliminated and absolute concentration values for one gas may be given if the concentration of the other gas is known. Thus, water vapor might be normalized on oxygen in moisture measurements, and oxygen might be normalized on water vapor, having a known concentration in a naturally thermostated human sinus cavity.

As already pointed out in the introduction, the interplay between absorption and scattering, and gas analysis on different spatial scales, constitute an exceedingly rich field of phenomena of both basic and practical interest. In particular, environmental and biomedical applications are very closely related, and differences mainly pertain to the spatial scales and to the mindset of the investigator. Further research and developmental efforts within the field of study in the present paper should be worthwhile.

DEDICATION

This paper is dedicated to the memory of Professor Herbert Walther, who passed away on July 22, 2006. He served as the Faculty opponent at the senior author's dissertation in Göteborg in 1972. As one of the pioneers in laser spectroscopy, he provided great stimulus to the initiation of this field in Sweden in 1973, and, through his early work on laser radar, published in 1974, he also gave stimulus to the lidar work initiated in the senior author's group in 1975. Out of this program, laser applications in the fields of combustion diagnostics and medicine were also developed, and are now vigorously pursued at the Lund Laser Center.

ACKNOWLEDGMENTS

This work was supported by the Swedish Research Council and the Knut and Alice Wallenberg Foundation, and is based on the dedicated and extremely competent work of a large number of additional graduate students and collaborators.

REFERENCES

1. S. Svanberg, "Electromagnetic Radiation in Scattering Media–Spectroscopic Aspects," in *Progress in Nonlinear Science*, Ed. by A. G. Litvak (Univ. of Nizhny Novgorod, Nizhni Novgorod, 2002), Vol. 2, p. 429.
2. S. Svanberg, "Some Applications of Ultrashort Laser Pulses in Biology and Medicine," Meas. Sci. Technol. **12**, 1777 (2001).
3. R. Grönlund., L. Persson, M. Sjöholm, et al., "Studies of Free Gas in Scattering Media at Micro- and Macroscopic Scales," *Proceedings of the International Symposium on Biophotonics, Nanophotonics and Metamaterials, Hangzhou, China, 2006*, p. 51.
4. S. Andersson-Engels, R. Berg, S. Svanberg, and O. Jarlman, "Time-Resolved Transillumination for Medical Diagnostics," Opt. Lett. **15**, 1179 (1990).
5. R. Berg, S. Andersson-Engels, and S. Svanberg, "Time-Resolved Transillumination Imaging," in *Medical Optical Tomography, Functional Imaging and Monitoring*, Ed. by G. Müller et al. (SPIE, Bellingham, 1993), SPIE Institute Series, Vol. 11, p. 397.
6. M. S. Patterson, B. Chance, and B. C. Wilson, "Time Resolved Reflectance and Transmittance for the Non-Invasive Measurement of Optical Properties," Appl. Opt. **28**, 2331 (1989).
7. C. af Klinteberg, A. Pifferi, S. Andersson-Engels, et al., "In Vivo Absorption Spectroscopy of Tumor Sensitizers with Femtosecond White Light," Appl. Opt. **44**, 2213 (2005).
8. T. Svensson, J. Swartling, P. Taroni, et al., "Characterization of Normal Breast Tissue Heterogeneity Using Time-Resolved Near-Infrared Spectroscopy," Phys. Med. Biol. **50**, 2559 (2005).
9. J. Johansson, S. Folestad, M. Josefson, et al., "Time-Resolved NIR/VIS Spectroscopy for Analysis of Solids: Pharmaceutical Tablets," Appl. Spectrosc. **56**, 725 (2002).

10. Ch. Abrahamsson, T. Svensson, S. Svanberg, et al., "Time and Wavelength Resolved Spectroscopy of Turbid Media Using Light Continuum Generated in a Crystal Fibre," Opt. Express **12**, 4103 (2004).
11. M. Sjöholm, G. Somesfalean, J. Alnis, et al., "Analysis of Gas Dispersed in Scattering Media," Opt. Lett. **26**, 16 (2001).
12. G. Fioccio and L. D. Smullin, "Detection of Scattering Layers in the Upper Atmosphere (60–140 km) by Optical Radars," Nature **199**, 1275 (1963).
13. *Laser Remote Sensing*, Ed. by T. Fujii and T. Fukuchi (CRC, Fla, 2005).
14. S. Svanberg, "LIDAR," in *Springer Handbook of Lasers and Optics Springer*, Ed. by F. Träger (Springer, New York, 2007).
15. R. M. Shotland, "Some Observation of the Vertical Profile of Water Vapour by a Laser Optical Radar," *Proceedings of the 4th Symposium on Remote Sensitive Environment, Univ. Mich. Ann Arbor, 1966*, p. 273.
16. S. Svanberg, "Differential Absorption Lidar," in *Air Pollution Monitoring with Optical Techniques*, Ed. by M. Sigrist (Wiley, New York, 1993), Chap. 3.
17. K. W. Rothe, U. Brinkman, and H. Walther, "Applications of Tuneable Dye Lasers to Air Pollution Detection: Measurements of Atmospheric NO_2 Concentrations by Differential Absorption," Appl. Phys. **3**, 115 (1974); Appl. Phys. **4**, 181 (1974).
18. W. B. Grant, R. D. Hake, Jr., E. M. Liston, et al., "Calibrated Remote Measurements of NO_2 Using Differential Absorption Backscattering Technique," Appl. Phys. Lett. **24**, 550 (1974).
19. *12th International Workshop on Lidar Multiple Scattering Experiments*, Ed. by C. Werner, U. Oppel, and T. Rother (SPIE, Bellingham, WA, 2003).
20. S. Svanberg, "Environmental and Medical Applications of Photonic Interactions," Phys. Scr., T **110**, 39 (2004).
21. S. Svanberg, *Multi-Spectral Imaging—From Astronomy to Microscopy—from Radiowaves to Gammarays* (2007) (to appear).
22. P. Weibring, H. Edner, and S. Svanberg, "Versatile Mobile Lidar System for Environmental Monitoring," Appl. Opt. **42**, 3583 (2003).
23. R. Grönlund, M. Sjöholm, P. Weibring, et al., "Elemental Mercury Emissions from Chlor-Alkali Plants Measured by Lidar Techniques," Atmos. Environ. **39**, 7474 (2005).
24. G. Somesfalean, M. Sjöholm, J. Alnis, et al., "Concentration Measurement of Gas Embedded in Scattering Media by Employing Absorption and Time-Resolved Laser Spectroscopy," Appl. Opt. **41**, 3538 (2002).
25. L. Persson, B. Andersson, M. Sjöholm, and S. Svanberg, "Studies of Gas Exchange in Fruits Using Laser Spectroscopic Techniques," *Proceedings of FRUITIC 05, Information and Technology for Sustainable Fruit and Vegetable Production, Montpellier, France, 2005*, pp. 543–552.
26. L. Persson, H. Gao, M. Sjöholm, and S. Svanberg, "Diode Laser Absorption Spectroscopy for Studies of Gas Exchange in Fruits," Opt. Lasers Eng. **44**, 688 (2006).
27. M. Andersson, L. Persson, M. Sjöholm, and S. Svanberg, "Spectroscopic Studies of Wood-Drying Processes," Opt. Express **14**, 3641 (2006).
28. G. Somesfalean, J. Alnis, U. Gustafsson, and S. Svanberg, "Long-Path Monitoring of NO_2 with a 635 nm Diode Laser Using Frequency Modulation Spectroscopy," Appl. Opt. **44**, 5148 (2005).
29. G. Somesfalean, M. Sjöholm, L. Persson, et al., "Temporal Norrelation Scheme for Spectroscopic Gas Analysis Using Multimode Diode Lasers," Appl. Phys. Lett. **86**, 184102 (2005).
30. P. Weibring, J. Swartling, H. Edner, et al., "Optical Monitoring of Volcanic Sulphur Dioxide Emissions–Comparison between Four Different Remote Sensing Techniques," Opt. Lasers Eng. **37**, 267 (2002).
31. H. Edner, G.W. Faris, A. Sunesson, et al., "Lidar Search for Atomic Mercury in Icelandic Geothermal Fields," J. Geophys. Res. **96**, 2977 (1991).
32. M. Sjöholm, L. Persson and S. Svanberg, "Gas Diffusion Measurements in Porous Media by the Use of a Laser Spectroscopic Technique" (in preparation).
33. L. Persson, K. Svanberg, and S. Svanberg, "On the Potential of Human Sinus Cavity Diagnostics Using Diode Laser Gas Spectroscopy," Appl. Phys. B **82**, 313 (2006).
34. L. Persson, M. Andersson, T. Svensson, et al., "Non-Intrusive Optical Study of Gas and its Exchange in Human Maxillary Sinuses," Proc. ECBO, Paper Number: 6628-3 (2007).
35. T. Svensson, L. Persson, M. Andersson, et al., "Non-Invasive Characterization of Pharmaceutical Solids Using Diode Laser Oxygen Spectroscopy," Appl. Spectroscopy (in press).

Paper XII

Gas monitoring in human sinuses using tunable diode laser spectroscopy

L. Persson, M. Andersson, M. Cassel-Engquist, K. Svanberg, and S. Svanberg.

Accepted by J. Biomed. Optics, (2007).

Gas monitoring in human sinuses using tunable diode laser spectroscopy

L. Persson, M. Andersson, M. Cassel-Engquist, and S. Svanberg
Division of Atomic Physics, Lund University, P.O. Box 118, SE-221 00 Lund, Sweden

K. Svanberg
Department of Oncology, Lund University Hospital, SE-221 85 Lund, Sweden

We demonstrate a novel non-intrusive technique based on tunable diode laser absorption spectroscopy to investigate the human sinuses *in vivo*. The technique relies of the fact, that free gases have spectral imprints which are about 10.000 times sharper than spectral structures of the surrounding tissue. Two gases were detected; molecular oxygen at 760 nm and water vapor at 935 nm. Light was launched fiber-optically into the tissue in close proximity to the particular maxillary sinus under study. When investigating the frontal sinuses the fiber was positioned onto the caudal part of the frontal bone. Multiply scattered light in both cases was detected externally by a handheld probe. Molecular oxygen was detected in the maxillary sinuses on 11 volunteers of which one had constantly recurring sinus problems. Significant oxygen absorption imprint differences could be observed between different volunteers and also left-right asymmetries. Water vapor could also be detected, and by normalizing the oxygen signal on the water vapor signal the sinus oxygen concentration can be assessed. Gas exchange between the sinuses and the nasal cavity was also successfully demonstrated by flushing nitrogen through the nostril. Advantages over current ventilation assessment methods using ionizing radiation are pointed out.

Keywords: infrared spectroscopy; diode lasers; molecular spectroscopy; medicine; scattering

Introduction

The human paranasal sinuses are air filled cavities embedded in the cranial skeleton. The frontal sinuses are located behind the frontal bone, while the maxillary sinuses are located below the orbital floor in the cheek bones. The sphenoidal sinus, split by a partial wall, is located centrally in the cranium. The ethmodial cells are multi-focal small cavities located on each side of the upper part of the nose cavity. The sinuses are lined with epithelium bearing glands and cilia, which transport mucosa towards the channel, or ostium, connecting the sinus to the nasal cavity. The frontal and maxillary sinus ostia connect to the middle nasal meatus. The function of the sinuses is still under discussion. They seem to be locations of nitric oxide production of importance for the ventilation functions [1, 2]. The anatomy of the head is shown in Fig. 1a with the sinuses schematically indicated; the frontal and maxillary sinuses are clearly discerned in the magnetic resonance image (MRI) shown in Fig. 1b.

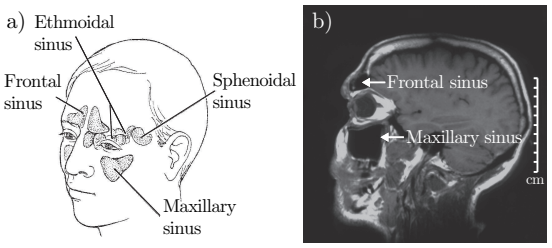

FIG. 1: a) Illustration showing the location of the human sinuses (adopted from Ref. [3]). b) MRI image indicating the location of human maxillary and frontal sinuses.

A good ventilation seems to be a requisite for healthy sinuses. Infection in the cavities, sinusitis, is affecting a very large number of patients, in the US alone about 37 million people are annually diagnosed [4]. Narrow ostia or partial or full blockage can cause severe problems and chronical sinusitis. Nasal polyps can be one cause. Excessive mucosal and pus production are secondary signs of sinusitis. Infection is frequently treated with antibiotics, and decongestants, such as oxymetazoline and zylometazoline, are prescribed to improve ventilation. Surgical intervention with intended ostial widening is necessary in severe cases for achieving long-term improvement. Clearly, a precise diagnosis of sinusitis is of importance, particularly for deciding on whether antibiotics should be administered or not. Common present diagnostics may include the use of ultrasound, capable to see from the echo structure if the cavity is air filled or not, and in severe cases the use of X-ray radiography. However, none of these techniques can assess the ventilation of the cavities or the composition of enclosed gas.

Ventilation studies for the paranasal sinuses have been pursued with intrusive and non-intrusive techniques. Among the former cannulae have been used to measure pressure in the sinuses and in the nasal cavity and their interrelation. Nitrogen gas has also been injected as well as gaseous radioactive isotopes, in particular Xe^{133}; with a half-life of 5.2 days. Scintillation cameras or SPECT (single photon emission computerized tomography) have been used to assess the transport of the gas. Xe^{133} has also been administered non-invasively through breathing followed by repeatedly performing Valsalvas maneuver [5]. Stable Xe gas, having a certain radio opacity

has also been used non-invasively followed by repeated computerized tomographic (CT) recordings [6]. Clearly, these methods expose the patients to a considerable radiological dose. Further, radioactive as well as stable Xe gas is very costly, as is the the use of SPECT and CT installations. Hyperpolarized ^{3}He has been used in MRI studies [7] - also costly investigations. Thus, there is a need for a complementary technique avoiding these hazards and costs while still allowing a detailed assessment of ventilation and gas composition.

We demonstrate in this paper the possibility to statically and dynamically non-intrusively study the human sinuses observing the normal physiological gases oxygen and water vapor. This is done by using tunable diode laser spectroscopy on the gases exhibiting narrow-band absorptive imprints in the near infra-red spectral region. The present study extends and establishes the methodology, which was first described in two recent exploratory papers [8, 9].

The new development became possible taking advantage of optical spectroscopic techniques refined in environmental monitoring of free gas, and an understanding of tissue optics, developed for purposes such as optical mammography and photodynamic therapy dosimetry (see, e.g. [10]). We could thus demonstrate the possibility to investigate the frontal sinuses using tunable diode laser spectroscopy employing phase sensitive detection of wavelength-modulated absorption signals [8]. The presence of molecular oxygen was measured close to 760 nm in a backscattering detection geometry. To understand the behavior of the expected signals a phantom was first investigated. It consisted of two Delrin plates separated by a variable air gap where the first plate represented the frontal bone, the air space the frontal sinus, and the second plate the underlying tissue. Some preliminary results from a human frontal sinus were obtained. These measurements have later on been modeled in Monte Carlo simulations, and the possibility of imaging using a scanned probe was discussed [11]. Since then the experimental techniques have been improved by using pigtailed lasers and balanced detection to suppress noise [12]. This allowed us to study gas exchange between the maxillary sinuses and the nasal cavity by using a transmission detection geometry. The fiber was placed inside the mouth on the palate and the detector externally on the cheek bone. During a short time the nasal cavity was flushed through the nostril with nitrogen gas and the decay of the oxygen signal was recorded on a healthy volunteer resulting in the conclusion that the channels between the cavities were open allowing free gas exchange. No such behavior could be observed on a volunteer with constantly recurring sinus problems [9].

In the present paper we demonstrate molecular oxygen measurements on the maxillary sinuses on 11 healthy volunteers using the transmission detection geometry discussed. The measured values have been compared with values obtained using Monte Carlo simulations of a model representing the maxillary sinuses. To further investigate the clinical potential of the technique, other different possible detection geometries have been explored allowing monitoring of both the maxillary and the frontal sinuses. A further gas - water vapor interrogated at 935 nm - has also been studied providing new information. Water vapor lines around 980 nm were studied in a previous paper on drying processes [13]. Since liquid water, always abundantly present in human tissue, also has an absorption peak at 980 nm, we now choose a shorter wavelength where most of the liquid water absorption is eliminated to allow depth penetration. Investigations of the gas exchange of the sinuses and the nasal cavity in the different geometries have as well been performed using pure nitrogen gas flushed through the nostril.

In the next section the experimental setup and the data analysis is presented. The gas monitoring procedure including the different detection geometries used are described followed by an explanation of the model used in the Monte Carlo simulations. Results of the measurements of the maxillary and the frontal sinuses using the different detection geometries are then presented and discussed. Finally, conclusions are drawn and suggestions for further work are put forward.

Materials and Methods

Experimental setup

A schematic drawing of the experimental setup used in this study is shown in Fig. 2. In the case of molecular oxygen detection a single-mode pigtailed distributed feedback (DFB) diode laser (Nanoplus, Germany) operating at around 760 nm with an output of about 4 mW is used as a spectroscopic light source. When performing measurements on water vapor, the laser is changed to another unit operating around 935 nm (Nanoplus, Germany) with similar output. The laser is scanned across an absorption line of the gas under study by supplying a sawtooth ramp (Hz) to the laser driver current. To achieve wavelength modulation spectroscopy (WMS) with lock-in detection, the operating current is also modulated by a sinusoidal wave at 9 kHz with a modulation index of about 2.2 in both gas cases. In the case of molecular oxygen the R11Q12 absorption line at 760.445 nm (vacuum wavelength) is used and in the case of water vapor the absorption line at 935.686 nm (vacuum wavelength) is used (vibration; (000)→ (121), rotation; J"=3→ J'=4, K_a"=0→ K_a'=0, K_c"=3→ K_c'=4).

The light is fiber-optically split 90/10(%) into two parts with a single-mode fiber-coupled beamsplitter (Laser2000, Sweden). The low-intensity part is directly guided to a silicon detector (UDT 10DP/SB). This part is later used in the analysis as the reference beam to obtain

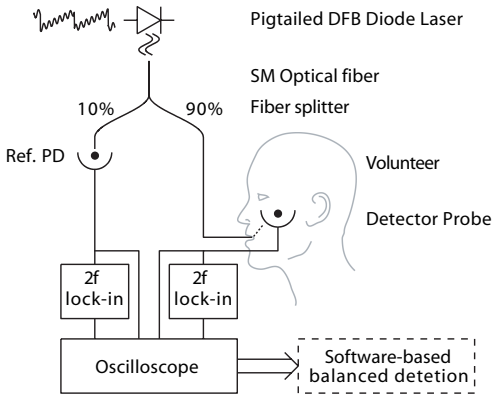

FIG. 2: Schematic drawing of the experimental setup used to study the human sinuses.

balanced detection for efficient noise subtraction [12]. The other part is guided to different positions on the human head and the multiply scattered light is detected externally on the human head according to different detection geometries further discussed in the section *Gas monitoring procedure*. In the case of molecular oxygen detection a photomultiplier tube, PMT, (Hamamatsu 5070A) with an circular detection area of 20 mm diameter is used and in the case of water vapor detection a photo diode (Hamamatsu S3584-06) with similar detection area is used. Both detectors are mounted as handheld probes.

The two detected signals are each divided into two parts. They are sent to a computer controlled digital oscilloscope, one directly, refereed to as the direct signal, and one via a lock-in amplifier where the signal at twice the modulation frequency is recorded, refereed to as the 2f signal. WMS is often refereed to as derivative spectroscopy since the different harmonic are proportional to the corresponding derivative of the signal. Thus, in the case of detection at twice the modulation frequency the 2f signal looks like the second derivative of the direct absorption.

Data analysis

The 2f signals are normalised with the direct signals to make them independent of the amount of light reaching the detector. The normalised 2f sample signal is then subtracted with a processed version of the reference signal to achieve a balanced-detection signal [12]. An ideal absorption signal is then fitted to the balanced-detection signal and from this the peak-to-peak distance is estimated, refereed to as the WMS value. For small absorptions the WMS value is proportional to the absorbance and thus to the product of the gas concentration and the path length travelled by the light. To transform the WMS value to a more meaningful quantity the standard addition method is used [14]. The standard addition procedure is to add known path lengths of ambient air in between the light source and the detector. At each distance the WMS value is measured. A so-called equivalent mean path length, L_{eq}, can then be estimated, corresponding to the air distance that the light has to travel in ambient air to obtain the same oxygen or water vapor absorption imprint. The calibration procedures for both gases were performed at a room temperature of 25°C and a relative humidity of about 20%. It should be noted that one would expect 100% humidity in the sinus cavities due to liquid water in the surrounding tissue, with a temperature close to 37°C. At such a temperature, the water vapor pressure is about a factor of 2 higher than at 25°C [15]. Thus, a particular water vapor signal from a sinus corresponds to about 1/10 of the surrounding air path length yielding the same signal. This factor will be further discussed in Sect. *Conclusion and Outlook*.

Gas monitoring procedure

The maxillary and frontal sinuses of human volunteers were investigated using the non-intrusive technique presented. In the case of the maxillary sinus, two different detection geometries were used (*PC* and *CC*) and in the case of frontal sinus studies, a single detection geometry was used (*OF*) as follows:

(PC) Palate - Cheek bone geometry: Fiber placed inside the mouth against the palate close to the sinus under study and the detector positioned on and around the cheek bone.

(CC) Cheek - Cheek bone geometry: Fiber placed outside on the cheek below the cheek bone and the detector positioned on the cheek bone.

(OF) Orbital edge - Frontal bone geometry: Fiber placed on the horizontal part of the frontal bone under the eyebrow pointing up towards the frontal bone and the detector placed at different positions on the frontal bone.

Before any measurements were performed on any human sinuses, two types of reference measurements were carried out to investigate any possible L_{eq} offset in the current setup. The oxygen and water vapor signal were measured through the cheek below the cheekbone and through the hand of the volunteers where no free gas is expected. These measurements resulted in a consistently non-detectable gas imprint signal showing that no gas offset is present due to gas between setup components.

Molecular oxygen measurements were performed with geometry *PC* on 11 volunteers, 10 of which have no history of sinus problems (volunteer I-X) and one with

constantly recurring sinus problems (volunteer XI). The detector was placed at three different positions; on the cheek bone, slightly towards the nose, and slightly under the cheek bone. At each detector position, 3 consecutive measurements were performed by removing and repositioning the fiber and the detector between each recording. The reproducibility of the measured L_{eq} values was also investigated by measuring 10 consecutive times at each detector position for one volunteer.

Measurements of oxygen and water vapor were performed with detection geometry *PC* on the maxillary sinuses on volunteer I, II and XI and on volunteer I also with geometry *CC*. In addition, frontal sinus measurements with geometry *OF* were performed on volunteer I. In the case of geometry *PC* and *CC* the detector was positioned on the cheek bone. In the case of frontal sinus study, detection geometry *OF*, the detector was positioned at three different locations on the fontal bone towards the particular sinus; about 10 mm and about 20 mm straight up above the light source, and about 10 mm straight up over the center of the eyebrow. At each detector position, 10 consecutive measurements were performed by removing the fiber and the detector between each recording. Molecular oxygen was measured first, followed by water vapor directly afterwards using the same procedure.

To study the communication and ventilation between the nasal cavity and the human sinuses, we investigated the transient response to pure nitrogen flushing of the nasal cavity for about 1 min through the nostril. These measurements were performed on volunteer I with all detection geometries and volunteer XI with detection geometry *PC*. Measurements were continuously recorded for about 8 min; 1 min before flushing, 1 min during flushing and 6 min after terminating the flush, all the time pursuing normal mouth breathing. Each recorded signal was averaged for about 15 sec. Measurements of molecular oxygen and water vapor were performed directly after each other. To investigate the stability of the recorded signals for the gas exchange study time period, the same procedure was also carried out without N_2 flush.

Simulations

Monte Carlo simulations were performed by using the Advanced Systems Analysis Program (ASAP) software [16]. In this paper we present a model according to Fig. 3a to simulate measurements on the maxillary sinuses employing detection geometry *PC* when detecting the multiply scattered light on and around the cheek bone. The position of the light source is indicated by a cross in the model. The maxillary sinus was represented by an ellipsoid with typical human dimensions. It was placed embedded in a scattering medium with optical properties set to g=0.87

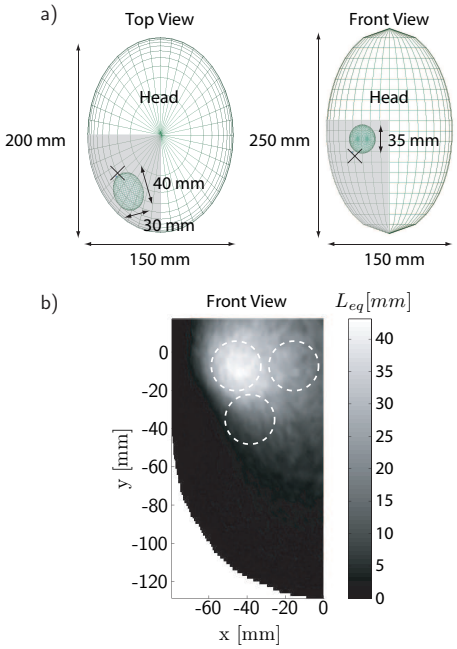

FIG. 3: a) A model used for Monte Carlo simulations created in ASAP^{TM} representing measurements on the human maxillary sinus according to detector geometry *PC*. The region where the rays were collected is indicated by the gray shaded area. The cross represents the location of the light source. b) The simulated L_{eq} for the model shown a. The different positions of the detector in the case of real measurements are also indicated.

(anisotropy factor), μ_s=16 mm^{-1} (scattering coefficient), and μ_a=0.0005 mm^{-1} (absorption coefficient) typical of bone [17].

The flux and the pattern through the model for rays reaching the detector were recorded. The distance each ray traveled in the ellipsoid was calculated. By summarizing the product of the distance in the cavity and the flux for each ray and normalising it with the total flux reaching the detector, the L_{eq} value could be estimated. Similar simulations have been presented in Ref. [11] for frontal sinus imaging.

Results and discussion

Maxillary sinus study

Fig. 3b shows L_{eq} obtained through simulation measurements on the maxillary sinuses according to detection geometry *PC*. It can be seen that L_{eq} values between 10 mm and 40 mm can be expected when performing

measurements on volunteers with typical maxillary sinus dimensions when the detector is placed on and around the cheek bone. These values are heavily influenced by the optical properties used in the simulations but can still be used as an indication of the experimental results to be expected. If, for example, a higher absorption coefficient is used, as was experimentally obtained by Hoshi *et al* [18], a decrease of L_{eq} would be obtained.

The results from the molecular oxygen measurements on the volunteers according to geometry *PC* are presented in Table I. The L_{eq} value shown is an average from the three different detector positions. It was observed that the lowest L_{eq} is always recorded when the detector is positioned below the cheek bone, in agreement with the simulation results, where the detection areas are also indicated (Fig. 3b). All volunteers with no history of sinus problems presented a detectable oxygen absorption imprint. However, no oxygen imprint could be recorded on the left side of volunteer XI. The reproducibility of the measured L_{eq} values was also investigated at each detector position for one volunteer. A standard deviation of about 10% was obtained when the average measured L_{eq} value was of the order of 30 mm. A clear left-right asymmetry was observed for volunteer XI as discussed above. Smaller asymmetries were observed also for other volunteers. However, it should be noted that the L_{eq} value depends on concentration as well as path length, and thus detailed analysis regarding anatomy are hard to draw.

The results from the measurements of oxygen and water vapor with detection geometry *PC* on the maxillary sinuses on volunteer I and II are shown in Fig. 4a and b. The average L_{eq} values are presented together with two standard deviations. It should be noted that the recorded L_{eq} for water vapor is about 8 larger than the value for oxygen for volunteer I and II. The same types of measurements were attempted on volunteer XI. An oxygen signal of L_{eq}=13 mm was detected for the right sinus, whereas, no signal could be observed for the left side. No water vapor signal could be detected on the right side due to heavy over-all absorption in the tissue and the partially filled sinus cavity.

As discussed previously, the estimated L_{eq} depends on both the concentration of the gas and the scattering properties of the tissue. It can be assumed that the scattering properties are approximately the same for the two different wavelengths used [19, 20]. However, the absorption coefficient may be different mostly depending on the degree of oxygenation of the blood and liquid water absorption [17, 19]. If the same volume has been sampled for the two wavelengths the ratio between the L_{eq} values for oxygen and water vapor could provide information on the oxygen concentration inside the sinuses since the water vapor concentration is always the maximum possible concentration at the given temperature (thermostated to about 37°C and 100% humidity in the

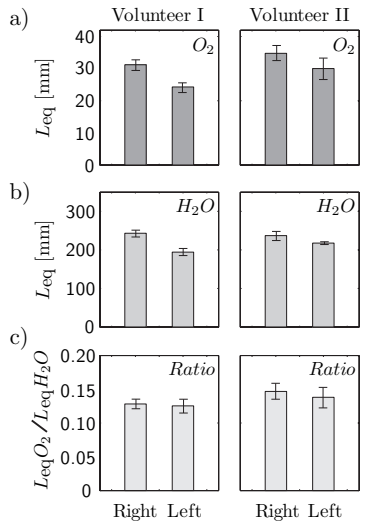

FIG. 4: L_{eq} for molecular oxygen (a) and water vapor (b) measured in left and right maxillary sinuses for volunteers I and II using detection geometry *PC* with the detector positioned on the cheek bone. The data shown correspond to the average of ten recordings together with two standard deviations. c) The ratios of the L_{eq} for oxygen and water vapor are shown.

cavities). In Fig. 4c, the ratios for the left and right maxillary sinus are shown. On volunteer I and II, it can be seen that this ratio is about the same for both sides. It can also be seen that the two volunteers maintain similar ratios. The average ratio is 0.13±0.01. Assuming that these volunteers have healthy and well ventilated sinuses with about 20% oxygen concentration, a reduced ratio may indicate a lower oxygen concentration in the cavity.

Gas exchange studies were performed on volunteers I and XI with the same detection geometry *PC*. A reduction of the oxygen absorption imprint could be observed on volunteer I when flushing with N_2, as well as the reperfusion of air when terminating the N_2 flush (Fig. 5a). In Fig. 5b the stability of the oxygen signal during the same timescale without N_2 flush can be seen. In the case of water vapor detection no reduction of the signal could be recorded during N_2 flush (Fig. 5c). A series of water vapor signal measurements is also shown in Fig. 5d illustrating the stability of the data. The results indicate that the flushing is not able to change the humidity in the cavities. Fig. 6 shows signals recorded at three different time intervals during the gas exchange study (indicated by corresponding numbers in Fig. 5). The fractional absorption was $8.6 \cdot 10^{-4}$ and $6.7 \cdot 10^{-3}$ for the largest signals observed for oxygen and water vapor, respectively. The signals from reference measurements through the cheek

Volunteer	I	II	III	IV	V	VI	VII	VIII	IX	X	XI
History	N	N	N	N	N	N	N	N	N	N	Y
Left L_{eq} **[mm]**	20±4	29±6	8±7	24±3	18±2	12±9	25±0	13±9	28±0	11±2	-
Right L_{eq} **[mm]**	27±7	31±3	17±2	16±4	21±8	13±6	23±1	12±6	29±9	12±2	10±3

TABLE I: Measured L_{eq} values for oxygen in the maxillary sinus for volunteers I-XI according to detection geometry *PC*. N represents volunteers with no history of sinus problems and Y the volunteer with constantly recurring sinus problems. The presented values are averaged from three different detector positions; on the cheek bone, slightly towards the nose and slightly under the cheek bone.

directly after the study are also shown. The same molecular oxygen measurements with nitrogen flushing were performed on the right maxillary sinus of volunteer XI. These measurements did not show any decrease in oxygen signal during the N_2 flush period indicating lack of communication with the nasal cavity.

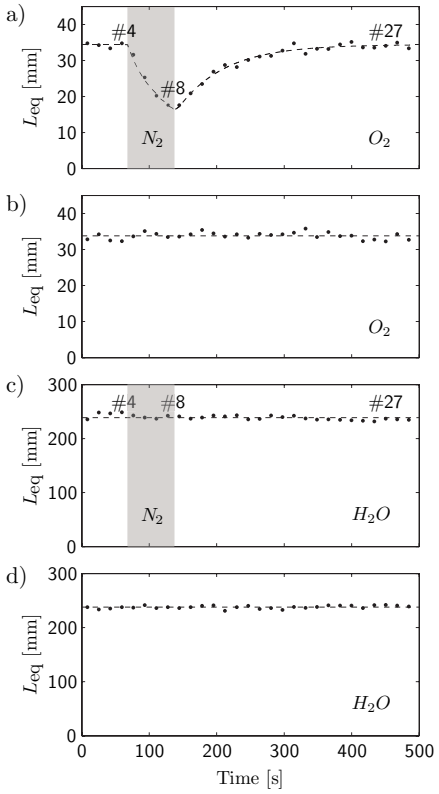

FIG. 5: Gas exchange study for the right maxillary sinuses using detection geometry *PC* on volunteer I (see text). a) L_{eq} for oxygen (solid dots) measured as a function of time with N_2 flushing together with a line drawn for guidance of the eye (dashed line). b) same as (a) without N_2 flushing. c) L_{eq} for water vapor (solid dots) measured as a function of time with N_2 flushing. d) same as (c) without N_2 flushing.

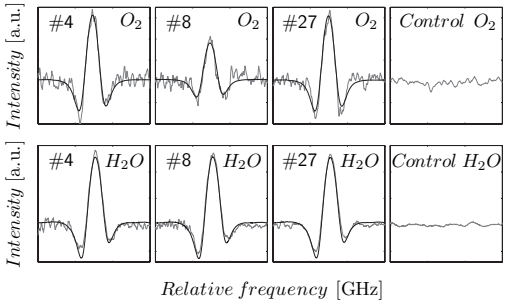

FIG. 6: Balanced-detection signals measured for oxygen and water vapor during the gas exchange study using detection geometry *PC*. The numbers correspond to the once indicated in Fig. 5. The relative frequency range is about 30 GHz. The control signals are also shown for both gases when measuring through the cheek.

Oxygen and water vapor were measured according to geometry *CC* on the maxillary sinuses of volunteer I, see Fig. 7a and b. We note a left-right asymmetry stronger than observed for the same volunteer with data shown in Fig. 4 (left) when using a different detection geometry. This indicates that tomographic information might be extracted regarding anatomy using multiple geometries. The ratio between the signals is shown for both sides in Fig. 7c. An average ratio of 0.12±0.01 is obtained for this geometry.

The same gas exchange procedure was carried out with detection geometry *CC* on volunteer I; see Fig. 8. The same behavior was observed as for detection geometry *PC*.

Frontal sinus study

Measurements of the frontal sinuses were performed on volunteer I with detection geometry *OF*. In Figs. 9a and b, the average L_{eq} together with two standard deviations is shown for the two gases and the three different detector positions discussed above and seen in the top of Fig. 9. The ratio between the L_{eq} for oxygen and water vapor can be seen in Fig. 9c. An average of 0.12±0.01 is

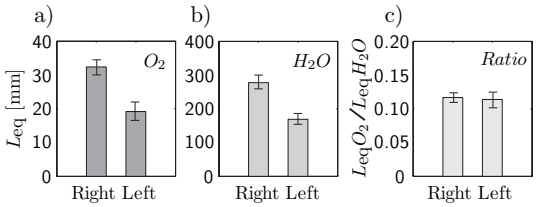

FIG. 7: L_{eq} for molecular oxygen (a) and water vapor (b) measured in left and right maxillary sinuses for volunteer I using detection geometry *CC*. The data shown correspond to the average of ten recordings together with two standard deviations. c) The ratios of the L_{eq} for oxygen and water vapor are shown.

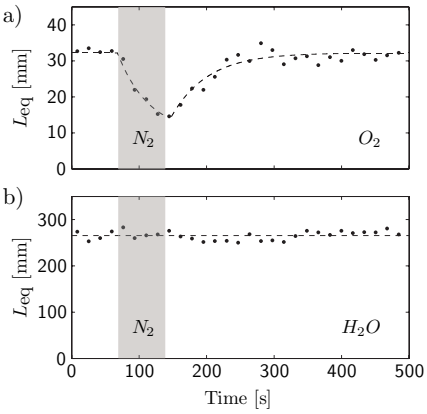

FIG. 8: Gas exchange study for the maxillary sinuses using detection geometry *CC* on volunteer I (see text). a) L_{eq} for oxygen (solid dots) measured as a function of time with N_2 flushing together with a line drawn for guidance of the eye (dashed line). b) L_{eq} for water vapor (solid dots) measured as a function of time with N_2 flushing.

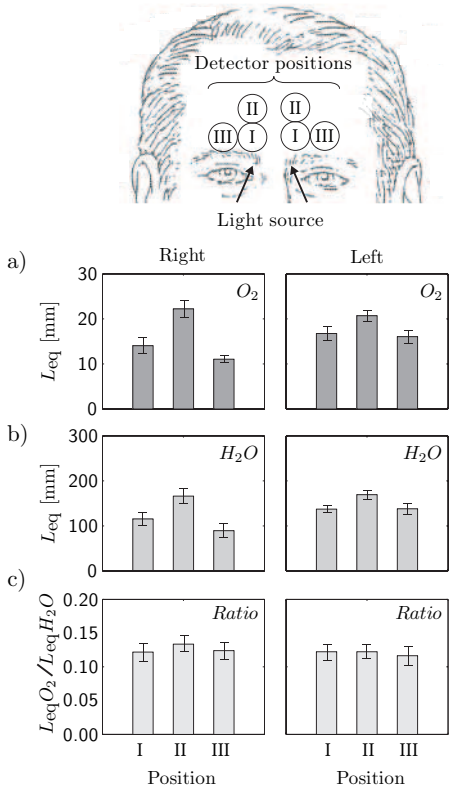

FIG. 9: L_{eq} for molecular oxygen (a) and water vapor (b) measured in left and right frontal sinuses for volunteer I using detection geometry *OF* and detection positions according to top figure. The data shown correspond to the average of ten recordings together with two standard deviations. c) The ratios of the L_{eq} for oxygen and water vapor are shown.

obtained.

The gas exchange between the nasal cavity and the frontal sinuses was also studied with geometry *OF*. In Fig. 10, the invasion of N_2 and reinvasion of ambient air can be seen for volunteer I when detecting oxygen. Again, no such phenomena could be observed when detecting water vapor.

Conclusion and outlook

We have shown that non-intrusive diode laser spectroscopy with monitoring of common physiological gases such as oxygen and water vapor is capable to assess important aspects of the human sinuses and their potential diseases. It was demonstrated that oxygen as well as water vapor could be detected within the maxillary and frontal sinuses on volunteers by employing different detection geometries discussed in Sect. *Materials and Methods*. Individual variations and left-right asymmetries were observed. The oxygen absorption imprint levels detected were in good agreement with the results from Monte Carlo simulations implemented with the ASAP^{TM} software. By forming the ratio between the two signals (normalizing the oxygen signal on the water vapor signal) it was shown that basically the same value was obtained for all well ventilated sinuses studied. This is to be expected if a constant concentration of (about 20%) oxygen is assumed in the healthy sinuses, and if 100% water vapor saturation develops in the sinus. Further, a prerequisite would also be that the scattering and absorption coefficients are the same at 760 nm and 935 nm resulting

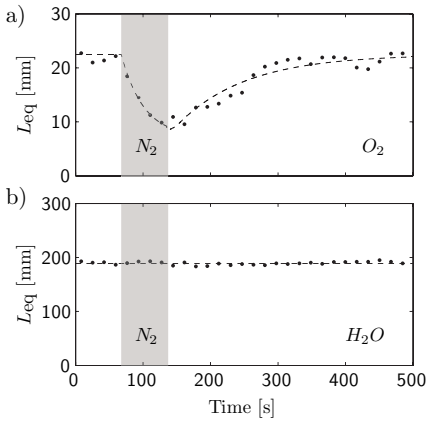

FIG. 10: Gas exchange study for the frontal sinuses using detection geometry *OF* on volunteer I (see text). a) L_{eq} for oxygen (solid dots) measured as a function of time with N_2 flushing together with a line drawn for guidance of the eye (dashed line). b) L_{eq} for water vapor (solid dots) measured as a function of time with N_2 flushing.

in the same effective path length through the gas filled cavity. Consulting the literature it can be found that this assumption is not fully warranted [17, 19, 20]. In particular, the absorption coefficient depends on the degree of blood oxygenation and amount of liquid water and would tend to increase the absorption at 935 nm as compared to 760 nm. The scattering coefficient could be expected to be the same within about 10 percent. The fact, that a very similar signal ratio is obtained for different volunteers, sinuses and geometries suggest that the assumption of a similar effective path length is reasonable. We notice, however, that the experimental ratio was found to be about 0.12. Going from 20% relative humidity to 100% influences the equivalent mean path length by a factor of 5. Likewise, going from 25°C to 37°C introduces a factor 2 in water potential pressure [15]. Thus an experimental ratio of 0.10 would be expected. The measured value of 0.12 could thus be interpreted in two ways; the air is not attaining 37°C in dynamic exchange but only about 33°C, which is not unlikely. A further explanation is that the effective sample pathway for the two wavelengths differ by a factor of 1.2 with a smaller path length at 935 nm due to increased absorption. A combination of the two effects could be present. Given that the experimentally observed effects are rather small it seems like it should be possible to perform an empirical correction after having gained clinical data. The results of the present work would mean that it would be possible to non-intrusively read off the oxygen concentration in a sealed-off sinus cavity, which might be of clinical value if a correlation to pathology could be established in a clinical trial. It should be noted that a water vapor signal is always expected as soon as there is a gas filled cavity. A zero reading for oxygen would then by necessity mean that no oxygen is present in the gas, not that the cavity contains no gas at all.

We also demonstrated that the ventilation of the sinuses (the ostial function) could easily be measured observing the oxygen signal, which is reduced when nitrogen gas is given through the nostril as a displacement gas while the patient is breathing normally through the mouth. By instead administering high-concentration oxygen gas a much stronger signal can favorably be achieved. The time constants for the gas exchange can be determined by fitting the curves. The convenience of a combination of a physiological gas and light for gas exchange studies is in strong contrast to the previous use of stable or radioactive xenon gas in combination with repeated CT scans or SPECT imaging, both leaving the patient with a considerable dose of ionizing radiation. It was found that the concentration of water vapor in the sinuses was not influenced by the flushing with dry nitrogen gas. The conclusion is that 100% water saturated gas is immediately obtained in the sinus. This fact also corrobates the finding above, that water vapor reliably can be used as a reference gas of known concentration in the well thermostated sinus (at 33-37°C). By recording the relative intensity of two suitable oxygen or water vapor lines, and their half-width with sufficient precision, the temperature and pressure can in principle be measured.

Sequential measurements were made on oxygen and water vapor in the present studies. In a clinically adapted system, the two types of measurements could in principle be made simultaneously using the same detector and different modulation frequencies. When exactly the same geometry pertains for both kinds of measurements an even better stability for the ratio signal could be expected. A clinical trial on sinus patients jointly with an ear-nose-throat (ENT) clinic is planned to assess the clinical practicality and potential benefits of the new technique.

The demonstrated possibility to non-invasively assess the oxygen concentration in a hollow organ by sending light through a substantial layer of human tissue suggests that the new technique might have important applications in assessing the lung function in newborn and small children. With higher power lasers, still without any noticeable thermal effect, corresponding measurements on the lung lobes in adults should be feasible in lung ventilation studies, where, however, the empirical path length difference correction might be larger.

Acknowledgment

The authors are grateful for fruitful discussions with N.G. Holmer, M. Jannert, K. Jonsson, L. Malm and K.

Prellner. We are grateful to L. Simonsson and E. Kristensson for collaboration on ASAP^{TM} simulations. This research was supported by the Swedish Research Council, the Medical Faculty at Lund University, and the Knut and Alice Wallenberg Foundation.

[1] P. Stierna, G. Karlsson, I. Melén, and M. Jannert, "Aspect on Sinusitis - Diagnosis and treatment in adults," Proceedings from the Meeting of the Swedish Association of Otorhinolaryngologists, HNS, Stockholm (1995)

[2] T. Runer and S. Lindberg, "Effects on nitric oxide on blood flow and mucociliary activity in the human nose," *Ann. Otol. Rhinol. Laryngol.* **107,** 40–46 (1998)

[3] http://cfcenter.stanford.edu/CFNews-Sinusitis.html

[4] Health Matters, Sinusitis, Nat. Inst. of Allergy and Infectious Diseases, US Dept. of Health and Human Services, Bethesda (2005)

[5] B. Paulsson, J. Dolata, I. Larsson, P. Ohlin, and S. Lindberg, "Paranasal sinus ventilation in healthy subjects and in patients with sinus disease evaluated with the 133-Xenon washout technique," *Ann. Otol. Rhinol. Laryngol.* **110,** 667–674 (2001)

[6] D. Leopold, S.J. Zinreich, B.A. Simon, M.M. Cullen, and C. Marcucci, "Xenon-enhanced computed tomography quantifies normal maxillary sinus ventilation," *Otolaryngol. Head Neck Surg.* **122,** 422–424 (2000)

[7] R.R. Rizi, I.E. Dimitrov, A. Thompson, G. Jones, T.R. Gentile, M. Ishii, R. Reddy, M.D. Schnall, and J.S. Leigh, "MRI of hyperpolarized ^{3}He in human paranasal sinuses," *Magn. Reson. Med.* **39,** 865–868 (1998)

[8] L. Persson, K. Svanberg, and S. Svanberg, "On the potential of human sinus cavity diagnostics using diode laser gas spectroscopy," *Appl. Phys. B* **82,** 313–317 (2006)

[9] L. Persson, M. Andersson, T. Svensson, M. Casselgren Engquist, K. Svanberg, and S. Svanberg, "Non-intrusive optical study of gas and its exchange in human maxillary sinuses", Proc. SPIE 6628-3 (2007)

[10] S. Svanberg, "Environmental and medical applications of photonic interactions," *Phys. Scripta* **T110,** 39–50 (2004)

[11] L. Persson, E. Kristensson, L. Simonsson, and S. Svanberg, "Monte Carlo simulations of optical human sinusitis diagnostics," J. Bio. Med. Opt (2007) in press

[12] L. Persson, F. Andersson, M. Andersson and S. Svanberg, "Approach to optical interference fringes reduction in diode laser absorption spectroscopy," *Appl. Phys. B* **87,** 523–530 (2007)

[13] M. Andersson, L. Persson, M. Sjöholm, and S. Svanberg, "Spectroscopic studies of wood-drying processes," *Opt. Express* **14,** 3641–3653 (2006)

[14] S. Svanberg, *Atomic and molecular spectroscopy, 4th ed.* (Springer-Verlag, Berlin 2004)

[15] C. Nordling and J. Österman, *Physics handbook, 4th ed.* (Studentlitteratur 1987)

[16] B. Michel and T. Beck, "Raytracing in medical applications," *Lasers & Photonics* **5,** 38–41 (2005)

[17] T. Vo-Dinh, *Biomedical Photonics Handbook*, (CRC Press LLC, New York, 2003)

[18] Y. Hoshi, M. Shimada, C. Sato, and Y. Iguchi, "Reevaluation of near-infrared light propagation in the adult human head: implications for functional near-infrared spectroscopy," *J. Biomed. Opt.* **10,** 064032 (2005)

[19] T. Svensson, S. Andersson-Engels, M. Einarsdottir, and K. Svanberg, "In vivo optical characterization of human prostate tissue using near-infrared time-resolved spectroscopy," *J. Biomed. Opt.* **12,** 014022 (2007)

[20] Claes af Klinteberg, Antonio Pifferi, Stefan Andersson-Engels, Rinaldo Cubeddu, and Sune Svanberg, "In vivo absorption spectroscopy of tumor sensitizers with femtosecond white light", *Appl. Opt.* **44,** 2213–2220 (2005)

Paper XIII

Flexible lock-in detection system based on synchronized computer plug-in boards applied in sensitive gas spectroscopy

M. Andersson, L. Persson, T. Svensson, and S. Svanberg.
Submitted, (2007).

Flexible lock-in detection system based on synchronized computer plug-in boards applied in sensitive gas spectroscopy

Mats Andersson, Linda Persson, Tomas Svensson, and Sune Svanberg*
Atomic Physics Division, Lund University,
P.O. Box 118, S-221 00 Lund, Sweden

We present a flexible and compact digital lock-in detection system and its use in high-resolution tunable diode laser spectroscopy. The system involves coherent sampling, and is based on the synchronization of two data acquisition cards running on a single standard computer. A software-controlled arbitrary waveform generator is used for laser modulation, and a four-channel A/D board records detector signals. Gas spectroscopy is performed in the wavelength modulation regime. The coherently detected signal is averaged a selected number of times before it is stored or analyzed by software-based lock-in techniques. Multiple harmonics of the modulation signal (1f, 2f, 3f, 4f, etc.) are available in each single data set. The sensitivity is in the order of 10^{-5}, being limited by interference fringes in the measurement setup. The system capabilities are demonstrated by measurements of molecular oxygen in ambient air, as well as dispersed gas in scattering materials, such as plants and human tissue.

PACS numbers: 07.05.Bx,39.30.+w,42.55.Px,42.62.Fi,42.60.Fc

I. INTRODUCTION

Analog lock-in techniques for tunable diode laser spectroscopy have been used for decades to improve performance in trace gas detection [1–4]. From the beginning, desk-top lock-in amplifiers were used in combination with mechanically chopped light. Today, external signal generators are used to superimpose sinus modulation signals on the laser operation current. The modulation signal also acts as phase reference and is fed to an analog lock-in amplifier. This lock-in amplifier is then capable of filtering out harmonic components generated when light passes an absorbing sample/gas cell. The major reason for using lock-in detection is to suppress noise by moving the detection frequency to a range that is normally less affected by noise (above 1 kHz) [5]. In the 1980s, modulation techniques such as wavelength- [6], frequency- [7], and two-tone frequency [8] modulation schemes were developed. Normally, direct absorption measurements (baseband detection) gives a detection limit of 10^{-3} to 10^{-4} while modulation techniques such as wavelength and frequency modulation give a detection limit of 10^{-6} or better [9]. During the last 10 years digital amplifiers have been used and currently small digital-signal-processing (DSP) based lock-in solutions are developed and used [10, 11].

Even if the use of modulation techniques, based on phase sensitive detection, in spectroscopy is straight forward, it is normally not easy to analyze and probe the raw signal, regarding error sources that affect the gas imprint signal, before the lock-in detection takes place. This is because the detected gas imprint signal is weak and heavily affected by noise. Thus, data out from the lock-in amplifier need to be averaged several seconds or minutes in order to achieve the needed signal-to-noise ratio (SNR). Often, it is not possible to average the raw signal without distortion. This is due to the fact, that an oscilloscope or a data acquisition card is synchronized with the modulation signal generator via a scan start trigger. Moreover, since lock-in detection normally takes place in real-time, another drawback is that the influence of a change in lock-in settings (for example, the selection of harmonic) cannot be evaluated later on. In addition to the lock-in technique, methods for signal improvements include balanced detection [12], coherent sampling [13], waveform averaging [14] and high-pass filtering prior to lock-in detection [13].

Coherent sampling is a well known technique, commonly used in spectrum analysis and signal processing for acoustics and telecom research and development. In coherent sampling, a master clock is used to create modulation waveforms and to control the detector signal sampling process. Coherent sampling requires an integer number of wanted waveforms to exist in the acquired data set and that the ratio between the sampling and the modulation frequencies (both scanning and modulation waveform) is an integer [15–17]. With this technique a number of scanned signals may be averaged before the lock-in detection is carried out. Periodic noise, that does not fulfill what is mentioned above, is averaged out (the coherent sampling process acts as a comb filter) together with non-periodic noise. It should be noted that coherent sampling opens up for complete post data processing. For example, this means that applications that earlier required several lock-in amplifiers, can now be realized using coherent data acquisition and subsequent harmonic demodulation at desired harmonics (e.g. $1f$ and $2f$). In addition, high-pass filtering can increase the dynamic range further, since it suppresses most of

*Electronic address: sune.svanberg@fysik.lth.se

the low-frequency content (e.g., below the $1f$ frequency).

This paper describes the construction of a compact and flexible digital lock-in detection system based on two plug-in boards for a standard computer. By employing coherent sampling, we enable raw data storage and post data processing in the time- or frequency domain. The system can be used for both traditional trace gas analysis, and the more recent high-speed combustion gas analysis requiring scan rates of 100 Hz or more. Experimental arrangements and data acquisition architecture are described in Sect. II. The required A/D resolution is also discussed. System calibration and applications are presented in Sects III and IV. Finally, advantages of using a detection system based on coherent sampling and plug-in boards are discussed, and several measurements examples are given.

II. MATERIALS AND METHODS

A. Optical Setup

An overview of the optical setup is shown in Fig. 1. Two different VCSELs (Vertical Cavity Surface Emitting Laser) are used alternatingly, and correspond to two different experimental configurations. The so called *free-running setup* is based on a standard single-mode VCSEL (ULM763-03-TN-S46FOP, Ulm Photonics) with a maximal output of 0.3 mW, operating at 0.25 mW at the sample. The wavelength is scanned across the P11P11 oxygen line at 764.281 nm (vacuum wavelength). The second configuration is referred to as the *fiber-based setup*, and employs a pigtailed single-mode VCSEL (L2K-P760-LD-SM, Laser2000, Sweden) with a maximum output power of 0.2 mW, operating at 0.085 mW at the sample. The wavelength is scanned across the R15Q16 oxygen line at 760.094 nm (vacuum wavelength). After the pigtailed laser, the light is split by a 10/90(%) single-mode fiber splitter (Laser2000, Sweden). The smaller fraction is guided to a reference detector, while the main part is either propagated through ambient air (for calibration purposes; see Sect. III), or guided to a scattering and absorbing sample. A collimating lens package (CFC-5-760, Thorlabs) is used in the case of ambient air measurements.

The laser frequency is scanned over the absorption lines by modulating (using a triangular waveform of 130 Hz) the operating current, which is provided by a standard VCSEL current controller (LDC200, Thorlabs). A temperature controller (TED200, Thorlabs) ensures general temperature stability. Wavelength modulation is achieved by superimposing a sinusoidal modulation of 133 kHz on the triangular modulation signal. The modulation signal is created in a PCI-based 12-bit arbitrary waveform generator (CH-3150, Exacq Technologies). This board allows the generation of arbitrary waveforms in the frequency range from a few Hz to a number of MHz. Its internal stable high-frequency clock is

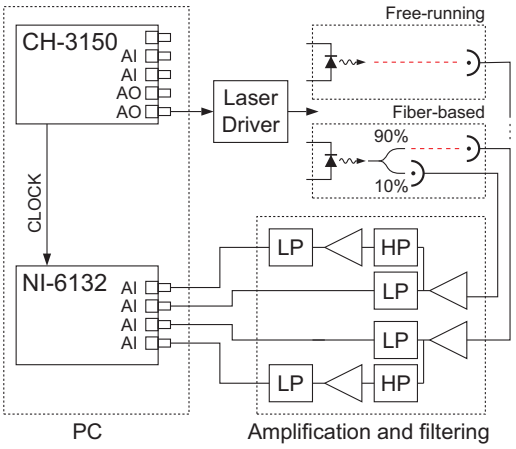

FIG. 1: The free-running and fiber-based experimental setups for measurement on ambient air by the use of VCSEL lasers. The lasers are modulated by an arbitrary waveform that is generated in a data acquisition board (CH-3150, Exacq Technologies). The amplified and high-pass filtered signals from the sample and the reference detectors are sampled coherently and synchronically by a four channel A/D board (NI-6132, National Instruments). See text for more details.

not only used to clock out such arbitrary waveforms, but also used to externally clock the A/D converters, via a short coax cable, on a second computer board (NI-6132, National Instruments). It is this manoeuvre that implements coherent sampling.

In the fiber-based setup, the light beams enter two detectors with built-in transimpedance amplifiers (UDT-455LN, OSI Optoelectronics). In the free-running setup only one of the above mentioned detectors is used. In the present case, the gain of the amplifiers is set to 10^3 in order to fulfill a bandwidth of about 1 MHz. Both the sample and the reference signals are amplified a factor of 1..1000 by an external amplifier in order to minimize external noise and for full utilization of the AD converter dynamic range. The reference and the sample signals are also filtered by a second-order high-pass filter (50 kHz cutoff frequency), and amplified once more by a factor of 100 in order to suppress low-frequency components created by the triangle wave. Measurements on scattering samples, such as bamboo or human tissue, require a large area detector due to the fact, that incident light is scattered and absorbed by the sample. In this case, the default sample detector is replaced by a cooled large-area (Ø=10 mm) avalanche photodiode module (SD 394-70-72-661, Advanced Photonix).

The advantage of using wavelength modulation techniques was estimated by measuring the relative intensity noise (RIN) of the free-running laser and comparing the noise floor level at low frequency and at the laser mod-

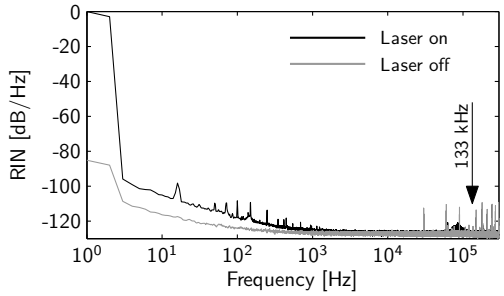

FIG. 2: Laser relative intensity noise (RIN) measurement with a spectral resolution of 1 Hz. Sensor data are recorded by a 14-bit data acquisition card at 600 kS/s during 100 seconds. The figure shows a power spectrum (RIN measurement) of the recorded detector data with or without unmodulated laser light turned on.

ulation frequency. RIN is defined in a 1 Hz bandwidth, and expressed in decibel, as

$$RIN = 20 \times \log_{10} \frac{V_{noise}}{V_{average}},$$

where V_{noise} is the spectral noise root-mean-square (RMS) voltage and $V_{average}$ is the averaged RMS voltage corresponding to the averaged optical power recorded at the optical detector [18]. The RIN measurement was done by measuring the noise spectrum of the recorded detector signal with the laser turned on without any modulation or ramp signal. As shown in Fig. 2, the noise level at 133 kHz, is about 20 dB (10 times) lower compared to the low-frequency noise level and gives information about expected performance increase when wavelength modulation technique is used. This depends on flicker noise from the laser that decreases the performance of a tunable diode laser system based on direct detection. In Fig. 2 the achieved dynamic range is measured to about 126 dB (2.0×10^6) at 133 kHz frequency. According to the data sheet of the laser the RIN value at 1 GHz is about -120 to -130 dB/Hz which sets the performance limit of a spectroscopy system based on this laser. As can be seen in the figure, any further improvement of the dynamic range is limited by the 14-bit data acquisition card since the noise floor is almost the same when the laser is turned off. Further, a detection limit of 10^{-6} requires a system dynamic range of about 120 dB (1×10^6). To be able to resolve such a weak signal a high-pass filter is mounted close to the detector to suppress any signal below the modulation frequency.

B. Data Acquisition

All signals are sampled synchronously and coherently to the laser modulation waveforms by an externally clocked four channel 14-bit A/D converter PCI board (NI-6132, National Instruments). The board is clocked at 2.496 MHz by the CH-3150 board; see Fig. 3. The first and the second channels record the signals from the sample detector (raw signal and high-pass filtered raw signal), while the third and the fourth channels record the signals from the reference detector (reference signal and high-pass filtered reference signal). These two last channels are only used in the fiber-based setup.

The data of the four channels are averaged in real time before further analysis. Normally 130-7800 averages (1-60 s) are carried out before averaged data are stored on disc and/or lock-in detected by a lock-in detection software module (Lock-in Toolkit for LabVIEW, National Instruments) executed in the computer. The phase reference, used by the lock-in detection module, is created by software. The waveform sync signal from the CH-3150 board is used as a start trigger to control when the NI-6132 board starts to record data.

The CH-3150 is a high-speed acquisition board with counters, digital input/output (DIO) ports, analog inputs, and analog outputs. It is designed for high-speed precision measurements and has two 12-bit D/A converters running at 40MS/s with analog reconstruction filters onboard. The noise level, at low output levels, is according to the data sheet extremely low.

A software program, based on LabVIEW, controls the arbitrary waveform acquisition board. At start an arbitrary waveform (scanning and modulation waveform for the laser) is created and loaded to an onboard Synchronous Dynamic Random Access Memory (SDRAM) as shown in Fig. 3. The maximum length of the waveform is 8 million samples, which is limited by the size of the SDRAM (16MB). The master clock is set to 79.872 MHz. When the board is started the data in the SDRAM are streamed to one D/A converter, which is connected to the laser driver. At the same time a waveform synchronization signal is streamed to an onboard DIO channel that goes high every time the data waveform is repeated by the board. This signal works as a start trigger to the second acquisition board. Meanwhile, the master clock is frequency divided by a factor of 32, by an onboard counter, in order to create an external clock of 2.496 MHz; see Fig. 3. All onboard actions are controlled by an onboard field programmable gate array (FPGA). Thus, during run time, the computer central processing unit (CPU) is free to carry out other tasks since the workload is handled by the onboard FPGA.

The second board (NI-6132, National Instruments) is a data acquisition board with four simultaneously sampled A/D converters (14-bits resolution, 3 MS/s maximum). All A/D converters are externally clocked and sample data blocks of 19200 samples that correspond to one scan or 1/130 second. A LabVIEW program controls the board and stores averaged raw data (blocks of 19200 samples, on hard disc for later analysis. Since coherent sampling has been used, data may be evaluated in the time domain by using software-based lock-in de-

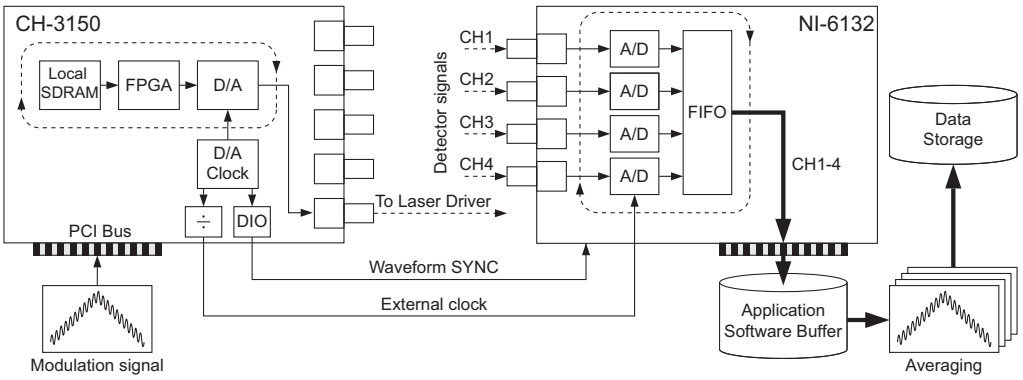

FIG. 3: Measurement system architecture. To the left the arbitrary waveform generator is shown (CH-3150, Exacq Technologies). The D/A clock is divided into an external 2.496 MHz clock via an internal counter. The desired waveform is created and loaded to the board memory before execution. As shown to the right, sensor signals are measured by a four-channel externally clocked board (NI-6132, National Instruments). Data recording starts when the "waveform sync" signal goes high. See text for more details.

tection techniques or by utilizing fast Fourier transform (FFT) methods described in Ref. [19]. In order to run the software, an application software buffer of 200-300 MB is allocated in the random access memory. Otherwise, the data in the first-in first-out (FIFO) register would over-write the contents in the buffer. It is also possible to study and store streamed data directly on disc without any averaging. Streaming measurements, of about 10MS/s, during minutes, have been tested successfully on a standard personal computer (2.4 GHz Pentium CPU, about 2GB of RAM). The only known limitation is the size and the speed of the disc.

To illustrate the potential of a digital lock-in detection system, based on wavelength modulation and coherent sampling, a measurement with the free running laser was performed on 10 cm of ambient air. Fig. 4(a) presents the recorded direct signal where the residual amplitude modulation (RAM) signal is clearly seen as a sinus signal that is present during a scan [20]. In the middle of the frequency scan, the absorption line (P11P11) is crossed resulting in amplitude changes of the direct signal and overtones are created (2f, 3f, 4f...). The amplitude of the RAM signal (40 mV_{pp}) is about 1.5 percent of the DC level of the signal (2.7 V). The recorded direct signal was filtered by four software-based band-pass filters (center frequency at 1f, 2f, and 4f) and data are presented in Fig. 4(b). This figure shows that the 2f signal (4 mV_{pp}) is weaker than the 1f signal (6 mV_{pp}) but still of similar amplitude compared to the direct signal dip since the amplitude of the 2f signal is about 0.1 percent of the direct signal amplitude. The amplitude of the harmonic signals are highly dependent on the modulation index that in this case is set to 2.2 [6]. A general rule of thumb is that the 1f signal amplitude cannot be larger than the absorption dip in the direct signal. Thus, the expected

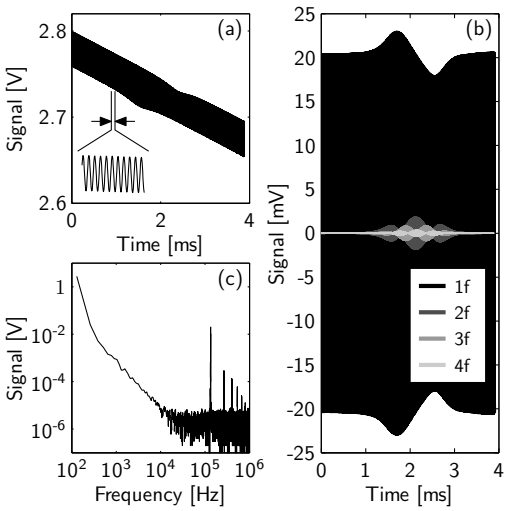

FIG. 4: Typical behavior of the recorded signal for a measurement of oxygen, based on wavelength modulation techniques, for 10 cm of air; 130 (1s) synchronously averages. Figure 4(a) shows the signal from the detector, Fig. 4(b) shows the bandpass filtered detector signals (3-pole Butterworth, 4 kHz bandwidth) of the detector signal, and Fig. 4(c) shows the spectral peak voltages based on a FFT of the detector signal presented in Figure 4(a). The spectral resolution of the FFT is 130 Hz. See text for more details.

fractional absorption may be used to calculate the needed dynamic range of the system. The absorption fraction for 10 cm of air corresponds to 2.45×10^{-3}. It is also shown

that the 3f and 4f signals (1.8 mV_{pp} resp. 0.7 mV_{pp}) are weak and that the RAM signal is strong compared to the peak-to-peak value for the 1f signal. Please note that the voltage indications pertain to a common scale in Fig. 4.

To get an overview of the recorded signal spectrum, a FFT of the data presented in Fig. 4(a) was carried out and presented in Fig. 4(c). The figure shows that the 1f signal (20 mV_p at 133 kHz) is about a factor of 100 weaker than the averaged signal from the detector (2.7 V). It is also shown that the system SNR, for 130 averages, is about 3×10^5. The SNR is measured at 133 kHz and with a measurement bandwidth of 130 Hz. Normally, SNRs are expressed in terms of a logarithmic (dB) scale according to

$$SNR = 20 \times \log_{10} \frac{V_{signal}}{V_{noise}},$$

where V_{signal} is the averaged detector RMS voltage level and V_{noise} is the RMS voltage level of measured noise. A SNR of 3×10^5 corresponds to a SNR of about 110 dB. If a high-pass filter is introduced, that suppresses signals below the 1f frequency, the required A/D dynamic range decreases with a factor of about 100 as shown in Fig. 4(c).

C. A/D Converter Resolution Impact

The free-running setup was used to study what impact the resolution of an A/D converter has on a coherent measurement system for spectroscopy. A number of streaming and scanning 2f detection measurements were performed for an ambient air distance of 10 mm. This corresponds to a fractional absorption of 2.45×10^{-4}. Four measurements, each recording during 1 minute (7800 scans) were done. The sample signal and high-pass sample signal were streamed to a hard disc at 2.469 MS/s. Raw data were stored, for each measurement, with different resolutions that corresponds to 8, 10, 12, and 14 bits of the A/D converter. By default, the A/D board has 14 bit resolution but this may be decreased by software during a streaming measurement (based on an application example provided by National Instruments). Thus, the impact of different A/D converter resolution could be studied. The streamed data were read from the disc, averaged, and lock-in detected. In Fig. 5 the 2f signals for a resolution of 8 and 14 bits are presented.

As can be seen in the left hand side of Fig. 5, an 8-bit A/D converter cannot resolve the oxygen absorption line even though 100 averages are performed. An absorption dip of 2.45×10^{-4} requires a dynamic range of the A/D converter of about 72 dB ($20\log(1/2.45 \times 10^{-4})$) to reach a SNR of one. However, an 8-bit A/D converter has only a dynamic range of about 48 dB and is too poor to resolve absorption lines in this test setup even though long time averaging is used. If more bits are used the absorption dip may be resolved, even with few or no data averages. 14 bits are enough to resolve an absorption dip of 2.45×10^{-4} since its theoretical dynamic range is about 86 db. 100 averages increases the dynamic range with an additional factor of 10 (20 dB).

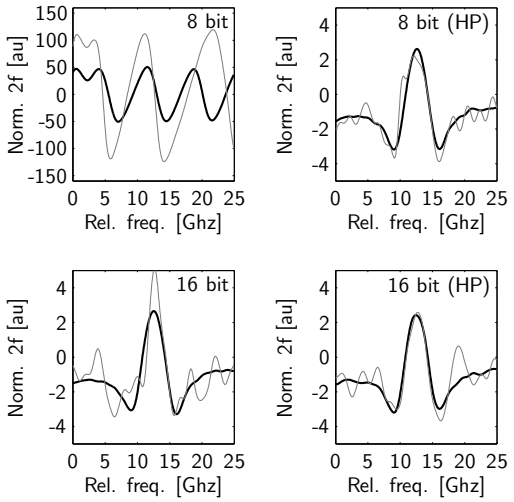

FIG. 5: Streaming measurements on 1 cm of ambient air (fractional absorption of 2.45×10^{-4}) with the free-running setup based on different A/D resolutions and signal filtering. The 2f signal for the P11P11 oxygen line at about 764.3 nm is measured for two different average settings; 1 (grey line) and 100 averages (block line). To the left the 2f signal, based on 2f detection on the sample signal, is shown for different A/D resolution and and measurement time. To the right similar data based on 2f lock-in detected high-pass filtered sample signals are shown.

The performance may be increased by the use of dithering [21] or high-pass filtering [19] as shown in the right hand side of Fig. 5. It can be seen that similar performance is reached regardless if a 8-bit or a 14-bit AD converter is used. If high pass filtering is used a weak absorption line (1×10^{-6} to 1×10^{-8}) should be possible to detect by using a 14-bit or a 16-bit A/D converter. In the right hand side of Fig. 5, it can also be seen that single scan data are not necessary improved by introducing more bits. This is due to the fact that data from one scan are heavily affected by mechanical vibrations introduced by vibration motors. Small vibration motors are mounted in the test setup in order to shake the laser and the detector to minimize persistent fringe generation.

III. SYSTEM CALIBRATION

The standard addition method was used to calibrate and to test the linearity and noise behavior of the sys-

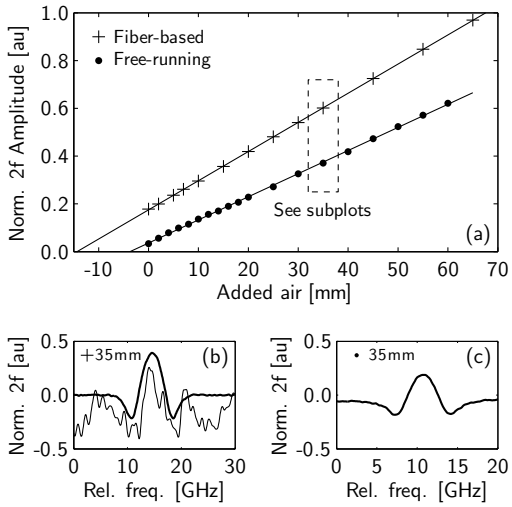

FIG. 6: a) Standard addition measurement results from the free-running and fiber-based measurement setups. Ten measurements (20 s measurement time) were made at every air distance ranging from 0 to 65 mm. b) Typical behavior of the 2f signal in the fiber-based setup for an air distance of about 35 mm. The figure shows the 2f signal of the sample signal (thin line) and the evaluated balanced signal (bold line). c) Typical behavior of the 2f signal in the free-running setup for an air distance of about 35 mm.

tem [22]. The method is based on adding a known ambient air distance between the laser and the detector and monitoring the amplitude of the 2f signal, divided by the DC level of the direct signal. The signal increases linearly as also shown in Fig. 6. The estimated air offset of 4 mm, in the free-running setup, is due to the fact that it is not possible to mount the detector directly connected to the the laser in the free-running setup. The estimated air offset of 14 mm in the fiber-based setup is due to air inside the collimator package used. It is possible to evaluate 1f-4f signals out of one measurement data file, since data are recorded synchronously almost 20 times for each modulation signal period. The figure also shows typical recorded signals of the 2f signal for an air distance of about 35 mm for the fiber-based and the free-running setup. As shown in Fig. 6(b), the 2f sample signal in the fiber-based setup is heavily distorted. The distortion is due to optical interference effects frequently occurring in pigtailed lasers. Periodic noise and fringes can be handled by using so-called balanced detection [22]. By detection of both the sample and reference beams synchronously, a balanced 2f detection signal is evaluated as shown in Fig. 6(b).

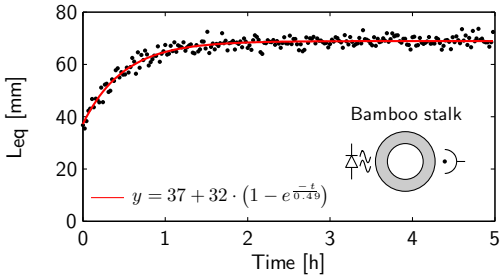

FIG. 7: Measurement on nitrogen discharge in a bamboo stalk with a diameter of 18 mm. As shown in the figure the 2f signal starts at an offset that corresponds to 37 mm of ambient air. This is partially due to that the stalk is mounted with some separation to the laser and the detector. Thus, light also passes ambient air, not only the stalk.

IV. APPLICATIONS

A. Gas Discharge Measurements on a Bamboo Stalk

To show the strength of using the digital lock-in detection system, we performed test measurements. The oxygen content inside a bamboo tree stalk was measured. Similar studies on wood have been carried out before, using a traditional spectroscopy measurement setup, based on desk-top analog lock-in amplifiers [23, 24]. The purpose of our measurements was to briefly show how the hollow compartment, inside a bamboo stalk, interacts with ambient air. The stalk of a bamboo consists of hollow jointed compartments. We performed measurements on a 23 cm long stalk with an inner diameter of 11 mm. The external diameter was in the order of 18 mm. Before the measurement was started the bamboo stalk was exposed to a non ambient gas by placing it in a bag containing nitrogen for 72 hours. Figure 7 shows the free-running measurement arrangement and also experimental data, showing that the discharge of nitrogen has a time constant of about 30 minutes.

The light reaching the APD detector is only in the range of 0.3 μW or 0.1 percent of the emitted light from the laser. Initial measurements showed noisy signals and no pure 2f signal could be detected for 20 s of averaging. This is due to interference fringes that appear between the laser, the bamboo stalk, and the detector. Small vibration motors were mounted on the laser and the detector in order to shake the test setup to minimize persistent fringe generation that otherwise overrides the 2f oxygen signal. Even though each measurement point in Fig. 7 is based on 20 s of averaging (2600 scans), measurement data still fluctuate. This could be the result of changing motor speed, backscattered light, interference fringes etc. that add noise and intensity fluctuations.

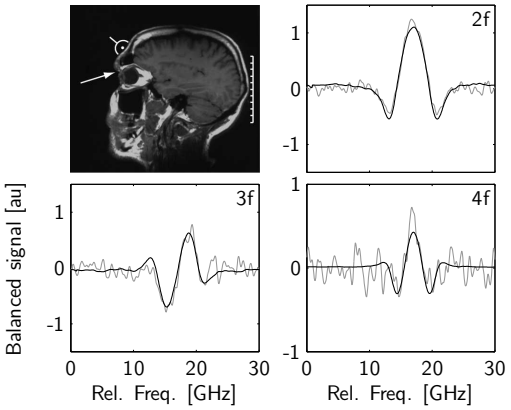

FIG. 8: Measurement on frontal sinuses on a healthy volunteer. The strength of the signal corresponds to an ambient air distance of 13 mm. The figure shows the behavior of the 2f - 4f signals for one measurement (60 s averaging). See text for more details.

B. Human Frontal Sinus Measurements

The frontal sinuses are air-filled cavities in the frontal bone in humans. Measurements on the frontal sinuses, on a healthy volunteer, were performed with the fiber-based setup. This setup was chosen since the measurement requires a device that may be positioned at any point on the human body. The tip of the fiber was positioned onto the caudal part of the frontal bone while the APD detector was positioned on the forehead about 3 cm from the fiber. The light that reaches the APD detector, was only in the region of 0.15 μW or 0.2 percent of the emitted light from the laser. Measurements, based on 60 s averaging, show a 2f signal that corresponds to an ambient air distance of 13 mm. The result is in agreement to what is reported in Ref. [25]. As expected, the SNR of the 2f signal is higher than for the 3f, and 4f signals as shown in Fig. 8. Expected measurement time, to get a signal with an appropriate signal quality, should be 10-30 s. Commonly, fringes dominate the noise floor and in some cases the 4f signal contains less such noise than the 2f signal [26]. Thus, the 4f signal may be a better choice for data analysis, in the case of large interference fringes. Still, the 4f analysis requires more light or less attenuation by the sample. This is due to the fact that the signal level of the 4f signal is lower than the 2f signal to a factor of 5 as shown in Fig. 4.

V. DISCUSSION

The CH-3150 board was chosen since it has a fast arbitrary generator onboard that may be used to modulate the laser. Any modulation frequency from direct current (DC) to several MHz may be created without loading the computer central processor unit (CPU). The two onboard analog input channels may be used to coherently sample detector signals at the same time. Thus, this board would be adequate to develop a flexible, powerful, cheap, and compact trace gas analysis system. This system may be used in general gas spectroscopy and in applications with fast changing environments such as in combustion measurements requiring a modulation ramp frequency in the order of 1 kHz. However, since four input channels were required for balanced-detection to suppress fringes, a second board was introduced (NI-6132) that contains four synchronized A/D converters clocked by the CH-3150 board. The clock signal and the waveform sync signal were fed to the A/D board via two coaxial cables mounted inside the computer. This action was taken to suppress noise and prevent cross talk between the clock and the detector signals.

Even though this system may be run incoherently, like an ordinary PC-based lock-in detection system, coherent sampling is used since that removes the requirement to lock-in data in real-time. Data can thus be averaged in real-time coherently and data may be processed after the averaging is finished or stored for later analysis. The user is free to analyze data in the time domain or frequency domain. This opens for the possibility to analyze signals from several channels and perform baseband analysis and lock-in detection (1f-4f) on the same data set. The current solution corresponds to the performance of standardized digital lock-in amplifiers. However, with this setup, baseband detection, 1f-4f detection, and fast ramp frequencies (4 Hz to 1 kHz) could be used by running different software applications without any hardware changes. The solution is compact and installed in an ordinary PC.

If higher performance is needed, high-pass filtering of the detector signal increases the dynamic range of the signal detection, since most of the low-frequency signals (below 1f) are thus suppressed. When this technique is used, the resolution requirement of the A/D converter is not critical. It should be enough to use a 12-16 bit A/D converter even for applications requiring a fractional absorbance of about (1×10^{-7}). The output resolution of the D/A converter is 12 bits, which adds quantization noise even though the CH-3150 board has analog reconstruction filters onboard. It is difficult to estimate how this limitation affects the resolution of the system since amplitude noise at the laser input is converted into amplitude and frequency variations in the laser at the same time. Still, since coherent sampling is used, quantization errors of the D/A converter are not averaged out by a coherent sampling system due to the fact that the D/A quantization error is seen as periodic noise. By replacing the laser and the detector with one resistor, the D/A quantization error impact of the system can be studied. The resistor value corresponds to the dynamic resistance of the laser which in this case is about 270 Ω. Initial

measurements show that the noise floor of the 2f signal, measured on the resistor, corresponds to an ambient air distance of 0.1 mm (2.45×10^{-6}) or lower. This is an estimation only, since measurements on scattering material such as tissue or wood have been limited by the interference fringes.

Another way to improve the performance of the system is to replace the current DAQ boards with boards with higher resolution. As an example a second measurement was performed to measure the laser noise using a 24-bit data acquisition board (NI-4472, National Instruments). The use of this board resulted in lowering the noise floor at 10 kHz with additional 30 dB. However, this board is too slow (about 100 kHz sampling frequency) for ,e.g., combustion measurements and it is not possible to clock it externally. Thus, this board may not be used in a coherent sampling system. It is also possible to add input channels by replacing the A/D board with a board with, for example, eight input channels. If a cheaper solution is needed, standardized external sound cards may be used. Today, these devices have excellent performance with 24-bit resolution A/D and D/A converters. The only drawbacks are that the sampling clock is limited to 196 kHz and no DC level can be measured. Still, this solution may be adequate in some applications.

VI. SUMMARY

By the use of plug-in boards for standardized computers, a powerful and flexible detection system for gas spectroscopy was developed. One of the greatest advantages with the system is that raw data, from a number of channels, may be streamed and stored on disc by the use of free-running and standardized software. There is no need for special designed computers, FPGAs, or embedded solutions. Coherent sampling allows that raw data may be analyzed at real-time or post-processed in the time- or frequency domain. It is our experience that the current system is limited by interference fringes in the optical setup.

VII. ACKNOWLEDGEMENT

This work was supported by the Swedish Research Council and the Knut and Alice Wallenberg Foundation. The authors are grateful for Lars Rippe for sharing his expertise in measurement technology.

[1] P. Werle, Spectrochim. Acta Part A **54**, 197 (1998).
[2] G. Galbcs, Appl. Spectrosc. Rev. **41**, 259 (2006).
[3] M. Allen, Meas. Sci. Technol. **9**, 545 (1998).
[4] K. Song and E. C. Jung, Appl. Spectrosc. Rev. **38**, 395 (2003).
[5] D. T. Cassidy and J. Reid, Appl. Opt. **21**, 1185 (1982).
[6] J. Reid and D. Labrie, Appl. Phys. **26**, 203 (1981).
[7] G. C. Bjorklund, Opt. Lett. **5**, 15 (1980).
[8] D. T. Cassidy and J. Reid, Appl. Phys. B **29**, 279 (1982).
[9] J. Silver, Appl. Opt. **31**, 707 (1992).
[10] R. Alonso, F. Villuendas, J. Borja, L. A. Barragn, and I. Salinas, Meas. Sci. Technol. **14**, 551 (2003).
[11] Integrated lockin amplifier for sensor applications (European Solid-State Circuits Conference, 1999).
[12] P. Vogel and V. Ebert, Appl. Phys. B **72**, 127 (2001).
[13] T. Fernholz, H. Teichert, and V. Ebert, Appl. Phys. B **75**, 229 (2002).
[14] P. Werle, R. Miicke, and F. Slemr, Appl. Phys. B **57**, 131 (1993).
[15] R. Rosing, H. Kerkhoff, and R. Tangelder, J. Electron. Test. **14**, 67 (1999).
[16] P. Heinonen, T. Saramaki, J. Malmivuo, and Y. Neuvo, IEEE Trans. Circ. Syst. **31**, 438 (1984).
[17] M. E. Takanen, Ph.D. Thesis, Helsinki University of Technology Department of Electrical and Communications Engineering Laboratory of Acoustics and Audio Signal Processing (2005).
[18] C. Thibon, F. Dross, A. Marceaux, and N. Vodjdani, IEEE Photon. Technol. Lett. **17**, 1283 (2005).
[19] R. Engelbrecht, Spectrochim. Acta Part A **60**, 3291 (2004).
[20] X. Zhu and D. T. Cassidy, J. Opt. Soc. Am. B **14**, 1945 (1997).
[21] J. Reid, M. El-Sherbiny, B. K. Garside, and E. A. Ballik, Appl. Opt. **19**, 3349 (1980).
[22] L. Persson, F. Andersson, M. Andersson, and S. Svanberg, Appl. Phys. B **87**, 523 (2007).
[23] M. Sjöholm, G. Somesfalean, J. Alnis, S. Andersson-Engels, and S. Svanberg, Opt. Lett. **26**, 16 (2001).
[24] J. Alnis, B. Anderson, M. Sjholm, G. Somesfalean, and S. Svanberg, Appl. Phys. B **77**, 691 (2003).
[25] L. Persson, M. Andersson, M. Cassel-Engquist, K. Svanberg, and S. Svanberg, J. Biomed. Opt, in press (2007).
[26] P. Kluczynski and O. Axner, Appl. Opt. **38**, 5803 (1999).